Author:
McNamara, Keri

Title:
Using lake sediment records to reconstruct volcanic histories

Examples from Aluto and Calbuco Volcanoes

USING LAKE SEDIMENT RECORDS TO RECONSTRUCT VOLCANIC HISTORIES: EXAMPLES FROM ALUTO AND CALBUCO VOLCANOES

Keri A. McNamara

Supervisors: Katharine V. Cashman & Alison C. Rust

A dissertation submitted to the University of Bristol in accordance with the requirements for award of the degree of Doctor of Philosophy in the Faculty of Science

School of Earth Sciences

December 7, 2018

Word Count:

35,376

ABSTRACT

Here I present a study of lake core deposits at two volcanic centres. The primary motivation of the study is elucidating the eruptive history of Aluto volcano in Ethiopia using tephra layers deposited into lakes. This is undertaken in two ways (1) a tephrostratigraphic study of Aluto Volcanic Complex and (2) a study of how deposition of volcanic material into lakes affects the sedimentation of particles and the subsequent deposit.

The study of tephra layers at Aluto involves two lake sediment cores which contain 20 and 25 individual tephra layers in Holocene-age sediment, equating to an eruption frequency of one eruption every ~250 years. Glass in the tephra layers is chemically-similar, making correlating the cores challenging using traditional methods. Instead, the five tephra layers are correlated between the cores (five in each core) using the proportions of different ash component types and textures, particularly microlite-containing fragments and glass shards combined with trace element data. The componentry results also reveal information about the eruption style and timing, with eruptions producing microlite-rich tephra clustered temporally.

The results of the two lake cores are also expanded and applied to tephra layers sampled on land from amongst palaeolake sediments deposited during lake highstand periods. The tephra layers are correlated in the same way with two other land sections, allowing some basic interpretations of eruption size; thickness and grain size data imply that the deposits were the product of Vulcanian to sub-Plinian sized eruptions. However, expanding the correlations presented challenges in the form of inconsistent glass chemistry, with the glass composition of Holocene tephras in more proximal sections inconsistent with the core tephras, and varying with the environment of preservation.

However, drawing interpretations about eruption size and style from tephra deposits in lakes relies on the lake records being a true representation of the fallout deposit. Consequently, this study explores the potential influences of lakes on tephra from the comparably-sized eruption of Calbuco in 2015 in Chile. The eruption deposited tephra in several lakes, which were cored and then compared to tephra on land. Overall I find that the Calbuco lake and land tephras are comparable, with the exception of tephra sampled from within 300m of a fluvial inlet.

The investigation into the settling of tephras is coupled with simple experiments involving the Aluto tephra, which comprise high proportions of low-density pumice. For many of the deposits, a percentage of the pumice floats when placed in water, before sinking over the course of hours to days before settling on top of the deposit. However, the deposits at Aluto virtually never display large pumices at the top and regularly show grading, both normal and reverse in consecutive deposits. As a result, I investigate reasons for the implied rapid sinking of pumice, including the effect of heat and the pumice permeability and structure.

Author's Declaration

I declare that the work in this dissertation was carried out in accordance with the requirements of the University's Regulations and Code of Practice for Research Degree Programmes and that it has not been submitted for any other academic award. Except where indicated by specific reference in the text, the work is the candidate's own work. Work done in collaboration with, or with the assistance of, others, is indicated as such. Any views expressed in the dissertation are those of the author.

.....

Keri McNamara

December 7, 2018

Acknowledgments

As with every thesis, I cannot take full credit for its completion- I simply couldn't have done it without the stalwart help of so many people.

Firstly, to my supervisors Kathy Cashman and Alison Rust, for being unbelievably supportive over the years, from my MSci to the PhD. I am incredibly grateful for the time and effort they afforded me and am so thankful for the fantastic opportunity they gave me with this PhD. I am truly honoured to have such amazing scientists as my mentors.

I am fortunate to have been supported by a studentship as part of the Natural Environment Research Council large grant 'RiftVolc' (NE/L013932/1) . I am grateful to the RiftVolc community, in particular Karen Fontijn and the rest of WP1, for their ideas and advice which helped develop this PhD.

I have been lucky enough to do fieldwork in some amazing places and am grateful to Amdemicheal Zafu, Firawalin Dessalegn, Javier Cerda and Leonora Jarpa for sharing not only their beautiful countries with me, but also for their help, knowledge and advice in the field. I would also like to thank Gezahegn Yirgu, Angelo Castruccio and Ana Abarzùa for their collaborations and contributions.

A huge thanks to everyone who has helped me at Bristol University, in particular Stuart Kearns and Ben Buse for their patience and time with the microbeam facilities. Also to my fabulous research group (past and present), especially Emma Liu, Hannah Buckland, Jen Saxby, Claudio Contreras and Frances Boreham for their ideas and input. I must also thank everyone at the Cabot Institute, specifically Amanda Woodman-Hardy for championing my science-writing dreams!

I am also incredibly grateful to Jo Tooze, Richie Moore, Evie Snee, Megan Sanderson, Mahzabeen Mahfuz and Lucy Rudd for giving up some of their precious summer break to volunteer in the lab. There is no way I could have produced the huge amount of clast data without their enthusiasm and dedication.

Also, to my 'colleagues'; Nicky, Becky, Ery, Ryan and Neil, I could not have done it without you. You have been with me through the worst and best of days and our tea breaks, pub trips and various other escapades have made this PhD a truly unforgettable experience. I am so grateful for your friendship and support.

I could not finish this without thanking the other lovely people who have helped along the way; especially Hannah and Beccy for encouraging me (and feeding me!) to the last. I also thank my parents for their generosity and support. I'm so grateful to you all! Finally to Nick, (who's put up with me at my grumpiest) for his unwavering belief in me.

Contents

List of Figures

List of Tables

Chapter 1

Introduction

1.1. Aims and motivation

This thesis investigates the features, uses and reliability of lake sediments as a tool to investigate volcanic processes. Specifically, this study focusses on reconstructing volcanic histories in environments where the only evidence is preserved in lake records. The fundamental goal is to use the lake sediments to construe information about eruption properties to inform and improve hazard assessment.

While this thesis employs lake sediments from two volcanic settings, the initial motivation was to elucidate the recent behaviour of surprisingly active and comparatively understudied Aluto Volcanic Complex (or Aluto volcano) in central Ethiopia. The aim is to develop a more comprehensive understanding of the Holocene eruptive history which has been subject to few dedicated studies. There have been no documented historic eruptions at the centre and, prior to this work, little was known about the volcano's recent behaviour.

Broadening the limited insights of activity of Aluto Volcano and other volcanoes of central Ethiopia is hindered by the poor terrestrial preservation of medial and distal volcanic material; a lack of exposure and restricted accessibility. The climate is semi-arid with little topography or vegetation meaning volcanic material on land is prone to resuspension. As a result, perhaps the most constructive source of information on Aluto's Holocene behaviour are two lake cores sampled within 30 km of the volcano's edifice which preserve multiple layers of volcanic material (tephra). To maximise the utility of these lake cores, and to ensure they represent an authentic record of eruptive activity, this thesis undertakes a detailed study of the fidelity of tephra layers preserved in lakes.

This involves a tephrostratigraphic study of the Aluto tephras and information about eruption timing, frequency and size presented (Chapters 2 and 3). This is accompanied by an investigation of tephra sedimentation from the 2015 eruption of Calbuco volcano in Chile which, in contrast to the Aluto eruptions, is very well understood. The volcanic material deposited in the lakes is compared to that deposited on land, and the results considered in the context of the Calbuco eruption (Chapter 4) as well the implications for deposition from Aluto (Chapter 5).

1.2. Background

1.2.1. Tephrostratigraphy

The word 'Tephra' comes from the Greek for 'ashes' and is the foundation for the fields of Tephrostratigraphy and Tephrochronology. Tephra is a volcanic product, formed from deposits of fragmented material ejected from a volcano during eruption and can be a rich and diverse source of information for a wide range of disciplines. Tephrochronology traverses many facets of earth science from climatology to volcanology and advances in the field can contribute a wide range of scientific challenges.

When a volcano erupts, the speed and temperature of the ejected material results in a buoyant ash

plume comprising a mixture of hot rock and gas, which rises until it reaches neutral buoyancy (e.g. Wilson et al., 1978; Bursik, 1996, 2001). Depending on the size and duration of the eruption, material in the cloud can be carried hundreds to thousands of kilometres from the source by atmospheric processes (e.g. Haflidason et al., 2000; Ponomareva et al., 2015; Fontijn et al., 2016). While the cloud spreads, the volcanic particles fall through the atmosphere at a speed related to their size, density and shape, and are deposited in the surrounding environment, providing a record of the eruption as long as the deposit is preserved.

The fundamentals of tephrochronology assume that resultant tephra layers are deposited effectively instantaneously (relative to the rate of deposition of sedimentary material either side) and act as a chronostratigraphic framework for the sedimentation of entire geological sequences. While a physical volcanologist will use tephra layers to unravel information about eruptive behaviour, an archaeologist or palaeoclimatologist may use tephra layers to constrain information about the sediment surrounding it.

Regardless of the scientific objective, tephrochronology requires characterisation of features of a tephra layer that can be used to identify corresponding tephras from the same eruption in different locations. This typically involves geochemical signatures, particularly glass geochemistry (e.g. Davies et al., 2003; Tryon et al., 2008; Vogel et al., 2010; Lowe, 2011; Davies, 2015) but can also include the features of the accompanying crystal population (e.g. Shane et al., 1998; Fierstein, 2007; Smith et al., 2011; Rawson et al., 2015), or textural and morphological features (e.g. Cioni et al., 2008; McNamara et al., 2018, Chapter 2 of this thesis).The range of methodologies used to fingerprint tephra deposits is discussed in more detail in Chapter 2.1.1. Correlating tephra deposits from a temporally well-constrained eruption means a deposit can be used as a chronostratigraphic marker for dating across multiple locations (e.g. Mangerud et al., 1984; Pyle et al., 2006; Davies et al., 2014; Lane et al., 2014). In the study of volcanic hazards, information from a collective dataset of correlated layers can be used to make estimates about properties of the eruption that produced them.

1.2.2. Using tephra to infer eruption properties

It is well known in physical volcanology that the grain size and thickness of tephra fallout deposits are determined by the eruptive column height, the eruption duration and the strength and direction of the wind (e.g. Eaton, 1963; Walker, 1981; Carey and Sparks, 1986; Pyle, 1989; Burden et al., 2011). For this reason, the use of tephra fallout data to reconstruct the eruptive conditions that produced them has been applied using multiple methodologies to a plethora of eruptions.

While the mechanisms of inversion of deposit properties for eruption parameters have varied, the underpinning principles have remained the same. Firstly, that thicker and coarser deposits occur below the dispersal axis of the ash cloud, and secondly, that deposits thin and fine with distance from the volcanic source. In each case these are controlled by (1) the unique wind conditions at the time of eruption and (2) the magnitude and intensity of the eruption. Perhaps the biggest

challenge in such studies, is distinguishing the effects of one from the other.

A number of techniques have been employed to this end, all of which involve measuring the thickness and/or the grain size of deposits at multiple locations (e.g. Pyle, 1989; Bonadonna et al., 1998; Bonadonna and Costa, 2012; Burden et al., 2013; Longchamp et al., 2011). More detailed information on reconstructing eruption features from fallout deposits can be found in Chapters 2.1.2 and 3.1. Because these methods are so reliant on accurate measurements of grain size and thickness, it is important to ensure that the environment of deposition has not influenced them. In the case where the only tephra records are from lake records this is particularly pertinent.

1.2.3. Lake sediment cores

Cores of sediments from the bottom of a lake provide a lacustrine equivalent of a terrestrial stratigraphic section. Lake records can contain information about a wide range of processes and, in volcanic settings, preserve sedimentation from tephra fallout that was been deposited into the water column. Lake cores can present advantages over land sections when used for elucidating volcanic histories; there is evidence to suggest that once emplaced, deposits are less likely to be disturbed or re-suspended (e.g. Lowe, 2011; Engwell et al., 2014; Fontijn et al., 2014). Consequently, lake cores have been widely used for both physical volcanology and tephrochronology. More detailed information on the use of lake cores is presented in Chapter 4.1.

However, the integrity of lake cores has also been shown to be affected by lacustrine and fluvial processes. In particular, the secondary input of volcanic material from the fluvial system, can thicken tephra deposits post-eruption (Thompson et al., 1986; Bertrand et al., 2014). Also, some pyroclasts with high vesicle-content (vesicularity) are of sufficiently low density to float, which may delay their settling into the water and allow redistribution by water currents (e.g. Frick and Kent, 1984; Von Lichtan et al., 2016). For these reasons, developing criteria for establishing whether lake tephra deposits represent the same record as the deposits on land is an important aspect of using lake cores for physical volcanology.

1.3. Geological and tectonic setting

The two volcanoes investigated in this thesis, Aluto volcano in Ethiopia and Calbuco volcano in Chile, arise from very different tectonic settings. As a result, the volcanism exhibited by the two volcanoes is different; specifically, the composition of the erupted products and the type of eruption. The key aspects of the settings which produced the types of volcanism studied are summarised below.

Figure 1.1: DEM of Africa constructed from ASTER GDEM (a product of METI and NASA). Red areas indicated areas of high-density faulting. Location of faults in the MER downloaded from http://ethiopianrift.igg.cnr.it/utilities.htm.

1.3.1. Ethiopia

Aluto volcano is one of ~60 volcanoes in Ethiopia, many of which have been reported as high risk due to the limited knowledge of typical eruptive behaviour. The volcanic regions in Ethiopia are populated, with an estimated 40 million people living within 100 km of an active volcanic centre (Aspinall et al., 2011). In addition, volcanism in East Africa is highly unusual and comprises unique styles of volcanism making studies of the volcanic hazard pertinent from both a geological and social perspective.

The tectonic system responsible for the activity is the East African Rift System (EARS), which is one of only two continental-continental rift systems in the world. Ethiopia lies at the northern end of the EARS; the Kenyan Rift Valley becomes the Main Ethiopian Rift in the southeast of Ethiopia before transitioning into the Afar triple junction in the northeast of the country. The area which comprises Aluto (and many of the high-risk silicic volcanoes) is the Central Main Ethiopian Rift (CMER; Fig. 1.1)

Volcano-Tectonic activity in the Main Ethiopian Rift (MER) began approximately 30 million

years ago in the form of plateau uplift inducing flood basalts which were erupted through Mesozoic sandstones and Precambrian basement rocks (Kamzin et al., 1980; Chernet et al., 1998). This triggered the activation of broadly rift-parallel segmented boundary faults ~6 Ma (Bonini et al., 2005) that encompass contemporary lake basins and the rift-centric region, including Aluto volcano (Abebe et al., 2005). After the abandonment of these Eocene boundary faults, the most recent 2 Ma has seen the formation of the Wonji fault belt, a series of echelon faults sub-parallel to perpendicular to the boundary faults and associated mafic volcanism (Oxburgh and Turcotte, 1974; Ebinger and Casey, 2001; Corti, 2009).

Volcanism in the CMER is typically bimodal with unevolved basaltic scoria cones near large silicic centres, coupled with gradual, whole-rift compositional changes. The diversity of volcanic activity in Ethiopia is attributed to spreading rates; oceanic spreading at the Afar triple junction produces a theolitiic composition while the MER produces more alkali volcanics as a consequence of slower continental spreading rates. Additionally, strain rate is particularly influential, whereby low strain rates allow for magmatic emplacement in the middle and upper crust, leading to differentiation and more evolved volcanism (such as that displayed at Aluto).

Conversely, high strain rates create fractures which provide pathways for unevolved basaltic magmas to erupt (Mazzarini et al., 2004). The two types of volcanism do not appear to be temporally or spatially linked and there is little to suggest they originate from the same crustal magmatic system in recent times (e.g. Peccerillo et al., 2003; Hutchison et al., 2016c). The detailed petrological story of how mid-rift silicic peralkaline melts evolve is somewhat unresolved although it is thought they are most likely a consequence of partial melting of a basaltic lower crust followed by considerable crystal fractionation (e.g. Gasparon et al., 1993; Pik et al., 1998; Peccerillo et al., 2003). This has been reinforced by more recent petrological modelling of Aluto and isotope data from MER rhyolites (Trua et al., 1999; Gleeson et al., 2017).

1.3.2. Aluto

As a consequence of the complex crustal mechanics and the subsequent unusual magmatic evolution, silicic centres such as Aluto erupt rhyolites high in alkali content. Indeed, Aluto has erupted predominantly rhyolites of peralkaline composition, which comprise high SiO_2 ($70-80$ wt%.) and with alkali content relative to aluminium oxide greater than unity; (Na_2O + K_2O) / Al_2O_3 = >1; Hutchison et al., 2016c; Gleeson et al., 2017; Fontijn et al., 2018). The high proportion of alkalis has a depolymerising effect, where alkali oxides break up the silicate networks chains responsible for high viscosities in typical rhyolites (e.g. Hess et al., 1995; Dingwell et al., 1998; Di Genova et al., 2013). The result is a high silica magma with a comparatively low viscosity which can produce pumice cone deposits, which form in a similar fashion to mafic scoria cones.

Since first activity at ~500 ka, Aluto has undergone one or possibly two caldera forming eruptions at ~306 to 316 ka. The more recent activity is less well constrained although it is thought to comprise smaller eruptions which produced pumice cones and lava flows found inside

the edifice, although these are poorly temporally constrained (Hutchison et al., 2016c; Fontijn et al., 2018). More detailed information about the recent volcanic history of Aluto is explored in Chapter 2.1.

1.3.3. Chile

Chile is home to 90 active volcanoes which occur as a result of the subduction of the Nazca and Antarctic plates under the South American plate. Much of the country comprises the Andean volcanic belt which is separated into four volcanic zones; the Northern, Central, Southern and Austral Volcanic Zones.

The Southern Volcanic Zone (SVZ), which comprises Calbuco, is marked to the north by the edge of the subducted Juan Fernandez ridge, while the southern end comprises the Chile rise triple junction. The zone comprises a fault system which exhibits right lateral movement and overlies a comparatively thin (~30 km) crust (e.g. Gilbert et al., 2014; Hickey-Vargas et al., 1995). The orientation of the fault system is responsible for the location much of the volcanism (~20 different centres), which comprise mostly basaltic products, although more evolved compositions are also observed, for example at Calbuco volcano.

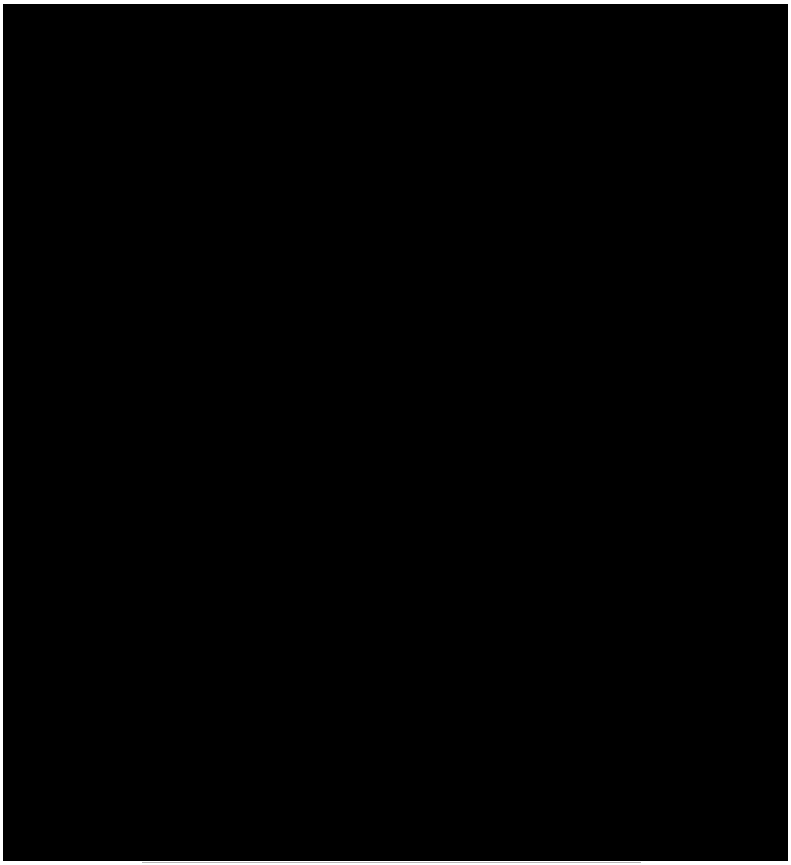

Figure 1.2: DEM of South America constructed from ASTER GDEM (a product of METI and NASA). Approximate locations of key tectonic and volcanic features are displayed. The black triangle indicates the location of Calbuco.

Calbuco

Calbuco has erupted predominantly Andesitic products in recent times. Activity began at ~300ka in the form of basaltic andesite lavas and breccias. In the last 100 ky, the volcano has produced andesitic to dacitic lavas, pyroclastic density currents (PDCs) and lahars. Holocene activity has comprised a number of basaltic to dacitic eruptions marked by lava dome growth and associated PDCs, lahars and block and ash flows (Selles and Moreno, 2011; Lopez-Escobar et al., 1995; Romero et al., 2016; Castruccio et al., 2016). More detailed information about recent activity of Calbuco is discussed in 4.2.1.

1.4. Work undertaken

This thesis comprises four science chapters (Chapters 2-5), each of which involves the use of lacustrine tephra deposits. The original intention was to include a more detailed study of the Aluto tephra deposits. However, this has been limited largely due to safety concerns preventing fieldwork in central Ethiopia in 2016. As a result, the decision was made to pursue a more general understanding of tephra deposition in lakes.

Chapters 2 and 3 comprise studies of the Aluto tephras, with the primary aim of correlating them in the cores and with tephra deposited elsewhere. These chapters summarise studies that correlate deposits when major element glass geochemistry is homogeneous; specifically using the proportions of different components to fingerprint different deposits. They then use the information to place constraints on eruption size, style and frequency. This is coupled with an investigation into the effects of the environment of preservation on the glass composition and hydration. Finally, I performed some simple ash dispersion forward modelling as an example of the potential impact of an eruption at Aluto.

The 2015 eruption of Calbuco presented a good opportunity to assess the fidelity of the stratigraphy of tephra deposited in lakes. The eruption was recent, well studied and featured multiple measurements of terrestrial grain size and thickness taken shortly after the eruption. Crucially, the volcano's location in Chile's Lake District and meteorological conditions during the eruption led to primary tephra deposition into multiple lakes. Furthermore, the eruption appeared to be a good analogy for Aluto; isopach maps indicate that the thickness of tephra in surrounding lakes was broadly comparable to thicknesses of tephra in the Aluto lake cores. Consequently, Chapter 4 comprises a study of the tephra deposited by the Calbuco eruption in three different lakes of varying sizes. The deposits' stratigraphy and particle settling regimes are considered in the context of the location of the cores relative to fluvial input and the lake depth.

Chapter 5 builds on some of the outcomes of Chapter 4, with specific application to Aluto. This chapter investigates the settling of the Aluto particles, which are considerably less dense than the Calbuco product. Most of this chapter comprises simplified laboratory experiments of particles settling in water and represents the least-well developed chapter in the thesis.

Chapter 2

Using Lake Sediment Cores to Improve Records of Volcanism at Aluto Volcano in the Main Ethiopian Rift

K. McNamara, K. V. Cashman, A. C. Rust, K. Fontijn, F. Chalié, E. L. Tomlinson and G. Yirgu, Using Lake Sediment Cores to Improve Records of Volcanism at Aluto Volcano in the Main Ethiopian Rift, *Gcubed*, (in press).

Author contributions and declaration: K. V. Cashman and A. C. Rust provided supervision. The data was acquired, processed and provided by K. McNamara. K. Fontijn provided assistance during core sampling, and suggestions for improvement of the manuscript before submission. F. Chalié provided access to the core facility, and permission to sample the cores. She also provided some general feedback on the final manuscript. G. Yirgu provided assistance with local terminology and feedback on the final manuscript. E. L. Tomlinson provided assistance using the LA-ICP-MS facility and feedback on the final manuscript. All content is included as displayed in the published paper, to aid with consistent presentation. The manuscript benefited from reviews by R. Cioni and editing by M. Edmonds.

ABSTRACT

Aluto is a silicic volcano in central Ethiopia, flanked by two large population centres and home to an expanding geothermal power plant. Here we present data from two lake sediment cores sampled 12 km and 25 km from the volcano, which record at least 24 distinct eruptions in the Holocene. Tephra layers from the two cores are correlated using a variety of techniques, including major and trace element geochemistry as well as textural and morphological features from SEM-BSE imaging. The purpose is to provide a Holocene reference section for further tephrostratigraphic studies of the volcano as well as to provide information on eruption frequency. The lake cores suggest that Aluto has had a variable eruption rate, with three eruption 'clusters' in the Holocene at ~3, 6.5 and 11 ka, with small Vulcanian to sub-Plinian eruptions separated by larger, Plinian eruptions. We infer that the smaller tephras are likely the product of pumice cone—and dome—forming eruptions. In addition, modern wind data suggest the likely direction of an ash cloud from Aluto is to the west and south west, which is towards population centres and is in agreement with thickness data from the cores. We conclude that current records underestimate the volcano's eruptive history and that hazard assessments should be updated accordingly.

2.1. Introduction

A report by Aspinall et al. (2011) that categorised levels of both volcanic hazard and uncertainty ranks 41 of the ~60 volcanoes in Ethiopia at the highest level of uncertainty, 11 of which also have the highest degree of population exposure. Interferometric Synthetic Aperture RADAR (InSAR) data show that many of these volcanoes in the Main Ethiopian Rift (MER) are actively deforming (Biggs et al., 2011; Hutchison et al., 2016a; Lloyd et al., 2018), some with associated seismicity (Wilks et al., 2017). One of these volcanoes – Aluto – is the target of this study.

Aluto is situated approximately 200 km from Ethiopia's capital city, Addis Ababa. The volcano is flanked by several population centers, including Ziway and Adami Tullu, which in 2007 had populations of ca. 43,600 and 10,000 respectively (World Bank Data Repository 2007). A geothermal plant inside the caldera of the volcano represents significant investment as well as a potentially important source of power for the region.

The risk to local populations and infrastructure underlines the need for additional data on which to build hazard assessments for Aluto volcano. Both the relative inaccessibility and poor terrestrial preservation of the volcanic products present challenges for retrieving details about individual eruptions. Indeed, the Smithsonian Global Volcanism Programme lists only one (poorly documented) Holocene eruption of Aluto around 2000 years ago. More recent studies indicate, in contrast, eruptive activity as recently as ca. 400 yr BP and at an average rate of an eruption every ~300 years (e.g. Hutchison et al., 2016c; Fontijn et al., 2018). Together, the recent signs of active deformation and seismicity, and the evidence of frequent eruptive activity, motivate our volcanological study of the Holocene tephra record.

Aluto forms part of the MER, a continental rift system bounded by faults on either side of a central plateau running from the northeast to the southwest of Ethiopia (Mohr, 1971; Ebinger and Casey, 2001; Corti, 2009, Figure 2.1). Scoria cones and basaltic lava flows dominate (although are not limited to) the rift margins while larger silicic centers, such as Aluto, punctuate the rift axis (e.g. WoldeGabriel et al., 1990; Abebe et al., 2007; Corti, 2009; Keir et al., 2015). The central volcanoes have erupted a range of compositions that include basalts and trachytes, although peralkaline rhyolites are most common (Mohr and Wood, 1976; Rooney et al., 2005; Hutchison et al., 2016a,b,c). Most of these centres experienced mid-Pleistocene caldera-forming eruptions followed by lower magnitude events, some of which have extended into the Holocene (Hutchison, et al., 2016c). Aluto and its most proximal volcanic neighbors, Shala and Corbetti, have all undergone such caldera-forming eruptions (Di Paola, 1972; Mohr et al., 1980; Hutchison et al., 2016b).

Shala caldera (approximately 40km south west of Aluto) has experienced limited post-caldera activity, with the possible exception of scoria cones to the south of the caldera (Mohr et al., 1980; Trua et al., 1999; Fontijn et al., 2018). There is also evidence of lower-magnitude post-caldera activity at the Tullu Fike complex immediately north of the caldera, which may be the source of late Quaternary pumice deposits located in the caldera walls (Mohr et al., 1980; Fontijn et al.,

Figure 2.1: Map of Aluto and surrounding area and its location in Ethiopia. Red circle indicates location of core ABII taken from lake Abijata (Chalié and Gasse, 2002). Blue circle indicates location of core LLIII taken from lake Langano (Gibert et al., 2002).

2018). In contrast, Corbetti, approximately 80 km south of Aluto, has ongoing seismicity and deformation that appear related to magmatic activity (e.g Biggs et al., 2011; Lloyd et al., 2018). It has produced several silicic Holocene eruptions, which have generated aphyric obsidian flows and/or pumice fall deposits and are documented in terrestrial sections and lake sediment cores up to 167 km from the volcano (Rapprich et al., 2016; Martin-Jones et al., 2017; Fontijn et al., 2018).

Aluto has erupted predominantly peralkaline rhyolites of pantelleritic composition, although initial trachytic flows began around 500 ka and preceded one, or possibly two, rhyolitic caldera-forming eruptions at ~306 to 316 ka (Hutchison et al., 2016b). There is little evidence of activity after this period, suggesting a possible hiatus until an eruption at ca. 55 ka of localised obsidian flows within the caldera and pumice cone-building events, the size and frequency of which are not well constrained (Hutchison et al., 2016b). Geophysical studies using magnetotellurics combined with well and core log data suggest that the shallow magmatic system at Aluto comprises a complex locked crystal mush below a geothermal reservoir (Gianelli and Teklemariam, 1993; Samrock et al., 2015). Combining these data with InSAR and soil CO_2 measurements suggests the hydrothermal system is fed by a (~4 km deep) magma reservoir which degasses via the geothermal reservoir in the upper 2 km of the volcano (Hutchison et al., 2016a). From this perspective, recent signals of inflation and subsidence (Biggs et al., 2011) may record cycles of fresh magma supply (causing inflation) followed by degassing (causing deflation).

There is only limited published information on the Holocene eruptive history except for descriptions of tephras in terrestrial sections on the edifice and to the west of the volcano where deep gorges expose Holocene-Pleistocene lacustrine sediments. A subset of these tephra deposits was chemically analysed and correlated by Fontijn et al. (2018), who proposed an initial Holocene tephrostratigraphic framework for the volcano. Holocene pyroclastic deposits are also present in more distal gorges and lake cores (Gasse and Street, 1978; Le Turdu et al., 1999; Benvenuti et al., 2002; Chalié and Gasse, 2002; Gibert et al., 2002) as well as in sediment cores from two lakes close to Aluto: Lake Abijata (Chalié and Gasse, 2002), and Lake Langano (Gibert et al., 2002). The timing, thickness and chemical composition of tephra layers in the cores has not been previously documented.

The Lake Abijata core (ABII) was drilled approximately 25 km southwest of Aluto (Fig. 2.1). Chalié and Gasse (2002) report eight pyroclastic layers and four layers of 'coarse sand' in the core log. Twelve ^{14}C dates were obtained from organic material sampled at regular intervals along the core, and indicate sediment deposition from ~0.2 to 11.4 cal. ka BP (Gibert et al., 1999), with pyroclastic layers present between ~4 and 12 cal. ka BP.

The Langano core (LLIII) was drilled ~12 km south of Aluto; here Gibert et al. (2002) describe 'air-fall pyroclastic layers' 1 – 3 cm thick at 960 and 820 cm depth, indicating 'recent explosive volcanic activity'. Additional pyroclastic layers are noted at 532 – 537 cm, 385 – 390 cm, 348 – 352.5 cm and 139 – 150 cm although there are no further descriptions of the material. Six

^{14}C dates indicate a sediment record from ~5.1 to 12.7 cal. ka BP, with volcanic material observed between ~5.6 and 11 cal. ka BP (Gibert et al., 1999).

While limited in detail, the lake core descriptions provide tantalising evidence for multiple Holocene eruptions of the volcano, consistent with assessment of the terrestrial sections. Here we characterise and correlate individual tephra layers in the two cores using both physical and chemical signatures, with the goal of establishing a robust Holocene stratigraphy. This stratigraphy can be used as a reference for further tephrostratigraphic study of the volcano and the wider region and to inform hazard assessment. At the same time, observations of tephra grain size and componentry provide important information on the range of eruption styles responsible for these tephra layers.

2.1.1. Uses of tephrostratigraphy

Correlating tephras is common in volcanology, archaeology and paleoclimatology (e.g. Tryon et al., 2008; Vogel et al., 2010; Lowe, 2011; Fontijn et al., 2016) and is most often used to determine isochronous features for dating sequences. In many cases, however, the value of the tephra layers for physical volcanology is overlooked. The primary correlation tool is geochemistry, including major and trace element concentrations in volcanic glass (e.g. Lowe, 2011). In more proximal settings, this is sometimes complemented by mineral chemistry (e.g. Smith et al., 2011) —particularly Fe-Ti oxides —which, where present, can help to identify the volcanic source (e.g. Shane et al., 1998; Fierstein, 2007; Rawson et al., 2015). Similarity coefficients and other numerical correlation techniques can be used to relate the glass composition of chemically similar tephras from a large dataset (e.g. Kuehn and Foit, 2006; Brendryen et al., 2010). Critically, the success of geochemical correlation techniques relies on an individual eruption producing chemically homogenous samples. Identifying different eruptions from the same volcano is also predicated on the existence of chemically-distinct samples within a large well-constrained dataset.

Lithological descriptions of ash particles have been used to supplement geochemical data when the chemical variation is insufficient to correlate the tephras, or where more information is required about eruption dynamics. For example, glass shard shape can be used to fingerprint eruptions, where shape is analysed qualitatively and categorised using a binocular microscope (Shane and Smith, 2000; Placzek et al., 2009). Alternatively, the 2D external shape of particles can be characterised using quantitative shape parameters (Dellino and La Volpe, 1996; Wei et al., 2003; Cioni et al., 2008; Liu et al., 2015, 2016). Grain size data and tephra thickness data can also be integrated into the dataset to constrain the eruption size (e.g. Wulf et al., 2004)).

Physical volcanology studies of tephra deposits aim to constrain eruption conditions using measurements of deposit thickness, and particle size, shape and density. These studies use isopachs (contours of constant thickness or mass) and isopleths (contours of constant grain size, either maximum or median) to infer eruption magnitude and intensity (e.g. Carey and Sparks, 1986; Pyle, 1989; Fierstein and Nathenson, 1992; Legros, 2000; Bonadonna and Houghton,

2005). Where there are only limited tephra sites, however, such methods are difficult to employ, particularly when a robust stratigraphic framework is not available.

2.1.2. Using tephra to constrain eruption processes

Textural studies of tephra deposits are more limited, but demonstrate the use of textures – grain size, shape, and components – to infer conditions of magma storage, ascent and eruption (e.g. Cashman and McConnell, 2005; Wright et al., 2012; Liu et al., 2015, 2017), as well as the extent of secondary modification of pumice populations (e.g. Jones et al., 2016; Buckland et al., 2018). Specifically, internal bubble and crystal textures can be calibrated using decompression experiments to identify the existence and extent of conduit-filling plugs, (Cashman, 2004; Clarke et al., 2007; Wright et al., 2012), to infer rates of magma ascent (Klug and Cashman, 1994; Wright et al., 2012) and to measure progressive abrasion in pyroclastic density currents (e.g. Jones et al., 2016; Buckland et al., 2018). External shapes of ash particles provide information on fragmentation conditions (e.g. Cioni et al., 2014; Liu et al., 2015, 2017). Only rarely have ash groundmass textures been used in combination with glass componentry to fingerprint deposits (e.g. Cioni et al., 2008; Di Roberto et al., 2018).

An important consideration in tephrostratigraphy is the variation in tephra components with distance from the vent. Lapilli and coarse ash particles typically fall singly at a rate determined by the terminal velocity, which is a function of particle size, shape and density (Bonadonna et al., 1998). For this reason, the proportion of different tephra components will vary when they have different settling velocities, depending on the eruption size, distance from the vent and the ash dispersion axis (e.g. Hildreth and Drake, 1992; Bursik, 1996; Cashman and Rust, 2016). This velocity sorting is responsible for crystal concentration zones (Scarpati et al., 2014) and distal enrichment in vitric components, particularly highly vesicular and/or platy glass shards (Liu et al., 2017).

Tephra components also vary with eruption style. Sustained high-intensity explosive (Plinian) eruptions produce high proportions of glass shards (e.g. Rose and Chesner, 1987; Cashman and Rust, 2016). This is because the magma ascent, and associated decompression-induced degassing, is too rapid to allow syn-eruptive crystallisation of microlites, except in hydrous mafic magmas. The result is a deposit dominated by microlite-free glass shards (Swanson et al., 1989; Geschwind and Rutherford, 1995; Hammer et al., 1999). Pulsatory sub-Plinian or Vulcanian eruption styles, in contrast, are characterised by inter-eruptive development of dense conduit-filling plugs or domes. Associated degassing (e.g. Hammer et al., 1999) drives rapid shallow crystallisation and associated microlite-rich glass (Cashman and McConnell, 2005; Clarke et al., 2007). In these conditions, the abundance and geometry of microlites can provide information on magma ascent rate, as well as plug thickness and location (Blundy and Cashman, 2001; Noguchi et al., 2006; Szramek et al., 2006; Wright et al., 2012; Miwa et al., 2013). For this reason, the presence of both microlite-free and microlite-bearing glass within the same deposit provides good evidence for Vulcanian/sub-Plinian eruption styles (e.g. Sparks, 1997; Melnik and Sparks, 1999; Blundy and Cashman, 2001; Cashman and McConnell, 2005).

In this study, we use analyses of tephra layers from the lake sediment cores near Aluto to constrain the chemical and physical characteristics of the layers. Using these characteristics, we correlate the tephras between the cores and make initial interpretations about eruption frequency, size and style.

2.2. Methods

Tephra layers in the lake sediment cores were sampled in May 2015. All cores had been kept sealed since they were retrieved in 1999 from Lakes Abijata (core ABII) and Langano (core LLIII). Every visible tephra was sampled across the entire layer, and most layers thicker than 4-5 cm were subsampled. This equates to 25 different tephra layers in ABII (five of which were subsampled) and 20 in LLIII (two of which were subsampled; Table 2.1).

Grain size data were gathered for each tephra deposit in each core. Bulk samples were oven-dried at 80°C, sieved from -5 to 3 (32 mmto 125 µm) at one intervals and weighed. The 3 ϕ fraction was then recombined with the finer (125 µm) material and analysed by laser diffraction with a Malvern Mastersizer 3000 at the University of Bristol; five runs were performed per sample. The sieve (in wt%) and Mastersizer (in vol %) data were combined to reconcile the overlapping grain size, assuming a constant density across all grain sizes (Coltelli et al., 1998).

Each sample was prepared for backscatter electron (BSE) scanning electron microscopy (SEM). In most cases 1, 2 and 3 ϕ grain size fractions were prepared, although where insufficient 2 or 3 ϕ particles were present, smaller grainsizes were used. Particles were mounted in epoxy in an aluminium ring and polished to expose particle interiors. Polished mounts were then carbon coated before imaging with a Hitachi S-3500N SEM at the University of Bristol. For each grain size fraction a ~25-image mosaic was obtained and then combined using FIJI grid stitching software (Schindelin et al., 2012) to generate a high resolution image. Each image had a 1024 x 769 pixel resolution and was taken at a working distance of ~20 mm and an accelerating voltage of 15kV or 20kV. Overall, between 150 and 1200 grains were imaged per sample, depending on the grain size and the number of particles available.

Componentry analysis was performed to quantify the different grain components that comprise each tephra deposit. Each grain examined was classified into one of six categories (Fig. 2.2): (1) lithic (microcrystalline) (2) crystal (proportion of mafic and felsic recorded), (3) crystal with adhered matrix (mafic and felsic recorded), (4) glass shard (presence of microlites recorded), (5) vesicular fragment, (6) vesicular fragment with microlites (Fig. 2.2). Lithics were identified by their blocky external 2D morphology and heterogeneous appearance. The heterogeneity is provided by high crystallinity and near-absence of large (>several microns) patches of glass (Fig. 2.2a).

Table 2.1: Summary of tephra layers sampled in cores ABII, cored from lake Abijata, and LLIII, cored from lake Langano. Table includes a description of each tephra layer, the position in the core, tephra thickness, OxCal modelled age range (68.2 % confidence interval) and a summary of the analyses performed on each layer. * indicates insufficient grains to characterise.

Sample	Description	Depth (cm)	Thickness (cm)	Md ϕ	Min. Age (yrs BP)	Max. Age (yrs BP)	Grain size	SEM	Comp.	EPMA	LA-ICP-MS
				ABII							
ABII-04-14	Very fine laminated sediment	314	<1	4.2	2423	3320	X	-	*	X	-
ABII-04-17	Beige fine-grained laminated sediment	317	2	5.0	2460	3329	X	X	X	-	-
ABII-04-33	Beige fine-grained laminated sediment	333	<1	4.8	2754	3399	X	*	*	-	-
ABII-04-40	Beige fine-grained laminated sediment	340	<1	4.2	2958	3439	X	*	*	-	-
ABII-04-62	Normally graded ash deposit. A			1.8			X	X	X		
ABII-04-67	thin fine ash layer at the base,	362	11	0.7	3167	3612	X	X	X	X	-
ABII-04-73	then fining upwards			1.7			X	X	X		
ABII-05-48	Whiteish fine ash	447	3	4.8	3608	3972	X	X	X	X	-
ABII-05-55	Light grey/white very fine ash	455	<1	5.8	3614	4025	X	X	*	*	-
ABII-05-60	Light grey, fine ash	458	8	4.2	3631	4066	X	X	-	X	-
ABII-06-77	Light grey, very fine ash	574	6	4.5	4266	5037	X	X	X	-	-
ABII-06-88	Not well preserved, dark grey ash	587	3	4.4	4318	5141	X	X	*	*	-
ABII-08-16	Darker grey, very fine ash	695	3	4.2	5412	5980	X	X	X	X	-
ABII-08-46	Medium grey fine ash	726	3	3.9	5555	6158	X	X	X	X	-
ABII-08-76				5.9			X	X	X	-	
ABII-08-78	Grey, normally graded ash	756	4	1.5	5677	6294	X	X	X	X	-
ABII-08-79				3.9			X	-	-	-	
ABII-09-03	Grey, medium-grained ash	773	2	0.9	5771	6509	X	X	X	X	X

Sample	Description	Depth (cm)	Thickness (cm)	Md ϕ	Min. Age (yrs BP)	Max. Age (yrs BP)	Grain size	SEM	Comp.	EPMA	LA-ICP-MS
ABII-09-08	Lighter grey, medium-fine ash	779	3	-2.2	5799	6540	X	X	X	X	X
ABII-09-31	Very light grey, medium ash	800	4	3.7	6005	6803	X	X	X	X	-
ABII-10-45	Pumice lapilli in dark grey mud	915	<1	-2.0	7979	8844	X	X	*	X	-
ABII-10-73	Normally graded lapilli layer, mixed white and grey ash	943	5	3.3	8542	9426	X	X	X	-	-
ABII-10-75				0.15			X	X	X	X	X
ABII-10-77				0.14			X	X	X	X	-
ABII-11-07	Light grey, medium ash	976	4	3.9	9186	10150	X	X	X	X	-
ABII-11-62	Medium to coarse dark grey ash at the base, light grey/white	1031	4	4.6	10680	10128	X	-	-	-	-
ABII-11-64				4.2			X	X	X	X	
ABII-11-79	Normally graded ash layer, darker at base	1048	4	6.5	10235	11118	X	-	-	-	-
ABII-11-81				4.6			X	X	X	X	X
ABII-12-11	Medium to light grey fine ash	1075	3	4.8	10427	11582	X	X	X	X	-
ABII-12-16	Medium to light grey fine ash	1080	3	3.9	10452	11597	X	X	X	X	-
ABII-12-24	Dark grey, medium-coarse ash and light grey lapilli	1089	2	1.3	10525	11681	X	X	X	X	-
ABII-12-69	Medium grey, medium to fine ash	1134	2	4.9	11258	12466	X	X	X	-	-
				LLIII							
LLIII-03-01	Fine lapillli in grey mud	222	1	0.9	5195	5938	X	X	-	X	-
LLIII-03-70	Dark grey, coarse ash	292	1	0.9	5545	6516	X	X	X	X	X
LLIII-03-110	Dark grey coarse ash to lapilli	331	1	1.2	5885	6827	X	X	X	X	X
LLIII-04-11	Fine ash with scattered lapilli	346	2	5.3	6034	6906	X	X	-	-	-
LLIII-04-18	Fine grey ash	348	6.5	4.5	6045	6916	X	X	-	-	-
LLIII-04-51	Medium grey ash	385	5	4.4	6567	7151	X	X	X	X	-
LLIII-05-23	Grey medium ash	470	5	3.5	6782	8132	X	X	X	X	-
LLIII-05-106	Lapilli	556	<1	1.4	6979	8929	X	-	-	-	-
LLIII-07-75	Medium grey ash	752.5	4.5	0.0	9003	10565	X	X	X	X	X

Sample	Description	Depth (cm)	Thickness (cm)	Md ϕ	Min. Age (yrs BP)	Max. Age (yrs BP)	Grain size	SEM	Comp.	EPMA	LA-ICP-MS
LLIII-07-105	Grey lapilli	782	2	3.3	9324	10669	X	X	X	X	-
LLIII-08-38	Grey medium to fine normally graded ash	829.5	1	4.5	9787	10841	X	X	-	X	-
LLIII-08-86	Beige lapilli	878	1	2.2	10170	11000	X	X	-	X	-
LLIII-08-90	Grey normally graded coarse ash	879	5	3.6	10175	11005	X	X	-	X	-
LLIII-09-01	Grey medium-coarse ash	886	2	3.4	10187	11009	X	X	-	X	-
LLIII-09-03	Light grey lapilli layer	888	2	0.7	10195	11010	X	X	X	X	X
LLIII-09-15	Fine grey ash	900	2	3.1	10279	11038	X	X	-	X	-
LLIII-09-22	Reversely graded coarse ash to lapilli	907	2.5	0.0	10326	11056	X	X	-	X	-
LLIII-09-23				1.6			X	X		X	-
LLIII-09-44	Grey normally graded coarse-fine ash	929	1.5	3.4	10494	11101	X	X	-	X	-
LLIII-09-60	Grey medium ash	945.5	3.5	3.6	10626	11132	X	-	-	X	-
LLIII-09-62				0.6			X	X		-	-
LLIII-09-74	Light grey fine ash	960	<1	4.8	10692	11148	X	X	-	X	-
LLIII-09-98	Coarse ash with some lapilli	984	1	1.3	10786	11226	X	X	X	X	-

Ash grains comprising a single crystal (or crystal fragment) were classified into 'mafic' and 'felsic' based on their greyscale in BSE images, where Fe-Mg silicates such as pyroxenes have a larger mean atomic number and thus appear brighter than high-Si phases such as quartz and feldspar. In addition, mafic phases often show cleavage planes. In general, all crystals are equant with a semi-quadrilateral 2D morphology and are compositionally homogenous (Fig. 2.2b). Specific identification of different mafic and felsic phases was not attempted from the BSE-SEM images, and so the proportions of different crystal types are not included.

Often, both felsic and mafic crystals retain some attached matrix of vesicular glass (presence of microlites recorded), or occasionally vesicle-free glass and rarely lithic fragments and are therefore counted as separate component. Grains were classified as 'crystal with an adhered matrix' when the matrix component was $<$90% of the whole grain. Where the crystal occupied $<$10%, the particle was classified as whatever component comprised the remaining 90% (usually vesicular glass; (Fig. 2.2c).

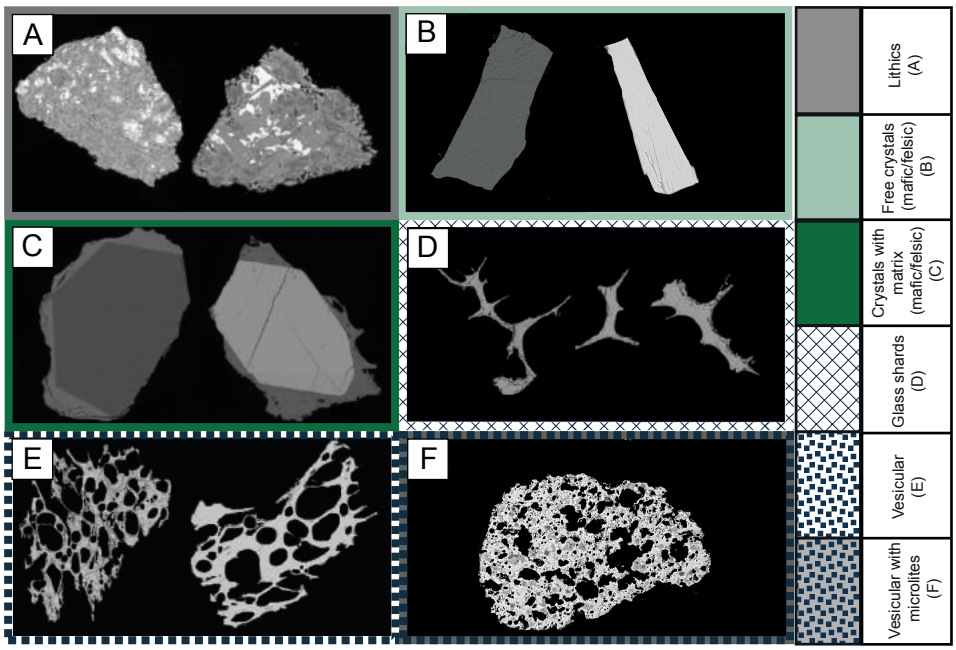

Figure 2.2: SEM-BSE images of different components counted from SEM imaging. (a) Microcrystalline lithic fragments, (b) mafic and felsic crystals (with no matrix attached) (c) mafic and felsic 'free' crystals with matrix attached, (d) glass shard fragments, (e) microlite-free vesicular grains, and (f) microlite-containing vesicular grains. All components in the 3 ϕ grain size fraction.

Glass shards were identified and characterised based on greyscale and morphology. Glass has a greyscale similar to quartz and feldspar, but typically has a more concave appearance than crystals (Fig. 2.2d). Vesicular grains were differentiated from glass shards as glassy particles that contained at least one entire, unbroken vesicle (Fig. 2.2e). The presence or absence of feldspar microlites ($<$20 µm crystals) in the glass was also documented. Feldspar microlites have only slightly lower mean atomic number than the surrounding glass, and so required large image contrast to be identified (Fig. 2.2f). The size, spacing, abundance and composition of the

microlites indicate crystallisation within the magmatic system rather than secondary rehydration.

To determine the component proportions, each SEM mosaic was divided into a 4x4 grid. The components in each grid square were then recorded by point counting. The proportions of components were determined for samples from both cores, but ABII was chosen for a more comprehensive analysis because it represents a longer time period and contains the most tephra layers (Table 2.1). Componentry analysis was performed for: (a) every major tephra sample (>~1cm thick; equating to 18 different layers in the ABII core for every 3 ϕ fraction (and usually 1 and 2 ϕ), (b) the thickest samples in the LLIII core, and (c) LLIII layers that appeared to display similar textural features to specific ABII layers.

Major element geochemical data were collected by EPMA using a JEOL JXA8530F Hyperprobe at the University of Bristol. Major elements were analysed using a 2nA beam current with a 10 µm spot size at a voltage of 15kV. Count times were varied by element to optimise analysis time and count number while minimising beam damage. Ca, Si, Al, Na and K were analysed first for 10 s, Ti for 80 s, Mg, F, Cl and Fe for 60s and Mn for 30 s. In some cases MnO was not recorded due to a hardware problem; MnO is content is typically <0.2 wt% and therefore is not expected to have a significant effect on the overall results. The KN18 secondary standard was analysed between each sample and was closely monitored throughout; no drift or deviation was observed during analysis. Only analyses with oxide totals over 94% were retained, although the majority are over 97%. The lower totals are ascribed to secondary hydration from the lacustrine preservation environment (Chapter 3.5.1). Where microlites were present in the glass, only microlite-free patches of glass large enough for a 10 µm spot size were analysed. All plotted data are normalised to an anhydrous basis. If possible, at least 20 individual pieces of glass were analysed per sample.

Laser Ablation Inductively Coupled Plasma Mass Spectrometry (LA-ICP-MS) was performed at Trinity College, Dublin. The analysis was undertaken using a Thermo Scientific iCAPQ ICP-MS coupled to a Photon Machines analyte 193 nm eximer laser ablation system with a Helix two volume cell via an ARIS sample introduction capillary and an in-house signal smoothing device (poshDOG). The spot size was 30 µm and the repetition rate 10 Hz with a count time of 35 seconds (or 350 pulses). The calibration was performed using the NIST612 standard and the internal standard was 29Si. The calibration was verified using the MPI-DING secondary glass standards ATHO-G and StHs6/80-G from the Max Planck Institute (Jochum et al., 2016). Accuracies are typically better than 10% for most elements and reproducibility is better that 5 RSD% for all trace elements. We attempted to analyse 20 points per sample, although this varied slightly depending on the availability of large areas of glass.

Radiocarbon dates published by Gibert et al. (1999) for Lake Langano and Gibert et al. (2002) for Lake Abijata (8 in LLIII and 14 in ABII) were obtained from shells and organic material removed from lake sediment. We recalibrated the published ages using the most recent IntCal13 calibration curve as part of Oxcal version 4.3; all ages presented in this paper represent these recalibrated values (Fig.2.3; Bronk Ramsey, 2008; Bronk Ramsey and Lee, 2013; Reimer et al.,

2013). To place more detailed constraints on the tephra ages, we further revised this existing chronology using Bayesian deposition modelling available through Oxcal (Bronk Ramsey, 2008; Reimer et al., 2013) which uses the ^{14}C ages of organic material in the core and the associated error to constrain an age for the tephra layers in-between. Tephras were modelled using the 'P sequence' function, including an outlier model (Bronk Ramsey, 2009). Oxcal ages are shown as ages ranges which represent at 68.2 % confidence interval for the age of each layer. Where a discreet date is shown for a layer, it represents the median of this confidence interval. The Oxcal code can be found in Appendix E.

2.3. Results

2.3.1. Core descriptions

The tephra in the two cores, ABII and LLIII, were easily distinguishable from lake sediments by colour and grain size. Tephra is typically lighter in colour, often beige to white, while lake sediments are darker grey and have a fine, homogenous grain size. Many of the tephras show grading (both normal and reverse; Fig. 3.1) and contain little or no diatomite-rich lake sediment, suggesting that most layers represent a distinct eruption rather than remobilisation events happening over a prolonged period of time. The top sections of both cores are missing, such that the time period accessible is 1.7 to ~12.5 cal. ka BP.

ABII has an 8.5 m long sediment record, which ^{14}C dates indicate spans 1.7 to ~12.5 cal. ka (Gibert et al., 1999; Chali and Gasse, 2002) and contains 25 distinct tephras (Fig. 2.3a) with an average median grain size (Md) of 3.3 ϕ (Table 2.1). The average tephra thickness is 3.64 cm, with the thinnest tephras $<$1 cm and the thickest 11 cm (Fig. 2.3a). There are four tephra layers with thicknesses $\geq$ 5 cm. The thickest of these is ABII-04-62:73 (one layer subsampled three times), which is an 11 cm thick normally graded deposit with pumice lapilli at the base, fining upwards to ash. The second thickest —ABII-10-73:75 (one layer, subsampled three times) —is 5 cm thick and shows normal grading with lapilli-sized pumice becoming coarser towards the base. The lower two of the three subsamples of this tephra have Md = 0.13 ϕ and 0.14 ϕ (one of the coarsest of all layers sampled from the core), whereas Md=3.3 ϕ in the uppermost subsample (Fig. 2.3a).

LLIII has a 7.62 m long record which spans from 5.6 to 11.1 cal. ka BP (Gibert et al., 2002) and contains 21 tephra layers (Fig. 2.3b) with an average median grain size of 2.7 ϕ (Table 1). The average tephra thickness is 2.3 cm, with the thinnest tephras $<$1 cm and the thickest 6.5 cm The thickest of these, LLIII-04-18, contains fine sediment with Md = 4.5 ϕ. The layer is described in the drilling log as a mixture of 'mud and pyroclastics' (Gibert et al., 2002), contains a large amount of lake sediment amongst the ash and does not display any grading or sorting. We infer that this layer to be the consequence of reworking, representing part of a turbidite deposit. These features are infrequently observed elsewhere in the core; the next three thickest layers (LLIII-04-51, LLIII-05-23 and LLIII-08-90) contain little lake sediment and preserve distinct boundaries

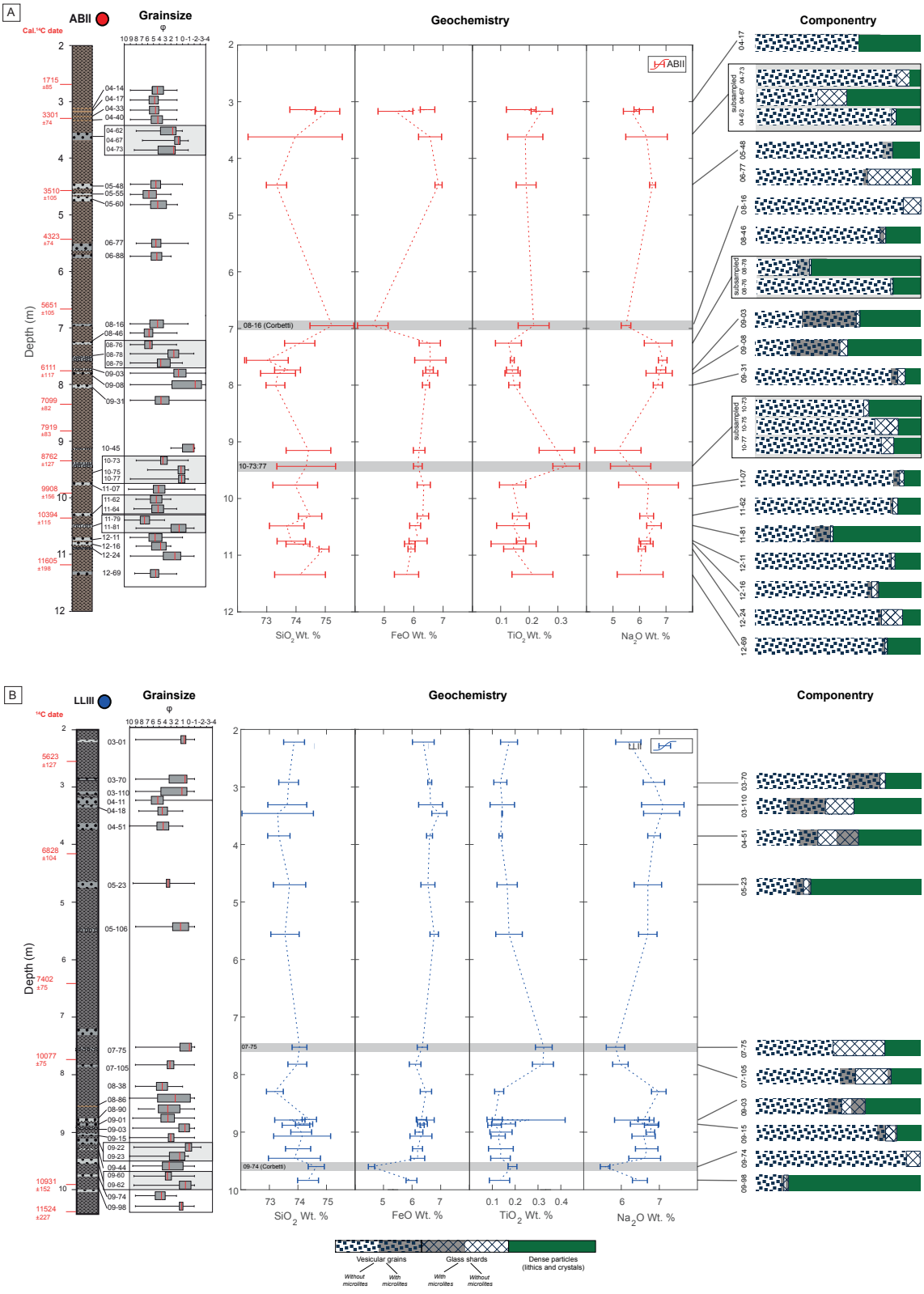

Figure 2.3: Caption on next page

Figure 2.3: (a) Core log of core ABII. Calibrated ^{14}C dates shown in red. Box and whisker plots of grain size data are shown for each sample and subsample. Red line indicates the median, the grey box indicates upper and lower quartile and the whisker indicates grain size range. Geochemistry for analysed tephras layers within each core is plotted with depth. Dashed lines are straight lines drawn between data points for legibility. Error bars represent one standard deviation to represent natural variation in the sample. The analytical error for each is calculated in Appendix C, but in every case is lower than one standard deviation. Componentry is displayed for all tephras for which there were sufficient grains in the 3 ϕ grain size fraction. Each bar represents 100%, with the coloured and patterned sections indicating the proportion of different components. Green portion contains 'dense' fragments described as crystals and lithics. Blue hatched pattern indicates glass shards, with the portion of microlite-containing glass shards in grey. Blue dots represent the vesicular portion, with microlite-containing vesicular grains shown in grey. Corbetti-sourced layer ABII-08-16 and glass shard layer ABII-10-73:77 are shown in grey. (b) Core log of core LLIII; legend as in (a). Componentry performed on all samples that could reasonably correlate with ABII based on an assessment of geochemistry, age and qualitative componentry. Corbetti-sourced layer LLIII-09-74 and glass shard layer LLIII-07-75 shown in grey

with the non-volcanic sediment above and below.

While we believe that LLIII-04-18 is the only turbidite deposit sampled, it is important to consider other forms of secondary reworking that may have affected additional tephra layers. In other settings, both secondary deposition via the fluvial system and redistribution by lake currents can generate $>$ cm-thick tephra deposits that can be misinterpreted as primary, especially where deposition occurs over the lake's watershed (Thompson et al., 1986; Bertrand et al., 2014). However, deposits cored from such settings are typically described as poorly sorted and contain pumices intermixed with finer ash and lake sediment. Deposits in Lakes Abijata and Langano often show clear grading, typically normal, which is not consistent with observations of fluvial deposits. In addition, the annual input to the modern Lakes Langano and Abijata, is several orders of magnitude less than the input to lakes in other environments where fluvially-thickened tephra layers are observed (i.e. Lake Puyehue in Chile), making it unlikely that large volumes of tephra will be deposited into the lake from the fluvial system (Ayenew, 2002; Zinabu et al., 2002; Bertrand et al., 2014). The depth of the lake must also be considered in the context of its effect on particle settling: both lakes have been subject to depth changes, with lake highstand periods sufficient to allow the two lakes to be connected in the early Holocene. While it is not possible to accurately constrain the influence of lake depth on the deposits, we note that the tephra layers do not show any systematic differences between the early Holocene (lake level highstand) and late Holocene. In some cases, normal and reverse grading is apparent in consecutive deposits indicating that temporally close deposits were not the product of the same secondary processes. As all tephra layers show slightly different features regardless of position in the core, we infer that the deposits are most likely primary. As such, we interpret these thicknesses to represent of the true thickness of the primary deposit.

2.3.2. Major element composition

Results of electron probe microanalysis (EPMA) are presented in Figures 2.4 and 2.5, and all data and secondary standards are reported in Appendices A and C. All analysed glasses are peralkaline in composition with 72 -76 wt% SiO_2, with an average of 74.1 wt% and a relative standard deviation of 0.8.

In ABII, 17 out of 25 layers were analysed for major elements. Of the eight layers not analysed, most were in the top two meters of the core, where they did not overlap temporally with LLIII. Of the 17 analysed, major element concentrations were largely invariant and displayed little or no changes in eruptive composition throughout the Holocene, (e.g. SiO_2 = 74.0 wt% $\pm$ 0.99% (1σ). This lack of geochemical variance was observed across all oxides and tephra samples, with the exception of three layers (Fig. 2.3a). The youngest of these exceptions, ABII-08-16, is chemically evolved with an average SiO_2 = 75.2 wt%, compared to a core average of 74.0 wt%. More noticeably, the layer has an average FeO = 4.6 wt%, which is 26 % lower than the core average (Fig. 2.3a). The other two geochemically distinct layers are ABII-10-45 and ABII-10-73:77, which both contain an average of 0.3 wt% TiO_2 (70% above the core mean) and Na_2O= 5.5 wt% (11% below the core mean; Fig. 2.3a; Fig. 2.5).

In LLIII, 20 layers were analysed for major element concentrations. Like the ABII core, the tephra glasses have homogenous major element concentrations with an average SiO_2 = 73.8 wt% $\pm$ 0.5 % (1). There is little variation in any major element oxides, with the exception of three layers (Fig. 2.3b). The youngest of these are layers LLIII-07-75 and LLIII-07-105, which occur consecutively in the core. These layers have a TiO_2 value of 0.3 wt% (100% above the core mean) and an NaO_2 value of 5.9 wt% (11% below the core mean; Fig. 3b; Fig. 2.5). The final layer with unique chemical characteristics is LLIII-09-74, which has a higher than average SiO_2 value of 74.6 wt%, and lower than average FeO of 4.6 wt% (compared to a core average of 6.3 wt%; Fig. 2.3b; Fig. 2.4).

2.3.3. Componentry

Componentry analysis was undertaken on 23 samples in ABII comprising 18 different tephra deposits. The proportion of dense (crystals and lithic fragments) to glassy (glass shards and vesicular grain) varies with depth in the core and does not appear to be systematic (Fig. 2.3). The only sample without dense particles is ABII-08-16 (Fig. 2.3a). The crystal components comprise a range of phases, with typical felsic components including quartz and alkali feldspar (sanidine), while the mafics include alkali pyroxene (aegirine), aenigmatite and Fe-Ti oxides.

Within the glassy portion, the presence and abundance of glass shards is also variable. Particularly notable for their high proportions (>10%) of glass shards are ABII-04-62:67 (one layer subsampled three times), ABII-06-77, ABII-08-16 and ABII-10-73:77 (one layer subsampled three times; Fig. 2.3a). Two of these layers (ABII-06-77 and ABII-10-73:77) have a distinctive shard morphology, with highly concave glass shard fragments that represent the

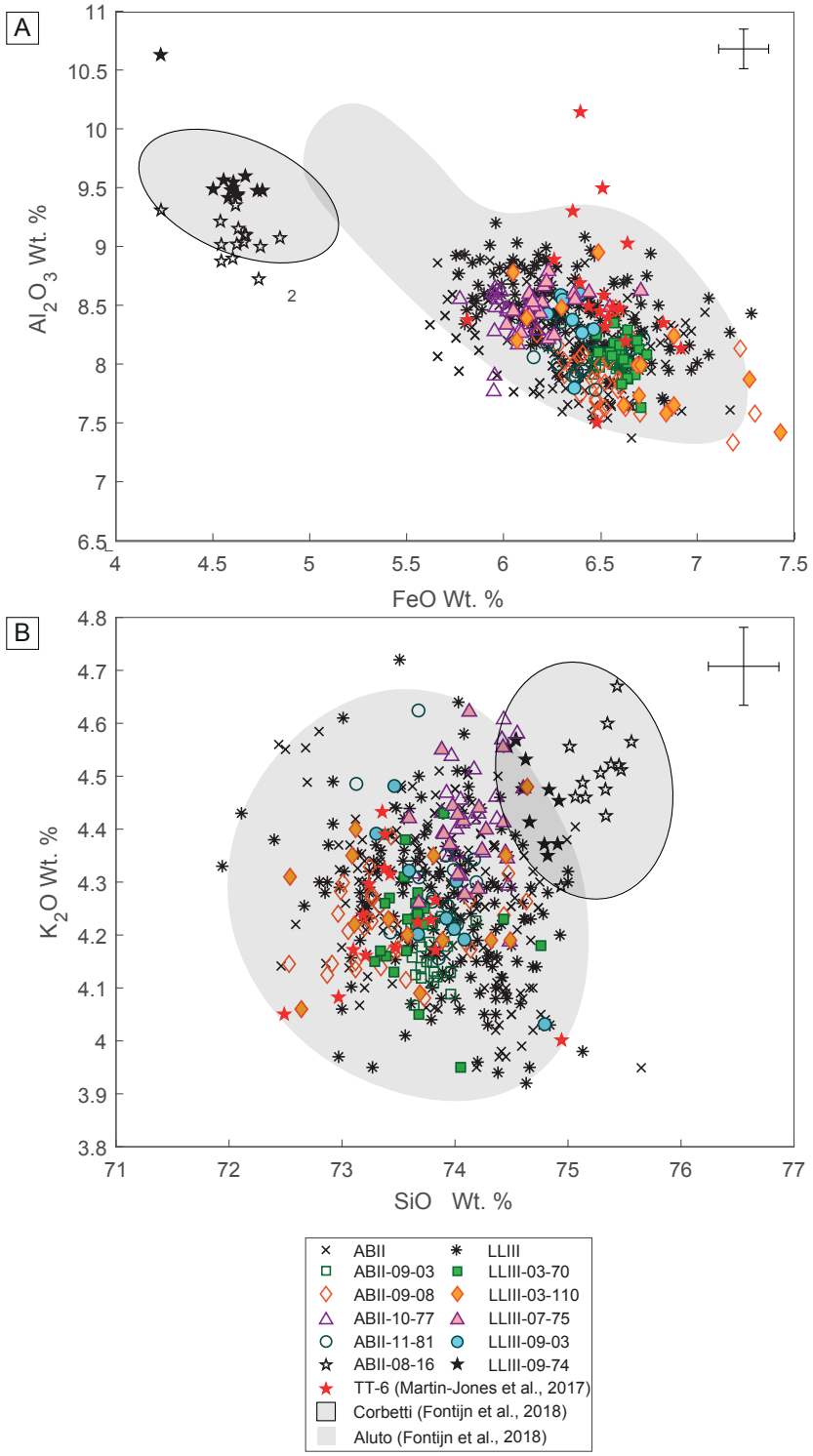

Figure 2.4: Bivariate plots of glass major element geochemistry. Certain layers are plotted in colour to highlight the difficulties with correlating using major element geochemistry with such a large number of units that occupy a small geochemical range. Reference glass geochemical data for Aluto and Corbetti from Fontijn et al., (2018) shown in grey field. TT-6 a tephra layer in sediment core from lake Tilo (~100 km SW Aluto) and thought to be sourced from Aluto (after Martin-Jones et al., 2017) is plotted as red stars. Layers thought to be from an eruption of Corbetti volcano are plotted as black 5-point stars. An average standard deviation for the plotted layers is shown in the top right.

remnants of walls of relatively large (~50 -100 μm) bubbles. These glass shards are accompanied by other grains that contain a smaller vesicle population (Fig. 6c).

The presence of microlites in the glass also varies, with layers ABII-09-03, ABII-09-08, ABII-11-07 and ABII-11-79:81 (one layer subsampled twice) showing particularly high proportions of microlite-bearing glassy particles. Of these, layers ABII-09-03 and ABII-09-08 contain densely packed microlites which affected vesicle growth, producing irregularly shaped vesicle networks in the grains (Fig. 2.6a). In contrast, microlites are more sparse in the vesicle-containing grains in the earlier layers (ABII-11-07 and ABII-11-79:81), and as a consequence most of the vesicles are near-circular in cross-section (Fig. 2.6b).

The proportions of components were quantified in only 10 layers of the LLIII core. These layers are not representative of the core, and some were chosen specifically because of anomalous componentry (e.g. high microlite content) based on qualitative assessment of BSE images. The only sample that does not contain any dense fragments is LLIII-09-74. The proportions of dense versus glassy grains is variable, with four layers containing high proportions of glass shards: LLIII-03-110, LLIII-04-51, LLIII-07-75 and LLII-07-105 (Fig. 2.4b). Of these, LLIII-07-75 contains shards with highly concave, bubble-wall shards (e.g., Fig. 2.6c). Layers LLIII-03-70, LLIII-03-110, LLIII-04-51, LLIII-07-105, LLIII-09-03 and LLIII-09-15 (Fig. 2.4b) are notable for having grains with microlites. Of these, two (LLIII-03-70 and LLIII-03-110) contain densely packed microlites which affected the vesicle structure (Fig. 2.6a).

2.3.4. Trace element composition

Because the major element chemistry was not sufficiently distinctive to uniquely fingerprint different tephra layers, we performed trace element analyses on selected samples with distinct textures: (1) high microlite content (ABII-09-03, ABII-09-08, LLIII-03-70 and LLIII-03-110; Fig. 2.6a), (2) lower microlite content (ABII-11-79:81 and LLIII-09-03; Fig. 2.6b), and (3) concave glass shards (ABII-10-73:77 and LLIII-07-75; Fig. 2.6c; Appendix B). While many trace elements varied with respect to particle textures, Ba shows the clearest variation (Fig. 2.5). The high-microlite-content layers have glass with relatively high Ba concentrations (348-532 ppm) and the low-microlite layers contain lower Ba (222-319 ppm); these variations are consistent with incompatible behavior of Ba. The glass shard layers contain Ba between 326 and 386 ppm; these layers are easily identified by their high TiO_2 values (Fig. 2.5). As it was not always possible to analyse the same grain for major and trace element compositions, the range of values for each unit is shown in Fig. 2.5, as well as the average of all grains analysed in each layer. Our values are within the range of published whole-rock data for Aluto (Hutchison, et al., 2016c).

2.3.5. Corbetti vs Aluto tephra source

The location of the coring sites means that we expect the tephras to be predominantly from Aluto and almost all have a peralkaline rhyolitic composition consistent with this source (c.f. Fig

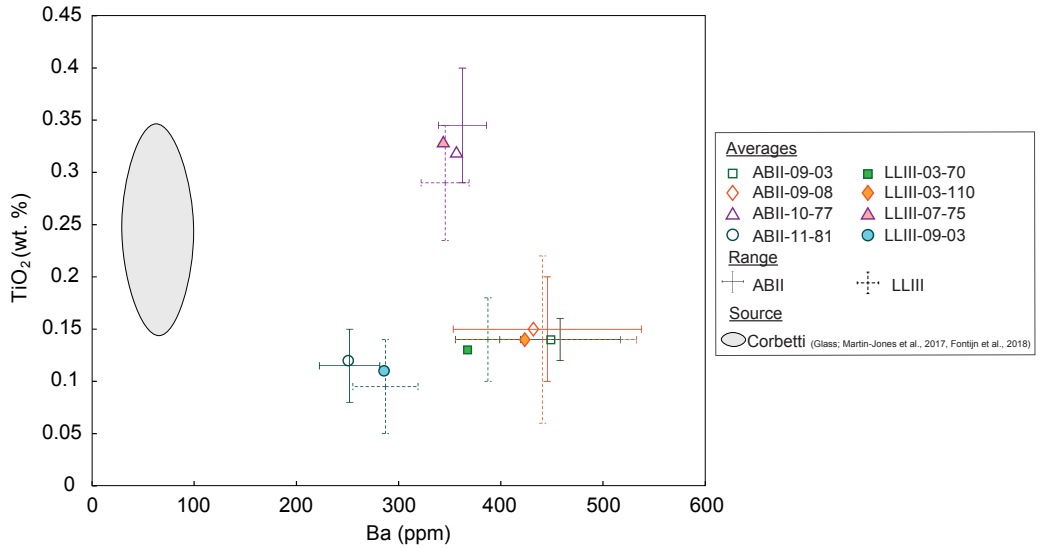

Figure 2.5: Plot showing Ba (ppm) and TiO_2 (wt. %). Ranges are shown for both as it was not always possible to analyse the same grain for the majors (i.e. TiO_2) and trace elements (i.e. Ba). Markers display the average value for each. For comparison, the TiO_2/Ba window for Corbetti is plotted (grey with black line) from Fontijn et al., (2018; TiO_2 data) and Martin-Jones et al., (2017; Ba data).

2.4; Fontijn et al., 2018). However, ABII-08-16 and LLII-09-74 have a clearly different glass composition and componentry (Fig. 2.3; Fig. 2.4). Their lower FeO content compared to all other samples, and relatively high SiO_2, K_2O and Al_2O_3, match the composition of products of Corbetti volcano, the silicic centre approximately 80 km south of Aluto, 50 km south of ABII and 60 km south of LLIII (Martin-Jones et al., 2017; Fontijn et al., 2018). ABII-08-16 and LLLII-09-18 are also the only two samples that contain no dense material, including no crystals (Fig. 2.3); the lack of crystals is consistent with most eruptions of Corbetti (Mohr, 1966; Schmincke, 1974; Fontijn et al., 2018). Modelled Oxcal ages indicate that ABII-08-16 was deposited between 5,410 and 5,980 cal. yr BP and LLIII-09-74 between 10,690 to 11,140 cal. yr BP, which agrees with known periods of explosive activity at Corbetti, as constrained by tephra deposits found in lake sediment cores south west of Corbetti (Lamb et al., 2002; Martin-Jones et al., 2017; Fontijn et al., 2018). We interpret the two tephra layers to be the product of two different eruptions of Corbetti. Given that they are the only entirely aphyric samples observed in the cores, and their distinct geochemistry, we are confident that these are the only Corbetti-sourced layers in our sample suite and exclude them from our subsequent study of Aluto's eruptive history.

2.4. Discussion

Our study of tephra from two lake cores provides detailed constraints on the Holocene eruptive history of Aluto. We believe Aluto to be one of the most frequently active volcanoes in the region (Hutchison et al., 2016ac; Fontijn et al., 2018) and so developing understanding of eruption size and frequency is key to improving hazard assessment. The two cores, LLIII and ABII, are positioned 12 km south and 25 km south west of the volcano respectively. When drilled, ABII

spanned the longest time interval, representing sediment deposition from ~0.2 to 13.4 cal. ka BP while LLIII spanned ~5.1 to 11.5 cal. ka BP. However, the top sections of both cores are now missing meaning the time periods available for this study are ~1.7 to 11.6 cal. ka BP and ~5.6 to 11.5 cal. ka BP respectively, and should overlap for the period of ~5.6 to 13.4 cal. ka BP.

The tephras in ABII are on average thicker than those in LLIII despite being further from Aluto. Wind reanalysis data from 2015 and 2016 indicate a west-south-west prevailing wind direction (as per the methods of Kalnay et al., 1996) which, is consistent with thicker ash fall deposits in ABII. Coupled with the fact that the lake cores are more likely to preserve fine ash than terrestrial sequences, they provide the opportunity to generate a well-constrained record of the volcano's Holocene activity. This record can be used in conjunction with (now) terrestrial distal deposits to determine eruption styles and frequency of activity at the volcano. Here we first discuss methods of correlating the lake core tephras, before evaluating the implications of the tephra record for eruption dynamics and Aluto's Holocene eruption history.

2.4.1. Correlating the cores

The majority of tephras in both cores have similar major element compositions. The only obvious exceptions to this are the samples interpreted as Corbetti-sourced samples which are discounted from further discussion. Beyond these, the only layers to display any geochemical distinction are LLIII-07-75, LLII-07-105 in LLIII and ABII-10-45 and ABII-10-73:77 in ABII. Unlike the Corbetti layers, these have FeO and $SiOpr_2$ values that are indistinguishable from other samples, but show variations in other elements, particularly TiO_2.

All four of these layers have TiO_2 values of ~0.33 wt% (approximately 80-100 % higher than the core mean; Fig. 2.3; Fig. 2.6). This unusually high TiO_2 is complemented by lower than average Na_2O (~11 % lower than the core mean) in the same layers (Fig. 2.3). The layers are preserved between ^{14}C dated material of comparable ages: ABII-10-45 lies between 7919 $\pm$ 83 and 8762 $\pm$ 127; ABII-10-73:77 lies between 8762 $\pm$ 127 and 9908 $\pm$156 cal. yr BP and LLIII-07-75 and LLIII-07-105 between 7402 $\pm$75 and 10077 $\pm$75 cal. yr BP. LLIII-07-105 is a fine, thin ash layer which, when examined on the SEM contained very little pyroclastic material larger than 100 µm. Similarly, ABII-10-45 is a thin (<1cm) layer, containing mostly sub-rounded lapilli and little other volcanic material. As such, we infer that the two thicker layers, which are 4.5 and 5 cm thick (ABII-10-73:77 and LLIII-07-75 respectively), represent the same eruption. The thinner layers may be smaller events that occurred before and after the larger eruption. It is also possible that, as ABII-10-45 appears after ABII-10-73:77, it is a reworked and redistributed component of the larger layer below. However, while the two layers show the same glass chemistry, ABII-10-45 does not show the same high component of glass shards as ABII-10-73:77 and we therefore interpret it as another, much smaller eruption with a similar composition.

While the identification of three high-TiO_2, low-Na_2O tephras was possible with major elements alone, the chemical similarity of the glass in most ash layers required other methods of correlation. Although the same grain size fraction is compared throughout, the proportion of

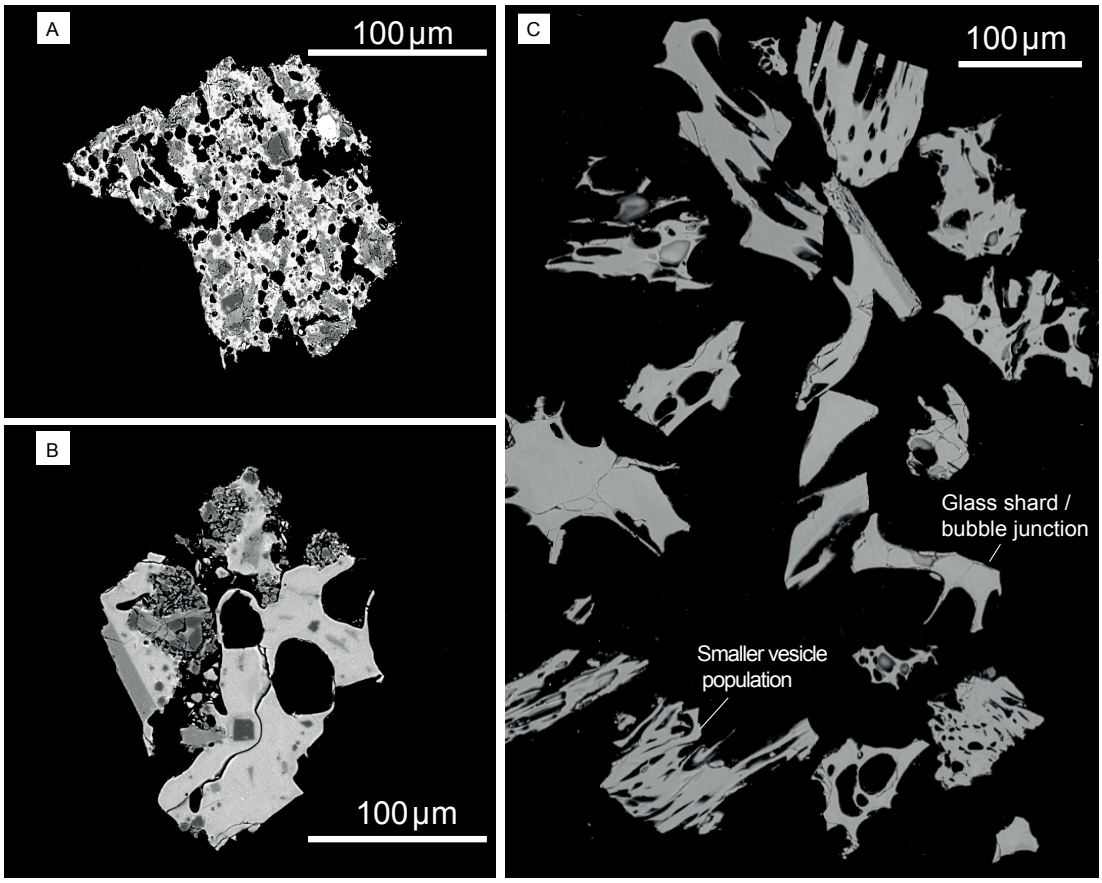

Figure 2.6: SEM BSE images showing the variations in microlite and glass shard texture. (a) indicates a vesicular grain from ABII-09-03 containing densely-packed microlites which have caused the vesicles to form in irregular vesicle networks. (b) indicates a microlite-bearing vesicular grain with fewer microlites from ABII-11-07. In this case, the microlites have had almost no effect on the formation of bubbles, which are comparatively spherical. (c) Image of LLIII-07-75. Displays the characteristic 'glass shards' which have formed from the fragmentation of a larger bubble population. A smaller bubble population is still preserved in the more vesicular grains.

dense versus glassy fragments was not a useful correlative tool, likely because of the factors relating to eruption size, direction and the settling of different components discussed in Section 1.3. However, variations in relative proportions of other grain components (as detailed in methods and Fig. 2.2) were useful for some correlations.

Particularly useful for correlation was the presence and abundance of microlites within glassy grains, and the presence and abundance of glass shard fragments. For example, the high TiO_2 layer in ABII (ABII-10-73:77) and an approximately isochronous high TiO_2 layer in the LLIII core (LLIII-07-75) contain a greater proportion of large (~125 – 250 µm) glass shards than surrounding tephras (Fig. 2.3). The shards themselves also have a highly convex morphology not observed elsewhere in the LLIII core (Fig. 2.6). This morphology indicates that they are remnants of bubble junctions rather than equant, blocky glass fragments (Fig. 2.6). The similarity in form and age suggest that these layers are likely the product of the same eruption (termed Aluto Glass Shard Layer -AGSL1- in this study; Fig. 2.7). Coupled with the TiO_2 signature, AGSL1 is a useful, identifiable marker unit. Indeed, we had identified this glass shard layer as the product of the same eruption before geochemical data were obtained to support the correlation. Another tephra with a high proportion of similarly concave glass shards was observed in the top half of the ABII core. However, this layer, ABII-06-77, (Oxcal age: 5323 – 5840 cal. yr BP) is likely too young to also be recorded in the LLIII core and therefore cannot be correlated.

The presence and textures of microlite-containing glass particles allowed correlation amongst more geochemically similar tephra layers. Microlites were documented in 12 of 19 layers in ABII, although the proportions of microlite-containing to microlite-free glass varied considerably within these layers. In the ABII core, the four layers that contain the highest proportion of microlite-containing glass relative to microlite-free glass are ABII-09-03, ABII-09-08, ABII-11-07 and ABII-11-79:81 (Fig. 2.3a). The first two appear consecutively in the core. Layer ABII-09-03 was deposited between ^{14}C dated material with recalibrated ages of 5651 and 6111 cal. years BP, and ABII-09-08 between material recalibrated to 6111 and 7099 cal. yr BP (Fig. 2.7). Here, microlite-rich grains constitute up to 33% of the total observed grains. SEM-BSE images show that the microlites are closely spaced and have produced irregularly shaped vesicle networks (Fig. 2.7). There are several microlite-rich layers in LLIII that were deposited during a similar time interval: three were deposited between 5623 and 6828 cal. yr BP and one between 6828 and 7402 cal. yr BP (Fig. 2.3b). Of these four layers, the first two (LLIII-03-70 and LLIII-03-110) and the second two (LLIII-04-51 and LLIII-05-23) are consecutive, meaning there are two pairs of microlite-rich tephras preserved within a time period comparable to the ABII microlite-rich tephras.

To determine which LLIII pair correlates with the ABII pair, the microlite and vesicle textures were examined in greater detail. In LLIII-04-51 and LLIII-05-23, the microlites typically occupy <~10% of the glass, the vesicles have simple, near-circular shapes in BSE images (Fig. 2.6b) and the grains containing microlites constitute a small proportion (between 7 and 15%) of the total glassy grains. The other pair, LLIII-03-70 and LLIII-03-110, have abundant (25-30%)

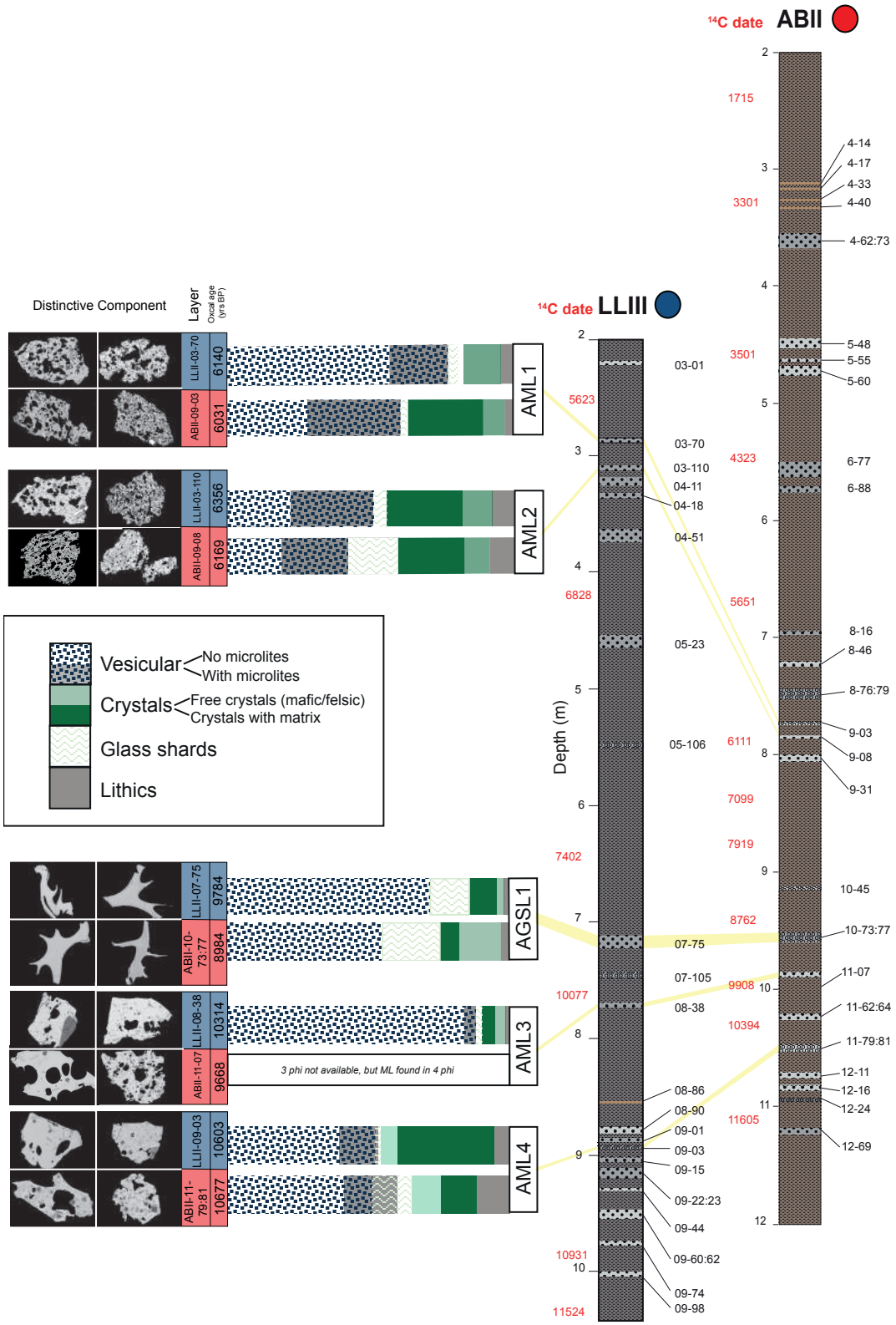

Figure 2.7: A summary of correlations made using componentry analysis. All componentry data shown is the for 2 ϕ grain size fraction. AML1 and AML2 are correlated based on the high proportion of microlite bearing grains, in which the microlites are closely spaced and affect vesicle textures. AGSL1 contains a high proportion of glass shard fragments, while AML3 and AML4 contain microlite bearing glassy fragments with sparse microlites. The medians of the Oxcal-modelled tephra ages are shown.

grains containing densely packed microlites and irregularly-shaped vesicle networks (Fig. 2.6a; Fig. 2.7). Consequently, we correlate these two tephras with the same eruptions that deposited ABII-09-03 and ABII-09-08; we call them tephras AML1 (Aluto Microlite Layer 1) and AML2, respectively (Fig. 2.7). Texturally and temporally equivalent layers to LLIII-04-51 and LLIII-05-23 are not present in the ABII core, suggesting that the eruptive deposits either did not reach, or were not preserved, in the more distal Lake Abijata.

The other microlite-rich layers in ABII, ABII-11-07 and ABII-11-79:81, were correlated with LLIII in much the same way as AML1 and AML2. Recalibrated ^{14}C dates suggest ABII-11-07 was deposited between 9908 and 10394 cal. yr BP and ABII-11-79:81 between 10394 and 10931 cal. yr BP. There are nine tephras deposited in the LLIII core within a similar time period. Of these, only three contain comparable proportions of microlitic material (LLIII-08-38, LLIII-09-03 and LLIII-09-15), with LLIII-09-15 containing a far lower proportion of microlitic material than the other two (Fig. 3b). Consequently, we correlate ABII-11-81 with LLIII-09-03 (eruption is termed AML3) and ABII-11-07 with LLIII-08-38 (eruption AML4; Fig. 2.7).

Trace element data for AML1, AML2, AML4 and AGSL1 support these correlations, with Ba found to be particularly effective in distinguishing between the correlated layers (Fig. 2.5). It should be noted that other trace elements, particularly Zn and Ca (Appendix B), have similar trends, although Ba is the most pronounced. The glasses in layers comprising AGSL1 have very similar Ba concentrations clustered tightly at around 350 ppm. The two layers that comprise AML4 contain 50 – 100 ppm less Ba than the other layers and thus appear distinctive and correlatable. Experimental data indicate that Ba partitioning into feldspar decreases with decreasing Ca content and consequently, increasingly peralkalinity. (Henderson and Pierozynski, 2012, F. Iddon per comms.). As a result, Ba may behave incompatibly in this setting, providing a useful element to assist with correlating by componentry. The glass compositions of tephras containing densely packed microlites (AML1 and AML2) are more variable however, (consistent with varying crystallinity) and thus harder to constrain using trace element data. The layers comprising AML1 showed some differences in Ba concentration, with LLIII-03-70 ranging from 350 to 430 ppm while ABII-09-03 ranged from 400 to 500 ppm. The layer immediately below it in the core (AML2) spans the range occupied by AML1, with Ba 350 to 500ppm (Fig. 2.5). For these layers we infer the crystallisation of microlites is causing localised changes in the melt concentrations of trace elements. Consequently, it appears that componentry analysis is the most effective method for correlating layers with complex microlite textures.

In summary, we have been able to correlate a total of five tephra layers between the two cores (Fig. 2.7; Table 2.2). To achieve this, we used several techniques which, when used in isolation, do not allow for confident correlations. Major element values showed large overlap but componentry analysis proved useful. Layers correlated using componentry show either distinctive glass shards with a unique chemical composition, or a considerably higher proportion of microlite bearing grains (~100% more in the ABII core) than other tephra layers in the core. This means that microlite-rich layers can be identified with relative ease using SEM analysis. Correlations of these layers are confirmed with trace element analysis (Fig. 2.5),

Table 2.2: Summary of correlations made between cores ABII and LLIII from lakes Abijata and Langano. The features which have allowed these five layers to be correlated are detailed, including the TiO_2 content of the glass, proportions of different ash components (quantified from SEM images) and the trace element glass composition- particularly Ba and Ca concentrations.

ABII layer	LLIII layer	Reasons for correlations		
		Geochemistry	Texture	Trace elements
ABII-09-03	LLIII-03-70	Non-unique major element concentrations	High proportion of dense microlites	e.g. High Barium concentration
ABII-09-08	LLIII-03-110	Non-unique major element concentrations	High proportion of dense microlites	e.g. High Barium concentration
ABII-10-73:77	LLIII-07-75	High TiO_2	High proportion of glass shards	E.g. High Calcium concentration
ABII-11-07	LLIII-08-38	Non-unique major element concentrations	High proportions of sparse microlites	e.g. Low Barium concentration
ABII-11-79:81	LLIII-09-03	Non-unique major element concentrations	High proportions of sparse microlites	e.g. Low Barium concentration

and are consistent with timing and position in the core. Importantly however, correlations are difficult to confirm using either geochemistry or textural data alone. Additionally, the many other tephra layers in the cores, while typically microlite-bearing, are not sufficiently distinct to allow definitive correlation.

Some tephra layers identified in lake sediment cores 40km WSW of Corbetti have similar compositions to our Aluto tephras; specifically, Martin-Jones (2017) identified indicate two non-Corbetti sourced tephras in a core of lake Tilo (~100 km south west of Aluto). One of these, TT-6, is ~1 cm thick and shows geochemical similarities to many of the Aluto core tephras (Fig. 2.4). From its Oxcal modelled age of 2672 – 2159 cal. yr BP we infer that TT-6 most likely corresponds to the thickest of the ABII tephras (ABII-04-62:73) which is 11 cm thick and has a modelled age of 3167 – 3612 cal. yr BP. However, this correlation is not confirmed with componentry or trace element data.

2.4.2. Calculating an eruption frequency

The lake sediment cores represent a continuous record of Holocene eruptive activity from Aluto volcano. Unlike terrestrial sections, which may be subject to remobilisation, erosion, and pedogenesis, lake tephras can record relatively small events (e.g. Kuehn and Negrini, 2010; Moreno et al., 2015) and consequently preserved a good record of Aluto's Holocene eruptive history. To quantify this, we have analysed the sequence of tephra ages obtained from Oxcal modelling.

The Oxcal model calibrates tephra ages starting with the ^{14}C dates provided from the two paleoclimate studies (Gibert et al., 1999, 2002; Chalié and Gasse, 2002). The model provides an upper and lower bound for each tephra layer but, for simplicity, we use the median values. As the only dates available are the ^{14}C values from the paleoclimate studies, the modelled tephra ages depend on the accuracy of these dates.

The medians of each of the correlated layers are shown in Figure 4.8 and Table 2.1. AML1, AML2 and AML4 have comparable Oxcal ages, with the medians of the modelled dates falling within ~200 years of each other. The median ages of AGSL1 and AML3, in contrast, differ in the two cores by several hundred years (Figs. 4.7 and 4.8): layers identified as AGSL1 are ~800 years apart while the units comprising AML3 are ~650 years apart. There is however, overlap between the upper and lower bounds of the Oxcal ages in both cases (Table 1) indicating that, despite the bigger gaps in the median ages, the ages are still within error.

It is possible that the low overlap in age for the AML3 and AGSL1 layers is because of the corrections made to ^{14}C dates in the cores. Lake Langano has been subject to CO_2 degassing through a fault system outcropping under the lake (Gibert et al., 2002). While the authors corrected for this CO_2 emission based on modern levels of CO_2 degassing, it is possible that the CO_2 output from the fault has not been constant over time. Lakes Langano and Abijata were also joined during a humid period in the early Holocene (Le Turdu et al., 1999; Benvenuti et al., 2002, 2013; Chalié and Gasse, 2002). Consequently, any reservoir effects may have affected both cores to an unknown degree. While the authors of both chronologies have applied corrections to the measure ages, it may not have been possible to fully account for the effects which influenced the ^{14}C ages and, as a result, our tephra Oxcal ages.

Core ABII contains 24 Aluto-sourced tephras deposited over a time span of 8990 years equating to, on average, one eruption every 375 years. LLIII contains 20 Aluto-sourced tephras over 5439 years, indicating one eruption every 272 years. It should be noted that LLIII is closer and so likely to record more eruptions. To assess the temporal variability we plot the survival function (S_T) for both cores (Fig. 2.8):

$$S_T = \frac{N-i}{N}, \tag{2.1}$$

where N is the total number of repose intervals and i the number of eruptions up to that point in time (e.g. Connor et al., 2003). As LLIII does not cover the same age range, the curve was modified based on the ages and locations of the ^{14}C-dated material, so the LLIII curve begins at the same time as a similarly-aged ABII point. This assumes that up to that point the LLIII core would have contained the same number of tephra layers as the ABII core, should its record have extended back as far. Layers in ABII occur at irregular time intervals. There are three periods where the gradient of the survival function is steeper (more eruptions per unit of time ~3.5, ~6 and ~11 ka) and two periods where it is flatter (fewer eruptions: at ~5 ka and ~8 ka) giving it a stepped appearance. LLIII shows similarly variable eruption recurrence intervals. The LLIII core is shorter however, and contains only two periods of increased activity (i.e. the survival function has a high gradient; Fig. 2.8a) and one lower-frequency period (at ~9ka). The two periods of heightened eruptive activity in the overlapping portion of the two cores are slightly offset, with the flat portion of the survival function beginning and ending ~800 years earlier in LLIII than ABII. This offset is consistent with the offset observed in the modelled ages of the

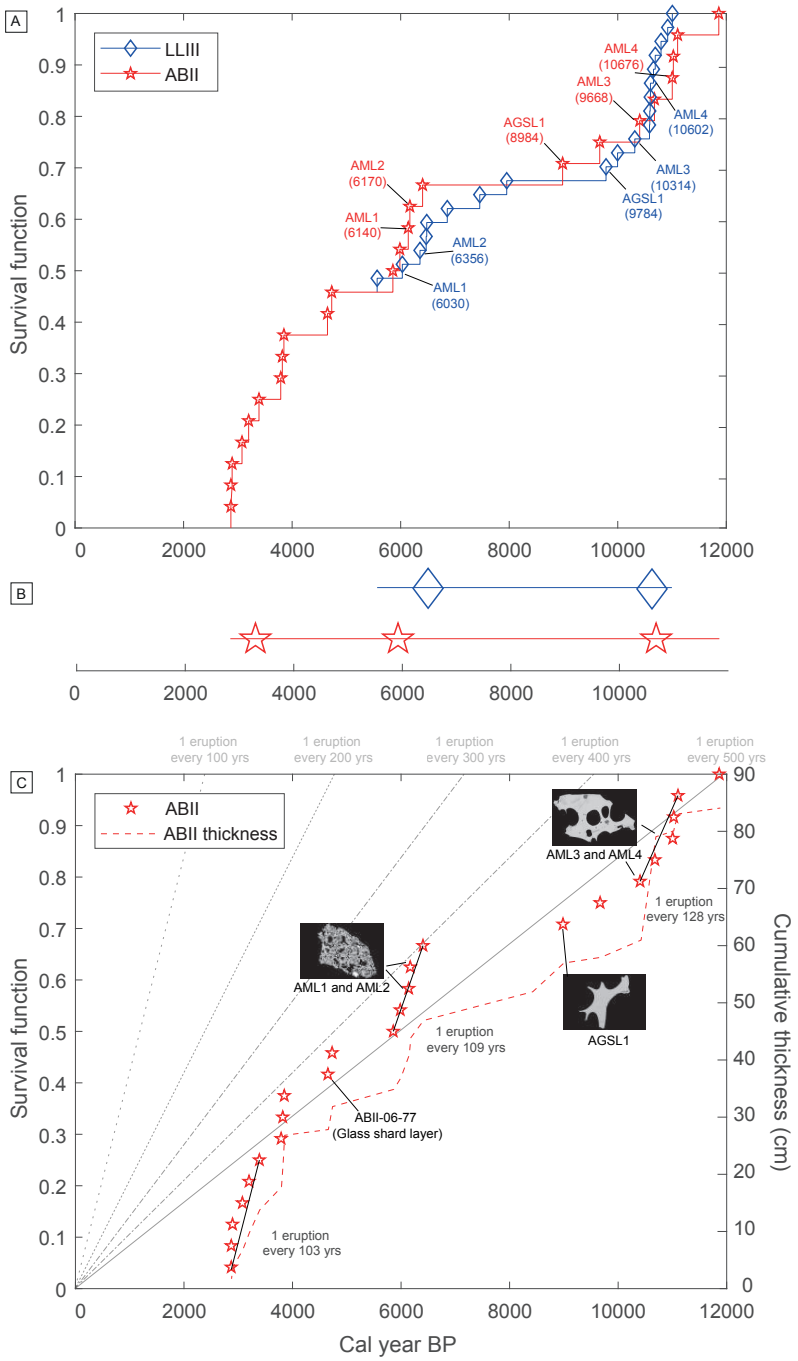

Figure 2.8: (a) Plot of survival function with time for core ABII (red) and core LLIII (blue). The correlated layers are labelled, with the ABII layers in red and the LLIII layers in blue. The medians of the Oxcal modelled ages are in brackets. (b) Centroids of the three main periods of increased activity are shown. This is defined as any cluster containing five or more tephras with an eruption frequency greater than one eruption every 150 years. (c) Plot highlighting the three clusters in ABII that correspond to periods of increased tephra deposition (red dashed line) and consequently, increased tephra thickness. Correlated layers with their unique textures are also shown. Note ABII-06-77 which is not correlated with a LLIII layer but has a high proportion of glass shards (as seen in AGSL1). Grey lines indicate the gradients of various eruption frequencies which can be compared to the gradients of the clusters as well as the period of repose

correlated tephra layers. The apparent offset between the two cores could be a consequence of the aforementioned CO_2 degassing into Lake Langano that may have affected ^{14}C dates. LLIII also records more eruptions than ABII, which is expected given its proximity to the volcano (Fig. 2.8a). While this may have resulted in some under-recording in ABII, because the cores record similar eruptive patterns (i.e. periods of increased activity) we interpret the non-linear eruption pattern to be real and not an artefact of tephra preservation.

The stepped-like appearance of the survival function for the two cores (Fig. 2.8a) indicates that the volcano has seen pulses of increased activity alternating with periods characterised by longer repose intervals. To quantify the eruptive 'pulses', cluster analysis was undertaken using the k-means function in Matlab vR2017a. The function uses a Euclidean distance measure and the k-means ++ algorithm. The cluster algorithm was run for a varying number of clusters from two to 10.

The clustering analysis was run separately for the two cores. Although, the algorithm yielded several clusters for each core, we focus on three clusters that represent heightened eruptive activity. In each case, these clusters include five or more consecutive eruptions with a maximum repose time of 150 years. The cluster centroids in both cores appear at approximately 3.5, 6 and 11 cal. ka BP (Fig. 2.8b). While there are other eruptions in the periods between the clusters, they occur at lower frequencies. The three 'active' periods represent eruptions every 103, 109 and 128 years (Fig. 2.8c) whereas the two intervening 'quiet' periods include activity every 519 and 1700 years. High frequency eruptive episodes deposited more tephra over a smaller time period, as illustrated by plots of cumulative thickness (Fig. 2.8c). Episodic behaviors on varying timescales have been observed in other volcanic systems, and are associated with the interactions between magma evolution, ascent, degassing and crystallisation (e.g. Fontijn et al., 2015; Sheldrake et al., 2016). As Aluto displays non-cyclicity in the eruption recurrence, methods of forecasting that assume a mathematically-constrainable periodicity (i.e. failure models such as a Weibull distribution; Ho, 1996) are not necessarily applicable (e.g. Connor et al., 2003).

2.4.3. Eruptive activity

While the cores provide key information about eruption frequency, it is difficult to estimate eruption magnitude without more detailed spatial information. Critically, the characteristics of a deposit at a single location depend on both the eruption dynamics (e.g. intensity and duration) and the strength and direction of the wind at the time of dispersal. We can make some preliminary inferences about wind direction. It is well established that fall deposits thin and become finer-grained with distance from the volcanic vent when measured along the dispersion axis (e.g. Pyle, 1989). However, the tephras in the more distal ABII core are, on average, slightly thicker than those in the more proximal LLIII core. This pattern suggests that the wind typically directed the ash clouds more towards ABII than LLIII. While we cannot corroborate this robustly, this interpretation is consistent with modern conditions which indicate an east-north-easterly prevailing wind (Kalnay et al., 1996, Appendix F). There are methods to estimate eruption size when a deposit is well sampled and documented, although it is not reasonable to apply them to

eruptions with data from only two locations (two lake cores), especially without total confidence in the wind direction.

However, we can make some estimates of eruption size based on the thickness of the deposits (e.g. Pyle, 1989). Both the magnitude of the eruption (M=log10[mass erupted in kg]-7) and the thickness of the deposit depend on the eruption intensity (mass eruption rate) and eruption duration. To illustrate the possible eruption sizes that produced the Aluto tephras, we compare the thickness of the deposits with those of other well-studied eruptions at equivalent distances. For example, the average thickness of tephra in the ABII core 27 km from the volcano is 3.8 cm. This is comparable to the fall deposit produced by the 2015 M ~4, sub-Plinian eruption of Calbuco in Chile, with tephra <5 cm thick at ~30 km from the volcano (Castruccio et al., 2016).

The thickest deposit in the ABII core is 11 cm thick. This is comparable to the thickness of tephra deposited during the wind-still ~4 ka Plinian eruption of Rungwe in Tanzania; the deposit from this M 5-5.3 eruption is approximately 15 cm thick at ~30 km from the volcano (Fontijn et al., 2011) with 1-3 cm deposition 115 km from the source. At least one tephra layer with a comparable major element composition to Aluto was found in lake cores ~100 km south west of Aluto by Martin-Jones et al. (2017) (Fig. 2.4). In lake Tilo, this layer (TT-6), is ~1 cm thick. If it represents the same eruption as the 11-cm ABII layer, then Aluto had at least one Holocene eruption with a maximum size comparable to the Rungwe Pumice wind-still eruption. In reality, the Aluto eruption likely displayed some ash cloud directionality to the southwest (as discussed above), meaning that it was probably smaller.

The thinnest tephras deposited in the ABII core are <1 cm. The 2011 sub-Plinian to Vulcanian eruption of Kirishima in 2011 produced a highly directional ash plume depositing tephra of up to 1 cm thick about 30 km from source along the dispersal axis (Miyabuchi et al., 2013; Nakada et al., 2013). Therefore, based on comparisons to dispersion patterns from eruptions of other volcanoes, we suggest that eruptions of Aluto between ~2 and 12 ka produced deposits comparable to those of volcanoes that underwent Vulcanian to sub-Plinian sized eruptions (VEI 2-4).

Component analysis also provides constraints on eruption style. Most important are the distinctive glass shard layers, and the layers with abundant microlite-bearing clasts, both of which are used to correlate tephras in the two cores. Interestingly, the two layers with distinctive glass shard morphology (ABII-06-77 and ABII-10-73:77 which comprises AGSL1) occurred at the beginning of, or during, the 'quiet' periods (Fig. 2.8). These glass-shard rich, microlite-poor eruptions are also often the thickest deposits in the cores; ABII-06-77 and ABII-10-73:77 are 6 cm and 5 cm thick respectively (compared to an average thickness of 3.6 cm) indicating they are the product of bigger eruptions than their microlite-rich counterparts. We infer that these glass shard layers were produced by more explosive eruptions with rapid ascent rates and a deeper, or less degassed source. The microlite-rich deposits (AML1 and AML2), in contrast, occur during periods of increased eruption frequency, and are ~2 – 3 cm thick in ABII. Importantly, the other layers in the clusters also comprise microlite-containing grains.

Microlite-rich layers may also provide some insight into the eruption dynamics. In general, the microlite-rich glass has the same major element composition as the microlite-poor glass. The glasses differ in trace element composition, however, as shown in Figure 4.5. This trace element difference can be explained by degassing-induced crystallisation of a eutectic melt and associated enrichment of the relevant incompatible elements (such as Ba; e.g. Scaillet and MacDonald, 2001). The trace element data support our interpretation that microlite-rich layers are produced by eruption of stalled, degassed magma from a shallow system (either a conduit plug or dome). Microlites in other settings have been found to grow in systems $\leq$4 km depth (e.g. Hammer et al., 1999; Cashman and McConnell, 2005), we infer that this was likely the case at Aluto where a ~4km deep magma storage is observed (Hutchison, et al., 2016a). Moreover, eruption of magma stored at varying depths prior to eruption has been shown to produce simultaneously-erupted microlite-rich and microlite-poor textures (e.g. Klug and Cashman, 1994; Cashman and McConnell, 2005); a feature frequently observed in the Aluto tephra layers.

The glass-shard rich eruptions also produced glass with high TiO_2 and low NaO_2 (Fig. 2.4), which suggests that the deeper, undegassed magmas experienced a different crystallisation history than the shallow-stored magma. We hypothesise that the TiO_2 variation is controlled by the crystallisation (or lack thereof) of aenigmatite, a mineral common in peralkaline settings (e.g. Di Carlo et al., 2010; Gleeson et al., 2017), and which contains 7 – 10 wt.% TiO_2. There is some debate as to where aenigmatite appears on the liquidus, although it is likely that it is a late-crystallising phase, precipitated after Al_2O_3 decreases from crystallisation of alkali feldspar (Di Carlo et al., 2010; Neave et al., 2012; Gleeson et al., 2017). As NaO_2 values are also unusually low, we infer the distinct composition reflects the crystallisation of other phases, particularly alkali feldspar.

Maps of Aluto's intra-caldera deposits show that pumice cones and obsidian coules are the most common form of Holocene activity from Aluto (Hutchison et al., 2016c; Fontijn et al., 2018). Therefore, it is likely that many of the deposits found in lake sediment cores, particularly the smaller microlite-rich eruptions, are the consequence of this type of activity. Pumice cone eruptions are typically inferred to be sub-Plinian to Strombolian (Orsi et al., 1989; Houghton et al., 1992); we anticipate, based on tephra thicknesses with distance, that activity from Aluto was of a similar size. We do not see any evidence for very large Plinian eruptions in the Holocene, which is important for hazard assessment of the volcano.

We infer Aluto has been quite active and the last burst of activity recorded in the cores was 3000 years ago. While any estimates of eruption size remain crude, our results provide a reference to which complex, and overlapping terrestrial deposits can be compared. This will in turn enable more realistic interpretations of eruption size in the future.

2.5. Conclusions

We have presented a study of tephra from the Aluto volcano from two lake cores ABII and LLIII. We have revised the age modelling in the cores and applied it to the tephra sequence. Invariance

in the major element geochemistry has made the tephra layers from these cores challenging to correlate and we find we are able to correlate some largely geochemically-similar deposits in cores ABII and LLIII through the use of componentry. Many deposits in the core however, remain uncorrelatable due to the chemical and textural similarities between most eruptions. While typical major elements used for correlations such as SiO_2 and FeO are not useful, certain other elements, particularly TiO_2 and NaO_2 can be used to correlate a minority of tephra layers. These variations however, have not been sufficient to correlate more than one layer confidently; for this reason, we combined geochemical data with textural information.

Textural data suggest five tephra layer correlations based on the presence and abundance of microlites in the constituent glass, as well as the abundance of glass shards. One glass shard layer was found to coincide with the observed geochemical variations and then independently supported by trace element data. The correlations provide a reference for further tephrostratigraphic study of the volcano which can be applied to more complex deposits.

The cores also provide a unique opportunity to constrain the volcano's surprisingly lively eruptive history. The ages of the tephras in the core reveal that Aluto has had at least 24 eruptions in the Holocene, which were mostly erupted in bursts of heightened activity, the most recent of which was at ~3.5 ka while the other two occurred at 6.1 and 11 ka. In general, the microlite-rich tephras occurred during the episodes of increased activity, while the glass shard-rich layers were erupted at the end of these periods or during periods of comparative repose.

While we have not made any definitive estimates of eruption size and style due to the lack of spatial data, we infer that the deposits are a consequence of pumice cone and/or dome-building eruptions, which are typically Vulcanian to sub-Plinian in size and style; an observation consistent with other evidence for pumice-cones and dome-building activity at Aluto.

Chapter 3

Using complex and sparse tephra records to constrain information about Holocene eruptions at Aluto Volcano

Author contributions and declaration: K. V. Cashman and A. C. Rust provided supervision. The data was acquired, processed and provided by K. McNamara. K. Fontijn, A. Zafu and F. Dessalegn provided assistance in the field.

ABSTRACT

Aluto volcano is a restless volcano in the central Main Ethiopian Rift with a Holocene eruption frequency of ~one eruption every 250 years. While the frequency of eruptions has previously been constrained using two lake cores, with five layers were correlated between these cores, limited exposure and complicated stratigraphy make this a challenging environment for a comprehensive physical volcanology study. Here we use tephra layers sampled on land closer to the volcano to refine estimates of eruption size. We can correlate all five of the identified lake core layers to corresponding layers in one land section, and one of the layers to an additional land section. The correlation process is complicated by glass weathering. As a result, there are only limited data (from a maximum of four locations) available with which to construct reasonable estimates of eruption size. Consequently, we use analogous eruptions to assess suitable eruption parameters and input them into the Tephra2 ash dispersion model. Using modern wind conditions we compare model and actual thickness and grain size data and infer the likely size, and impact of an eruption of Aluto.

3.1. Introduction

Aluto volcano (or the Aluto volcanic complex) is a silicic volcano in the central Main Ethiopian Rift (MER) with a complicated and understudied volcanic history. Aside from initial trachytic lava flows, the volcano has erupted predominantly peralkaline rhyolites, undergoing one, or possibly two, large caldera forming eruptions at ~360ka (Hutchison et al., 2016a,c; Fontijn et al., 2018). Recent studies indicate that Pleistocene and Holocene activity has comprised mostly pumice cone and dome building eruptions producing localised pyroclastic density currents (PDCs) and obsidian lava flows and coulees. The timing and frequency of Holocene eruptions is explored in Chapter 2.

The volcano is close to population centres and is home to smaller communities living in and around the volcanic edifice. The area immediately surrounding the volcano is semi-developed and comprises agri-businesses and quarries. A newly-built geothermal power plant resides inside the edifice, and is expected to be an important source of renewable energy. Any future eruption would likely have a considerable impact on this facility and local communities.

To increase preparedness, it is necessary to have some indication of the types and extent of hazards likely to be produced by the volcano. As there have been no historic eruptions, our interpretations must be supported by geological data. To improve knowledge of the volcano's eruptive potential, constraints on size, style and frequency of past eruptions are essential. Forecast models, which are an important aspect of hazard management at any volcano, rely on a set of input parameters that are ideally based (at least in part) on information about past eruptions and sourced from the stratigraphic record (e.g. Volentik et al., 2010; Marzocchi and Bebbington, 2012; Maeno et al., 2014). In the case of ash dispersion modelling, the primary input parameters are, among other things, the tephra grain size and erupted mass. Determining both is reliant on accurate and multiple measurements of grain size and thickness at varying locations from the same eruption. This, in turn, depends on the presence of multiple tephra sites and a clear stratigraphy that allows disseminated deposits to be correlated.

To identify deposits from the same eruption, it is necessary to constrain features within an eruptive unit that are unique to that eruption and consider them in the context of stratigraphic constraints. This is typically undertaken using geochemical analyses of the volcanic glass, usually major element concentrations but sometimes also trace element concentrations, which can vary between volcanoes and between eruptions from the same volcano (e.g. Lowe, 2011, and references therein). The various features and processes used for correlating tephras are discussed in detail in Chapter 2.1.1. In the case of Aluto, the Holocene deposits display invariant major element concentration in the glass (Chapter 2), making correlating using traditional techniques challenging. Instead, deposits in two lake cores were correlated based on the physical morphology of the constituent tephra and the trace element glass geochemistry.

If spatially separate deposits from the same eruption can be correlated, measurements of thickness and grain size can be used to elucidate information about eruption magnitude through

the construction of isopleths and isopachs. These can be combined to produce a total grain size distribution and an erupted volume for an individual eruption (Carey and Sparks, 1986; Pyle, 1989; Fierstein and Nathenson, 1992; Legros, 2000; Bonadonna and Houghton, 2005; Alfano et al., 2011). Information about erupted mass and column height can be determined by quantifying deposit thinning and fining (Carey and Sparks, 1986; Bonadonna and Houghton, 2005) or by inverting tephra dispersion models to solve for eruptive conditions (e.g. Volentik et al., 2010; Fontijn et al., 2011; Johnston et al., 2012).

In the past, isopachs and isopleths were often drawn by hand, although less subjective techniques are now often used, including B-spline interpolation methods (Engwell et al., 2014; Maeno et al., 2014). In some scenarios, the construction of isopachs and isopleths is bypassed entirely, and statistical methods employed to determine deposit thinning; statistical fits produce more realistic values for eruption height and erupted mass (e.g. Biass and Bonadonna, 2011; **?**; Yang and Bursik, 2016). Additionally, Bayesian statistics have been utilised to compute the uncertainties, making the models more applicable to complicated natural systems (Rhoades et al., 2002; Burden et al., 2013). Each of these techniques, however, relies on a well-populated dataset of thickness and grain size sampled over a reasonable spatial density.

In certain cases, such as at Aluto, is not possible to gather sufficient data, either because there is not enough exposure, or because the stratigraphic record is so complicated that only a few sections can be confidently correlated. In these scenarios, it is necessary to make inferences about eruption size using sparse data. In sparse-data environments more complex statistical methods have been developed to include information on individual tephra sites and specific wind effects (e.g. Green et al., 2016). However, these methods rely on considerable prior knowledge about the volcano's behaviour, including information from other well-characterised eruptions as well as data on the individual environment of preservation of each deposit. These methods are unworkable in a scenario such as Aluto where 'typical' activity is unknown, and where there are no well-defined eruptions. In such environments, eruption scenarios can be made only as order-of-magnitude approximations. In other settings this has involved estimating the erupted volume from deposit thickness data at a single location (Fontijn et al., 2015), although even this is dependent on at least one eruption in the sequence being well constrained to act as a comparison. In the case of Aluto, where there are no historic eruptions, it is impossible to benchmark against another eruption from this volcano.

Here we correlate tephra layers from various locations to gather thickness and grain size information from as many locations as possible. We then compare the grain size and thickness data from well-constrained eruptions of assumed-analogue volcanoes to the limited information from Aluto. We use these data to create an order-of-magnitude estimate of the size of eruptions at Aluto, and then use bracketing eruption scenarios to model ash dispersion based on modern wind conditions and compare to results from the deposits.

Figure 3.1: Map showing the location of the lake cores and the land sections included in this study. Patterned areas indicate palaeolake level as in Benvenuti et al. (2002).

3.2. The deposits

We studied tephra samples from two sources: (1) two lake cores drilled for a palaeoclimate studies in 1994 and 1995 and re-sampled from the core storage facility in 2015 (Chapter 2) and (2) terrestrial sections of exposed lacustrine deposits, sampled in the field in 2015. The large number of tephra layers, limited exposure and reduced time in the field allow us to consider only three terrestrial sections in this study.

3.2.1. Lake cores

The lakes cores have provided important information about eruption frequency as they are temporally well-constrained by multiple ^{14}C dates. Tephra layers in the two lake cores have been analysed for thickness, grain size, componentry, geochemistry and timing and five tephra layers correlated between cores (Chapter 2).

The two cores represent sediment deposition from the same time period, with ^{14}C dates obtained from organic material deposited between the tephras indicating ages between ~1.7 and 12.5 cal. ka BP. (Gibert et al., 1999, 2002; Chalié and Gasse, 2002). LLIII and ABII, were sampled 12 and 27 km from the volcano respectively in lakes Abijata and Langano (Fig. 2.1) and LLIII contained 21 tephras, while ABII contains 25.

The glass geochemistry of tephras analysed using EMPA revealed homogenous compositions across the different tephras in both cores. The only clear exceptions are two tephra deposits that are attributed to the eruption of neighbouring Corbetti volcano (Fig. 2.4). Tephra layers in both cores comprise peralkaline rhyolites with 72 – 76 wt% SiO_2, and an average of 74.1 wt%. The only oxide to display some heterogeneity between the tephra layers is TiO_2.

To disentangle the compositionally homogenous tephra in both cores, componentry analyses were undertaken using backscatter electron secondary electron microscope (BSE SEM) imagery to capture the variation in clast type. This was complemented by LA-ICP-MS trace element geochemical analyses of selected tephras.

The result of these analyses was the identification of three distinguishing 'types' of deposits determined by the ash texture and Ba and TiO_2 content of the glass; (1) a high proportion of glassy grains containing a high density of microlites with average TiO_2 and high Ba (2) high proportion of concave microlite-free glass shards with high TiO_2 and average Ba (3) high proportion of glassy grains with a sparse microlite population with low Ba and average TiO_2 (Figs. 2.5, 2.6).

In total, five layers in each core were identified as falling into one of the above categories (Fig. 2.3); two in the first (termed AML1 and AML2), one in the second (termed AGSL1) and two in the third (termed AML3 and AML4). A full summary of these correlated layers can be found in Chapter 2 (Table 2.2; Fig. 2.7).

3.2.2. Terrestrial sections

We found that little or no tephra is preserved in a terrestrial depositional environment, such that all well-preserved tephra layers were found amongst lacustrine sediments, indicating they were deposited into a palaeolake. Consequently, the tephras available to sample are constrained by lake highstand periods of the Holocene, which are well studied and shown in Figure 3.1.

An additional challenge was exposure. The rift centre is a ~30 km wide plateau with very little topographic change. Consequently, almost all exposure was in quarry walls, road cuttings and river-cut gorges, particularly the gorge of the Bulbulla river (Fig. 3.1). This significantly limited the spatial resolution and variability of our sampling capabilities.

Three major sections were sampled (MER050, MER046 and MER048) along with some deposits along the edifice (Figs. 3.1, 3.2). Stratigraphic logs of each sampled deposits are shown in Fig. 3.2. Each section comprised interbedded diatomite and tephras. In general, the different volcanic deposits were easily identifiable by grain size and colour, although rarely, the deposits comprised a mixture of volcanic clasts amongst a matrix of fine lake sediment, which complicated thickness measurements. For each layer in each section, bulk tephra was sampled or, if the sample appeared reworked or contained a high concentration of lake sediments, only pumice was sampled (Table 3.1).

The most distal of the three sections is MER050, located 13 km from the volcano (Fig. 3.1)

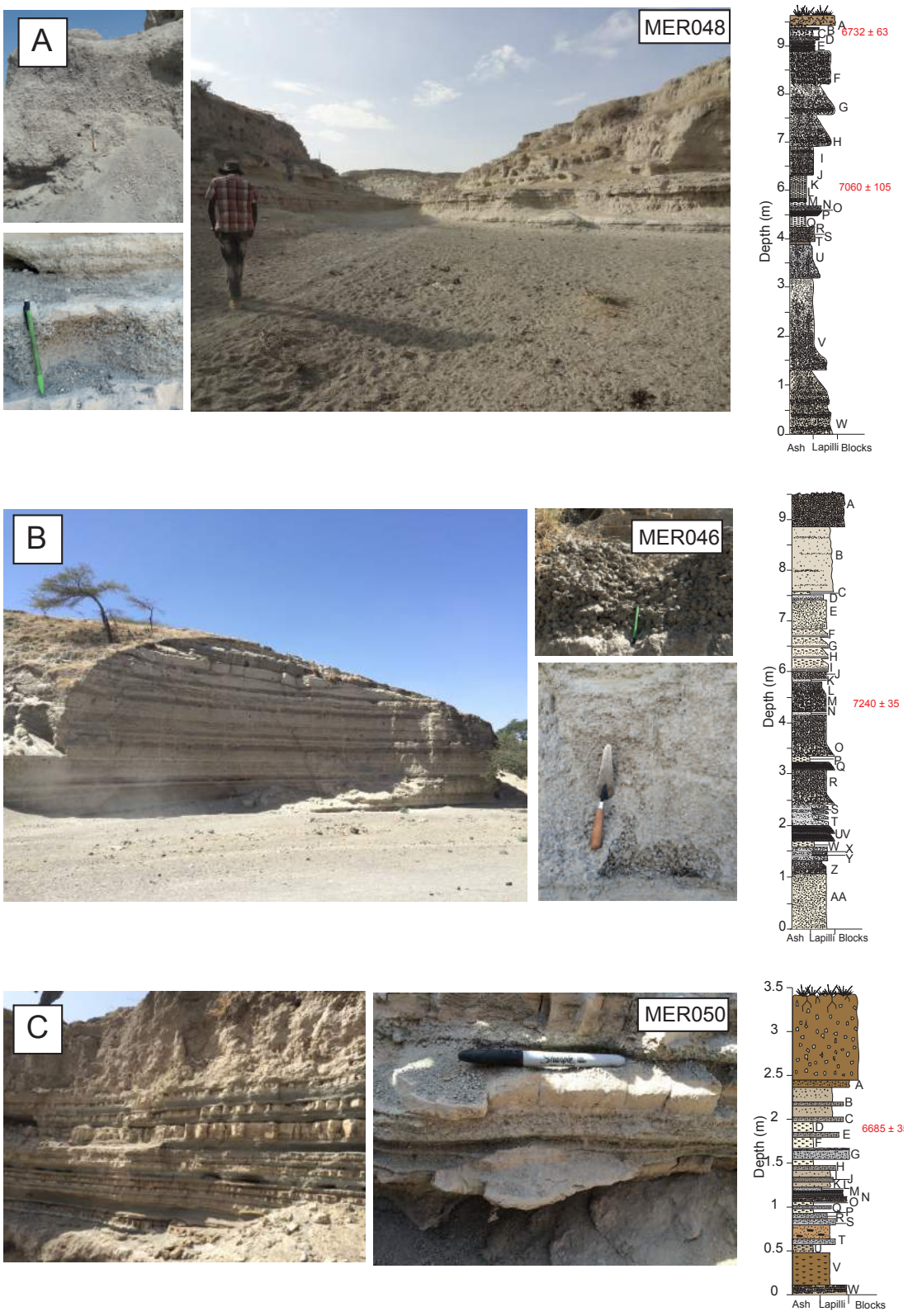

Figure 3.2: Photos of three land sections samples with a stratigraphic log of each. ^{14}C dates are shown in red, while the different units sampled are indicated by letters.

and exposed by a road-cutting in the town of Bulbulla. The section is 3.5 m high and contains 17 tephras (Fig. 3.2). The deposits are typically graded, with both normal and reverse grading observed. MER048 is the next-closest section to Aluto, located ~8 km from the centre of the caldera and ~6 km from the edifice, and contains 14 tephras with interbedded diatomite layers. The seven uppermost tephra layers were sampled from a quarry-cut section, while the rest were exposed by a seasonal river gorge (Fig. 3.2). MER046 is the most proximal section, located ~7 km from the centre of the caldera and ~4 km from the edifice and comprises 17 tephras.

3.3. Methods

Most methods used in this chapter are described in Chapter 2, including methods for analysing major elements (using EPMA) and trace elements (using LA-ICP-MS), as well as methods for granulometric and componentry analysis.

Here we also analysed melt inclusions using EMPA. As the melt inclusions were typically $<10\,\mu m$ in size, it was necessary to adjust the analytical conditions from the standard glass analysis. Melt inclusions were analysed with a 3 µm defocussed beam at 2nA. For each analysis, the time dependant intensity (TDI) correction was run to account for a drop in count rate as a result of alkali migration due to the small spot size. Secondary standards were run between each analysis and no drift was observed.

Raman analyses of glasses were undertaken using a micro-Raman spectrometer (HORIBA; XploRa-Raman-System). A green argon ion laser (532nm) was used at 3mW with a four second exposure time and a 50 µm confocal pinhole. Calibration was performed on peralkaline silicate standards from Di Genova et al. (2015). Water content of glass was obtained as per the methods of Di Genova et al. (2017).

3.4. Characterising the deposits

Each section was analysed for granulometry, geochemistry and componentry as per the methods developed in Chapter 2. Here we summarise the results of each of the analyses for the terrestrial sections MER048, MER046 and MER050.

3.4.1. Radiocarbon dating

^{14}C dates were obtained in three terrestrial sections from gastropod shells and analysed by Beta-Analytic's radiocarbon dating lab in Miami. The shells were sampled from diatomite layers MER048C, MER048K, MER046M and MER050D (Fig. 3.2). Uncalibrated ^{14}C data can be found in Appendix K. The resultant ^{14}C data indicate all sections are Holocene; MER048C is dated as 6732 $\pm$ 63 cal. yrs BP, MER048K as 7060 $\pm$ 105 cal. yrs BP, MER046M as 7240 $\pm$ 35 cal. yrs BP and MER050D as 6685 $\pm$ 35 cal. yrs BP (Fig. 3.2). This means that all three of the sections should record (at least in part) the same tephra deposition as the lake cores (1.7 -12.5 cal. ky BP), meaning all locations should preserve some tephra in common.

Table 3.1: Summary of samples, their depth in the section and analyses undertaken. Depth and thickness in cm.

Sample	Description	Depth	Thickness	Md ϕ	Grainsize	SEM	Componentry	EPMA	LA-ICP-MS
		MER050							
MER050A	Pyroclast conc. under soil	8	8	0.7	X	X		X	
MER050B	Pyroclastic unit	11	4	0.5	X	X	X	X	X
MER050C	Pyroclastic unit	50	4	0.4	X	X	X	X	
MER050D	Diatomite	65	15						
MER050E	Pyroclastic unit	73	8	0.4	X	X		X	
MER050F	Diatomite	89	16						
MER050G	Pyroclast conc., fine lapilli	104	15	0.2	X	X		X	
MER050H	Pryoclastic unit, fine lapilli with free crystals	110	5	0.4	X	X	X	X	X
MER050I	Brown silt/fine sand with pumice particles	122	7	1.3	X				
MER050J	Bedded coarse grey ash, 8th unit	126	4	1.9	X	X	X	X	
MER050K	Brown poorly sorted silt with pumice and obsidian particles	131	5	3.9	X				
MER050L	Light grey fine ash below	134	3	3.6	X				
MER050M	Fine bedded lapilli	142	8	0.9	X	X	X	X	
MER050N	Fine pumice lapilli	146	4	0.2	X	X		X	X
MER050O	Diatomite	152	6						
MER050P	Fine pumice lapilli	154	2	0.3	X				
MER050Q	Diatomite	158	4						
MER050R	Bedded coarse ash / fine lapilli	163	5	1.2	X	X	X	X	
MER050S	Fine pumice lapilli	170	7	0.1	X	X		X	
MER050T	Fine lapilli bottom, fine ash top	196	6	3.8	X	X	X	X	
MER050U	Brown diatomite	206	10						
MER050V	Soil under bottommost lacustrine pyroclastics	246	40						
MER050W	Pumice lapilli	247.5	1.5	-0.9	X	X	X	X	

Sample	Description	Depth	Thickness	Md ϕ	Grainsize	SEM	Componentry	EPMA	LA-ICP-MS
			MER048						
MER048A	Diatomite (lower half)	5	5						
MER048B	Small pumice conc.	10	20	-0.7	X	X		X	
MER048C	Shells	30							
MER048D	Fine grey pumice lapilli	35	8	0.2	X	X		X	
MER048E	Fine brown-grey pumice lapilli (capped with shells)	43	8	-0.7	X	X		X	
MER048F	Normally graded pumice lapilli breccia, top part	110		-1.8	X	X		X	
MER048G	Normally graded pumice lapilli breccia, middle part	177	200			X			
MER048H	Normally graded pumice lapilli breccia, bottom part	244		-2.5	X	X		X	
MER048I	Pumice lapilli breccia, pumices (poorly sorted in top)	324	80			X		X	
MER048J,K	Diatomite and shells	374	100						
MER048K	Shells in diatomite	424							
MER048L	Diatomite from bottom of unit	442							
MER048M	Pumice particles from bottom of unit	442							
MER048N	Pyroclasts/diatomite alternation,pumices from upper half	470	28	-0.2	X	X		X	
MER048O	Diatomite mid-unit	470							
MER048P	Pumices from bottom	480	10					X	
MER048Q	Lacustrine pyroclasts, pumices	540	60						
MER048R	Diatomite	544	4						
MER048S	Grey pumice lapilli, some ash matrix	564	20	-0.6	X	X			
MER048T	Brown-beige silt (coarser than diatomite)	573	9	3.9	X			X	
MER048U	Crudely bedded pyroclasts, bulk from bottom	633	60	-4.3	X	X	X	X	X
MER048V	Lacustrine pyroclasts, pumices from bottom	793	1.6					X	
MER048W	Lacustrine pyroclasts, pumices from bottom	873	160						
			MER046						
MER046A	Bulk, coarse pumice lapilli breccia	60	60	-4.4	X				

Sample	Description	Depth	Thickness	Md ϕ	Grainsize	SEM	Componentry	EPMA	LA-ICP-MS
MER046B	Bulk, matrix- supported pumice flow	179	119	3.6	X	X		X	
MER046C	Diatomite	185.5	6.5						
MER046D	Bottom, cemented deposit with rounded pumices	195	55	-0.5	X	X		X	
MER046E	Pumice, poorly sorted, rounded	250							
MER046F	Pyroclastics from top unit (alternating diatomite/pyroclasts)	270	81						
MER046G	Diatomite	290							
MER046H	Pyroclastics	310		-1.2	X	X		X	
MER046I	Coarse pyroclastics at the bottom of unit	331		-2.8	X	X		X	
MER046J	Poorly sorted ash / pumice lapilli unit	341	10					X	
MER046K	White ash layer	347	6	4.4	X	X		X	
MER046L	Coarse pumice at the bottom	377	30	-1.7	X	X		X	
MER046M	Shells from coarse pumice unit	437	60						
MER046N	Poorly sorted deposit, grey ash top	443	87						
MER046O	Pumices only	530							
MER046P	Diatomite covering bedded pyroclasts	539	9						
MER046Q	Pyroclastics	548		0.2	X	X		X	
MER046R	Poorly sorted deposit (pumices sampled)	618	70					X	
MER046S	Diatomite, alternating with pyroclasts	623							
MER046T	Pyroclastics (pumices)	663						X	
MER046U	Normally graded pyroclasts (pumices sampled)	718	55						
MER046V	Black coated pumices	740		-2.0	X			X	
MER046W	Bedded fine pyroclasts (pumices sampled)	750	22						
MER046X	Clast-supported pyroclastic deposit, bottom pumices	778	28	-1.7	X	X		X	
MER046Y	Ash bottom	798		-0.8	X				
MER046Z	Pumice conc. at bottom of matrix-supported unit	808	10	-2.5	X	X	X	X	X

3.4.2. Grain size and thickness

Grain size information is summarised in Fig. 3.3. A description of each of the layers, as well as a summary of analyses performed, can be found in Table 3.1. In the more proximal sections (MER048 and MER046) the deposits often comprise closely interbedded lake sediment and tephras, or pumice lenses in amongst lake sediment. As a result, it was not always possible to sample bulk tephra, and so grain size data were not gathered for every layer. The pyroclastic particles in both sections are also mixed with lake sediments, often in the form of pumice lenses amongst diatomite, or cross-bedding consistent with secondary reworking or deposition as part of a flow.

Consequently, we interpret that many of these deposits were not the product of primary air fall deposition. For this reason, thickness and grain size data reported below (and in Fig. 3.3) include only units which contain purely pyroclastic material and not those which appear to have been thickened and fined by the addition of lake sediment.

The pyroclastics in the most proximal section, MER046, are generally the coarsest, with median grain size (Md) = -0.32 ϕ. MER046 also contains the thickest tephra deposits, which range from 10 cm to 81 cm and an average of 50 cm. The tephras preserved at MER048 are slightly finer with Md = -0.16 ϕ. They are also slightly thinner, with range of 8 to 80 cm and an average of 31 cm. Tephras in the more distal MER050 range in thicknesses from 3 to 15 cm and an average of 6.8 cm. Md = 1 ϕ which, while finer than the other two land sections, is still coarser than the deposits in cores ABII and LLII which have Md = 3.2 ϕ and Md = 2.5 ϕ respectively.

The thickness of interbedded diatomite varies; diatomite layers between the lake core tephras are generally thicker than those between the terrestrial tephras. We attribute this to differences in sediments deposition in different lakes, and different areas of the palaeolake.

3.4.3. Glass Geochemistry

Glass compositions were obtained for samples from each of the tephras as per the methods detailed in Chapter 2. All data, including secondary standard data, can be found in Appendices A and C. As with the cores, all glasses from terrestrial sections are peralkaline rhyolites, with SiO_2 contents between 71 and 76 wt% with an average of 74 $\pm$ 1.1% (1) and total alkali (K_2O + Na_2O) 10.27 wt%.

SiO_2 and K_2O are generally invariant across the tephras in all three sections (Fig. 3.4). TiO_2 however, varies between ~0.1 wt% and ~0.4 wt%. In sections MER046 and MER050, most tephra layers contain TiO_2 ~0.2 wt%, with the exception of five layers: MER046R, MER046Z, MER050H, MER050N and MER050T which contain ~0.3 wt% TiO_2 (Fig. 3.3). In section MER048, four successive tephra layers, MER048L,N,P and U contain TiO_2 >0. 25 wt%.

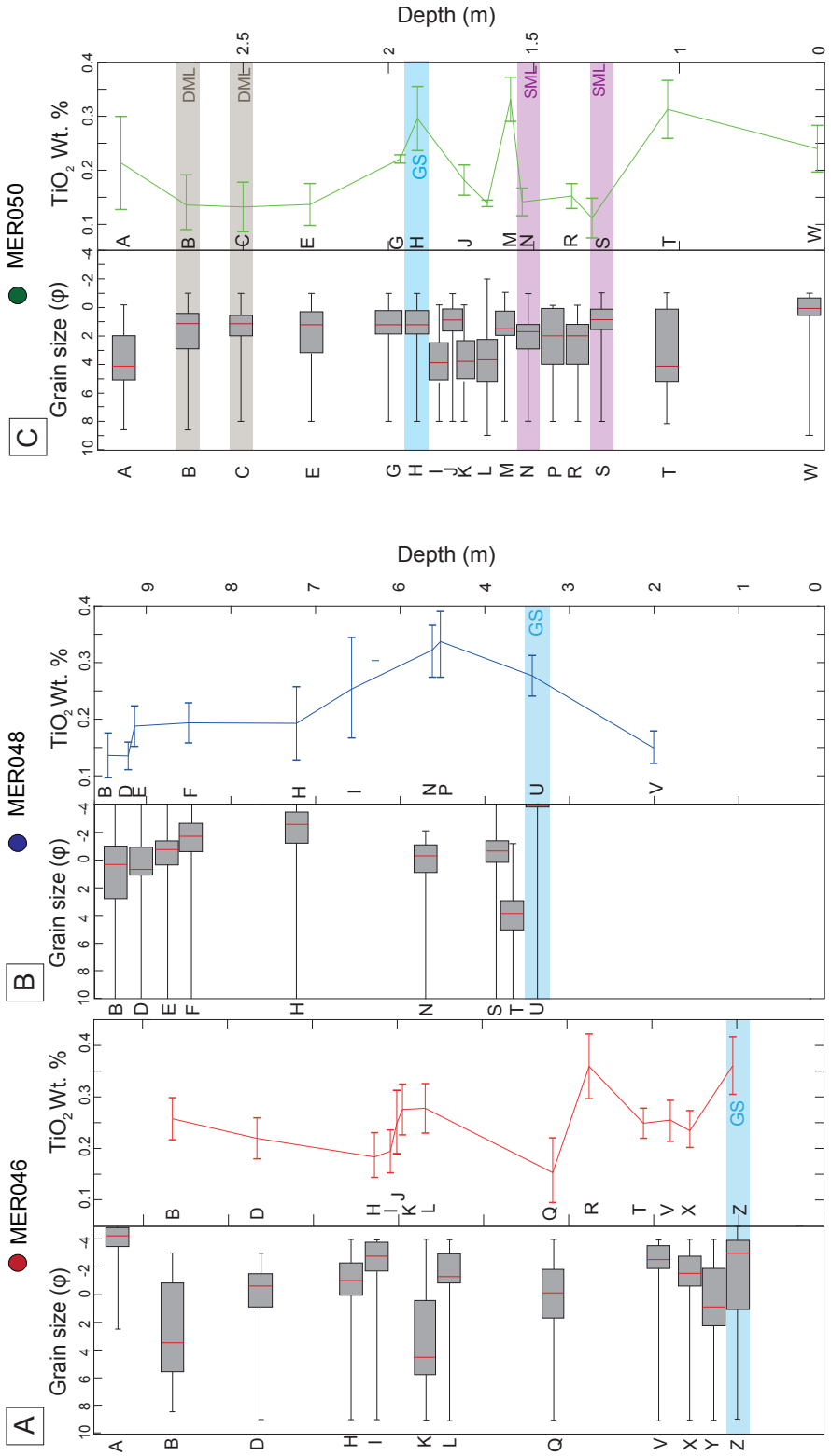

Figure 3.3: Grain size and TiO_2 data for each of the land sections plotted with depth. Boxes indicate the upper and lower quartile, while the red line represents the median. Whiskers indicate the grain size range. TiO_2 data are joined by a line for clarity. Error bars indicate the standard deviation. Layers with unique textural properties are highlighted in colour. See Fig. 3.4 for detailed explanation of the textural classification.

More notably, Al_2O_3 and FeO concentrations vary both between sections and within tephra layers. Glass in all the tephras in MER050 contain between 5.5 and 7.5 wt% FeO and between 7.5 and 9.5 wt% Al_2O_3, with the exception of MER050A (the uppermost tephra in the deposit). By contrast, glass in the MER048 section has a greater range of both oxides, with FeO varying from ~4.5 – ~7 wt% and Al_2O_3 concentrations from 7.5 – ~11 wt%. Glass in tephras in MER046 has more restricted compositions, with FeO and Al_2O_3 values of ~5 – 6.5 wt% and 8 – 10.5 wt% respectively (Fig. 3.4).

Also variable were the EPMA oxide wt% total values, such that the totals tend to be lower for the terrestrial sections than for the lake cores. The average oxide total (Tot_{av}) in the lake cores is 97.1 %, while in MER046 Tot_{av} = 95.9 % and in MER048 Tot_{av} = 96.7 % and MER050 Tot_{av} = 95.7 %. A low total value indicates water in the glass, which is often ascribed to secondary hydration of the glass by meteoric water after deposition. To confirm that secondary hydration caused the low total values, each of the probe analyses was recalculated to include water in the matrix correction (water by difference—WBD). A selection of grains measured by EPMA from two of the terrestrial sections and both lake cores were then analysed by Raman spectroscopy to obtain a second water measurement for comparison. This was performed on both matrix glass and on melt inclusions.

In general, the WBD values and the Raman water contents agree, with all but four grains falling within a 20% of a one to one ratio (Fig. 3.5). These data confirm that matrix glass measured in the lake cores has a lower water content than in the land sections (~0 to ~3 wt%). Matrix glass in the land sections, MER046 and MER048, in contrast had a range of water content, from ~0 to ~6 wt%. As expected, the melt inclusions in all locations had higher water contents than the matrix glass, with water contents between ~3 and 6 wt% in both cores and land sections (Fig. 3.5). High water contents in melt inclusions are consistent with other measurements of water from Aluto melt inclusions from other Aluto deposits, with magmatic water contents found to be between 4 and 8 wt% (Iddon et al., in prep).

As it is not possible to determine the water species using Raman or EMPA measurements, we cannot determine if the water concentrations have varied because of the magmatic water content, or from secondary hydration. However, since the water content seems to vary by section as well as by tephra layer we infer that the environment of preservation has influenced the water content. In seeking to explain why the land sections have been hydrated more than the lake cores, it is important to remember that the 'land' sections were initially deposited during a lake high stand, meaning that all the tephras were deposited in water. In addition, there is no correlation of water content with age in the core, suggesting that even though the tephra has been preserved among lake sediment for many years, the availability of water for secondary hydration may be short lived. Additionally, many of the tephras exposed in the land sections were exposed in river-cut gorges, implying they were exposed to meteoric water long after the lake core tephras had been buried.

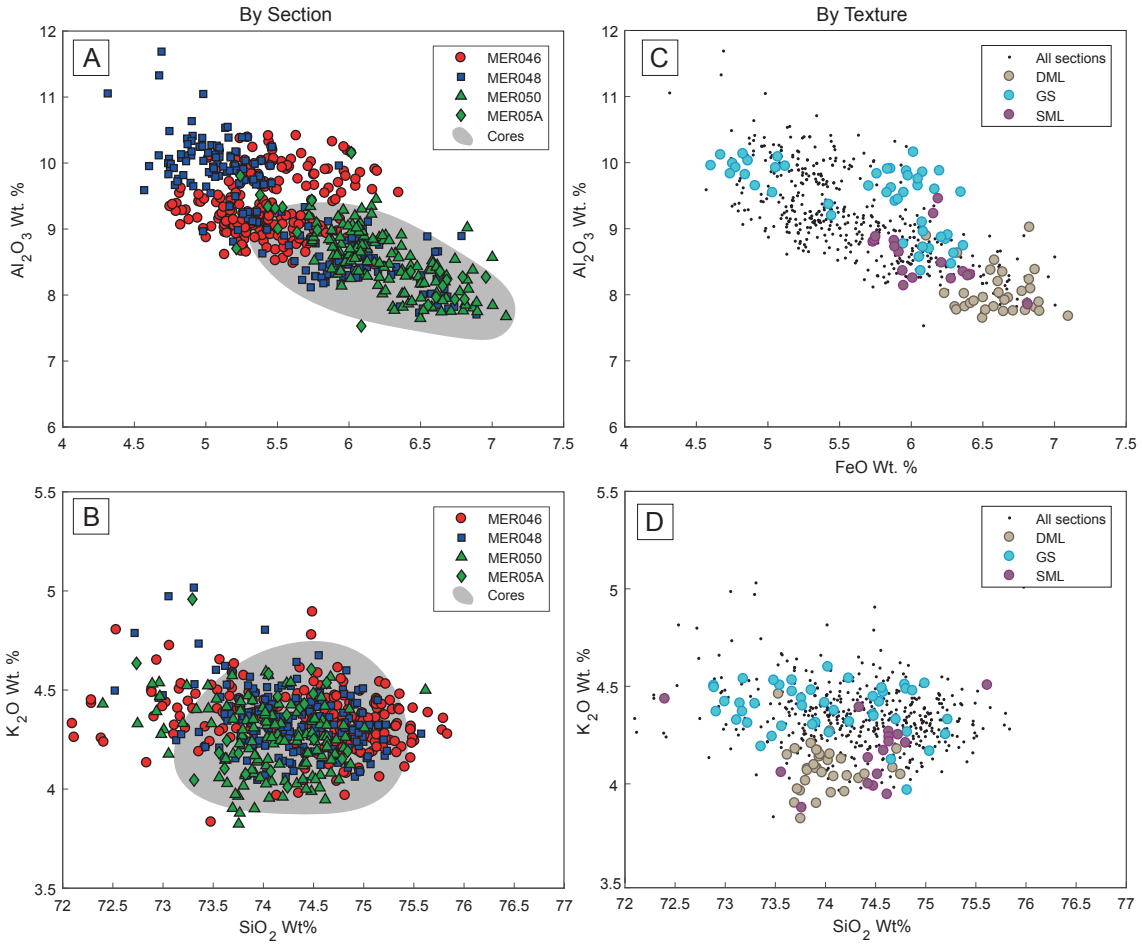

Figure 3.4: Bivariate major element geochemistry plots of glass from all three land sections. The data are plotted (a & b) by section to show variation between isochronous land sections, and (c & d) by texture to indicate any possible geochemical variation with different texture. Shaded grey areas indicate the range of composition of the lake core tephra layers, which is different to range occupied by the three land sections.

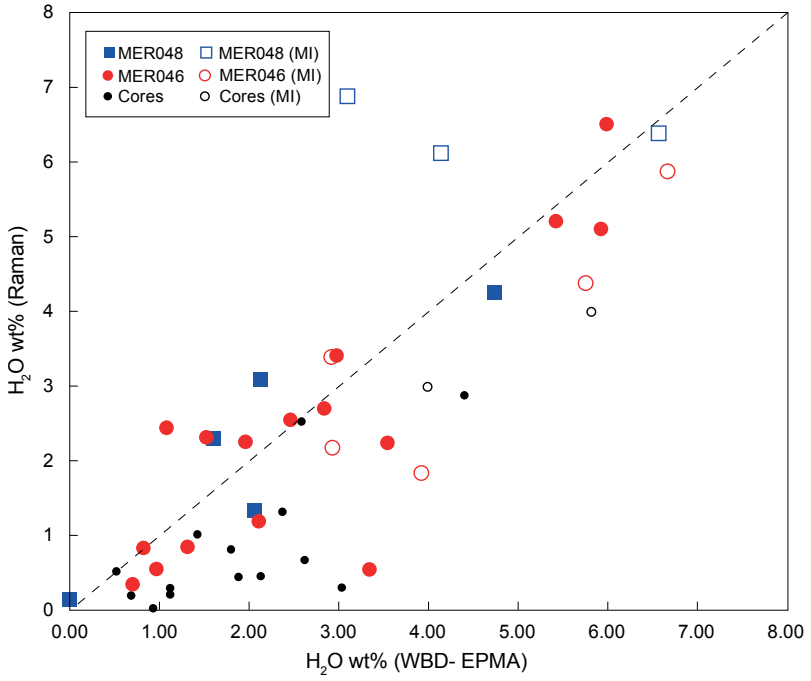

Figure 3.5: A plot of H_2O content in a selection of glasses for MER048, MER046 and the lake cores. The axes indicate two different methods for measuring water content—water by difference (where EMPA major element totals are <100% and the remainder is assumed to be water) and using Raman spectroscopy. Open circles indicate data from melt inclusions, while closed circles indicate data from matrix glass. The black dashed line indicates a one to one relationship.

3.4.4. Componentry

Sections were prepared for BSE SEM analysis and an image containing between 300 and 1000 grains obtained for the 1,2 and 3 ϕ grain size fractions. Each image was scrutinised for the key components identified in similar analysis of lake core samples in Chapter 2. As point counting is time-consuming, quantitative componentry analyses were not performed for every layer, but rather for those which displayed componentry similar to the key correlated layers in the two lake cores. The three features used to correlate the layers in the two lake cores were (1) high proportions (>30%) of densely packed-microlite containing glass (DM) (2) high proportions (>30%) of glass sparse microlite-containing glass (SM) (3) high (>10%) proportions of glass shard fragments (GS; Fig. 2.5, 2.6, 3.6).

In the most distal section MER050, five layers contain one of these three distinctive textures (DM, SM, GS; Fig. 3.3). MER050B and MER050C contain grains comprising 24% and 25% glass with densely-spaced microlites while grains in MER050H comprise a high proportion (23%) of glass shards (Fig. 3.6). MER050N and MER050R were also distinctive, comprising 14% and 15% grains with sparsely-spaced microlites, respectively. In other sections, MER048U and MER046Z contain a high proportion of glass shards (34 and 42%, respectively).

3.4.5. Trace element chemistry

The layers with unusual componentry (Figs. 3.3, 3.6; Appendix D) were then analysed for trace elements, for total of five layers (Table 3.1 and Appendix B). While many of the trace elements showed little difference, key elements were useful for distinguishing the layers (Fig. 3.7). MER050N (SM layer) has Ba values between 200 and 300 ppm, while MER050C (DM

layer) has Ba between 350 and 500 ppm. MER050H (GS layer) has a Ba concentration of 250 – 400 ppm but higher Zn concentrations than all the other MER050 layers, with between 2000 and 2600 ppm Zn. MER046Z (GS layer) has similar trace element composition to MER050H with higher Zn and average Ba concentrations compared to the rest of the dataset. MER048U, in contrast, has very low Ba, with values between 100 and 200 ppm.

3.5. Integrating land sections

Radiocarbon dates indicate that the two lake cores (ABII and LLIII) and the three land sections (MER048, MER046 and MER050) are of comparable age. As such we infer that all should, at some point, have recorded the same tephra deposition even if the more proximal sections (MER048 and MER046) record a higher eruption frequency than the more distal sections (MER050, ABII and LLIII).

Ten layers generated by five eruptions have been correlated in the lake cores using a combination of textural and geochemical data (Chapter 2). Here we attempt to expand these correlations to the three terrestrial sections by applying the methods developed in Chapter 2; we then explore the reasons for inconsistencies between the deposits.

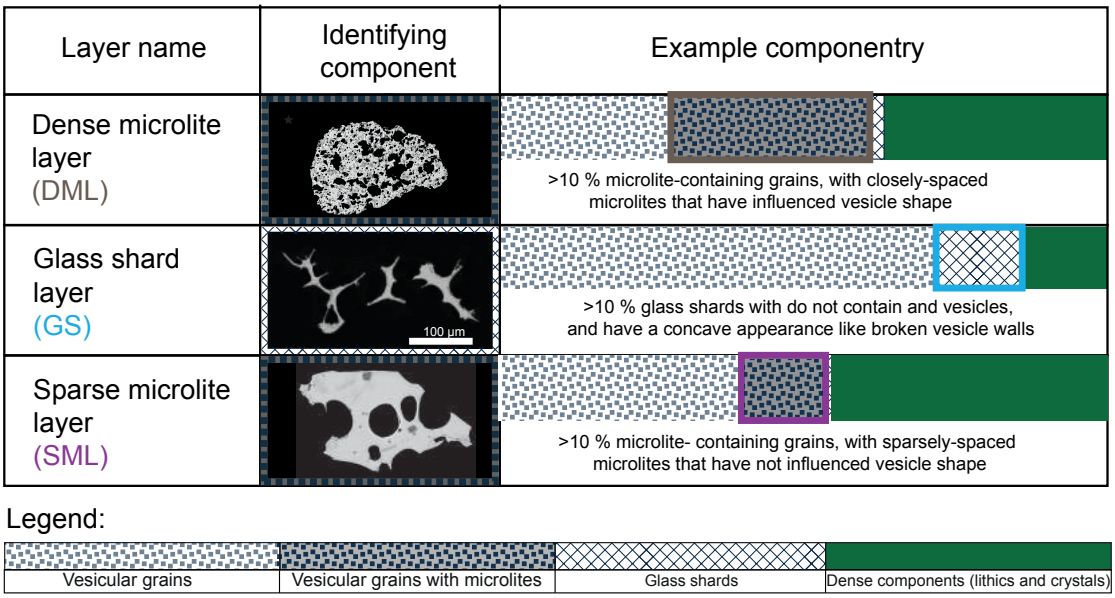

Figure 3.6: The three different componentry types used to correlate the tephras from Aluto: a dense microlite layer, a glass shard layer and a sparse microlite layer. The bar charts indicate the proportions of different components and the coloured squares highlight the key category for distinguishing the componentry type. An SEM image of these distinguishing component type is also shown. Each is from the 125 µm – 250 µm grain size fraction

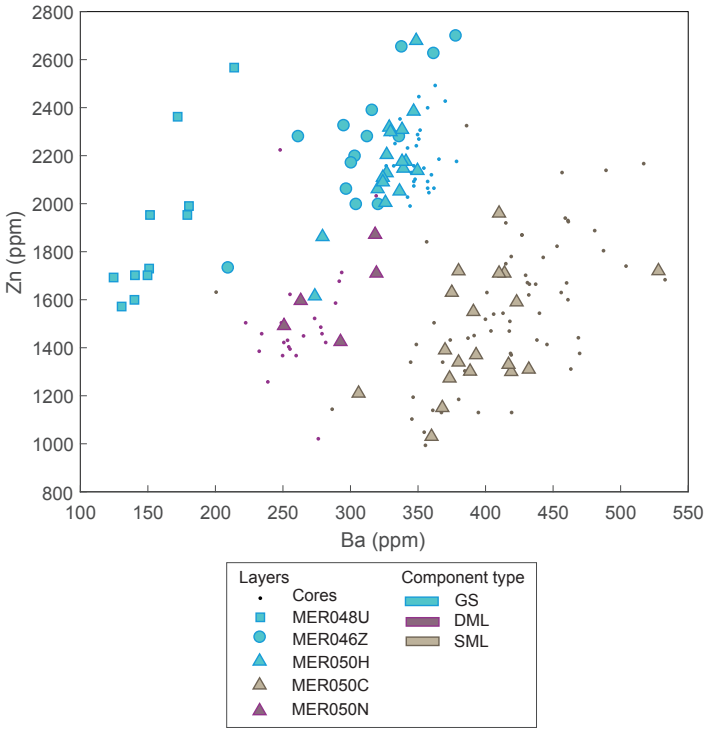

Figure 3.7: Trace element data from select samples from the three land sections. In each case, the symbol shape indicates the section, while the colour represents the texture. Lake core tephras containing grains with comparable textures are shown in the same colour but as dots.

3.5.1. Correlating tephras

In each tephra section and core, there was at least one layer which contained high TiO_2 (>0.25 wt%) while also containing the high proportions (>10%) of glass shards (GS layers). In the cores, this deposit was termed AGSL1 and comprised the layers LLIII-07-75 and ABII-10-73:77. In the three land sections, layers with comparable TiO_2 and componentry values are MER050H, MER046Z and MER048U.

Ash grains in MER050H comprise 23% glass shards and have a glass TiO_2 concentration of 0.3 wt% (Fig. 3.3), while grains comprising MER046Z contain 42% glass shards and a TiO_2 concentration of 0.35 wt%. Similarly, grains in MER048U contain 34% glass shards and 0.28 wt% TiO_2. While in all three sections there are other layers with comparatively high TiO_2, these three layers are the only ones to display both high TiO_2 and high proportions of glass shards. The trace element concentration for each of these layers is also consistent with AGSL1, with the exception of MER048U. MER050H and MER046Z have Ba values between 250 and 400 ppm. MER048U however, contains a much lower concentration of Ba (100 – 150ppm), suggesting either that it is not the same deposit as the others, or that Ba has been lost.

Tephras in the lake cores were also correlated based on microlite textures. Indeed, the more distal MER050 section records a variety of microlite textures. For example, consecutive layers MER050B and MER050C have a high proportion (24 and 25%) of closely spaced microlites

which are similar in appearance to microlite-rich grains observed in the consecutive AML1 and AML2 (Fig. 2.3). Both are positioned directly above diatomite-layer MER050D which contains shells dated as 6685 $\pm$ 35 cal, BP. As a result, both layers are younger than 6685 $\pm$ 35 cal, BP meaning they are broadly isochronous with core tephra layers AML1 (which has a median Oxcal age of ~6100 cal. BP) and AML2 (which has a median Oxcal age of ~6200 cal. BP). The major element compositions are also similar across all four deposits (Appendix A) and MER050C shows comparable trace element composition to AML1 and AML2 with similar Zn and Ba values (Fig. 3.7). MER050B was not analysed for trace element compositions, however given its stratigraphic and textural similarity to the AML1 deposits we are confident it is the product of the same eruption. Likewise, we infer that MER050C is part of the AML2 deposit (Fig. 3.7).

We were also able to correlate an additional two deposits with the core-identified deposit AML3 and AML4, which contained high proportions (~5 – 15 %) of glass with sparse microlites (Figs. 2.2, 2.7tex studio compile on pc butex tex, 3.6). These layers are MER050N (14 % of microlite-containing grains) and MER050R (15% microlite-containing grains). This correlation is supported by trace elements where MER050N and AML4 glasses have consistent Ba and Zn values. Both MER050N and MER050R are stratigraphically below the dated units, which indicate eruptive ages >6608 cal. years BP, in agreement with the better-constrained ages of the AML3 and AML4 (~10 ka and 10.6 ka; Fig. 2.7).

The proximal sections MER048 and MER046 however, contain little to no microlite-rich material. These sections were both the recipients of a much greater volume of volcanic material than the lake core locations and represent deposition from a much smaller window of time. As such, we suspect that these microlite rich eruptions (most common in the early and late Holocene) are simply not exposed at these outcrops. In fact, we cannot correlate tephra in MER048, the section closest to the volcano, with any of the other sections or cores using textural of geochemical constraints. Its proximity to the volcano implies that much of the deposition here may be a result of block and ash flows from dome collapses, or cone building events. Much of the section is highly weathered (Fig. 3.2) and the stratigraphy is complicated. For this reason, we do not include this location in our estimates of eruption size, below.

3.5.2. Geochemical anomalies

An additional complication to correlating the terrestrial sections is the variation in major element glass data in MER046 and MER048, in particular FeO, Al_2O_3 and Na_2O, relative to the lakes cores and MER050. Interestingly, the glass composition of MER046 contains almost no tephra with a chemical composition comparable to the lake cores despite also comprising Holocene tephras. It also has very little tephra with a similar composition to the nearby MER048 (Fig. 3.4). Notably, MER046Z (the layer attributed to eruption AGSL1 based on componentry and glass Ti, Ba and Zn content) has a different FeO, Al_2O_3 and Na_2O glass composition to the other layers attributed to the AGSL1 eruption. If the variation is magmatic (i.e. the composition is the result of a different eruption), then it implies a miscorrelation. However, similar compositional

offsets occur throughout the section.

The MER048 tephras are also unusual in that the major element glass compositions are bimodal when plotted as FeO and Al_2O_3. Layers MER048B to MER048I plot in the region occupied by the lake cores and the MER050 tephras. The lower half of the section (MER048M to MER048V) however, has lower FeO and Na_2O, and higher Al_2O_3. This is not consistent with any deposits in either lake core, or in MER050 (Figs. 3.4, 3.8) and yet ^{14}C dates from both MER048 and MER046 indicate deposition at the same time as the cores.

We suggest two possible explanations for this discrepancy between proximal and distal deposits. The first is that the ^{14}C dates are incorrect, and that the tephra deposition in proximal sections is the product of an entirely different time period where the volcano erupted compositionally heterogenous material. The second option is that the geochemical variance is the product of secondary alteration, and that the tephras which do not match the chemical composition of the cores (MER048M to MER048V and MER046A to MER046Z; Figs. 3.4 and 5.8) have not retained their original magmatic composition.

If the first possibility is correct (flawed ^{14}C dates) then the layers in the proximal sections cannot be correlated with the tephras in the lake cores and MER050. In this case, the sections would represent an earlier record of the volcano's history, perhaps Pleistocene, with little to no tephra preserved from Holocene activity. Because there is limited compositional overlap between MER048 and MER046, this interpretation requires that the tephras in the two sections were deposited by different eruptions, and so represent a different time period not only to the lake cores and MER050, but to each other. Considering their proximity to each other (~3 km), this is unexpected. It also would indicate a surprisingly compositionally heterogenous and highly active period prior to the Holocene.

To explore the second possibility (that the glass compositions have been affected by weathering), we examined differences in preservation environment between and within the sections. Interestingly, the layers comprising the top half of MER048 (MER048B to MER048I), which show comparable compositions to the lake cores, were recently exposed by a quarry cutting (Fig. 3.8). Here it was necessary to follow the section from the quarry exposure into a dry river-cut gorge where the lower half of the stratigraphy was exposed. It is these river-exposed tephras which comprise the anomalous (low FeO, high Al_2O_3, low Na_2O) glass chemistry. Tephras sampled at MER046, which all show anomalous glass compositions (low FeO, high Al_2O_3, low Na_2O), were also sampled from a dry river-cut gorge that forms a tributary of the Bulbulla river (Fig. 3.2). In both cases, the gorges were sampled during the dry season, but we infer that both channels are seasonally filled with water. Conversely, tephras in MER050, which display more homogenous glass chemistry consistent with the lake core tephras, were sampled from a road-cut section in the village of Bulbulla which was first constructed in the 1970's (and therefore has been recently exposed). The only exception is the uppermost layer (MER050A; Fig. 3.4), which was a mixture of ash and soil and could easily be altered.

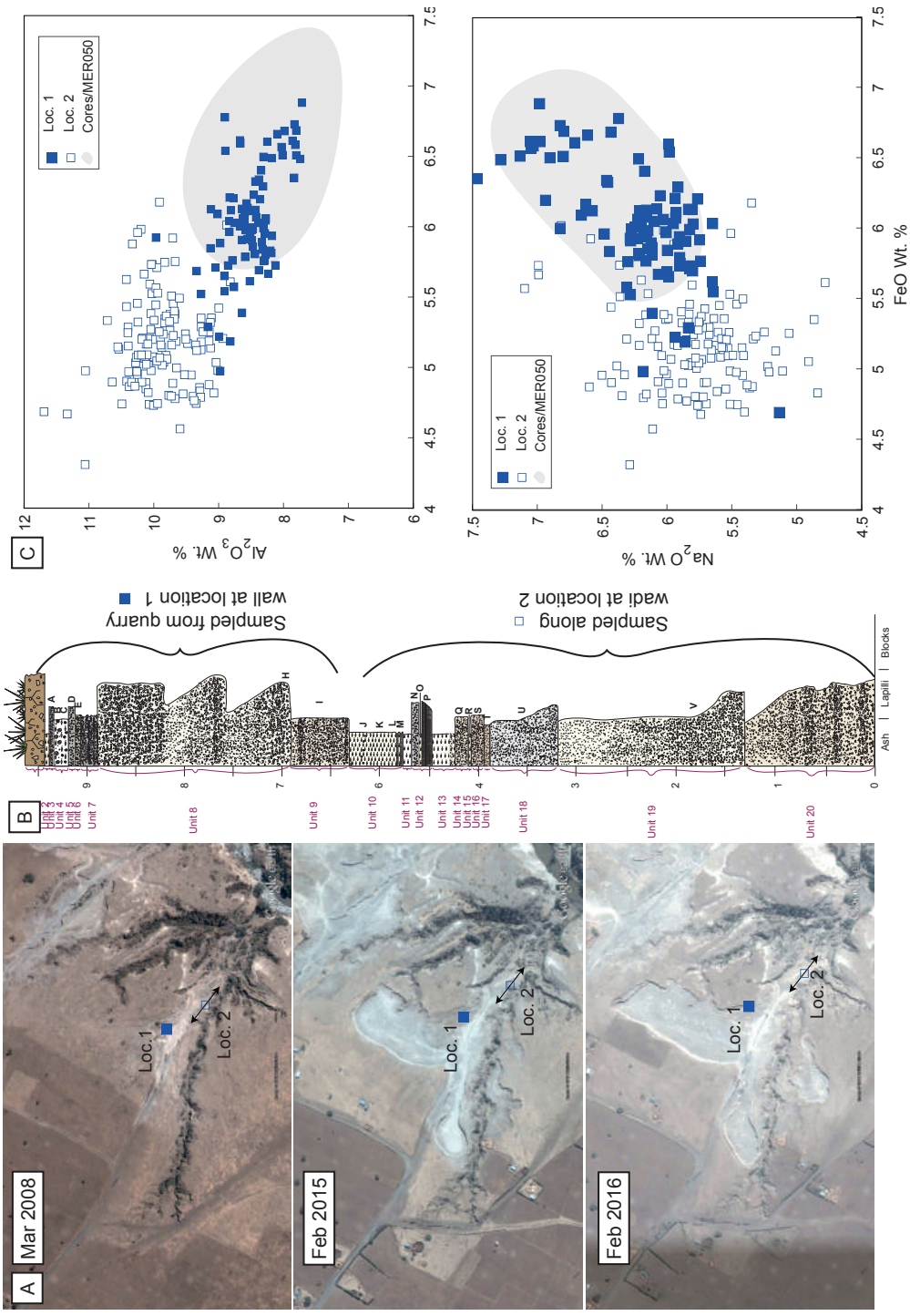

Figure 3.8: (a) Google Earth images of location MER048 taken in 2008, 2015 and 2016 highlighting the recent construction of the quarry which exposed the upper tephras in MER048. (b) indicates which tephras were sampled from which locations, while (c) shows the geochemical variance between the upper and lower tephras.

There is considerable evidence that Na is one of the first elements leached during secondary hydration of alkaline glasses, which causes enrichment of insoluble Al_2O_3 (e.g. Aramaki and Lipman, 1965; Cerling et al., 1985). This may explain the Na_2O and higher Al_2O_3 of the river-cut sections. Ti is known to be one of the most immobile elements (e.g. Zielinski, 1985; Kiipli et al., 2017), which may indicate why TiO_2 signatures remain correlatable. The loss of FeO suggests that Fe may also be mobile.

To investigate this concept further we compared major element glass analyses of melt inclusions in phenocrysts in tephras from MER050, MER046 and MER048 to the chemistry of the matrix glass. We hypothesise that the glass in the melt inclusions will have been protected by the host crystal from the effects of secondary alteration, and thus will preserve the initial glass composition. We note, however, that melt inclusions preserve melt compositions at the time of crystal formation meaning, upon eruption, they will not necessarily comprise the same chemistry as the erupted interstitial melt (e.g. Stewart and Pearce, 2004; Blundy and Cashman, 2005).

A total of nine melt inclusions were analysed by EPMA from three different tephras: two from MER046 (046I and 0646V) and one from MER048 (048N). All three tephras comprised matrix glass with a low FeO and high Al_2O_3 composition (Figs. 3.5, 3.9). In all three layers, the melt inclusions have different FeO and Al_2O_3 contents to the matrix glass, with all containing FeO and Al_2O_3 more comparable to the glasses from tephra in lake cores and MER050 (Fig. 3.9a). There are some differences however; Al_2O_3 is higher in MER046I melt inclusions than in any of the core tephras. Most of these melt inclusions were hosted in aegirine (or other alkali pyroxenes), which crystallises relatively early. As such, the Al_2O_3 content may be higher in the inclusions due to the later crystallisation of alkali feldspar, which would have lowered melt Al_2O_3 concentrations in the residual melt, preserved as matrix glass (Fig. 3.9c).

Because the melt inclusion data indicate fractionation trends and values consistent with the lake core/MER050 composition, we suggest that the variation in major element geochemistry is a consequence of secondary alteration of the glass (leaching of Na and Fe, and resulting enrichment of Al) from its river-cut environment. We hypothesise that repeated and short periods of exposure to meteoric water during the wet season increased the effective water:rock ratio over time. The fact that the lake core tephras do not show increasing hydration with depth in the core (or variation in glass chemistry) indicates that the deposits may have been relatively isolated from the water supply after burial.

If our weathering hypothesis is correct, we can correlate a total of five layers across three different locations (two lake cores and one land section), and one layer across four (two lake cores and two land sections): The four microlite-rich layers (AML1 – AML4) can be correlated across the lake cores and MER050, while the glass shard-rich, high-TiO_2 layer (AGSL1) can be correlated to the additional MER046 (Fig. 3.10).

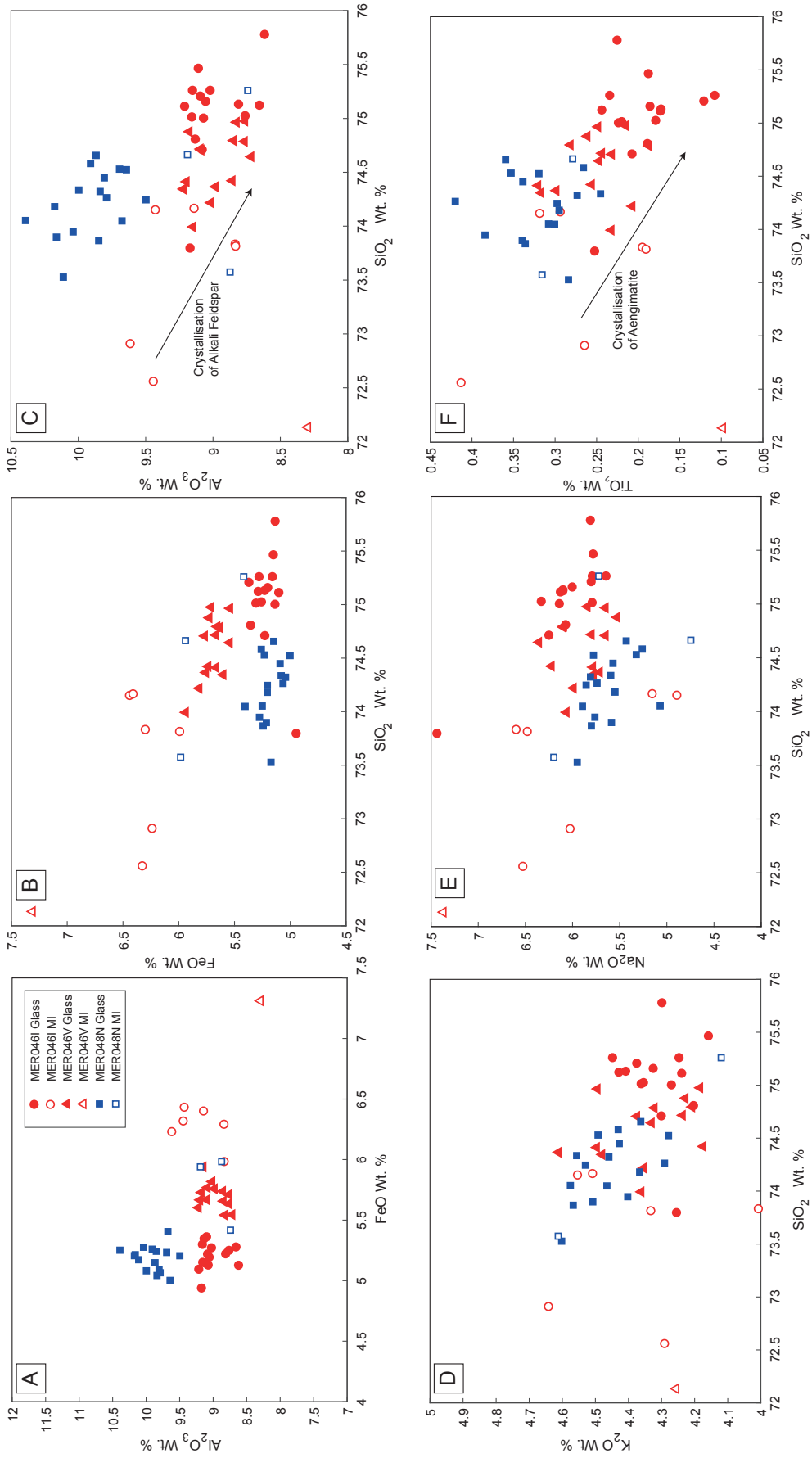

Figure 3.9: Plots of melt major element glass data from matrix glass and melt inclusions in three of the geochemically different samples. Open symbols indicate melt inclusions, while closed symbols indicate matrix glass.

3.6. Eruption Properties

Determining eruption size is challenging as we have only been able to correlate five deposits, over a limited number of localities. Even the most well-characterised deposit, AGSL1, has been identified in only four locations. Methodologies typically used to quantify eruption size from the air fall deposits, in contrast, depend on more complete spatial coverage. To further constrain the size of eruption that produced AGSL1, we have modelled the eruption using the Tephra2 ash model (Bonadonna et al., 2010). The major challenge to this exercise was to constrain input parameters such as total erupted volume, column height and total grain size. Toward this end, we have used deposits from analogous, well constrained eruptions to derive eruption-specific parameters that are then used in the dispersion model.

3.6.1. Use of analogous eruptions

To determine a set of possible analogous eruptions, we compare the grain size and thickness data from the correlated Aluto sections to that of other well-sampled and similarly-sized eruptions (Fig. 3.11). In each case, the parameters are compared with respect to distance from the vent. These data create an envelope that indicates the rate of deposit thinning and fining, while allowing sensitivity of the location of the sample site relative to the ash dispersal axis and the wind speeds. This approach also helps to constrain the likely ash dispersal axis, which we can compare both to other eruptions and to modern wind data.

As AGSL1 has been correlated across the most sections, we use this deposit as a case study. The rate at which the deposit's grain size fines with distance is comparable to the fining of deposits from, for example, the 2015 eruption of Calbuco in Chile, and the 2011 eruption of Kirishima in Japan (Fig. 3.11a). Within the resolution of our data, however, AGSL1 has an Md= -2.5 ϕ at 9 km from the volcano, while tephra from the 2015 eruption of Calbuco has Md = -1.3 ϕ at 8.3km from vent. The more distal deposits have a comparable grain size, with Md = ~0 at 25 km for Aluto and Md = 0.1 ϕ at 23 km for Calbuco. The thickness of the AGSL1 deposit is also comparable to that of the 2015 Calbuco eruption, with all the deposit thicknesses within the range observed at varying distance from the Calbuco vent (Fig. 3.11b). Comparison of both thickness and grain size data suggests that other eruptions of Aluto were smaller. The finest of the Aluto deposits that we managed to correlate at multiple sites (AML4) has a distal Md similar to that of the 2010 eruption of Eyjafjallajökull at a comparable distance form the source.

3.6.2. Dispersion modelling

Given the, albeit limited, constraints on eruption size and style (i.e. Calbuco), we then explored the potential impact of a modern eruption of a similar size to AGSL1 using the Tephra2 model. Tephra2 is a semi-analytical forward model that calculates tephra fall using an advection-diffusion equation; it can produce isomass maps by outputting the tephra mass per unit area at varying locations from the vent. In this way, we can also compare the model to our limited thickness data, even though we do not know Holocene wind conditions. The model

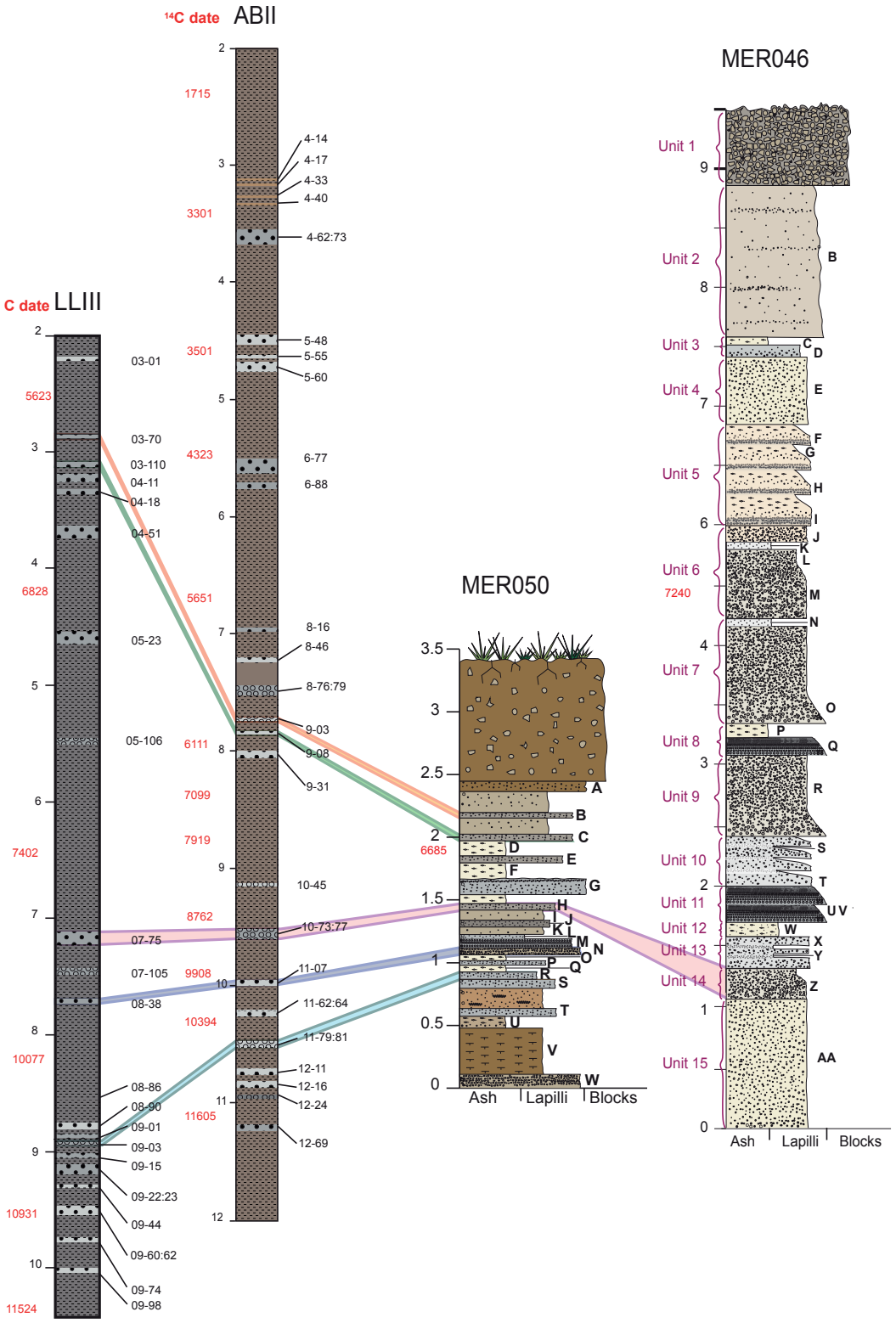

Figure 3.10: Summary of correlations made between land sections and lake cores.

computes particle diffusion, advection and sedimentation in a stratified atmosphere using a mass conservation equation and particle settling accounting for the Reynolds number (Suzuki, 1983; Armienti et al., 1988; Bonadonna and Houghton, 2005; Bonadonna et al., 2010). The model assumes all particles are spherical and released instantaneously.

Tephra2 requires several input parameters, including the wind field (we use data from 2016), deposit grain size, density and eruptive column height. To examine the effect of seasonal changes in the wind field, wind profiles were computed for each month of 2016 (Appendix F) using wind reanalysis data (Kalnay et al., 1996) and TephraProb (Biass et al., 2016). The prevailing wind direction is west south west, although for the months November – April, there is a tendency for westerly winds (towards the east) at altitudes >10km. Because there is some seasonality in the wind conditions, we ran Tephra2 using wind data from different days at different times of the year (Fig. 3.12).

The remaining input parameters (grain size, particle density and column height) are typically determined from measurements of the fallout deposits. The model also requires two parameters which cannot be directly calculated from the deposits: the Fall Time Threshold (FTT), which indicates the time at which diffusion changes from power-law (which controls the sedimentation of small particles) to linear (large particles) and the diffusion coefficient, which specifies the horizontal diffusion of large particles. In scenarios where the parameters are unknown, solutions can be found by running inversions of spatial thickness data (thickness of the deposit at varying locations from the vent) in Tephra2 to solve for the best fit parameters (e.g. Connor and Connor, 2006; Johnston et al., 2012).

However, because we have only four datapoints from the AGSL1 eruption, running inversions is not feasible. Indeed, previous studies using sparse data have found the results to be highly variable and inconsistent across different inversion methods (Pfeiffer et al., 2005; Scollo et al., 2007; Bonasia et al., 2010; Kratzmann et al., 2010; Johnston et al., 2012). As most of these sparse-data inversions use a bigger dataset than ours, we do not attempt to solve for the input parameters by this method. Instead, we use the physical properties of the 2015 eruption of Calbuco to populate the input parameters for the AGSL1 eruption as the eruptions are comparable in grain size and thickness (Fig. 3.11). A full summary of the parameters used can be found in Table 3.2. Where possible data from the AGSL1 are included, specifically information about the deposit density from measurements of pumice and lithic clasts from MER046Z (Chapter 2). However, grain size data are estimated from measurements of deposits from Calbuco (Segura et al., 2015; Castruccio et al., 2016; Romero et al., 2016), and the erupted mass is derived based on the thinning relationship of the deposits (Castruccio et al., 2016; Romero et al., 2016). Variations in erupted mass reported in the literature (due to differences in method of calculation) between 2.69×10^{11} kg and 2.76×10^{11} kg are insufficient to notably affect the model output. Consequently, we input the average erupted mass to Tephra2 for all runs.

The range of column heights considered is also based on the Calbuco eruption column height of

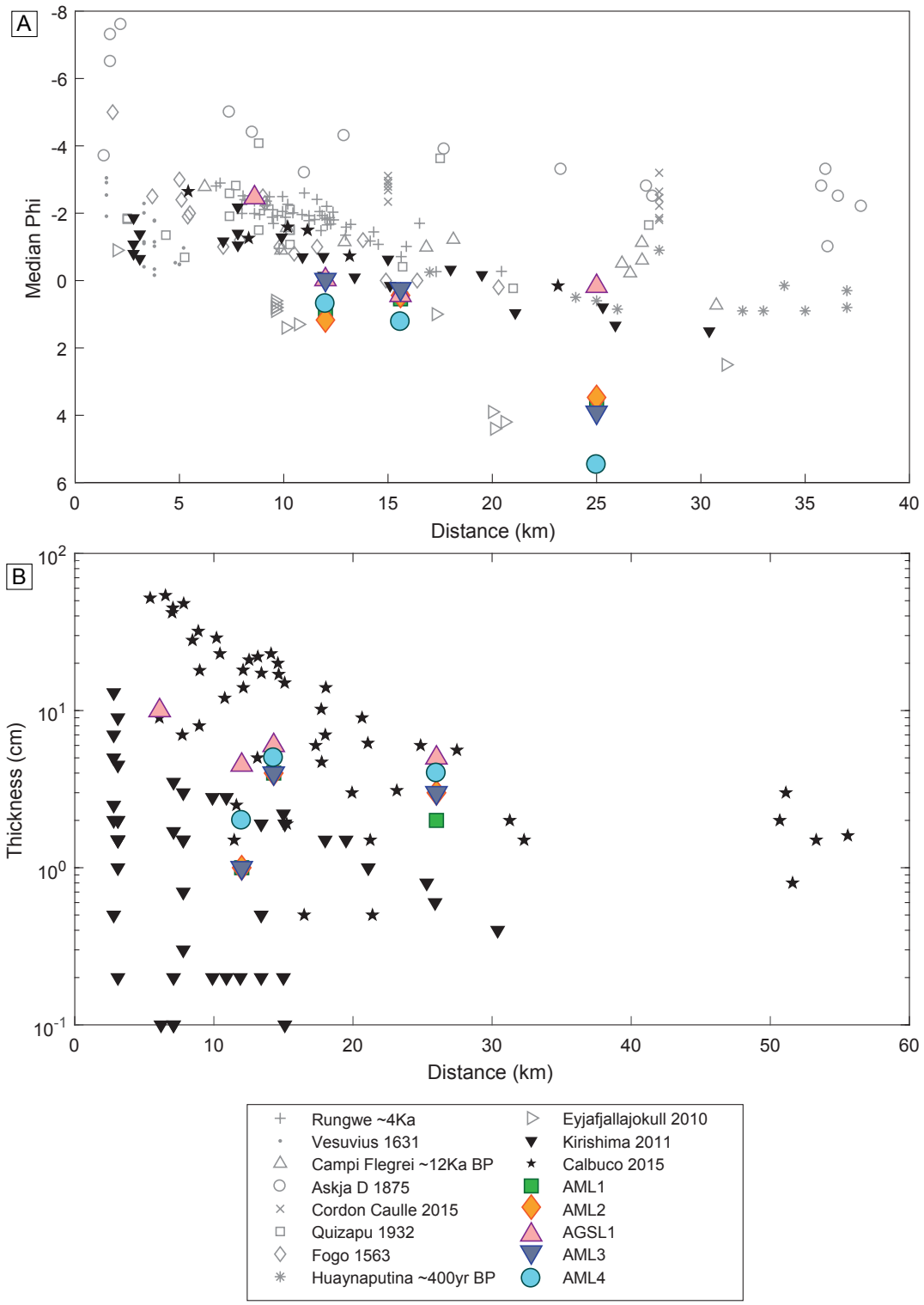

Figure 3.11: (a) Plot of Md phi with distance from tephra deposits from a range of eruptions as well as the correlated eruptions from Aluto (Walker and Croasdale, 1971; Sparks et al., 1981; Hildreth and Drake, 1992; Scarpati et al., 1993; Adams et al., 2001; Arrighi et al., 2004; Bonadonna et al., 2011; Fontijn et al., 2011; Miyabuchi et al., 2013; Pistolesi et al., 2015; Castruccio et al., 2016) and (b) thickness data with distance for the Aluto tephras and two comparable eruptions of Calbuco in 2015 (Castruccio et al., 2016) and Kirishshima in 2011 (Miyabuchi et al., 2013).

Table 3.2: Input parameters into Tephra2 model and the source

Tephra 2 input	Value	Data Source
Plume height (km)	10, 15, 20	Calbuco
Eruption Mass (kg)	2.70E+11	Calbuco
Max grain size (phi)	-5	Calbuco
Min Grain size (phi)	4	Calbuco
Median Grain size (phi)	1	Calbuco
Standard Grainsize (phi)	3	Calbuco
Vent Easting (UTM)	473823	Aluto
Vent Northing (UTM)	862162	Aluto
Vent Elevation (m)	2077	Aluto
Eddy Constant	0.04	-
Diffusion Coefficient (ms^{-1})	100	-
Fall time Threshold (s)	1000	-
Lithic Density (kgm^{-3})	2190	Aluto
Pumice Density (kgm^{-3})	636	Aluto
Column Steps	100	-
Plume model	0	-
Plume Ratio	0	-

13 – 18 km, determined from a combination of satellite observations and calculations of deposit thickness as per the methods of Carey and Sparks (1986) (Castruccio et al., 2016; Romero et al., 2016; Van Eaton et al., 2016). Because the wind field at Aluto varies greatly between altitudes of 10 and 20 km (Fig. 3.12) we ran the model for column heights of 10, 15 and 20 km to represent a range of outcomes of a VEI 4 eruption scenario.

The advection and diffusion parameters (FTT and Diffusion Coefficient) that best fit the Aluto AGSL1 deposit were determined by manually changing the input through a range of reasonable values in a series of the forward model runs (while keeping all other parameters constant). The values selected are displayed in Appendix G. The two parameters control, amongst other things, the dispersion of particles and therefore can influence axial ratio of the plume. To determine the most appropriate values for the Aluto eruption, the results of the forward model were compared to the thicknesses of the deposits, and the parameters producing a plume shape which best fitted the thickness data were used. A summary of the values varied, and the models output can be found in Appendix G. The best-fit values were determined by re (diffusion coefficient = 100 and FTT = 1000) are within the range of values used for other Plinian and sub-Plinian eruptions (e.g. Johnston et al., 2012; Mannen, 2014; Biass et al., 2016).

The output of the Tephra2 runs is displayed in Fig. 3.12 as maps showing isopachs of deposit thickness. These were calculated from the Mass/Area Tephra2 output by assuming a total deposit density of 791 kgm^{-3} (assuming the deposit comprises 90% pumice and 10% lithics). The results of the model indicate that tephra deposition is predominantly towards the west and south west with all but three of the model runs depositing ash in all four of the locations correlated. Overall, a 15 km plume appears to be most consistent with the AGSL1 deposit, with the model runs from April, July and September predicting ~5 cm of tephra fall in both lake core locations (AGSL1 = 5 cm and 5 cm in ABII and LLIII respectively) and between 20 and 50 cm of deposition at

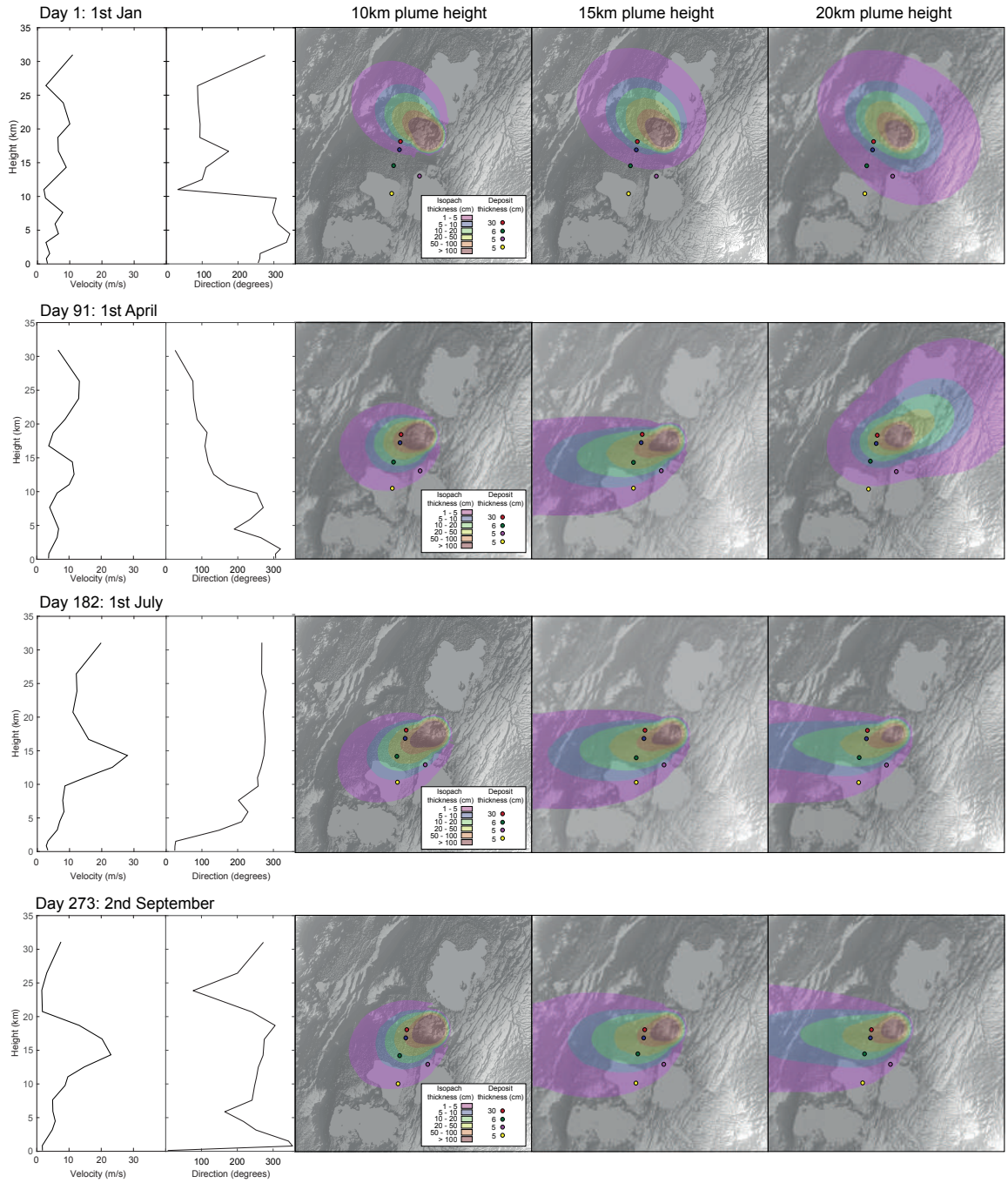

Figure 3.12: Teprha2 dispersion modelling of Aluto eruption using parameters from the 2015 eruption of Calbuco at different days throughout 2016 accompanied by the relevant wind profile, including the wind speed and direction with height. Isopachs are in cm and the input parameters for the models can be found in Table 3.2.

MER046 (AGSL1= 30 cm; Fig. 3.12). The AGSL1 deposit in MER050 fits least well, with the model generally predicting between ~10 – 30 cm of tephra deposition despite AGSL1 being 6 cm thick at this location. Overall however, the deposits at MER050 are thicker on average (6 cm) than those in the cores (3.3 cm and 2.5 cm), consistent with the model.

The fit of the model to the observed AGSL1 deposit data confirms that the eruption was about VEI 4, like the Calbuco eruption. We believe that ASGL1 is one of the largest eruptions in the Holocene (as the deposit is among the thickest and coarsest in the lake cores) and therefore indicates a worst-case scenario. From this perspective, we note that the model predicts >1 cm of ash deposited in at least one of the three major population centres of Bulbulla, Adami Tullu or Ziway (Figs. 3.1, 3.12). In general, conditions in November – February (which comprise more southerly and westerly winds) favour ash deposition to the north west, and subsequently towards Ziway. Wind conditions for the remainder of the year favour deposition towards Bulbulla and Adami Tullu to the west and south west of the volcano. While more detailed hazard modelling is required to better constrain the risk to these population centres, our results indicate that Aluto would pose a significant hazard should it undergo a similar eruption to the largest in the Holocene.

3.7. Conclusions

This chapter expands the correlations made in chapter four to include several land sections (Fig. 3.10). All the land sections considered comprise tephra layers deposited amongst lake sediment as part of a paleolake. Overall, we find that the methods developed for the cores are also useful for correlating land sections, with one section (MER050) displaying very comparable textural and geochemical similarities to the cores. As a result, we have correlated the four microlite-rich layers AML1, AML2, AML3 and AML4 with layers in MER050 as well as the glass shard rich, high TiO_2 layer AGSL1 (Fig. 3.10).

The other two land sections investigated, MER046 and MER048, contain little microlite-rich material meaning they do not contain the deposits pertaining to AML1 – 4. Both sections however, contained a layer with features attributed to the eruption AGSL1 particularly high TiO_2 and glass shards. The layer in MER046 also contains trace element concentrations consistent with AGSL1 implying a correlation. The layer in MER048 however, does not have comparable trace element content, and so is not correlated.

The major element geochemistry of the land sections is different to the cores. MER050 has comparatively similar major element geochemistry to the cores, although the uppermost layer (MER050A) has lower FeO, higher Al_2O_3 and lower Na_2O. This anomalous geochemistry is also observed in MER046 and the bottom half of MER048 despite ^{14}C dates indicating the layers were deposited during the Holocene. The tephra layers with the anomalous geochemistry were sampled from river-cut sections and are generally more hydrated than the tephra layers from the lake cores. As a consequence, we suggest that these layers have been affected by the leaching of Na and Fe and the subsequent enrichment of Al, resulting in different major element

glass geochemistry. If this is indeed the case, it highlights the importance of using more than one means of correlation in setting where the secondary alteration and hydration of glass is unknown.

The complex nature of the sediments, and the high number of tephra deposits has meant that only four sections can be correlated. As this is insufficient to make any detailed estimates about eruption size, we instead model the eruption using the ash dispersion model Tephra2. As Tephra2 requires a number of input parameters which we could not source from our limited dataset, we instead use analogous eruptions which have comparable deposit fining and thinning trends to that of AGSL1. The results of the modelling are consistent with our interpretation that AGSL1 was a sub-Plinian sized eruption with the main ash dispersal axis towards the south west. Overall, based on the thinning and fining of the deposits we suggest that the predominant ash dispersal direction for the majority of the deposits was towards the west and south west, which is consistent with modern wind conditions. Any future eruption of this size would likely have an impact on the populations centres in this vicinity, particularly Bulbulla and Adami Tullu, although wind conditions during November to February indicate that ash deposition is more likely towards the larger town of Ziway.

Chapter 4

Comparison of lake and land tephra records from the 2015 eruption of Calbuco Volcano, Chile

McNamara, K., A. C. Rust, K. V. Cashman, A. Castruccio and A. Abazùa, Comparison of lake and land tephra records from the 2015 eruption of Calbuco Volcano, Chile, *Bulletin of Volcanology*, (in review).

Author contributions and declaration: K. V. Cashman and A. C. Rust provided supervision. The data was processed and provided by K. McNamara. A. Abazùa and provided equipment, including the corer and assistance organising fieldwork as well as comments on the final manuscript. A. Castruccio provided information on 2015 Calbuco terrestrial deposit, including grain size and thickness data from Castruccio et al. (2016), and comments on the final manuscript. All content is included as displayed in the submitted paper, to aid with consistent presentation.

ABSTRACT

Tephra layers in lake sediment cores are regularly used for tephrostratigraphy as isochronous features for dating and recording eruption frequencies. However, their value for determining volcanic eruption size and style may be complicated by processes occurring in the lake that modify the thickness and grain size distributions of the deposit. To assess the reliability of data from lake cores we compare tephra deposited on land during the 2015 eruption of Calbuco Volcano in Chile to records in sediment cores from three different-sized lakes that are known to have received primary fall deposits. In general, the thickness and granulometry of the deposit in lake cores and nearby terrestrial sections are very similar. As anticipated, however, cores sampled within 300 m of fluvial inflows were affected by sediment deposition from the lake's catchment; they differed from primary deposits not only in their greater thickness and organic content but also in poor sorting and lack of grading. Cores 850 m away from the inlet were not affected. We consider our results in the context of the particle settling regime as well as each lake's location, bathymetry and catchment area. We find that the particle settling regime is important in more distal settings where the ash deposition is finer meaning particle settling occurs in density plumes rather than as individual particles. We conclude that lake cores can be useful for physical volcanology providing consideration is given to eruption parameters such as particle size and mass flux, as well as lake features such as bathymetry and catchment area.

4.1. Introduction

Lake sediment cores (lake cores) are an invaluable source of information in many spheres of Earth Science such as climatology and volcanology. They can record information about the evolution of water chemistry and aquatic life on time scales of millennia while also preserving deposits from short-lived events such as landslides and volcanic eruptions (e.g. Williams et al., 1997; Van Daele et al., 2015). Such events are used to study the associated hazard and as palaeomarkers for correlation and dating (e.g. Horrocks et al., 2005; Lowe et al., 2008; Stern, 2008; Lane et al., 2013; Smith et al., 2013). There are, however, many processes that can interfere with a volcanic deposit in a lake and prevent it from recording primary volcanic deposit. Here we explore these processes as they apply to the 2015 eruption of Calbuco volcano in Chile.

Lake cores provide a record of the volcanic material deposited during an eruption. This usually comprises pyroclastic material that is released from the ash cloud and settles through the atmosphere onto the lake, but can also include deposits from pyroclastic density currents and lahars transported as gravity-driven flows. Fall deposits generally become finer-grained and thinner with distance from the volcano. Lake cores provide important records and samples of distal volcanic deposits, in particular, because lakes are more likely to preserve fine ash that is liable to resuspension and erosion in terrestrial settings (e.g. Lowe, 2011; Engwell et al., 2014; Fontijn et al., 2014). In some cases, lake cores provide key data to evaluate a volcano's eruptive potential (e.g. Moreno et al., 2015; McNamara et al., 2018) and thus can have considerable implications for hazard management.

In environments where the preservation of tephra on land is particularly poor, lake cores may provide the only record of a volcano's eruptive history. In these scenarios, tephra layers in cores are considered in conjunction with material that can be dated (usually organics or carbonates) to establish an eruption chronology. Such a chronology can be expanded and correlated with land sections or other lake cores (e.g. Davis, 1985; Shane et al., 1998; Matthews et al., 2012; Fontijn et al., 2016). Measured thickness and grain size can also be used to create isopach and isopleth maps used to estimate eruption size and intensity (e.g. Pyle, 1989; Fierstein and Nathenson, 1992; Legros, 2000; Rhoades et al., 2002; Bonadonna and Houghton, 2005). Furthermore, changes in the grain size and componentry (proportions of clast types) through a deposit can indicate changes in the intensity and style of the eruption with time. These characteristics also provide features for correlating tephra layers found in different locations, particularly in cases where geochemistry is non-diagnostic (McNamara et al., 2018). The applicability of all of these methods rely on the assumption that the primary features are preserved in lake cores.

A significant concern in the application of lake cores to physical volcanology is the potential for reworking and emplacement of additional tephra due to lacustrine and fluvial processes. Previous studies of volcanic deposits in lake cores have cited evidence of secondary redistribution such as turbidity currents, which can thin or thicken tephras as sediments slump down the edges of lake basins (e.g. Benett, 1986). Also, sediments cored very close to the lake edge may be disturbed because of the higher energy environment due to wave action (e.g. Riggs et al., 2009).

Furthermore, a fluvial system delivering tephra from the lake's catchment area can artificially thicken a tephra layer as well as deposit volcanic material in sediments that post-date the eruption (Thompson et al., 1986; Bertrand et al., 2014).

Even without fluvial input or lateral redistribution of volcanic material by currents, settling in the water column can affect the vertical distribution of clasts of different sizes and densities within the deposit. Grading of deposits can be caused by changes to eruption intensity and/or proportion of types of clasts erupted (i.e. primary features) or can be caused by settling processes (i.e. secondary features). Indeed, graded deposits in sea and lake cores have been interpreted as the result of differing rates of particle settling, where larger particles overtake smaller particles while falling through the water column to produce a normally graded deposit (e.g. Ledbetter and Sparks, 1979).

An additional complication is that volcanic material can be highly variable in density; the high vesicle content of pumice may even allow some clasts to float until sufficient pore space is filled with water (e.g. Whitham and Sparks, 1986). Large pumiceous grains are usually less dense than finer particles, which often comprise crystals or lithic fragments (e.g. Liu et al., 2017). If a portion of the fall deposit comprises pumice that is less dense than water, these pumices may be redistributed (e.g. by wind) on the lake surface while other clasts settle to the lake floor (e.g. Fiske et al., 2001). The result is finer and thinner deposits in areas where the pumice is removed, and thicker and coarser deposits where they eventually saturate and settle (e.g. White et al., 2001; Von Lichtan et al., 2016). Delayed deposition of relatively coarse pumice can also affect the sorting, grading and componentry of the tephra layer, which complicates interpretations of eruption dynamics.

Finally, clasts do not necessarily settle individually in the water column: It has been shown that with sufficient rate of tephra deposition onto the sea (for a clast size and density, and sufficient water depth) the tephra can fall through the water as dense plumes of particles (Carey, 1997; Fiske et al., 2001; Rose and Durant, 2009). The higher viscosity and density of water compared to air means that clasts falling through the air slow down drastically when they land on water. This can generate higher concentrations of particles near the top of the lake, potentially forming a gravitationally unstable layer that develops into plumes of particles that descend to the base of the water column. These plumes of particles fall much faster than individual-particle settling speeds (Cashman and Fiske, 1991; Carey, 1997; White et al., 2001; Jacobs et al., 2013, 2015) and are consequently less liable to lateral redistribution by currents (Ninkovich and Shackleton, 1975; Manville and Wilson, 2004). This type of sedimentation can preserve the primary grain size distribution of tephra on the scale of the destabilised layer because the particles are not segregated by individual settling speeds. However, it will not preserve grading or fine-scale variations in grain size with stratigraphic height that reflect changes in grain size landing on the water surface with time.

Given the various processes that can interfere with primary tephra deposition in lacustrine environments, an important question is how to recognise when a tephra layer represents primary

deposition. Also important is identifying the best place to look for pristine tephras within a specific lake. Recent eruptions provide the opportunity to assess the effectiveness of lake core records in a well constrained environment where both the tephra on land and in the lakes can be compared and contrasted (Bertrand et al., 2014).

The 2015 eruption of Calbuco Volcano in Chile provides such an opportunity because the sequence of events is well constrained by direct observations and remote sensing, tephra layers were directly measured and sampled on land, and tephra was deposited in lakes of different sizes and locations. Importantly, the accessibility of the proximal fall allowed the tephra deposition to be monitored during and immediately after the eruption. For this reason, the fall deposit is well documented and sampled many kilometres from the vent (e.g. Segura et al., 2015; Castruccio et al., 2016; Romero et al., 2016). As a result, we can compare the deposits in the lake cores to the primary deposition without concern over whether the terrestrial samples have, themselves, been subject to secondary processes. For this study, we cored three proximal lakes. We consider each of the cored tephras in the context of the coring location, proximity to fluvial inputs and the particle settling regime.

4.1.1. Calbuco Volcano

Calbuco is an active volcano located in the Southern Volcanic Zone (SVZ) of the Chilean Andes. It is one of the most hazardous volcanoes of southern Chile due to the frequency and explosivity of its eruptions, with the towns of Puerto Montt and Puerto Varas located within a 30km radius of the vent. It is also close to several smaller towns and villages, including the village of Ensenada (~14km north of the vent).

Activity at the volcano began at 300 Ka in the form of andesitic lavas and pyroclastic density currents (PDCs). Holocene activity has produced sub-Plinian and Plinian fall deposits, and lava flows and PDCs of predominantly andesitic composition (Lopez-Escobar et al., 1992; Selles and Moreno, 2011; Castruccio et al., 2016). Activity in the past century has included a range of sub-Plinian and Vulcanian eruptions with the four most recent in 1945, 1961, 1972 and 2015 (Castruccio et al., 2016).

The 2015 eruption of Calbuco began on April 22nd with very little precursory activity. Over a twelve hour period, it produced two sub-Plinian phases which occurred ~5.5 hours apart, with a maximum plume height of 25 km and ash deposited at least 300 km from the vent. The ash cloud propagated towards the northeast, depositing ash across the Chilean-Argentinian border and causing numerous flight cancellations and delays. The village of Ensenada was particularly affected, with residents evacuated and damage to houses and infrastructure from the volume of tephra deposition.

The second sub-Plinian phase was the most explosive and its products comprise most of the fallout deposits (Van Eaton et al., 2016). The eruption also produced numerous pyroclastic flows as well as several lahars which followed river channels, causing damage to roads and bridges before entering Llanquihue and Chapo lakes to the north and south of the volcano (Castruccio

Figure 4.1: Map of Calbuco Volcano and the 2015 fallout deposit, including all locations of sampling and isopach map as determined by Castruccio et al. (2016).

et al., 2010).

Tephra sampling and analyses of the fall deposit (Segura et al., 2015; Castruccio et al., 2016) indicate four units numbered 0-3 (bottom to top; Fig. 4.2), with Layer 0 attributed to the first 1.5-hour eruptive phase and Layers 1-3 to the second 6-hour phase. Of these units, Layer 0 is the thinnest and finest-grained, and consists largely of brown scoria. Layer 1 is the coarsest and contains brown to tan scoria. Layer 2 is typically the second-coarsest and encompasses a mix of tan/brown scoria, and some denser dark-grey scoria and juvenile lithics. Layer 3 contains dense dark-grey juvenile fragments and grey scoria clasts, which are often coarser grained than those found in Layer 2. The easily distinguishable variations in colour, componentry and granulometry with depth in the deposit make this a good eruption for a comparative study of lake and land records of an eruption sequence. In addition, the scoria has a density of $1.3 - 1.4\,\mathrm{gcm^{-3}}$ (denser than water; Castruccio et al., 2016) and so sank immediately upon deposition into the lake.

4.1.2. The Lakes

'Los Lagos' or 'The Lakes' region of Chile comprises the central portion of the SVZ (in which Calbuco is located) and is home to some of the largest lakes in the country. In immediate proximity to Calbuco are Lagos Chapo, Llanquihue and Todos Los Santos (TLS; Fig. 4.1). The latter is located directly below the 2015 dispersal axis and, consequently, received substantial primary tephra deposition, while the SE sector of Llanquihue lake lies on the northern edge of the fallout area. The region also includes many smaller lakes, some of which are fed by rivers and streams which drain the slopes of Calbuco and nearby Osorno volcanoes. The largest of

these small lakes is the elongate Laguna Patas, which is positioned to the east of the volcano, perpendicular to the primary fall axis (Fig. 4.1). These three lakes comprise our study.

Llanquihue is a piedmont lake with an area of 870km^2 and a maximum depth of 317 m, making it the second largest lake in Chile (Geller, 1992; Soto, 2002). Llanquihue and neighbouring Todos Los Santos lie in the same large Quaternary glacial depression, which was partially filled by volcanic products from Calbuco and Osorno volcanoes to create the two distinct lakes (Herschy, 2012). Llanquihue lies ~12km to the north and northeast of Calbuco and received most tephra deposition in its SE tip. It has several fluvial inflows, with the main three comprising Rio Pescado, Rio Blanco and Rio Tepu, all of which are sourced on or near the flanks of Calbuco and flow into the southern shore of the lake (Fig. 4.1; Campos et al., 1988; Arismendi et al., 2011). The lake's primary fluvial outflow is the Maulln river which flows from the town of Llanquihue in the southwest of the lake.

Todos Los Santos (TLS) is a monomictic lake positioned approximately 28 km northeast of Calbuco in the Vicente Perez Rosales National Park, directly beneath the 2015 ash dispersion axis (Fig. 4.1). The lake has a surface area of 178.5km^2 and a maximum depth of 337 m (Herschy, 2012). It has three major fluvial inflows (rivers Blanco, Pichi-Blanco and Negro), all of which enter the eastern end of the lake. The most easterly 5 km basin of the lake has a maximum depth of 50 m because of sediment deposition from the rivers. Its western basin is much deeper, reaching 330 m in some places. The major lake outflow is located at the most westerly extent of the lake and constitutes the source of the Petrohué river (Fig. 4.1).

Laguna Patas is a small lake to the east of Calbuco with a surface area of 0.6km^2. It is fed from a small river (Estero El Caballo) entering in the southeast end of the lake whose catchment comprises part of the easterly flank of Calbuco but is nearly dry during the summer season (Bretón et al., 2006). The lake feeds the Rio de los Patos, a larger tributary of the main Petrohué river (Fig. 4.1). To our knowledge, no bathymetric information exists for the lake, however our measurements with an echo-sounder during coring suggest typical depths between 10 and 30m.

4.2. Methods

All cores were obtained during fieldwork in March 2017 using a UWITEC gravity corer and 60 mm sampling tubes. Equipment limitations meant the maximum water depth through which we could core was 40 m so all cores were taken within 300 m from the lake shore, where the water depth varied from 8.5 m to 40 m.

All cores were measured, photographed and described immediately after coring and then subsampled on return from the field. We aimed to sample the core every two cm, however due to the coarse nature of the sediments, it was difficult to control the removal of the core from its casing and so subsampling was sometimes at inconsistent intervals. A summary of the cores and samples taken can be found in Table 4.1.

Selected terrestrial sections are also included in this study (Table 4.1). These comprise tephra

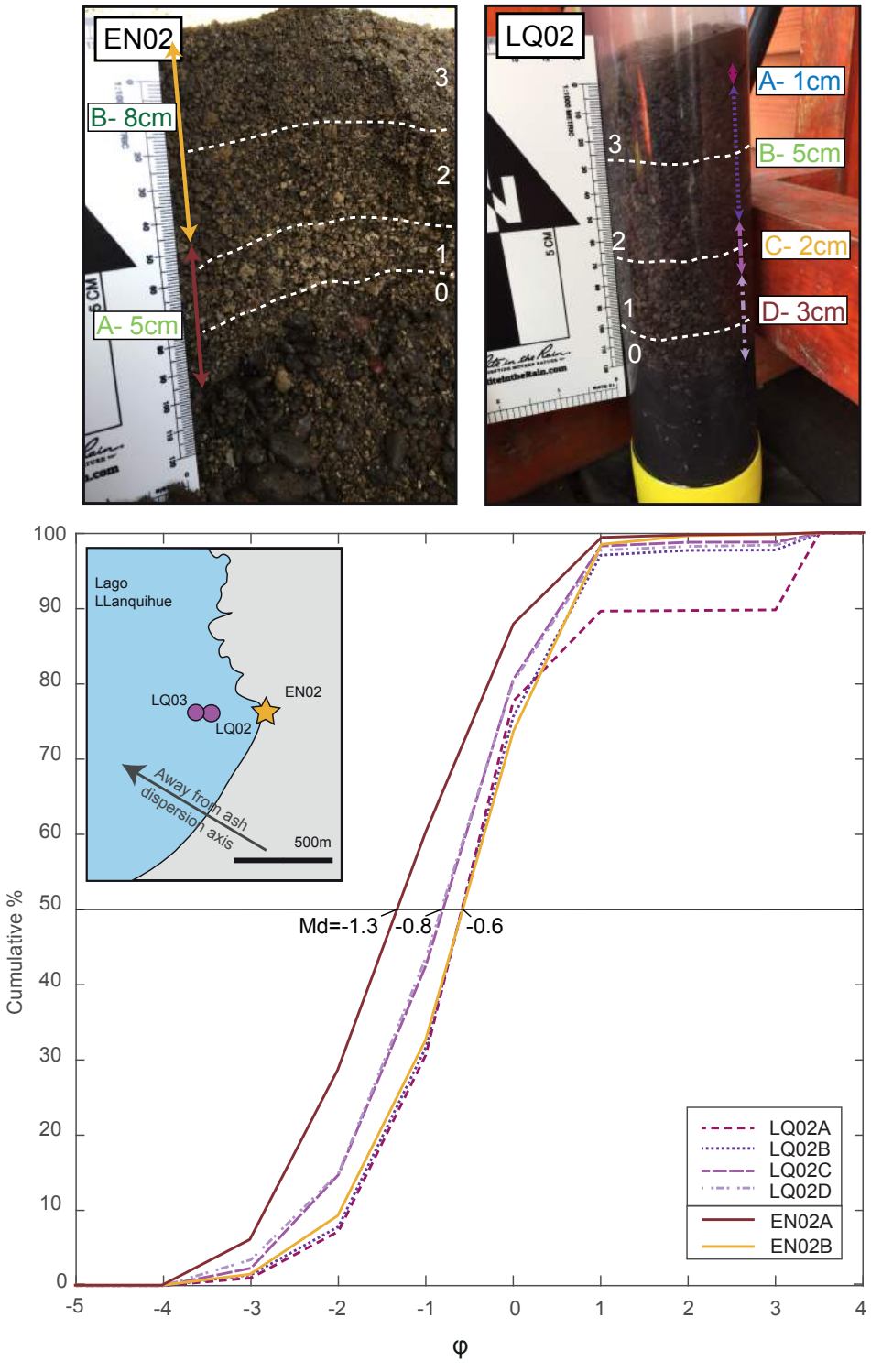

Figure 4.2: Grain size data of different sub samples in the terrestrial section on the shore of Llanquihue (EN02) and lake core (LQ02) sampled ~200 m from the shore. Both show coarser sediment in the lower half of the deposit. The distinctive eruptive units as defined by Castruccio et al., (2016) are highlighted in white on photos. The coloured lines and arrows correspond to each subsample (lettered A-E). The line dash and colour is the same for the relevant grain size distribution of the subsample.

Table 4.1: Summary of cores and subsamples for each of the lakes. 'Macro-organics' indicates if large organics were removed when placed in water.

Sample	Location		Thickness	Subsample thickness (cm)							Macro-
	S	W	(cm)	A	B	C	D	E	F	G	organics
Land sections											
EN02	41 13.418	072 31.820	13	5	8	-	-	-	-	-	
KAL-49	41 08.924	072 25.810	6	-	-	-	-	-	-	-	
KAL-06	41 18.408	072 27.246	5	1	2	2	1	-	-	-	
KAL-12	41 12.194	72 32.251	15	-	-	-	-	-	-	-	
Lake Llanquihue											
LQ02	41 12.291	072 32.486	13	1	5	2	3	2	-	-	
LQ03	41 12.293	072 32.534	13	3.5	3.8	2	3	-	-	-	
Laguna Patas											
LPT01	41 17.726	072 27.480	8	1	1	1	1	1.5	1	1	Y
LPT05	41 17.756	072 27.426	8	2	2	2	2	2	-	-	Y
LPT06	41 18.033	072 27.362	7	1	1	1	1	1.5	1	1	Y
LPT07	41 18.296	072 26.964	12	2	2.5	2	2	2	2	-	Y
LPT08	41 18.245	072 27.043	10	2	2	2	2	2	-	-	Y
Lake Todos Los Santos											
TLS03	41 07.615	072 21.235	5	1	1	1	1	1	1	-	

sampled at the time of coring as well as sections sampled by Segura et al. (2015) and Castruccio et al. (2016) immediately after the eruption. We compare sections close to the cored lakes to allow a direct comparison of both granulometry and componentry between the terrestrial tephra deposit and the lacustrine material. In addition, we compare grain size and thickness data from deposits at intervals along the ash dispersion axis from Castruccio et al. (2016) with the lake core samples (Fig. 4.1). Thickness data from these localities were used to draw isopachs by Castruccio et al. (2016), which are also shown on Figure 4.1.

Grain size data were gathered for each subsample in each core and deposit. The samples were oven-dried, sieved from -5 ϕ to 3 ϕ (32 mm to 125 µm) at 1 ϕ intervals and weighed. Samples with macroscopic organic content (leaves and twigs; Table 4.1) were subsequently resaturated in water and all floating organic material was manually removed before the remaining sample was re-dried. In order to determine the total grainsize for each core, the weights of the subsample were summed for each grain size fraction and combined into a distribution. A full list of grain size analyses can be found in Appendix H.

Backscatter electron (BSE) scanning electron microscope (SEM) images were obtained for the uppermost and two lowermost subsamples in three of the Laguna Patas cores. In each case the 2ϕ, 3ϕ and $>3\phi$ grain size fractions were imaged. Particles were mounted in epoxy and grain interiors exposed by polishing before being carbon coated. Mounted grains were imaged using a Hitachi S-3500N SEM at the University of Bristol. A ~25-image mosaic was obtained for each size fraction comprising images with a 1024 x 769 pixel resolution taken at a working distance of ~20 mm and an accelerating voltage of 15kV or 20kV. The images were combined using FIJI grid stitching software (Schindelin et al., 2012).

To better understand the secondary input of ash into the lakes we delineated the drainage basins

for each lake using the drainage analysis feature of the spatial analyst toolbox in ArcGIS, which models water accumulation based on topography and computes boundaries between drainage areas. The data were calculated using a 30 m DEM from SRTM data. The process uses the ArcGIS hydrology toolset to model the flow of water over a surface based on the topography (e.g. Strager et al., 2009). See Appendix I for detailed methods.

4.3. Deposit properties

Several land sections (described below) were selected for comparison based on their proximity to the cores, or position relative to the ash dispersal axis. In addition, eight cores were obtained across the three lakes: Lago Llanquihue (two cores), Lago Todos Los Santos (one core) and Laguna Patas (five cores; Fig. 4.1). The maximum sediment depth cored was 50 cm, although most cores were ~30 cm deep (Fig. 4.1). The results of each are discussed below. Core numbers (Table 4.1) reflect the order in which they were collected at a given lake; gaps in the numbering correspond to unsuccessful attempts to retrieve core (e.g. the tube broke or was empty).

4.3.1. Tephra on land

The majority of tephra in this study was sampled immediately after the eruption (Segura et al., 2015; Castruccio et al., 2016). The only exception is a sample from a shallow pit on the shore near Ensenada (location EN02; Fig. 4.1) which was dug at the time of coring to compare to the cores sampled 200 m to the WNW in Lago Llanquihue. The sample is 13 cm thick, and all four units determined by Castruccio et al. (2016) are identifiable (Fig. 4.2). We subsampled the top and bottom half of the tephra deposit. The deposit contains darker pyroclasts in the upper ~4 cm, the lower ~4 cm contains large sub-angular tan-coloured pyroclasts. The upper 6 cm of the deposits is finer (Md = -0.6 ϕ), while the lower 5 cm is considerably coarser (Md = -1.3 ϕ; Fig. 4.2).

Tephra sampled immediately after the eruption in nearby Ensenada village (KAL-12), is ~400 m closer to the vent than EN02, and was recorded as 15 cm thick (Segura et al., 2015; Castruccio et al., 2016). A further sample, collected at the same time close to the village of Petrohué, south west of Todos Los Santos (~24 km from the vent) is used to compare with the core sampled from Todos Los Santos. The deposit was recorded as 6 cm thick immediately after deposition (site KAL-49; Fig. 4.1), with the lower 3 cm slightly coarser than the upper three (Fig. 4.3). The grain size variations are less obvious than in the more proximal deposits.

Ash on the shore of Laguna Patas (KAL-6) was recorded as 5 cm thick immediately after the eruption by Castruccio et al. (2016) and Segura et al. (2015) and can be compared to the cores taken from Laguna Patas. However, samples for granulometry were not taken from this site and so grain size cannot be compared directly.

For reference, we also include data from tephra sampled very close to the dispersal axis, ~5.5 km from the vent (Sample KAL-26; Fig. 4.1). The deposit, also sampled immediately after the

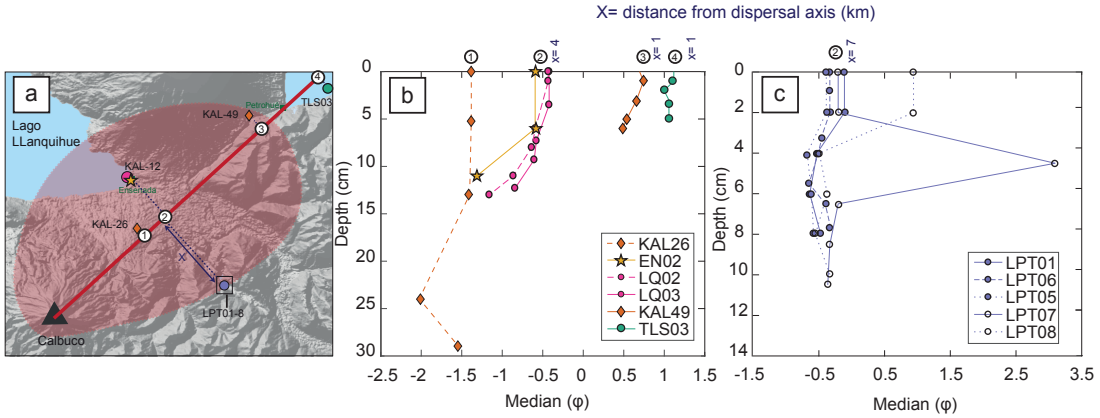

Figure 4.3: Median grain size (Md phi) with depth for all lake cores and land sections. Generally, all deposits show reverse grading. (a) shows Md phi with depth for lake cores TLS03, LQ03, LQ03 and land sections KAL49 and EN02. (b) shows Md phi with depth for all Laguna Patas Cores. Note that Laguna Patas is off axis from the main dispersal axis (see Fig. 4.1).

eruption, is 30 cm thick and, as seen in EN02, is coarser in the lower half, with the basal layer (Layer 0) is slightly finer (Md= -1.6) than the thicker Layer 1 above it (Md= -2; Fig. 4.3).

4.3.2. Llanquihue cores

The two cores taken from Lago Llanquihue (LQ02 and LQ03) were sampled 50 m apart and ~200 m from the shore and ~15 km from the volcano (Figs. 4.1 and 4.2). The tephra has a sharp contact with lake sediment below, although this was not always apparent until sub sampling as sediment became smeared along the edge of the core tube during coring. Tephra deposits in both cores had thicknesses of ~12 cm (Fig. 4.2) and there was a ~1 cm layer of lake sediment on top of the tephra. The grain size and colour varied visibly in the deposit: the upper half of the layer was generally finer and darker grey in colour, while the lower half was coarser and comprised a band of tan-coloured 5-10 mm sized scoria above a finer layer of darker brown scoria.

The grain size distributions varied with depth (z) in both cores. Both cores were subsampled: LQ02 four times (A-D; top to bottom) and LQ03 five times (A-E top to bottom; Table 4.1). Of the four LQ02 subsamples, the two lowest are coarser with median grain size (Md) = -0.8 ϕ (LQ02A and LQ02B), while in the upper two Md = -0.6 ϕ (LQ02C and LQ02D; Fig. 4.2 and 3). The LQ03 tephra layer includes five subsamples, with the upper three (LQ03A, LQ03B and LQ03C) more fine-grained than the lower two (LQ03D and LQ03E), mirroring the overall grain size trends of the LQ02 deposit (Fig. 4.3). There is more variation in the Md in LQ03 (each subsample has a slightly different Md), however, and as the sampling intervals are not the same for both cores, some differences are expected.

4.3.3. Todos Los Santos cores

Coring was attempted only in the deeper, westerly basin of TLS where we retrieved one core (TLS03). This core was taken ~31 km from the volcanic vent. It was the longest core obtained

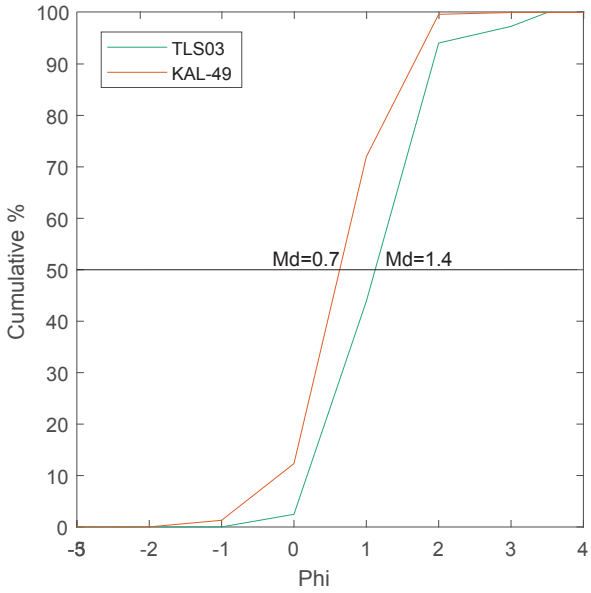

Figure 4.4: Grain size of Todos Los Santos core (TLS03) compared to the nearby land section (KAL-49).

and contained at least two separate tephra deposits. The uppermost tephra (the 2015 tephra) is 5 cm thick and is clearly distinct from surrounding lake sediment in grain size, sorting and colour. The tephra shares a clear boundary with the lake sediment below and above. The grain size of the deposit does not change dramatically with depth, and Md= ~1.4 for all subsamples (Fig. 4.4).

Laguna Patas cores

Five cores were taken from this lake, which lies ~13 km from the vent, at intervals along the lake axis: LPT07, LPT08, LPT06, LPT01 and LPT05, (in order of increasing distances from the river entry; Fig. 4.1). We separate the core samples into two groups: (1) the thinner tephras in cores LPT06, LPT01 and LPT05, which thicken to the northwest (7 cm, 8 cm, and 8 cm, respectively) and (2) the thicker tephras (LPT07 and LPT08) which thin towards to northwest, away from the river source (12 cm and 10 cm, respectively).

The three thinner tephra layers have distinct boundaries with lake sediment above and below and contain very little lake sediment amongst the ash. Each core showed systematic grain size variation across the subsamples of the tephra layer, with the upper 2 cm finer than the lower 6 cm. In all three cores, subsamples from the middle (z= 4 – 6 cm) are the coarsest, with Md= ~0.6 ϕ, while those from the bottommost 3 cm are finer (Md= ~-0.5). LPT06 displays slightly more heterogeneity in grain size than the other two cores and has a finer-grained lower 3 cm (Md= 0.4; Fig. 4.3).

The thicker tephras closer to the river mouth comprise ash interspersed with lake sediment and organic material, including leaves and twigs, and have less distinct boundaries with the surrounding lake material. They also differ from the thinner cores in their grain size trends: they

are generally finer-grained and show inconsistent variation with depth. LPT07 contains a lens of very fine material at z= 4 cm, while LPT08 is much finer-grained in the upper 2cm than any of the other cores (Fig. 4.3). While the overall grain size of both cores is on average smaller, both deposits contain large (~2 cm) lithic fragments.

4.4. Comparison of lake and land tephras

The primary purpose of this study is to compare the tephra that has settled directly into lakes to the tephra that settled in the surrounding terrestrial environment. We do this by comparing basic physical observations of the tephra deposits from both preservation environments. Grain size and thickness are regularly used to estimate eruption size and intensity; for this reason we compare the thickness and granulometry of each of the lake core deposits to nearby ash on land. Also important is the location of each lake site to fluvial inflows as well as to the lake size and catchment. We also consider the features of the deposit in relation to the eruption properties and resultant particle settling regime.

All 2015 tephra used in this study was sampled from within an area affected by primary deposition from the 2015 eruptive plume. The three lakes that were cored—Lago Lanquihue, Lago Todos los Santos and Laguna Patas—are of varying sizes and types. Laguna Patas is the closest to the volcanic vent (~13km), although it did not receive the thickest tephra of the lakes cored because of its position southeast of the dispersal axis, which is set by the wind direction during the eruption. The most tephra deposition was recorded in cores from Lago Llanquihue, which is ~15 km from the vent and close to the dispersal axis. The thinnest 2015 tephra layer was sampled in Todos Los Santos, close to the main ash dispersal axis but ~31 km from the vent (Fig. 4.1).

4.4.1. Grain size and thickness comparisons

The thicknesses of the 2015 tephra in both cores taken from Lago Llanquihue (LQ02 and LQ03) are within the range expected based on the isopach map constructed from primary land deposits by Castruccio et al. (2016). They also show grain size and colour changes with depth comparable to the section sampled on land close to the lake edge (EN02; Figs. 4.2 and 4.3). In both cores, the lower half of the deposit is coarser than the upper half, and the same four units were identifiable from grainsize and colour (Fig. 4.2). The lake core, however, is slightly finer-grained in the lower two subunits than in the lower half of the land section. In LQ02, for instance, Md= -0.8 in the lower two subsamples, while Md= -1.3 in the lower half of EN02 (Fig. 4.2). We interpret this to be a result of the distance of the cores from the primary dispersion axis, which is consistent with the layer in the cores also being slightly thinner than at EN02. Additionally, it is not reasonable to directly compare the bottommost subsamples from the lake cores and the land sections, as they represent a different proportion of the overall deposit.

As seen in Lago Lanquihue, the core from Todos Los Santos (TLS03) contains 2015 tephra with a thickness consistent with the isopach contours based on deposits on land. Although the closest

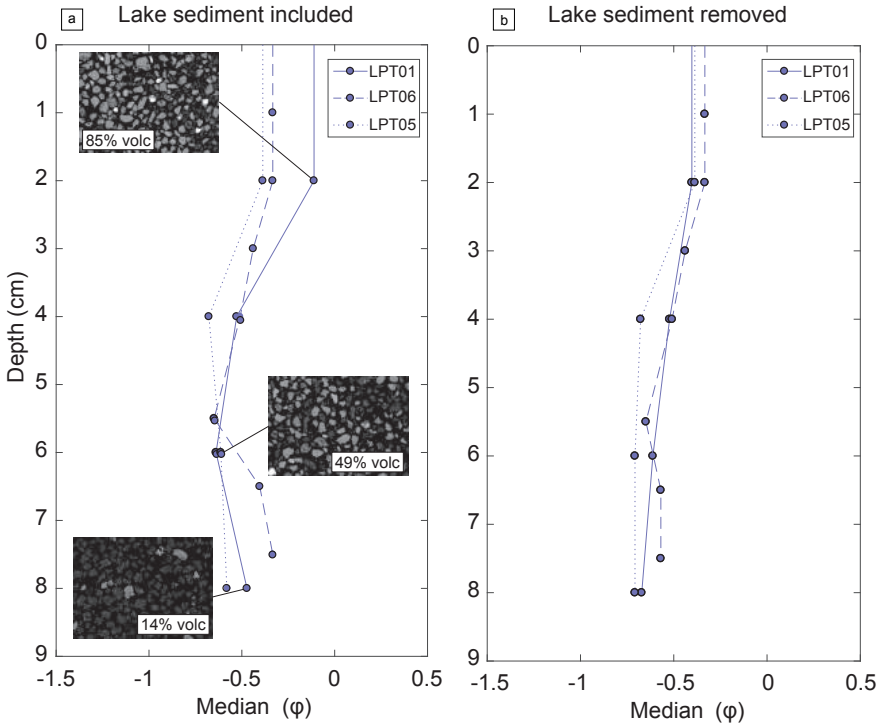

Figure 4.5: Median grain size with depth for the three non-fluvially thickened lake cores from Laguna Patas. (a) Without lake sediment removed; SEM images show proportions of lake sediments in the 3 phi grain size fraction. (b) with lake sediment removed.

tephra section on land (KAL-49; Segura et al., 2015) is coarser than the lake core, it is ~6 km closer to the volcano (Figs. 4.3 and 4.4). Additionally, the normal grading observed in all the land sections is not as apparent in TLS03 (Fig. 4.3), although even on land the four units become less distinctive with distance from the volcano (Castruccio et al., 2016).

In Laguna Patas, the smallest of the lakes sampled (Fig. 4.1), the characteristics of the tephra varied with the positions of the cores relative to the primary dispersal axis and the lake's fluvial inflow. In the three cores closest to the volcano (LPT01 to LPT05 and LPT06) the tephra layer thins with increasing distance from the dispersal axis, consistent with the well-constrained primary deposit on land. The grain size trend is consistent across these three cores but not with observations of land sections and our cores from other lakes, in which the bottom half of the deposit is coarser than the top (Fig. 4.3a). After the samples were dried, however, we identified a contribution of lake sediment in the bottom 2 – 4 subsamples in all three cores. To investigate the impact of this mud on the grain size distribution, the finest three grain size fractions were imaged by SEM. In each case, we observed aggregates comprising mostly diatomite and some organic material. The proportions of volcanic and non-volcanic particles were quantified by point counting, and the non-volcanic portion was removed from the grain size fraction to create a primary grain size distribution (Fig. 4.5). The revised (purely volcanic) grain size indicates normally graded deposits, consistent with normal grading displayed in land sections and in Llanquihue cores (Fig. 4.3).

The tephra layers in the other two cores (LPT07 and LPT08), however, have thicknesses and grain sizes that contrast with the other three cores; we attribute this difference to their proximity to the lake's fluvial inlet (Estero El Caballo; Fig. 4.6). Specifically, the tephra layers were considerably thicker and finer-grained than their co-lake counterparts (Figs. 4.3 and 4.6) and contained lenses of mud and organic material amongst the tephra (Fig. 4.3). They also contained large lithic fragments of andesitic lava distributed randomly throughout the deposit, unlike the other cores, which typically contained more dense fragments towards the top.

We interpret these cores to contain material washed in from the lake catchment, which explains the overthickening and the grain size trends (Figs. 4.4 and 4.6). As no portion of the overthickened cores matches the stratigraphy in the cores away from the inlet (LPT01, LPT05 and LPT06), it appears that volcanic material from the river was deposited in the lake during the eruption and disturbed the primary fall material as it washed in. It should be noted that these overthickened deposits comprise mostly tephra despite the included organic matter.

In summary, most of the deposits in the lake cores preserved grain size and thickness information comparable to land sections and accurately represent the primary deposits. Moreover, the cores were sampled only ~100 m from the lake edge, which indicates that, despite their location, the effect of wave action on sedimentation is negligible.

4.4.2. Fluvial inflows and drainage basins

We also investigated the effect of different drainage basins on the tephra deposits in lakes using drainage basin analysis in ArgGIS (Fig. 4.7). This is important because in other settings, deposition of volcanic particles carried into the lake from rivers has been shown to interfere with primary deposition and cause discrepancies between land and lake records. For instance, immediately north of Lago Llanquihue is Lago Puyehue which, after the 2011-2012 eruption of Cordón Caulle, was found to contain mm-thick tephra deposits across most of the lake (which has a surface area 164 km^2) that were not consistent in thickness or grainsize with nearby primary land deposits (Bertrand et al., 2014). In this scenario, volcanic material was washed in from the fluvial system (primarily the river Golgol) that was fed from a catchment area directly under the ash dispersal axis.

Interestingly, the fluvial input of the Calbuco lakes appears much less important. It is not surprising that the core in Todos Los Santos (TLS03) has not been affected as the lake's catchment area does not lie directly under the area of substantial primary ash deposition and the core is 10 km from the nearest inlet. However, the catchments of the two other lakes do contain substantial fallout from Calbuco and the cores were all collected close to river inlets.

In Laguna Patas, only cores within 300 m of the inlet have been affected by fluvial inputs (Fig. 4.6); a core 850 m from the inlet is consistent with land records and appears primary. Our drainage basin analysis indicates that Laguna Patas is fed from a catchment that comprises the eastern flank of Calbuco (Fig. 4.7). This may explain the presence of large lithics amongst fine sediment, as well as the poor sorting and grainsize trends. There are no published data on Estero

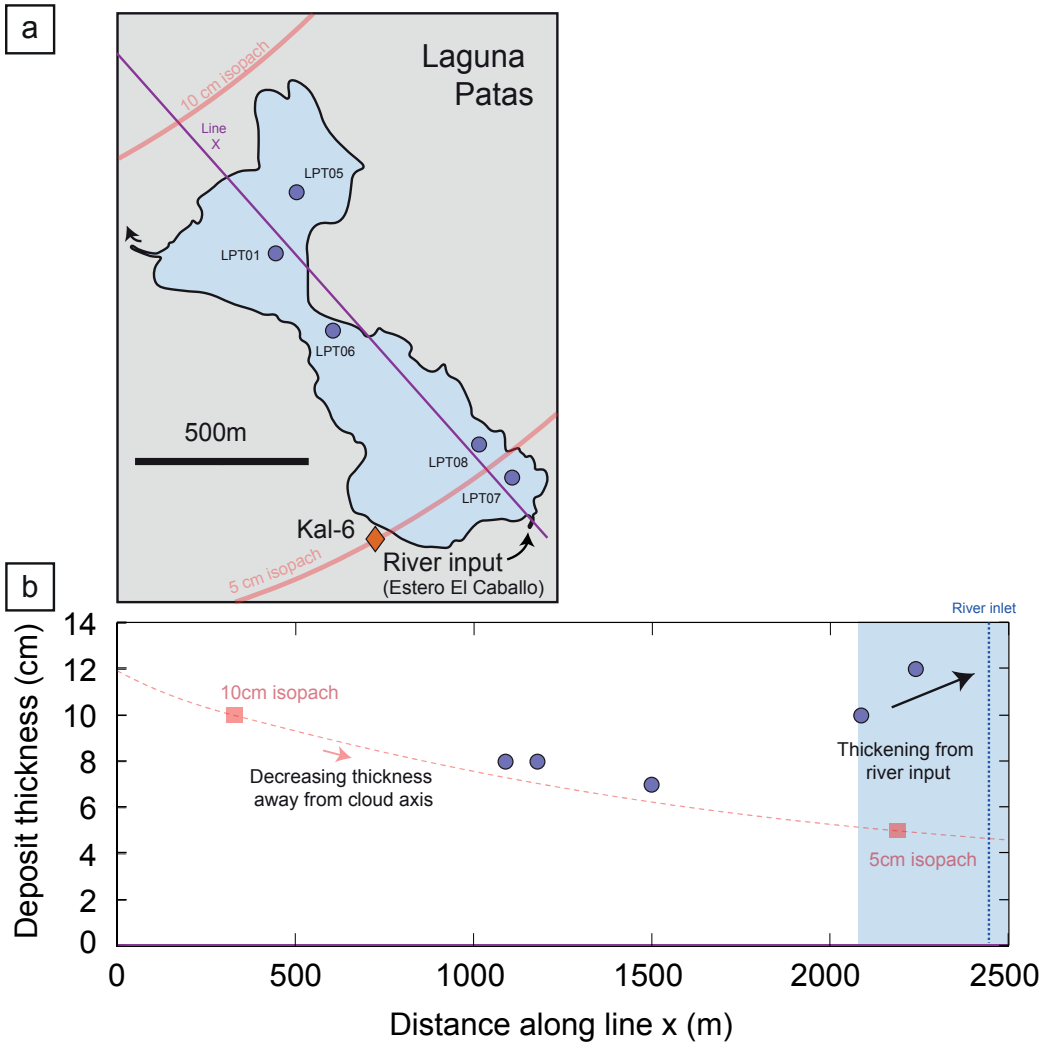

Figure 4.6: Thickness of the tephra deposit in Laguna Patas lake cores. (a) Purple line marks a transect approximately perpendicular to the ash cloud dispersal axis. (b) The position of the cores along the purple line (determined by orthogonal projection of the points onto the line). Red squares indicate the point at which the isopach contours cross the transect and red dashed line indicates an interpolation between the points at which the 20, 15 10, 5 and 1 cm isopachs cross the transect (the curve is only displayed for the range of line X shown on map however). Blue shaded area indicates area affected by thickening from the fluvial inflow.

El Caballo, the river supplying Laguna Patas, but Google Earth images indicate that the river is ~2.5 km long and so is expected to have carried only a small volume of tephra.

Perhaps most surprising is the lack of secondary tephra deposition in cores of Lago Llanquihue, which is fed by larger river systems. The cores (LQ02 and LQ03) were taken only ~5 km from the inlet of the Tepu river which fed several lahars during the eruption. Lago Llanquihue is almost five times the size of Lago Puyehue, but any Calbuco ash entering via the river systems does not seem to have been distributed to the same extent as the ash transported into Puyehue after the Cordón Caulle eruption. The catchment areas for both lakes (Llanquihue and Puyehue) are under the primary dispersal axes for the Calbuco and Cordón Caulle eruptions, respectively (Fig. 4.7; Bertrand et al., 2014), and so will have received ash. However, the Golgol river is 55 km long and has a discharge rate of 73 – 274 m^3s^{-1} (e.g. Campos et al., 1988; Arismendi et al., 2011). In contrast, the Tepu river is 18 km long with an average monthly runoff of 2 – 5 m^3s^{-1} (Campos, 1986) and a drainage area of 32 km^2 (only 2% of the whole Lago Llanquihue drainage basin Arismendi et al., 2011). In addition, Lago Puyehue has a catchment area of 1510 km^2, comparable to that of Llanquihue (1605 km^2) despite the area of the lake itself being five times smaller.

Therefore, we infer that the thick layer of secondary tephra deposited in Puyehue was a consequence of a longer fluvial network, a higher discharge rate and a large catchment area in comparison to Llanquihue. It is also perhaps important that the drainage boundary closest to the Llanquihue cores (in the village of Ensenada) is the boundary between Calbuco and Osorno drainage basins (Fig. 4.7). It is possible that the area close to the bay in Ensenada did not receive run off from Calbuco, which would have limited the effects of secondary deposition.

4.4.3. Particle settling regime

Volcanic particles settle in water (1) as individual particles, or (2) in plumes as part of a particle-laden vertical density current (e.g. Ledbetter and Sparks, 1979; Wiesner et al., 1995; Carey, 1997; Carey and Schneider, 2011). While the settling regimes of volcanic particles deposited in oceans are fairly well understood (e.g. Wiesner et al., 1995; Carey, 1997; Manville and Wilson, 2004; Shane et al., 2006), they have not been considered in detail for a lacustrine setting where water depths are shallower. Our results show that the lake cores (at least in the proximal lakes Lago Llanquihue and Laguna Patas) are representative of the deposits on land, so we infer that the particles settled individually, rather than by collective settling in plumes. To obtain a clear understanding of this process, we tested this theoretically for each lake.

To quantify the timescales of individual particle settling in the lakes, we calculated fall velocities for the range of particle sizes in the cores. Assuming spheres and a particle density of 1350 kgm^{-3} (Castruccio et al., 2016), we calculated settling velocities using the formulation of White (1974; Eq. 4.1), which is appropriate for the full range of Reynolds numbers (Re) from viscous-dominated drag ($Re << 1$) for smallest particles, to inertial-dominated drag ($Re >> 1$) for largest particles;

Figure 4.7: Drainage basins calculated using hydrology toolbox in ArcGIS. Area of 5 cm isopach defined by Castruccio et al., (2016) shown in red.

$$C_D = C_1 + \frac{24}{Re} + \frac{C_2}{1+\sqrt{Re}}. \tag{4.1}$$

For each particle size, we started by establishing the velocity according to Stokes Law (Re$<<$1) and calculated Re based on this velocity. We then determined the Re-dependent velocity according to White (1974) and iteratively recalculated velocity (with updated Re) until the values converged. The effect of the drag on settling times (=depth/velocity) for the range of particle sizes in the cores is shown in Figure 4.8a.

In order for the individual particle settling regime to transition into collective settling, the relatively particle-rich (and hence dense) layer that accumulates in the upper water column must destabilise. As more particles enter the water, this particle-bearing layer thickens with time until it reaches a critical thickness (h_{crit}). At this thickness, the timescale for an individual particle to fall through the layer (τ_{ind}) equals the timescale for dense plumes of particles to develop by Rayleigh-Taylor instabilities (τ_{coll}) (Marsh, 1988; Carazzo and Jellinek, 2012; Jacobs et al., 2015). In order for this collective settling to occur in a lacustrine setting, the lake must be deeper than h_{crit}.

To investigate whether the lakes are sufficiently deep for the Calbuco tephra to settle collectively,

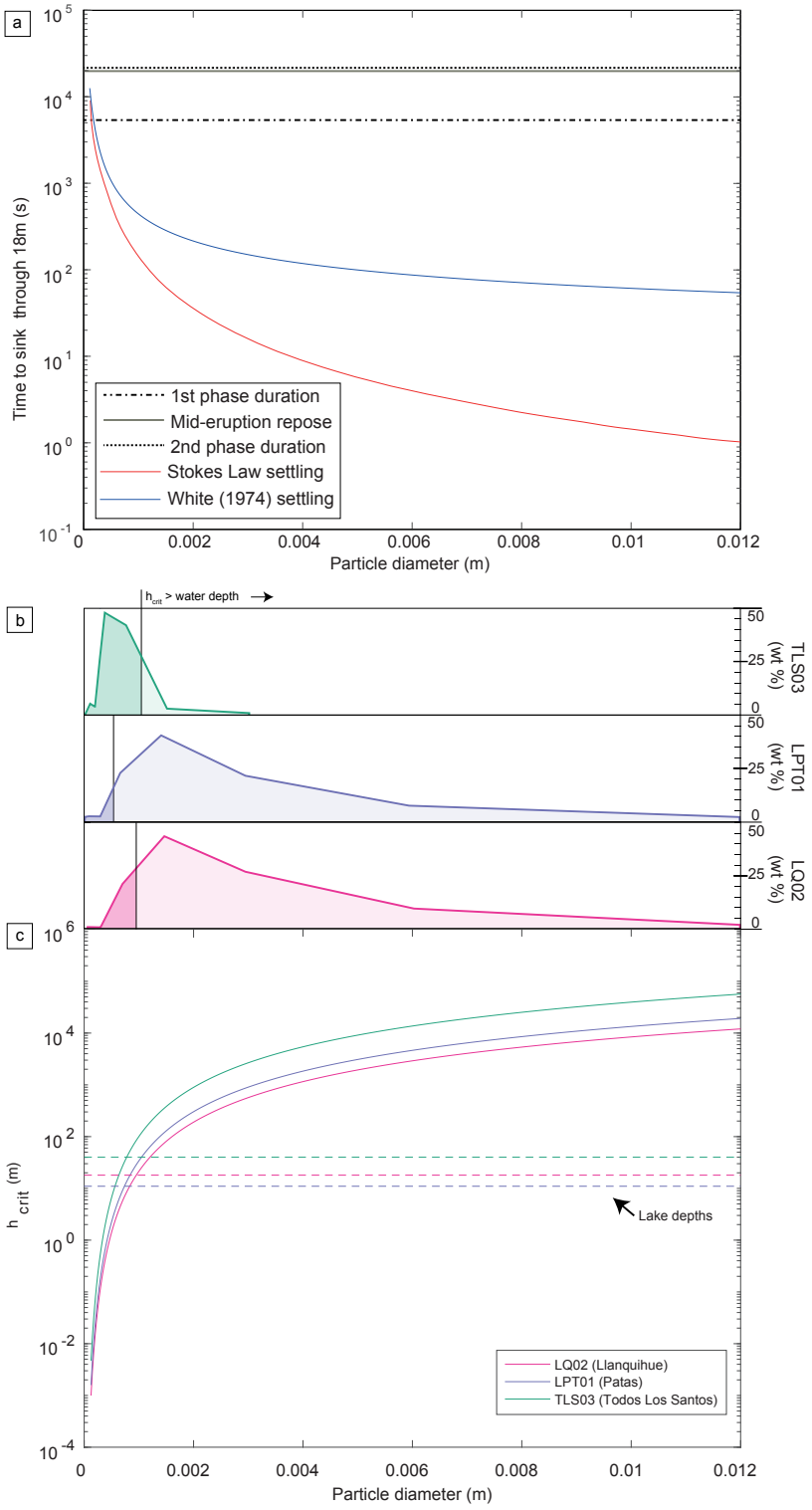

Figure 4.8: Summary of the effect if particle size on h_{crit} and on particle settling velocity. (a) indicates the time for the range of particle sizes to settle via stokes law settling through 18 m of water (depth of water for LQ03 core). The durations of the two sub Plinian phases, as well as the repose time in between are shown in dashed lines. (b) displays grainsize distribution for a core (binned at 1 ϕ intervals) from each of the three lakes. Black line indicates the particle size where water depth $>h_{crit}$ (assuming all particles the same size). (c) indicates values for h_{crit} for the range of particle sizes in the cores. Dashed lines indicate the water depths at each coring location.

h_{crit} was calculated for the range of particles sizes in the cores (Fig. 4.8c). We use the derivation for the timescale of collective settling from Jacobs et al. (2015) to derive an equation for h_{crit} that includes the effects of viscous and inertial drag on the settling velocities of individual particles as well as the effect of inertial drag on the plumes of particles. The timescales can be written as;

$$\tau_{ind} = \frac{h}{u_i}, \tag{4.2}$$

and

$$\tau_{coll} = \sqrt{\frac{4\rho_f h u_i}{(\rho_\rho - \rho_f) V_p g}}. \tag{4.3}$$

As $\tau_{coll} = \tau_{ind}$ when $h = h_{crit}$,

$$h_{crit} = \frac{4\rho_f u_i^3}{(\rho_f - \rho_f) V_p g}, \tag{4.4}$$

where h is the thickness of the particle-rich layer and u_i is the individual settling velocity of the particle (considering Re), ρ_f is the fluid density, ρ_p is the particle density, g is gravitational acceleration and V_p is the volumetric particle flux. The volumetric particle flux for each lake is calculated from

$$V_p = \frac{M_p}{\rho_p A t_e}, \tag{4.5}$$

where M_p is the mass of tephra in the core, A is the core area and t_e the duration of the eruption (excluding the eruption repose). We then calculated h_{crit} as a function of particle size for each lake using Eq. 4.4 with u_i calculated as per White (1974) as described above. This h_{crit} calculation is a simplification as for each particle size it is assumed that the entire mass of tephra (M_p) is comprised of particles of that size. We surmise that the collective settling regime dominates if most of the mass of the deposit comprises particles that are sufficiently small for a layer containing that grain size alone to have settled collectively.

In all three lakes, h_{crit} is less than the lake depth for the smallest sampled particle sizes (Fig. 4.8c). In Todos Los Santos, which is the deepest lake and contains the finest deposit, our analysis indicates that collective settling would occur for most of the grain sizes in the deposit (Fig. 4.7b). In Laguna Patas and Lago Llanquihue, which are shallower and received coarser-grained tephra, only a small portion (<20%) of the whole deposit mass would be sufficiently fine to settle collectively (Fig. 4.8b).

The calculated times for individual particles to fall through the entire water column (where we cored) are less than five minutes, which is much shorter than the eruption duration (1.5 and 6 hours for sub-Plinian phases 1 and 2, respectively). Therefore, despite the range of settling velocities of the particles in the deposit, if the particles settled individually, then the stratigraphy on the lake floor should reflect what landed on the lake as a function time, in the same way as

the terrestrial stratigraphy. This explains why the deposits at Lago Llanquihue and Laguna Patas display similar stratigraphy to nearby sites on land.

The deposit in Todos Los Santos has a less clear stratigraphy with height than in the other lakes (Fig. 4.3), which may be a consequence of a more complicated settling regime. Our calculations imply that ~80% of the mass of the deposit was sufficiently fine-grained for the particles to settle collectively if the whole mass of the deposit were composed of that size of particle (Fig. 4.8b). A collective settling regime may explain why the grain size of the whole deposit is consistent with land sections but the grain size changes with stratigraphic height in the deposit are not distinct. As there was an eruption repose of 5.5 hours, the timescales of settling indicate that ash from the first eruptive phase would have been deposited as part of a density plume that was separate from that of the second eruptive phase. The impact of successive plumes is hard to corroborate however, as the range of grain sizes deposited becomes smaller with distance from the vent (as the largest particles have already been deposited; Fig. 4.8b). Thus, any changes to the grain size with stratigraphic height will be small and may not be resolved by our grain size analyses.

4.5. Conclusions

We cored three lakes surrounding Calbuco volcano to sample the 2015 tephra deposit and compare it to nearby deposits. The lakes are of different types, sizes and location relative to the ash dispersal axis. We then examined the tephra in the lake in the context of the lake's catchment, the location of the cores relative to the fluvial network, the effect of lake sediment on the grain size distributions of the tephra and the particle settling regime.

Overall, we found that tephra deposited on the lake bed was a true representation of the terrestrial deposits. As the eruption had a distinct eruption sequence, it produced scoria of varying sizes, colour and density. The lake sediments displayed the same patterns in these three variables as the terrestrial sections.

The only exceptions were two cores sampled 300 m and 160 m from the mouth of a river inflow in Laguna Patas. In these cases, the tephra in the core was poorly sorted and contained lenses of fine non-volcanic material. It was also considerably thicker than expected (when compared to the thickness of the nearest land sample), and thicker than predicted by the deposit isopachs, indicating an additional contribution of dominantly volcanic sediment from the river. The lack of correspondence in grain size and componentry with the nearby primary counterpart, even at the base of the deposit, indicates that river input of tephra started during the eruption.

Our results highlight that when choosing coring locations, the river basins and lake catchment areas should be considered. Lakes fed from large catchment areas that directly underlie the ash plume are likely to be affected by secondary ash deposition. However, the discharge, size and catchment of the fluvial inflow must all be considered as some large lakes comprise many smaller fluvial inflows: Lago Llanquihue is the second largest lake in Chile, yet only primary tephra deposition is recorded only a few km from a river inflow fed from the flanks of the volcano. Smaller lakes are useful as they are typically subject to lower fluvial discharge rates and smaller

catchments meaning any secondary deposition will have a small spatial extent. Additionally, they tend to be shallower and so easier to core with gravity corers at multiple intervals along the lake.

We also find that the particle settling regime is relevant to the stratigraphy of lacustrine tephra deposits. For the size, density and mass flux of particles landing at the locations we cored, if the water had been >40 m deep, settling would have been as vertical density currents rather than as individual particles. Therefore, in contrast to deep-sea cores, there is the potential for settling in lakes to be as individual particles as we conclude was the case in the proximal lakes (Llanquihue and Laguna Patas). Importantly, the particles landing on these lakes were sufficiently large to settle to the lake floor in a time much shorter than the duration of the eruptive phases, explaining why the primary stratigraphy is preserved in the cored tephra. However, our calculation indicated that settling in the more distal Lago Todos Los Santos, occurred (at least in part) as plumes of particles due to the finer grain size of the volcanic material, which may explain the homogenous median grain size with depth in the deposit.

We conclude that coring of lakes to gain primary volcanic records should generally avoid shallow, sediment-rich fluvial sediment fans at river mouths, and cores close to river inflows should be treated with care (or ideally not used). In addition, shallow water depths receiving coarser grain sizes are more likely to form deposits that preserve information on the temporal evolution of the eruption as the particles settled individually, not collectively as plumes.

Where the location relative to the river input is unknown (i.e. in paleolakes), or in a situation where lake core tephras provide the only opportunity for sampling, then the features of the deposit should be carefully examined. If the deposit does not show any grading and is a poorly sorted mixture of volcanic material, then thickness and grain size information should be treated with caution.

Chapter 5

Sinking unsinkable pumice: Experimentally constraining the settling of the Aluto lake tephras

Author contributions and declaration: K. V. Cashman and A. C. Rust provided supervision. J. Tooze, R. Moore, M Sanderson, E. Snee and M. Mahfuz assisted acquiring density and grain size measurements while working as summer volunteers. L. Rudd assisted with settling experiments as well as with sieving and density measurement. The data were analysed and interpreted by K. McNamara.

ABSTRACT

When interpreting volcanic material deposited into lakes, it is important to understand whether their physical properties have been influenced by secondary processes. In the case of tephra deposits from Aluto Volcano, this is especially pertinent given that tephra deposition is preserved almost exclusively in lacustrine sediments, and so processes occurring in the lake could obscure interpretations of eruptive processes based on the deposit. Furthermore, some particles have densities less than water and so may have floated before final deposition, affecting the grain size trends of the tephra deposits. Interestingly, the Aluto tephras show both reverse and normal grading in multiple deposits at varying locations, implying that the processes controlling the granulometric trends are not the same throughout. Here we present data on the permeability, grain size and density of several Aluto tephras, accompanied by the results of simple settling experiments performed to constrain the deposit features. The experiments involve both individual clasts and bulk samples with varying initial temperatures settling through room-temperature water in tanks of different depths. We find that greater water column depths facilitate the generation of graded deposits. We also find that the sorting and grading of deposits at the base of the tanks are different for bulk samples heated to $>200^{o}$C than for room-temperature samples. However, calculations of particle cooling in the atmosphere during eruptions indicate that the particles were probably cooler than 200^{o}C when they reached the lake water at most of the locations sampled, suggesting other reasons for the grain size features.

5.1. Introduction

Understanding the mechanisms of settling of volcanic particles in water is an important aspect of using lake sediment deposits for physical volcanology. In Chapter 4, tephra fallout deposits from the 2015 eruption of Calbuco were extracted from lake beds and compared to tephra fall out deposits on land. The results indicate that lacustrine tephra deposits can be a good representation of terrestrial tephra deposits although the fidelity of lake tephras can be influenced by a range of factors including the lake depth, proximity to fluvial inflows and the densities of clasts. Because physical volcanology studies rely on measurements of thickness and grain size to determine eruption properties, ensuring that lacustrine tephras retain primary features is vital. One of the main aims of this thesis is to undertake a physical volcanology study of Aluto Volcano in Ethiopia using proximal and distal tephra fallout. However, due to the poor preservation potential of tephra on land, all deposits are sampled from amongst lacustrine stratigraphy; either from paleolake sediments now exposed on land or lake sediment cores. Because the terrestrial deposition of the Aluto eruptions is not well constrained, we are unable to conduct a similar comparison study to Chapter 4.

Chapter 4 investigated a range of controls on tephra sedimentation in the water column, including the properties of individual particles (density, mass and size) and the properties of the particles collectively (particle mass flux). The interplay of these dictates whether particles will settle individually or collectively as particle-laden vertical density currents (e.g Carey, 1997; Jacobs et al., 2013, 2015). In a lacustrine setting, where water depths are considerably less than the ocean, the dominant settling process could depend on the lake depth. Our analysis of the Calbuco deposit suggests that, if most particles are of a sufficient size, their settling velocity is high enough to preclude the formation of vertical density currents over the depths of most lakes. As a result, we were able to infer that deposits which showed no obvious grading and contained little lake sediment amongst the volcanic particles likely represented primary deposition.

The tephra deposits from Calbuco and Aluto are comparable in respect to grain size and thickness (Chapter 3.6.1). The modern lake depths are also comparable; sediment cores containing Aluto tephra were taken from Lakes Abijata and Langano at water depths of 7 m and 15 m respectively although the lake depths have fluctuated over the Holocene (up to 120 m), making it impossible to precisely constrain the depth through which each of the Aluto deposits settled. Critically however, we assumed that all the particles sank immediately upon reaching the air-water interface, something that does not occur with all volcanic products.

Fallout deposits often comprise high proportions of vesicular fragments (scoria/pumice). Vesicularity, the volume fraction of gas in a clast, is controlled by several factors, including eruption style and magma discharge rate. The peralkaline rhyolite pumices commonly erupted at Aluto have very high vesicularities (between 75 and 85 %) and correspondingly low densities (0.55 - 0.9 gcm^{-3}; e.g. Hughes et al., 2017).

The low-densities of pumice mean it can float on water (which has a density (ρ) ~1 gcm^{-3}); an

observation noted in a range of both submarine and terrestrial eruption scenarios. The timescales of sinking of low-density pumice can be on the order of seconds to years (e.g. Whitham and Sparks, 1986) and, in scenarios where large volumes of pumice remain afloat for long periods, can pose hazards to water transportation (e.g Frick and Kent, 1984; Von Lichtan et al., 2016). The tendency for pumice to sink depends on a range of factors beyond density, including clast permeability, size and temperature (e.g Whitham and Sparks, 1986; Manville et al., 1998; Tait et al., 1998; Dufek et al., 2007; Allen et al., 2008). In the context of an entire deposit, the denser, vesicle-free particles (i.e. crystals and lithics fragments) tend to comprise the finer ($<$~2 ϕ) grain size proportions (e.g Liu et al., 2017).

The permeability of pumice is determined by the extent to which individual vesicles are connected to one another. The development of pumice permeability occurs prior to deposition, when the pumice is still molten and is influenced by eruption dynamics including volatile content, decompression rate and magma viscosity. Indeed, the permeability of magma may be a primary control on fragmentation. Fragmentation occurs when magma permeability precludes volatile escape, meaning pumice vesicle networks can preserve information about pre-eruptive processes (Whitham and Sparks, 1986; Klug and Cashman, 1994; Rust and Cashman, 2004).

As well as influencing pre-eruptive conditions, permeability can affect the timing of water saturation of pumice if clasts are deposited on water in subaerial eruptions. Calculations of the speed of pumice saturation typically assume that porosity (vesicularity) and permeability are correlated and can be estimated using an empirical relationship (Klug and Cashman, 1996; Manville et al., 1998). All particles that float have a period where their settling velocity is zero, the duration of which depends on the speed of pumice saturation. Previous studies suggest that the primary control on the timing of pumice saturation is clast size, where larger clasts will saturate more slowly than smaller clasts (Manville et al., 1998) contributing to a reversely graded deposit.

However, this relationship does not hold when the pumices are heated. Experiments by Whitham and Sparks (1986) show that all pumices, regardless of density, can saturate and sink immediately on impact with water if heated above 700^{o}C, although the majority sink if heated above 400^{o}C. This effect is observed in pumice produced by submarine eruptions which have densities considerably lower than water, yet remain submerged after eruption (e.g Fiske et al., 2001; Wright et al., 2003; Allen et al., 2008). Two mechanisms are hypothesised to explain this phenomenon. Firstly that, at lower temperatures (~150^{o}C), rapid cooling will cause the hot air occupying vesicle spaces to contract, thereby drawing water into the pore spaces. Secondly, at higher temperatures water penetrating the vesicle networks will be converted to steam which flushes out air in the pore spaces and, after cooling, condenses inside the vesicle network causing saturation and subsequently sinking. In submarine eruptions, the condensation of steam inside vesicles has also been shown to decrease pore pressure increasing the ingestion of water (Kato, 1987; Cashman and Fiske, 1991; Fiske et al., 2001). Recent experiments indicate that the condensation of steam is the first phase upon submersion in water, followed by the thermal contraction of remaining trapped gas by conductive cooling (Fauria and Manga, 2018). The

Figure 5.1: ABII-6-62:7—photo of a normally graded deposit in the sediment core from lake Abijata. MER050R,B,M—from recently exposed lacustrine/pyroclastic sections. Pumices are shown at the bottom and middle of the deposit which suggest they did not float on the surface of the lake despite their low density but sank before the finer particles above were deposited. MER050R shows approximately normal grading, while MER050M and MER050B display large pumice in the centre and bottom of the sample

processes by which heat influences the settling of bulk deposits however, is not well constrained.

If pumice becomes saturated near-instantaneously on impact with water, then the deposit is more likely to display grading features comparable to deposits on land rather than reversely graded deposits from the late-sedimentation of relatively large, low-density particles. The lake core deposits at Aluto show both normal and reverse grading, and in consecutive deposits; (Fig.5.1; Tables 2.1 and 3.1) with no anomalously large particles on top of the units (as would occur if the larger pumices floated for timescales longer than the eruption before sinking). The variations in grading indicate that the processes which produce the grading cannot be the same for all deposits and therefore cannot be entirely a consequence of clast sorting due to depositional processes in the water. Indeed, in Chapter 4, we use the different grading textures to indicate that the deposits are primary. In this case, it implies there must be some primary control on the granulometry such as change in eruption intensity (column height) or size distribution of clasts erupted. To investigate this further we undertook analyses of the physical properties of the Aluto clasts, as well as simple experiments to better understand the mechanism controlling their settling in water.

5.2. Methods

Grain size data for MER050W, MER050B, MER050M, MER050G (Figs. 5.1 and 5.2) and MER038A were obtained by sieving the deposits to phi intervals from 4 to -4 ϕ and weighing the material in each sieve bin. MER050 and MER038 samples were selected for experiments as there was insufficient lake core sample for experiments.

Particle density measurements were undertaken on the -1, -2 and -3 ϕ grain size fractions for a range of deposits from MER046, MER048 and MER050 (Appendix J). Clasts from each size fraction were weighed in air and then water. To prevent water ingestion into the pore spaces during submersion, each clast was wrapped in impermeable parafilm before being weighed in water. The specific gravity was determined and then converted to a density and vesicularity for each clast as per the methods of Houghton and Wilson (1989). Vesicularities were generated using the dense rock equivalent value for peralkaline glass (2.52 gcm^{-3}) calculated by Hughes et al. (2017).

Permeability measurements were obtained from two relatively large pumice clasts from MER046R and MER046A. A 15 mm diameter cylinder was drilled from each clast, and the length dictated by the maximum length achievable from the clast (13.6 mm for MER046R and 27.86 mm from MER046A). MER046R did not display any obvious vesicle orientation, although for MER046A, the clast was drilled approximately along the orientation of the pore tubes. A core of MER038A was attempted, however the pumice did not hold together once cored on account of its very fine vesicle walls.

Sample permeabilities were measured using a custom-built permeameter at the University of Bristol. The cylinder was clamped inside a chamber, and the gas flow to the chamber inlet increased incrementally. The pressure inside the chamber [Pa] was measured for each increase in the air flow [$lmin^{-1}$]. The viscous permeability (k1) was then calculated as per the methods of Rust and Cashman (2004) using the following relationship:

$$\frac{P_i^2 - P_o^i}{2PL} = \frac{\mu}{k_1}\upsilon + \frac{\rho}{k_2}\upsilon^2, \tag{5.1}$$

where $K_2$is the inertial permeability, P_o is the pressure at the entrance to the chamber, and P_i the pressure at the exit, P is the pressure of the fluid at which the viscosity and velocity were measured, L is the sample length, μ the fluid viscosity, ρ the fluid density, and υ the filter velocity. The flow rate was converted to a filter velocity by dividing by the area of the cylinder.

Experiments were undertaken on both bulk deposits and individual clasts. All but one (MER038A) of the pumice deposits used were sampled from the lacustrine deposits, and so sank at some point after eruption. There were two main variables: (a) tank depth and (b) deposit temperature. Both tanks are cylindrical with a diameter of 5 cm: Tank 1 one is 50 cm in length and Tank 2 is 200 cm (Fig. 5.2). In both cases, the tanks were filled completely with water at ambient temperature. All experiments were performed by pouring or dropping particles directly

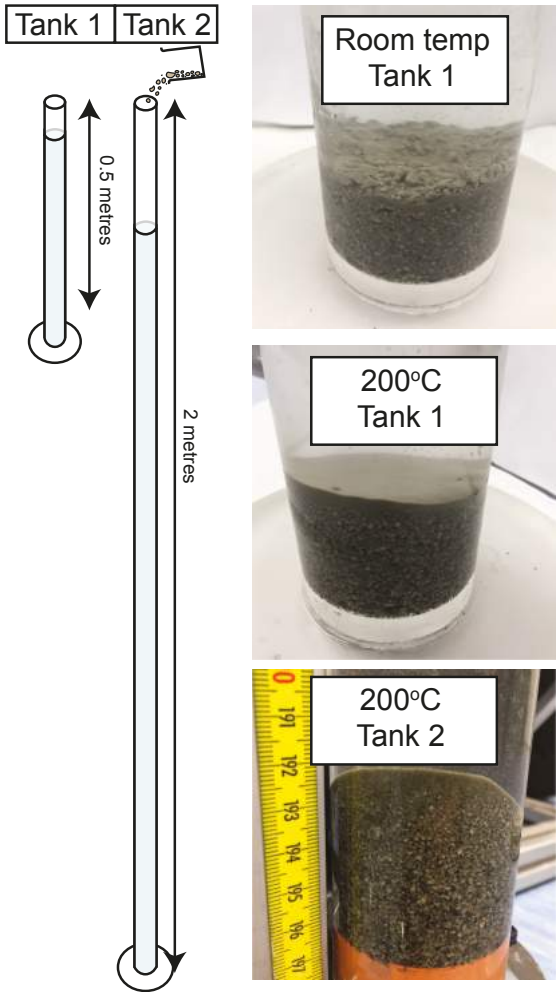

Figure 5.2: (a) Schematic of experimental set up with different tank sizes (b) Photo of deposit that was allowed to settle at room temperature in the smaller tank. Larger pumices added at room temperature floated on the surface for hours to days. (c) Photo of deposit produced when the sample was heated to 200°C and poured into the shallow tank. The deposit is poorly sorted, all pumices sank immediately and the fine particles (which settle slowly and are deposited on top of the poorly sorted pumice deposit). (d) Photo of deposit of particles at 200°C settling in the large tank. Deposit shows normal grading, with particles fining gradually to the top.

into the tanks.

The particles used in the experiments were heated in an oven for at least five hours. For each experiment, particles were removed from the oven and immediately transferred to the tank to minimise cooling in air. Experiments were performed with (1) 30 individual clasts with a range of density and comprising the -4, -3 and -2 ϕ grain size fractions heated to 100°C and 200°C in 25 cm water depth and (2) bulk samples heated to 100°C and 200°C. In all cases, the water in the tanks was at room temperature. Each experiment was filmed at a frame rate of 50 fps and particle fall times calculated from the footage. If the clast did not sink in 5 minutes, the experiment was terminated.

5.3. Results

5.3.1. Density Measurements

The average densities of the -2, -3 and -4 ϕ grain size fractions across all deposits measured are 0.67, 0.73 and 0.7 gcm^{-3}, respectively. Each grain size fraction has a standard deviation of ~0.3 gcm^{-3} and a median ~0.7 gcm^{-3}, indicating there are no distinctive changes in density with grain size for the Aluto tephras (Fig. 5.4). Across all clasts analysed, the majority have densities <1 gcm^{-3}, with the upper and lower quartiles of each distribution between 0.52 gcm^{-3} and 0.82 gcm^{-3} for each. The only exception is the -2 ϕ distribution, in which ~9 % of the grains are denser, with an average density of 1.3 gcm^{-3}.

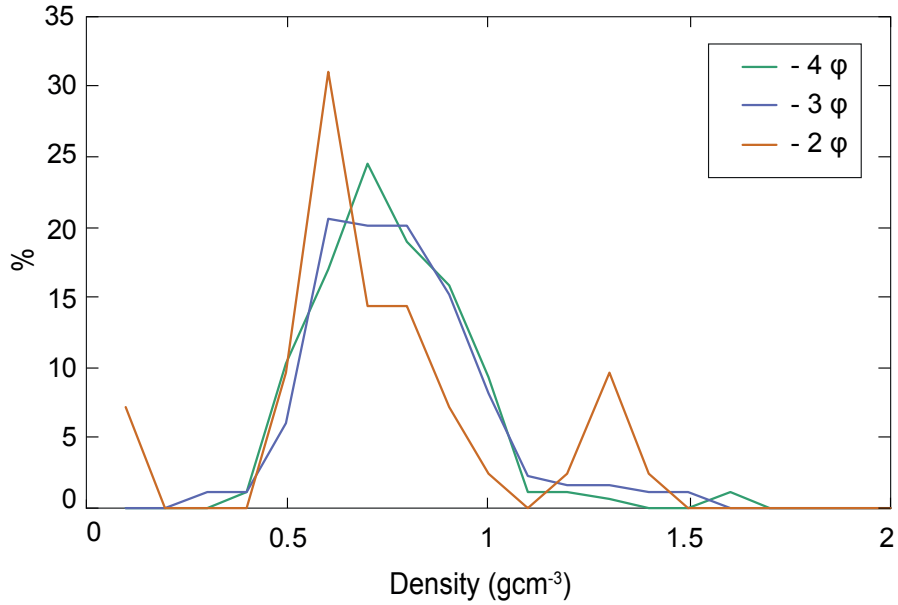

Figure 5.3: Density distribution of samples from all density measurements for samples in three different grain size fractions. Samples are binned to phi intervals, which may have affected the shape of the distribution.

5.3.2. Permeability

Measured permeabilities fall in the range of pumice samples at other volcanoes. MER046R has a k1 = 1.43 x10^{-10} m^2 while MER046A k1 = 3.2 x 10^{-11} m^2 (Fig. 5.4). Both pumices plot amongst a range of permeabilities observed in tube pumice samples, which is higher than for most pumice samples from other eruptive settings. An additional sample taken from MER046A has a permeability of 6.6 x 10^{-12} m^2 and a connectivity of 0.8 (C. Contreras per comms). The sample with the highest permeability (MER046A) was the sample cored parallel to the vesicle elongation, indicating that the vesicle orientation has contributed to the permeability of the sample.

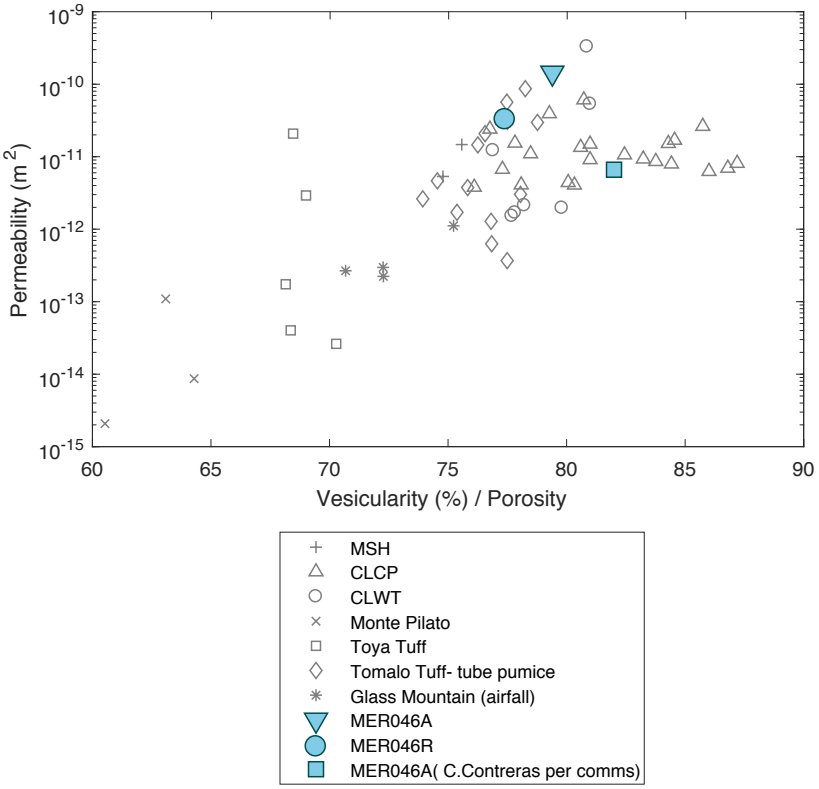

Figure 5.4: Plot of porosity versus permeability for the three Aluto clasts compared with data from other pumice samples from other settings.

5.3.3. The grain size of floating pumice

To understand the extent to which the Aluto pumices float and to establish a control for further experiments, we also poured bulk samples into a tank of water at room temperature. This was undertaken for three different bulk samples: MER050W, MER050B and MER050M. In each case, a proportion of the deposit floated for hours to days before sinking. The result was an inversely graded deposit, with the smaller dense particles on the bottom and the larger, low-density pumice clasts eventually settling on the top (Fig.5.2a). This was done for two different tank depths, although the deposits in both tank types produced very similar deposits.

To determine the extent to which particle size was affecting which samples sank, the samples were re-dried and re-added to water. The particles that floated were immediately (within a few seconds) removed from the top, and the particles that sank removed from the water; the two subsamples were then dried and sieved. This was undertaken on five separate samples (MER050B, MER050G, MER050M, MER050W and MER038A). In each case, the deposits contained particles with densities <1 gcm^{-3}, meaning in all cases the deposits should have some particles that floated. In addition, when sampled in situ, the deposits all contained large pumice either in the middle or at the bottom of the deposit (Fig.5.1).

The proportion of the overall deposit that floated or sank varied between samples; MER050W had the highest proportion of floating particles, while almost all particles in MER038A sank,

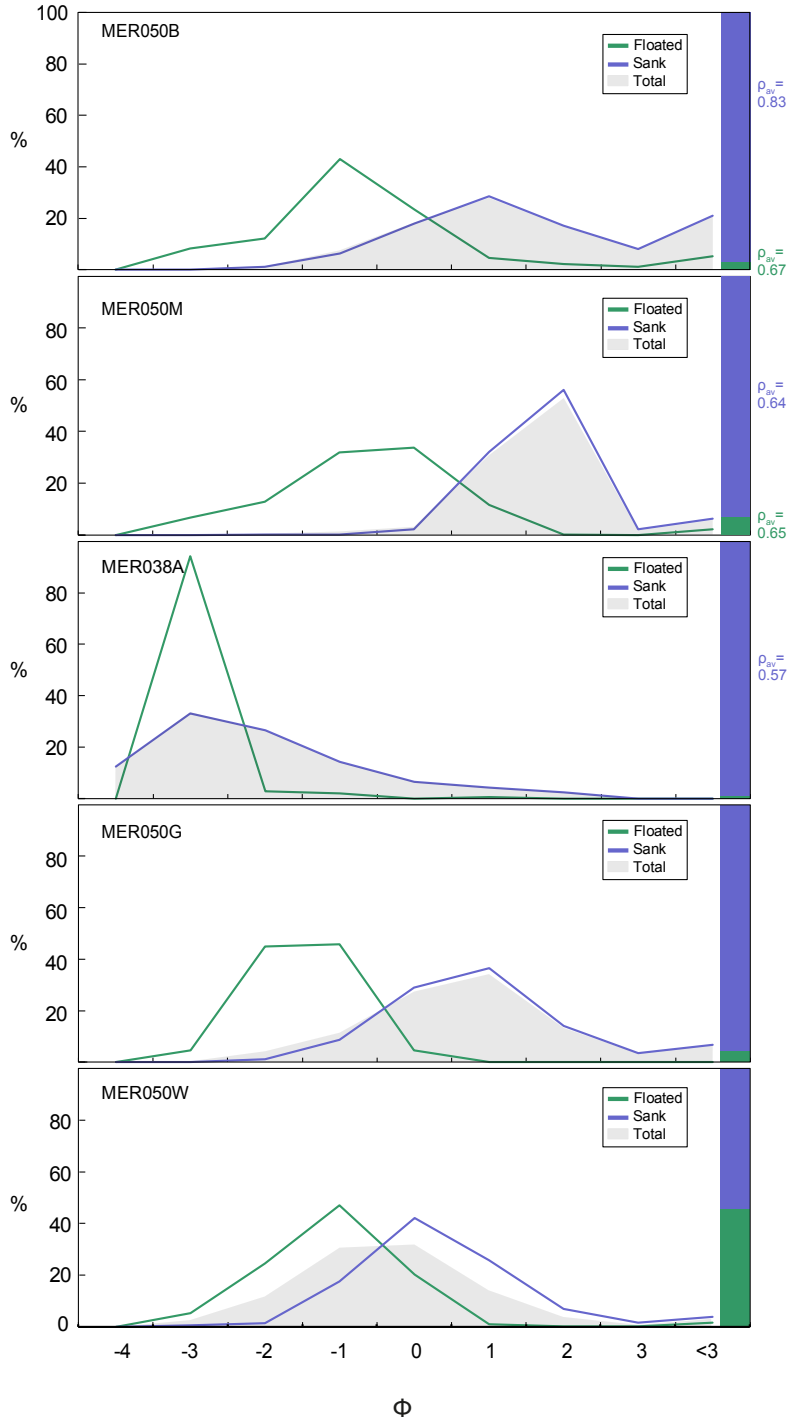

Figure 5.5: Line plots show grain size distribution of particles that sank and floated at room temperature. Grey shaded areas indicate the total grain size distribution of the whole sample. The coloured bar to the right indicates the proportion of grains that floated and sank in each of the deposits. Where density measurements were obtained, the average density of the clasts is displayed on the far right.

despite the fact that the sinking particles had an average density of 0.57 gcm^{-3}). Interestingly, for the MER038A deposit, the median grain size (Md ϕ) of the clasts that sank was similar to that of those that floated (Md = -3 ϕ). In contrast, the particles that floated from the MER050 samples all had coarser median grain sizes than those that sank (Fig. 5.5). Overall however, (with the exception of MER050W) the majority of the deposit sank, with $<$10% (by weight) remaining floating.

Density measurements were undertaken on all particles greater than 4 mm for the samples for MER050B, MER050M and for those that sank in MER038A. The results indicate that the floating particles did not always have a lower density than the sinking ones. In MER050M the average density (ρav) of the particles that sank and those that floated was similar (ρav = 0.65 gcm^{-3}), although in MER050B the floating particles were slightly less dense, with ρav = 0.67 gcm^{-3} for the floating particles, and ρav = 0.83 gcm^{-3} for those that sank.

5.3.4. Heated particle settling

Experiments were performed with both individual and bulk samples. The 30 individual clasts used were randomly selected from those that floated at room temperature. When heated to 100°C, all clasts remained floating; however, when heated to 200°C, all but five sank. Of the clasts that remained floating, three were in the -2 ϕ grain size fraction, and two were in the -4 ϕ grain size fraction, suggesting that controls on particle sinking are not strongly related to the size of the clast. In addition, of the particles that sank there is no correlation between time taken to sink and particle size (Fig. 5.6). Furthermore, there is little obvious correlation between density and time taken to sink; samples of densities between 0.4 gcm^{-3} and 0.7 gcm^{-3} took between four and 26 seconds and samples with different densities often took approximately the same time to sink. The only exceptions were the two higher density samples (with ϕ = ~1 gcm^{-3}) which both sank more quickly than the other samples, an expected result given they are close to the density of water when dry (Fig. 5.6).

To constrain whether the variation in sinking time was a result of the particle settling velocity, or the rate at which particle saturation occurred, theoretical sinking times were calculated for each of the particles, assuming they are 50% saturated with water (the minimum amount of saturation needed for all particles to have a density $>$1 gcm-3). This semi-saturated density was obtained from the particle vesicularity by assuming that 50% of the pore space was filled with water (the minimum amount of saturation required for all of the pumice samples to have a density $>$1 gcm^{-3}). The fall speeds were calculated taking into account the Reynold's number as per the methods of Chapter 4.4.3. The calculated fall speeds are generally higher than the actual fall speeds, with all particles predicted to have settled within five seconds. The equations do not account for the time taken for the particle to accelerate to terminal velocity, and therefore will always slightly underestimate the fall speed. This does not explain, however, the variation that in sinking time (5 to 25 seconds). As a result, we conclude that the particles are not saturating immediately on impact with the water but take some time to saturate during sinking.

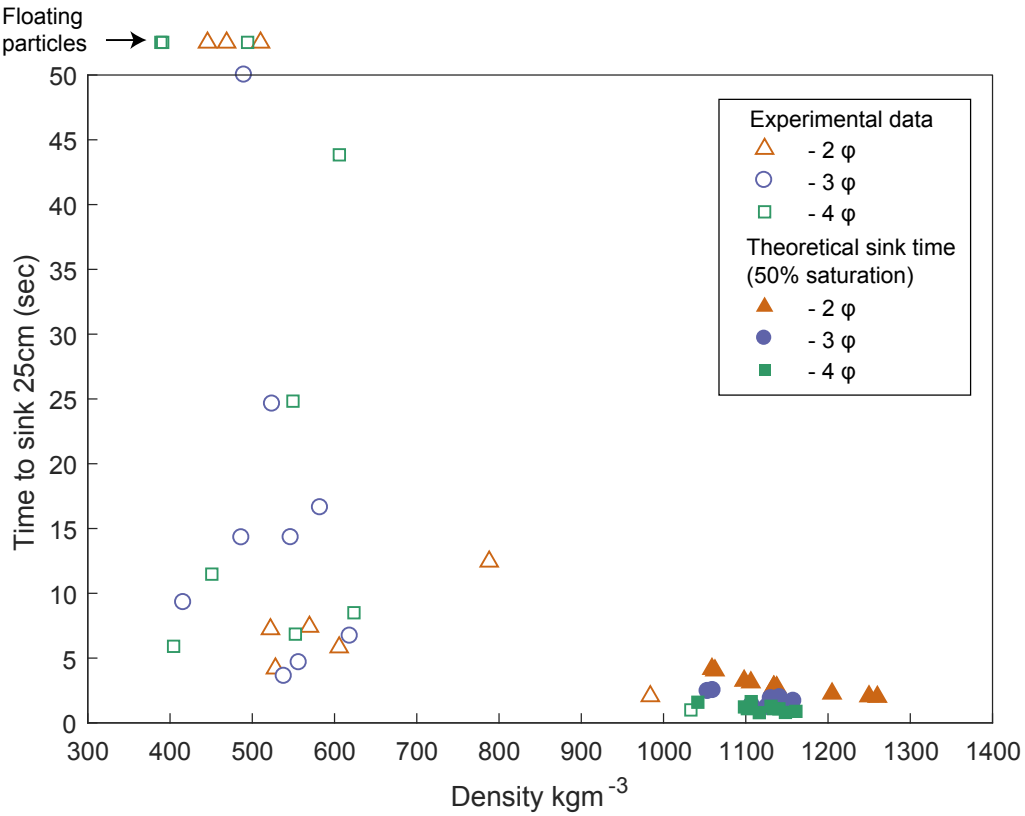

Figure 5.6: Plot of clast density with sinking time for a range of clast sizes at 200°C deposited on room-temperature water 25 cm deep. 'Time to sink' includes the time from when the particles first touched the water, to when it touched the bottom of the tank. In some cases, the particles remained at the surface for up to a few seconds before sinking, while other sank immediately upon interaction with the water. The data plotted above, labelled floated, remained floating for at least 5 minutes when the experiment was terminated. As a point of comparison, the theoretical sinking times are calculated for the particles for 50% of the pore space was filled with water. This saturation proportion was chosen as the minimum amount of saturation required for all of the pumice samples to have a density >1 gcm^{-3} (and consequently dense enough to sink). These indicate that the majority of the particles saturated near instantaneously, and then settled according to their predicted velocity. A small proportion of the particles settled slower, which we attribute to a delay in the speed of saturation.

While there is little correlation between size, density and settling time of individual particles at 200°C, it is hard to constrain the effect of this on a bulk tephra deposit with variations in size and density. Therefore, similar settling experiments were undertaken with bulk tephra for the same samples that were allowed to settle at room temperature (MER050W, MER050B and MER050M). Because there was little change in the tephra sedimentation at 100°C, the experiments were mostly conducted with samples heated to 200°C.

In all cases, the heated samples produced a different deposit than that produced when the bulk tephra was allowed to settle at room temperature. Importantly, all particles began to sink within 10 seconds of deposition into water and none were left floating on the surface. Experiments in the 50 cm tank produced poorly sorted deposits with a layer of very fine particles on the surface (Fig. 5.2c). Experiments in the deeper (2 m) tank produced normally graded deposits with the larger pumices on the bottom gradually fining upwards into the fine sediment which settles slowest.

5.4. Discussion

The grading observed in the experiments with Aluto pumices indicates there are a variety of possible processes that can affect the deposit features. White et al. (2001) suggest that pumice deposition in an aqueous environment can be defined three ways: (1) stranding, where pumices float, become lodged and then are deposited when water drains away, (2) waterlogging, where pumices sink after being saturated with water and (3) saturated-clast redeposition, where waterlogged clasts are redistributed by secondary processes.

The sharp boundaries observed above and below the Aluto tephras, as well as the inclusion of dense smaller volcanic particles in the same deposits as larger pumices, indicate that the Aluto tephras are not a stranded pumice deposit. For similar reasons, we infer that the clasts are not the product of saturated-clast redistribution, as there is no evidence of cross-bedded structures (White et al., 1997) or lenses of lake sediment material amongst volcanic material (Chapter 4). Therefore, we interpret the deposits at Aluto as the product of sinking waterlogged pumices. For this reason, perhaps the most vital component in constraining the sedimentation of the Aluto pumice is determining the speed of saturation (or waterlogging) and the processes controlling it.

Our results indicate that at temperatures of 200°C the pumices will saturate near-instantaneously, meaning there is little or no pause in deposition between release from the eruption plume and lake bed. However, at lower temperatures some of the pumices still float suggesting that any pumices deposited below these temperatures must be saturating by a different mechanism.

Our experiments with two tank depths also indicate that, even when all the pumices are waterlogged, grading can be produced by segregation in the water column. The difference between experimentally produced deposits at 200°C in the 2 m deep tank (normally graded deposit) and the shallow (50 cm deep) tank (poorly sorted deposit) indicates the particles are sorting by size (and therefore settling velocity) while falling through the water column; an observation noted in pumice deposits in other settings (e.g. Cashman and Fiske, 1991).

The observation that both normal and reverse grading are observed in the Aluto tephras, however, requires a more complex or varying set of processes influencing the tephra settling. To understand these processes, we investigate the types of pumice saturation that could have occurred at Aluto. We first examine the likelihood that pumices with an internal temperature >200°C reached the sampled location; we then explore additional controls on cold pumice saturation.

5.4.1. Sinking of hot pumice

To investigate whether the temperature of the particles could be the reason for the normal grading in some deposits, the cooling rates of four different-sized spheres are calculated in the context of the thermal properties of pumice and the fall speed of the particle. The results are examined to establish how far a particle will fall before it cools below 200°C. The calculations assume a spherical volcanic particle is released from an ash cloud at a temperature of 800°C. As the sphere falls it is cooled by the surrounding fluid by convection. The time it takes the particle to cool depends on the thermal properties of the particle, its size and the speed through which it moves through the fluid, which can be calculated using the Biot number (*Bi*; dimensionless heat transfer resistance) and the Fourier number (dimensionless time). The former, is the ratio of the heat transfer coefficient (h), the particle radius (r) and the thermal conductivity of the particle (κ):

$$Bi = \frac{hr}{\kappa}, \tag{5.2}$$

where κ is 0.67 W $m^{-1}K^{-1}$, a standard value for pumice (e.g. Bagdassarov and Dingwell, 1994; Van Manen and Wallin, 2012). The heat transfer coefficient (h) varies with density and depends on the speed of the air relative to the particle. Furthermore, because the particles in the deposit are of different sizes (and therefore masses for the same density) their fall velocity will vary. The Reynold's number (*Re*) is a function of the particle fall velocity and can be used to calculate h by the following relationship determined experimentally by Stroberg et al. (2010):

$$h = \frac{2 + aRe^{\frac{1}{2}}Pr^{\frac{1}{3}}\kappa_{air}}{2r}, \tag{5.3}$$

where a is correlation coefficient that relates *Re* and *Pr* to particle density (0.31 for ρ_p of 0.63 gcm^{-3}), *Pr* is the Pradtl number for air at 20°C (0.709) and κ_{air} the thermal conductivity of air (0.0257 W $m^{-1}K^{-1}$). h was calculated for a particle of each size based on a value for Re calculated as per the methods of Chapter 4.4.3. For all four particle sizes investigated, *Bi* >0.01 indicating that all the particles have a radial temperature gradient, where the core is a different temperature to the surface, and therefore cannot be considered as a lumped analysis.

The time for the particle to cool is calculated using the Fourier number (dimensionless time);

$$Fo = \frac{\alpha t}{r^2}, \tag{5.4}$$

where t is time and α the thermal diffusivity (1.3 x 10^{-7} m^2s^{-1}; Hardee, 1981). The internal and external temperature of the particles was calculated from 0 seconds (when the entire particle is at 800°C) to 500 seconds to quantify the cooling rate (Fig. 5.7) as per the methods of Recktenwald (2010).

The calculations indicate that all particles will have cooled to below 200°C before falling up to 1.8 km (Fig. 5.7). We infer that the majority of eruptions of Aluto were Vulcanian or Sub-plinian in size (Chapters 2 and 3) which have typically column heights of 10 – 20 km. Consequently, all particles had probably cooled to ambient temperature before being deposited into the lakes. Therefore, the rapid sinking of the low-density pumices at Aluto (as is implied by the normal grading) must have occurred for a different reason. The results of our hot experiments however, may still be relevant for the study of volcanic ash deposits in other settings, where lakes are more proximal to the volcano, and ash may have entered while still hot.

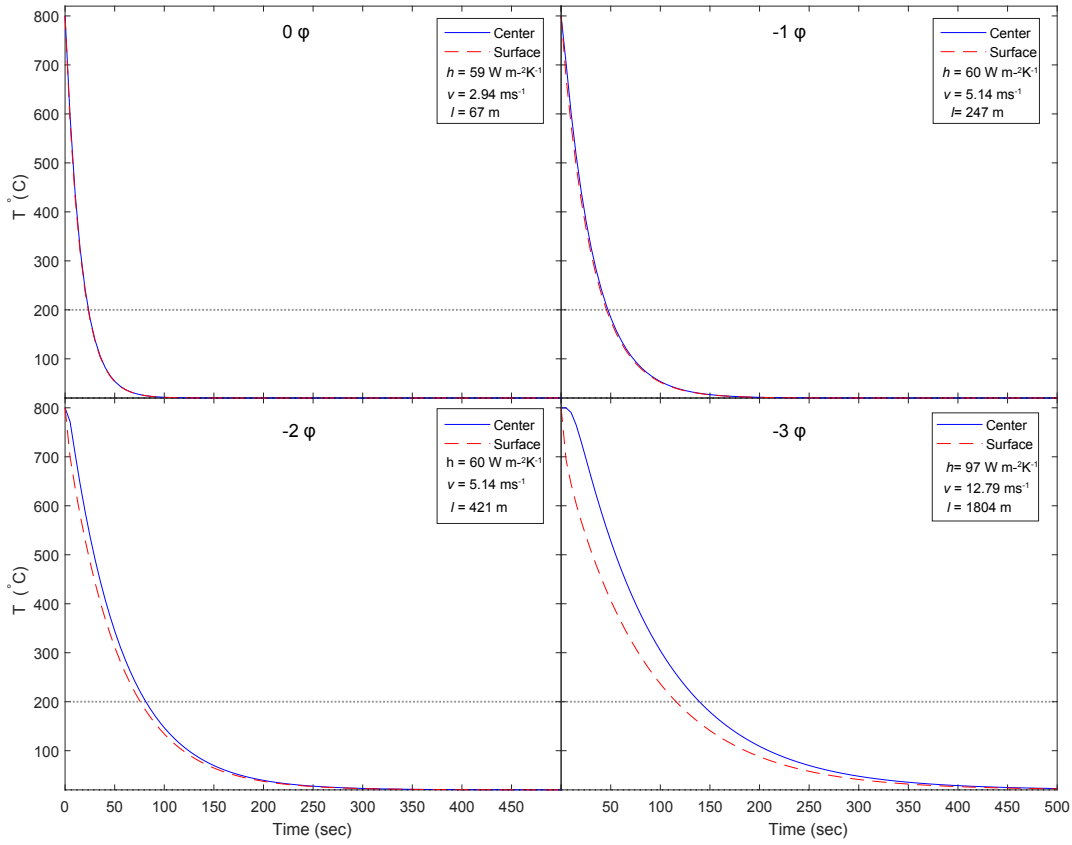

Figure 5.7: Fall sinking time in 20°C air for spheres of 0, -1, -2, -3 ϕ. Each has a different heat transfer coefficient (h) which is dependent on its density and Reynolds number. Based on a particles terminal velocity (v) the distance each particle would fall before cooling to 200°C (l) is calculated as per the methods of Chapter 4.4.3. We infer almost all particles will have cooled to ambient temperature before reaching the lake.

5.4.2. Sinking of cold pumice

The sinking of cold pumice has been shown experimentally to depend on the clast size and the internal vesicle dimensions and connectedness. Generally, pumice clasts that come into contact with water undergo two stages of water absorption. Most is absorbed in the first five minutes of interaction with water (Whitham and Sparks, 1986; Manville et al., 1998; Fauria et al., 2017) followed by a very slow water uptake until the density reaches 1 gcm^{-3}. After the initial absorption, the processes governing water uptake are poorly understood and do not follow the typical time-dependant laws observed in diffusion processes. It appears, however, that pumices with $\rho > 0.8$ gcm^{-3} can float for days to years before becoming waterlogged.

Because many of the Aluto pumices have densities below this threshold, their presence at the bottom of volcanic deposits is surprising; pumices which floated in lab experiments were sampled from the middle and the bottom of the in-situ deposits (Figs. 5.1 and 5.5). Indeed, as both normal and reverse grading are observed, in at least some cases, pumice clasts must have waterlogged and sank within eruptive timescales. Importantly, previous pumice-saturation experiments, where clasts float for long times, have involved pumice carefully placed in undisturbed tanks. In our experiments, however, small perturbations in the water had a large effect on the saturation speed; specifically, pumices that had floated for hours to days would sink rapidly because of vibrations from a door shutting 5-10 metres away.

Long-term pumice floating is probably the result of gas isolation, where water in the pore throats traps air inside the clast. The pumice is only able to sink after the trapped gas has diffused (Fauria et al., 2017). However, sinking as the result of small perturbations in the water implies that that the gas is not being lost by diffusion, but because the structure of the pumice is allowing gas to escape once disturbed.

We hypothesise that this effect may be caused or exacerbated by the pore structure of the Aluto samples; the samples are highly permeable compared to pumice of other compositions (Fig. 5. 4) due to their peralkaline composition. Peralkaline magmas have lower viscosities than typical rhyolites, which contributes to extreme pore structures, particularly elongate pores and tubes (e.g. Hughes et al., 2017). As a result, the clasts commonly display tubular pores with rather than the 'ink bottle' shaped pores with narrow throats that are common in other pumices (Manville et al., 1998; White et al., 2001). Measurements of an Aluto clast using X-ray tomography indicate ~98% connectivity of the pore space (Contreras per comms) which is a high value for pumice (e.g. Nakamura et al., 2008). Consequently, we infer that the pumice saturated more rapidly than predicted by other models (e.g Vella and Huppert, 2007; Fauria et al., 2017). In a natural setting, floating pumice would be subject to small waves/surface disturbances that may have caused the Aluto pumices to saturate quickly and sink within the timescales of the eruption.

One additional factor could help to produce normally graded deposits: even if larger particles float for several minutes, they may still reach the bottom of the lake faster than the smaller particles. Calculated particle settling times over the range of depths of the core lakes observed

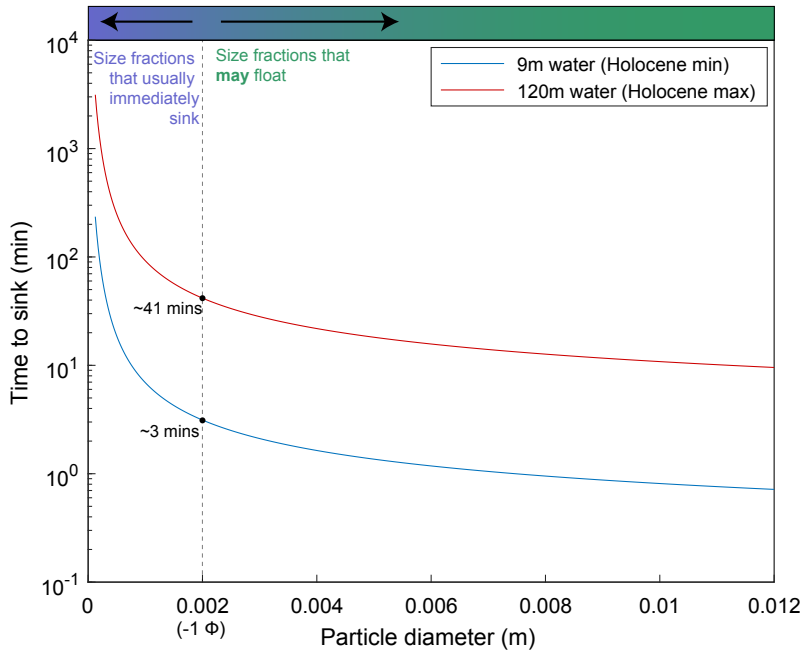

Figure 5.8: The theoretical settling time for particles of varying sizes with a constant density of (1130 kgm^{-3}, the density of a pumice 50% saturated with water) for the minimum and maximum water depth in the Holocene. While it is not a completely accurate picture (the smaller particles will be denser and therefore settle quicker than predicted by this calculation), it implies that large particles may float for several minutes before sinking, without dramatically affecting their stratigraphic height in the final deposit.

in the Holocene (Chalié and Gasse, 2002) indicate that, particles with fall velocity appropriate for a density just above water (1.1 gm^{-3}) could float for between 3 and 41 minutes and still reach the bottom of the lake before a smaller particle deposited at the same time (Fig. 5.8). Judging the potential importance of this process is difficult, however, particularly because we cannot accurately constrain the lake depths at the time of deposition for each eruption.

However, the speed of settling through the water column is controlled by a range of factors i.e. particle settling regime, or segregation by fall velocity (Chapter 4.4.3) meaning it is difficult to consider the precise effect this will have. However, our results from Chapter 4 suggest that, over the timescales of a typical eruption, the mass flux of particles into the lake is sufficiently slow that particles likely settled individually. While it is impossible to constrain the eruption duration for the products of Aluto, we have no reason to suggest that they would have a greater mass flux than those at Calbuco.

5.5. Conclusions

All the material considered in this study has been collected from a lake, and so sank at some point despite products of Aluto >2 mm clasts having densities less than water. Indeed, simple experiments indicate that, at room temperature, a proportion of the pumice floats. When bulk samples are added to water, large pumices float and then settle on top of finer deposits

producing a reversely graded deposit. That this is not observed in the natural setting—normal grading is a common feature of the lake core deposits—suggests that the pumices settled either instantaneously, or at least within the timescales of the eruption.

We show experimentally that, when large low density pumice clasts are heated to 200^{o}C, the large particles settle instantly, as noted by previous researchers. Calculations of particle cooling for the Aluto pumices however, indicate that they would have reached ambient temperature before being deposited into the lakes, implying that heat was not the cause of the comparatively rapid pumice saturation and sinking. In contrast, the observation that floating Aluto particles sank with small perturbations in the water surface suggests that the internal pore structure of the particles is particularly sensitive to disturbances and that small movements can cause water to flood the particles. In the context of an eruption, then pumices landing on lake would be subject to movement from small waves and wind and therefore may have saturated quickly and sank. However, these interpretations require more information to be confirmed, and a more detailed study of the saturation speeds of different pumice compositions and structures would be needed to quantify this effect.

Chapter 6

Concluding Remarks

6.1. Summary

This thesis explores two themes, across two different volcanic settings. Firstly, it undertakes study of tephra deposits in lakes from Aluto volcano in Ethiopia. Secondly, it examines the fidelity of tephra stratigraphy in lake records and their application to physical volcanology. The latter is explored through a study of Calbuco volcano in Chile.

6.1.1. Chapters 2 and 3: The Holocene history of Aluto

Two chapters investigate the eruptive history of Aluto, a poorly understood and active volcano with sparse exposures and chemically-similar tephra deposits. The Smithsonian Global Volcanism Program database for this volcano only includes one Holocene eruption. However, this thesis presents data from tephra layers in two lake cores drilled within 30 km of the volcano, which contain between 20 and 25 ash layers of Holocene age. The tephras themselves have homogeneous glass chemistry and so I used componentry to fingerprint and correlate the deposits in the two cores. Specifically, I used the proportions of different ash types (microlite-containing particles and glass shards) to determine ash layers from the same eruption. These correlations were confirmed with trace element analyses (Chapter 2).

The use of componentry to correlate tephra deposits has potential in a wide range of environments. It has the obvious advantage of not relying on geochemical measurements and therefore, can be utilised when magma compositions are non-diagnostic or the glass is devitrified or leached. Componentry also offers rapid, low-cost constraints on tephras: with just a hand lens or simple microscope, it is often feasible to recognise whether an ash sample is crystal-rich or consists of glassy bubble shards based on the shape and lustre of grains. Because tephrostratigraphy encompasses several disciplines, the technique has potential beyond volcanology, to areas of study such as climatology or archaeology.

For a volcanologist, undertaking componentry has the additional advantage of providing information about the eruption dynamics, which cannot be obtained from other means of tephra correlation. In this thesis, the componentry has been related to both the eruption size and frequency, with smaller (thinner) tephras, tending to comprise the microlite-rich particles, and the glass shard-containing deposits comprising thicker layers. This relationship implies that the eruption properties are different between the two, a factor that would have been overlooked without componentry. Furthermore, it was observed that these textural differences vary not only with deposit thickness, but with deposit frequency; the microlite-rich layers are clustered temporally, compared to the glass-shard layers.

The componentry data allowed not only the two lake cores to be correlated, but also layers in two additional Holocene palaeolake sections now exposed on land. One of these sections (MER050) showed remarkable textural similarities to the cores, as well as comparable major and trace element geochemistries throughout; all five layers correlated in the cores were identified. One of the correlated tephra layers (AGSL1; Chapters 2 and 3) was also located in a fourth section,

meaning that one deposit was correlated to four different locations. Some approximations were made about eruption size using these four data points, which were consistent in thickness and grain size with other sub-Plinian-sized eruption deposits. As four locations are not enough to inversely model eruption parameters, similarly sized eruptions were used as analogies and consequently provided input parameters for simple tephra dispersion forward modelling of the Aluto eruption (Chapter 3).

One of the most challenging aspects of this thesis has been the difference in major element geochemistry observed between tephra sections of the same age in close proximity to one another. There is a distinct change in certain element oxides, specifically Al_2O_3, FeO and Na_2O. Interestingly, they vary by stratigraphic section, rather than by individual layer. Furthermore, the sections with different oxide concentrations to the lake cores are sections exposed by river-cut gorges, while the others are more recently exposed by quarry cutting and road cuttings. The implication is that the environment can impact the composition of the glass. That hydration and leaching effects the major element geochemistry of Aluto glass that appears pristine by scanning electron microscopy, has ramifications for the use of glass geochemistry as a correlative tool in other environments.

6.1.2. Chapters 4 and 5: Tephra deposits in lakes

Tephra deposits in lake cores are commonly employed as chronostratigraphic markers across a huge range of disciplines, in the study of wildfires, vegetation, ecosystems and climate etc. The use of lake tephra deposits in all relevant disciplines however, rely on the ability of the user to identify if the tephra deposit is primary, or the result of redistribution and re-sedimentation of volcanic material at a later time. In physical volcanology however, lake cores are perhaps not used to their full potential as concerns over the effect of lakes on the deposit often prevent detailed study. Indeed, in this study of Aluto, the preservation of the tephra layers in the lake sediment motivated an entire additional study of lake tephras in a different volcanological setting.

This comprised a comparison study of deposits of the 2015 eruption of Calbuco volcano in lakes, with tephra deposited on land. Overall, I found that the lake deposits were a good representation of the land deposits, with the exception of cores collected proximally to fluvial inlets. I also undertook a study of the lake settling in the water column, and found that the majority of material likely settled as individual particles, rather than as particle-laden density plumes: The size of the particles and the depth of the lake was insufficient to accumulate the dense particle-rich layer at the top of the water column necessary for the development of gravitation instabilities. Furthermore, the particle mass flux into the lake was small enough that most particles will have had time to settle within the time-scales of the eruption, allowing the lake records to be a good representation of the land record. These results highlight the perhaps-overlooked value of lake tephra deposits for physical volcanology, providing care is taken with the coring location and that attention is given to the sorting and composition of the deposits.

Deposits from Aluto are typically well-sorted and often display grading, a feature that allowed

me to infer they were the result of primary tephra deposition. This is surprising given that, in simple lab experiments, the large pumices floated, producing reverse graded deposits or poorly sorted deposit with large pumices on the surface. While low-density pumice can saturate and sink immediately at high temperatures, calculations suggest that the majority of the Aluto pumice would have reached ambient temperature before landing in the lake. Therefore, the pumices must have saturated for other reasons, which could be attributed to the Aluto pumices high permeability and connectivity. Overall however, I infer that the vast majority of the Aluto pumice in the lakes is the result of primary deposition and the layers are used accordingly.

6.2. Future work

There are many more avenues open to extend this work. In particular, there are several areas in which the results remain somewhat inconclusive, or could easily be improved. Perhaps the most useful from a hazards perspective, would be an additional lake core, either elsewhere in Abijata, or if possible, in Lake Ziway (north west of Aluto; Fig. 2.1). Tephra correlations with tephra sourced from the latter would allow more sophisticated interpretations about the probable orientation of the ash dispersion axis of Holocene eruptions based on the grain size and thickness of the tephra. The addition of further correlations would, in turn, permit more robust and detailed interpretations of eruption size and style. Furthermore, an additional core could provide crucial detail about the last ~1 ka which are missing from the Abijata and Langano core records.

An additional inconclusive aspect is the influence of environment of preservation on the glass geochemistry in the river-cut tephra exposures. Understanding whether this effect is magmatic or secondary is vital if terrestrial tephra deposits are to be used in future studies of the volcano. Perhaps the easiest way to be sure that there are not inaccuracies in the ^{14}C dates (whereby the geochemically heterogeneous sections would be the product of eruptions from a different time period to those of the core) would be to find more material for ^{14}C dating. Further dates, which could place detailed temporal constraints on the tephra layers with different composition to the cores, could elucidate more information about whether or not they were deposited at the same time as the core tephra layers. Should this be the case, then a more detailed study of the hydration of the peralkaline glasses could reveal information about the causes of the discrepancies in major element data between the cores and sections. This could comprise more chemical analyses of the glasses, as well as experiments on glass-water interactions.

The causes for the discrepancies could be further elucidated by the addition of more trace element data. In particular, LA-ICP-MS analysis of glass in tephra layers exposed in the river-cut sections—as trace element concentrations should not be affected by secondary processes—could provide information as to how they relate to the core stratigraphy. Additionally, undertaking LA-ICP-MS analyses on glass comprising the other microlite-textures (which could not be correlated by texture alone) may also be beneficial if there are additional trace element constraints that could be used to further combine the core and land stratigraphies.

Perhaps the least developed aspect of this thesis is the question of how and why the low density

pumices often appear in the middle and bottom of deposits. A study of the peralkaline pumice textures, perhaps including tomography and more sophisticated measurements of porosity and permeability, could expand this. Building on the work of Wright et al. (2006) and Fauria et al. (2017), an examination of how the tubular/elongate pores saturate and the rate of saturation would provide an interesting point of reference for the Aluto pumices. In the case of the Aluto-specific problem, well-constrained experiments whereby floating samples are subject to surface perturbations (such as waves or vibrations) of varying intensity and timing would help aid understanding of the grading features observed. Indeed, such a study could be useful for a range of low-density eruptions that have produced lake core deposits that appear inconsistent with floating pumice deposits.

6.3. Wider implications

This thesis is part of the NERC RiftVolc project, a consortium which seeks to understand volcanism in the Main Ethiopian Rift, which comprises three work packages. The first, is dedicated to understanding the past of several key volcanic centres. The second, is dedicated to the present state of the centres and includes volcano monitoring, while the third will address the future including producing hazard maps and hazard assessment. My work on Aluto is part of the first work package and will feed into the third work package, which involves the development of probabilistic volcanic hazard assessment for the key volcanic centres, including Aluto.

In this light, perhaps the most crucial finding of this thesis is Aluto's eruption frequency of one eruption every ~250 years. Aluto comprises a wide and comparatively fertile caldera, which is home to many small communities and associated agriculture. The surrounding area is also subject to considerable development, in the form of power plants, vineyards and infrastructure associated with flower-growing for the international cut-flower market. Should the volcano undergo another Vulcanian to sub-Plinian eruption (as indicated in the tephra record), it would pose not only a threat to the lives of those living on the edifice, but also to economic growth of the area and subsequently the livelihoods of many living nearby. As a result, I hope that the information in this thesis will contribute to developing a comprehensive volcanic hazard mitigation plan for the volcano and surrounding area.

References

Abebe, B., Acocella, V., Korme, T., and Ayalew, D. (2007). Quaternary faulting and volcanism in the Main Ethiopian Rift. *Journal of African Earth Sciences*, 48(2-3):115–124.

Abebe, T., Manetti, P., Bonini, M., Corti, G., Innocenti, F., Mazzarini, F., and Pecskay, Z. (2005). Geological map (scale 1: 200,000) of the northern Main Ethiopian Rift and its implication for the volcano-tectonic evolution of the rift. *Geol. Soc. Am. Map Chart Ser., MCH094*.

Adams, N. K., de Silva, S. L., Self, S., Salas, G., Schubring, S., Permenter, J. L., and Arbesman, K. (2001). The physical volcanology of the 1600 eruption of Huaynaputina, southern Peru. *Bulletin of Volcanology*, 62(8):493–518.

Alfano, F., Bonadonna, C., Volentik, A. C. M., Connor, C. B., Watt, S. F. L., Pyle, D. M., and Connor, L. J. (2011). Tephra stratigraphy and eruptive volume of the May, 2008, Chaitén eruption, Chile. *Bulletin of Volcanology*, 73(5):613–630.

Allen, S. R., Fiske, R. S., and Cashman, K. V. (2008). Quenching of steam-charged pumice: Implications for submarine pyroclastic volcanism. *Earth and Planetary Science Letters*, 274(1):40–49.

Aramaki, S. and Lipman, P. (1965). Possible Leaching of Na20 During During Hydration of Volcanic Glasses. *Proceedings of the Japan Academy*, 41(6):467–470.

Arismendi, I., Sanzana, J., and Soto, D. (2011). Seasonal age distributions and maturity stage in a naturalized rainbow trout (Oncorhynchus mykiss Walbaum) population in southern Chile reveal an ad-fluvial life history. *Annales de Limnologie - International Journal of Limnology*, 47(2):133–140.

Armienti, P., Macedonio, G., and Pareschi, M. T. (1988). A numerical model for simulation of tephra transport and deposition: applications to May 18, 1980, Mount St. Helens eruption. *Journal of Geophysical Research*, 93(B6):6463–6476.

Arrighi, S., Principe, C., and Rosi, M. (2004). Violent strombolian and subplinian eruptions at Vesuvius during post-1631 activity. *Bulletin of Volcanology*, 63(2):126–150.

Aspinall, W. P., Auker, M., Hincks, T., Mahony, S., Nadim, F., Pooley, J., Sparks, S., and Syre, E. (2011). Volcano Risk Study Volcano Hazard and Exposure in GFDRR Priority Countries. Technical Report 20100806.

Ayenew, T. (2002). Recent changes in the level of Lake Abiyata, central main Ethiopian Rift. *Hydrological Sciences Journal*, 47(3):493–503.

Bagdassarov, N. and Dingwell, D. (1994). Thermal properties of vesicular rhyolite. *Journal of Volcanology and Geothermal Research*, 60(2):179–191.

Benett, K. D. (1986). Coherent slumping of early postglacial lake sediments at Hall Lake, Ontario, Canada. *Boreas*, 15(3):209–215.

Benvenuti, M., Bonini, M., Tassi, F., Corti, G., Sani, F., Agostini, A., Manetti, P., and Vaselli, O. (2013). Holocene lacustrine fluctuations and deep CO2 degassing in the northeastern Lake Langano basin (Main Ethiopian rift). *Journal of African Earth Sciences*, 77:1–10.

Benvenuti, M., Carnicelli, S., Belluomini, G., Dainelli, N., Di Grazia, S., Ferrari, G. a., Iasio, C., Sagri, M., Ventra, D., Atnafu, B., and Kebede, S. (2002). The Ziway-Shala lake basin (main Ethiopian rift, Ethiopia): A revision of basin evolution with special reference to the Late Quaternary. *Journal of African Earth Sciences*, 35:247–269.

Bertrand, S., Daga, R., Bedert, R., and Fontijn, K. (2014). Deposition of the 2011 - 2012 Cordón Caulle tephra (Chile, 40S) in lake sediments: Implications for tephrochronology and volcanology. *Journal of Geophysical Research : Earth Surface*, 119:2555–2573.

Biass, S. and Bonadonna, C. (2011). A quantitative uncertainty assessment of eruptive parameters derived from tephra deposits: The example of two large eruptions of Cotopaxi volcano, Ecuador. *Bulletin of Volcanology*, 73(1):73–90.

Biass, S., Bonadonna, C., Connor, L., and Connor, C. (2016). TephraProb: a Matlab package for probabilistic hazard assessments of tephra fallout. *Journal of Applied Volcanology*, 5(10):1–16.

Biggs, J., Bastow, I. D., Keir, D., and Lewi, E. (2011). Pulses of deformation reveal frequently recurring shallow magmatic activity beneath the Main Ethiopian Rift. *Geochemistry, Geophysics, Geosystems*, 12(9):1–11.

Blundy, J. and Cashman, K. (2001). Ascent-driven crystallisation of dacite magmas at Mount St Helens, 1980–1986. *Contributions to Mineralogy and Petrology*, 140(6):631–650.

Blundy, J. and Cashman, K. (2005). Rapid decompression-driven crystallization recorded by melt inclusions from Mount St. Helens volcano. *Geology*, 33(10):793–796.

Bonadonna, C., Connor, L., Connor, C. B., and Courtland, L. M. (2010). Tephra2.

Bonadonna, C. and Costa, A. (2012). Estimating the volume of tephra deposits: A new simple strategy. *Geology*, 40(5):415–418.

Bonadonna, C., Ernst, G., and Sparks, R. (1998). Thickness variations and volume estimates of tephra fall deposits: the importance of particle Reynolds number. *Journal of Volcanology and Geothermal Research*, 81(3-4):173–187.

Bonadonna, C., Genco, R., Gouhier, M., Pistolesi, M., Cioni, R., Alfano, F., Hoskuldsson, A., and Ripepe, M. (2011). Tephra sedimentation during the 2010 Eyjafjallajkull eruption (Iceland) from deposit, radar, and satellite observations. *Journal of Geophysical Research: Solid Earth*, 116(12).

Bonadonna, C. and Houghton, B. F. (2005). Total grain-size distribution and volume of tephra-fall deposits. *Bulletin of Volcanology*, 67(5):441–456.

Bonasia, R., Macedonio, G., Costa, A., Mele, D., and Sulpizio, R. (2010). Numerical inversion and analysis of tephra fallout deposits from the 472AD sub-Plinian eruption at Vesuvius (Italy) through a new best-fit procedure. *Journal of Volcanology and Geothermal Research*, 189(3-4):238–246.

Bonini, M., Corti, G., Innocenti, F., Manetti, P., Mazzarini, F., Abebe, T., and Pecskay, Z. (2005). Evolution of the Main Ethiopian Rift in the frame of Afar and Kenya rifts propagation. *Tectonics*, 24(1).

Brendryen, J., Haflidason, H., and Sejrup, H. P. (2010). Norwegian Sea tephrostratigraphy of marine isotope stages 4 and 5 : Prospects and problems for tephrochronology in the North

Atlantic region. *Quaternary Science Reviews*, 29(7-8):847–864.

Bretón, B. P., Campos, P., Tíjaro, R., Medina, E., Sielfeld, W., Vega, C., Feest, P., Guard, S., and Godoy, C. (2006). Bases Técnicas y Ambientales para la Elaboración de un Plan de Manejo y Reglamentación de la Pesca Recreativa en el Río Petrohué y sus Afluentes. Proyecto FIP Nº 2004-32. Technical report, Universidad Artuo Prat.

Bronk Ramsey, C. (2008). Deposition models for chronological records. *Quaternary Science Reviews*, 27(1-2):42–60.

Bronk Ramsey, C. (2009). Dealing with Outliers and Offsets in Radiocarbon Dating. *Radiocarbon*, 51(03):1023–1045.

Bronk Ramsey, C. B. and Lee, S. (2013). Recent and Planned Developments of the Program OxCal. *Radiocarbon*, 55(02):720–730.

Buckland, H. M., Eychenne, J., Rust, A. C., and Cashman, K. V. (2018). Relating the physical properties of volcanic rocks to the characteristics of ash generated by experimental abrasion. *Journal of Volcanology and Geothermal Research*, 349:335–350.

Burden, R. E., Chen, L., and Phillips, J. C. (2013). A statistical method for determining the volume of volcanic fall deposits. *Bulletin of Volcanology*, 75(6):707.

Burden, R. E., Phillips, J. C., and Hincks, T. K. (2011). Estimating volcanic plume heights from depositional clast size. *Journal of Geophysical Research: Solid Earth*, 116(11):1–13.

Bursik, M. (1996). Tephra dispersal, in The Physics of Explosive Eruptions. *Geological Society, London, Special Publications*, 145:15–144.

Bursik, M. (2001). Effect of Wind on the Rise Height of Volcanic Plumes. *Geophysical Research Letters*, 28(18):3621–3624.

Campos, H., Steffen, W., Aguero, G., Parra, O., and Zun iga, L. (1988). Limnological study of Lake Llanquihue (Chile), morphometry, physics, chemistry, plankton and primary productivity. *Arch. Hydrobiol.*, Suppl., 81:37–67.

Carazzo, G. and Jellinek, M. a. (2012). A new view of the dynamics, stability and longevity of volcanic clouds. *Earth and Planetary Science Letters*, 325-326:39–51.

Carey, S. (1997). Influence of convective sedimentation on the formation of widespread tephra fall layers in the deep sea. *Geology*, 25(9):839–842.

Carey, S. and Sparks, R. S. J. (1986). Quantitative models of the fallout and dispersal of tephra from volcanic eruption columns. *Bulletin of Volcanology*, 48(2):109–125.

Carey, S. N. and Schneider, J.-L. (2011). Volcaniclastic Processes and Deposits in the Deep-Sea. *Developments in Sedimentology*, 63:457–515.

Cashman, K. V. (2004). Volatile Controls on Magma Ascent and Eruption. *Geophysical Monograph Series*, 150(19):109–124.

Cashman, K. V. and Fiske, R. (1991). Fallout of Pyroclastic Debris from Submarine Volcanic Eruptions. *Science*, 253(5017):275–280.

Cashman, K. V. and McConnell, S. M. (2005). Multiple levels of magma storage during the 1980 summer eruptions of Mount St. Helens, WA. *Bulletin of Volcanology*, 68(1):57–75.

Cashman, K. V. and Rust, A. C. (2016). Volcanic ash: generation and spatial variations. In Mackie, S., Cashman, K. V., Ricketts, H., Rust, A., and Watson, M., editors, *Volcanic Ash: Hazard Observation*, pages 5–21. Elsevier.

Castruccio, A., Clavero, J., and Rivera, A. (2010). Comparative study of lahars generated by the 1961 and 1971 eruptions of Calbuco and Villarrica volcanoes, Southern Andes of Chile. *Journal of Volcanology and Geothermal Research*, 190:297–311.

Castruccio, A., Clavero, J., Segura, A., Samaniego, P., Roche, O., Le Pennec, J. L., and Droguett, B. (2016). Eruptive parameters and dynamics of the April 2015 sub-Plinian eruptions of Calbuco volcano (southern Chile). *Bulletin of Volcanology*, 78(9).

Cerling, T. E., Brown, F. H., and Bowman, J. R. (1985). Low-temperature alteration of volcanic glass: Hydration, Na K, 18O and Ar mobility. *Chemical Geology*, 52:281–293.

Chalié, F. and Gasse, F. (2002). Late Glacial-Holocene diatom record of water chemistry and lake level change from the tropical East African Rift Lake Abiyata (Ethiopia). *Palaeogeography, Palaeoclimatology, Palaeoecology*, 187:259–283.

Chernet, T., Hart, W. K., Aronson, J. L., and Walter, R. C. (1998). New age constraints on the timing of volcanism and tectonism in the northern Main Ethiopian Riftsouthern Afar transition zone (Ethiopia). *Journal of Volcanology and Geothermal Research*, 80(3-4):267–280.

Cioni, R., D'Oriano, C., and Bertagnini, A. (2008). Fingerprinting ash deposits of small scale eruptions by their physical and textural features. *Journal of Volcanology and Geothermal Research*, 177(1):277–287.

Cioni, R., Pistolesi, M., Bertagnini, A., Bonadonna, C., Hoskuldsson, A., and Scateni, B. (2014). Insights into the dynamics and evolution of the 2010 Eyjafjallajökull summit eruption (Iceland) provided by volcanic ash textures. *Earth and Planetary Science Letters*, 394:111–123.

Clarke, A., Stephens, S., Teasdale, R., Sparks, R., and Diller, K. (2007). Petrologic constraints on the decompression history of magma prior to Vulcanian explosions at the Soufrière Hills volcano, Montserrat. *Journal of Volcanology and Geothermal Research*, 161(4):261–274.

Coltelli, M., Carlo, P. D., and Vezzoli, L. (1998). Discovery of a Plinian basaltic eruption of Roman age at Etna volcano, Italy. *Geology*, 26(12):1095–1098.

Connor, C. B., Sparks, R. S. J., Mason, R. M., Bonadonna, C., and Young, S. R. (2003). Exploring links between physical and probabilistic models of volcanic eruptions: The Soufrière Hills Volcano, Montserrat. *Geophysical Research Letters*, 30(13):1997–2000.

Connor, L. J. and Connor, C. B. (2006). Inversion Is the Key to Dispersion: Understanding Eruption Dynamics by Inverting Tephra Fallout. In *Statistics in Volcanology*, pages 231–242.

Corti, G. (2009). Continental rift evolution: From rift initiation to incipient break-up in the Main Ethiopian Rift, East Africa. *Earth-Science Reviews*, 96(1-2):1–53.

Davies, S. M. (2015). Cryptotephras: The revolution in correlation and precision dating. *Journal of Quaternary Science*, 30(2):114–130.

Davies, S. M., Abbott, P. M., Meara, R. H., Pearce, N. J., Austin, W. E., Chapman, M. R., Svensson, A., Bigler, M., Rasmussen, T. L., Rasmussen, S. O., and Farmer, E. J. (2014). A North Atlantic tephrostratigraphical framework for 13060kab2k: new tephra discoveries, marine-based correlations, and future challenges. *Quaternary Science Reviews*, 106:101–121.

Davies, S. M., Wastegård, S., and Wohlfarth, B. (2003). Extending the limits of the Borrobol Tephra to Scandinavia and detection of new early Holocene tephras. *Quaternary Research*, 59(3):345–352.

Davis, J. O. (1985). Correlation of Late Quaternary Tephra Layers in a Long Pluvial Sequence near Summer Lake, Oregon. *Quaternary Research*, 23(1):38–53.

Dellino, P. and La Volpe, L. (1996). Image processing analysis in reconstructing fragmentation and transportation mechanisms of pyroclastic deposits. The case of Monte Pilato-Rocche Rosse eruptions, Lipari (Aeolian islands, Italy). *Journal of Volcanology and Geothermal Research*, 71(1):13–29.

Di Carlo, I., Rotolo, S. G., Scaillet, B., Buccheri, V., and Pichavant, M. (2010). Phase equilibrium constraints on pre-eruptive conditions of recent felsic explosive volcanism at Pantelleria Island, Italy. *Journal of Petrology*, 51(11):2245–2276.

Di Genova, D., Morgavi, D., Hess, K. U., Neuville, D. R., Borovkov, N., Perugini, D., and Dingwell, D. B. (2015). Approximate chemical analysis of volcanic glasses using Raman spectroscopy. *Journal of Raman Spectroscopy*, 46(12):1235–1244.

Di Genova, D., Romano, C., Hess, K.-U., Vona, A., Poe, B., Giordano, D., Dingwell, D., and Behrens, H. (2013). The rheology of peralkaline rhyolites from Pantelleria Island. *Journal of Volcanology and Geothermal Research*, 249:201–216.

Di Genova, D., Vasseur, J., Hess, K.-U., Neuville, D. R., and Dingwell, D. B. (2017). Effect of oxygen fugacity on the glass transition, viscosity and structure of silica- and iron-rich magmatic melts. *Journal of Non-Crystalline Solids*, 470:78–85.

Di Paola, G. M. (1972). The Ethiopian Rift Valley (between 7 00' and 8 40' lat. north). *Bulletin Volcanologique*, 36(4):517–560.

Di Roberto, A., Smedile, A., Del Carlo, P., De Martini, P. M., Iorio, M., Petrelli, M., Pantosti, D., Pinzi, S., and Todrani, A. (2018). Tephra and cryptotephra in a ˜ 60,000-year-old lacustrine sequence from the Fucino Basin: new insights into the major explosive events in Italy. *Bulletin of Volcanology*, 80(3):20.

Dingwell, D., Hess, K.-U., and Romano, C. (1998). Extremely fluid behavior of hydrous peralkaline rhyolites. *Earth and Planetary Science Letters*, 158(1-2):31–38.

Dufek, J., Manga, M., and Staedter, M. (2007). Littoral blasts: Pumice-water heat transfer and the conditions for steam explosions when pyroclastic flows enter the ocean. *Journal of Geophysical Research: Solid Earth*, 112(11):1–16.

Eaton, G. P. (1963). Volcanic ash deposits as a guide to atmospheric circulation in the geologic past. *Journal of Geophysical Research*, 68(2):521–528.

Ebinger, C. and Casey, M. (2001). Continental breakup in magmatic provinces : An Ethiopian example. *Geology*, 29(6):527–530.

Engwell, S. L., Sparks, R. S. J., and Carey, S. (2014). Physical characteristics of tephra layers in the deep sea realm: the Campanian Ignimbrite eruption. *Marine Tephrochronology*, 398:47–64.

Fauria, K. E. and Manga, M. (2018). Pyroclast cooling and saturation in water. *Journal of Volcanology and Geothermal Research*, page (in press).

Fauria, K. E., Manga, M., and Wei, Z. (2017). Trapped bubbles keep pumice afloat and gas diffusion makes pumice sink. *Earth and Planetary Science Letters*, 460:50–59.

Fierstein, J. (2007). Explosive eruptive record in the Katmai region, Alaska Peninsula: an overview. *Bulletin of Volcanology*, 69(5):469–509.

Fierstein, J. and Nathenson, M. (1992). Another look at the calculation of fallout tephra volumes. *Bulletin of Volcanology*, 54(2):156–167.

Fiske, R. S., Naka, J., Iizasa, K., Makoto, T., and Klaus, A. (2001). Submarine silicic caldera

at the front of the Izu-Bonin arc, Japan: Voluminous seafloor eruptions of rhyolite pumice. *Geological Society of America Bulletin*, 113(7):813–824.

Fontijn, K., Costa, F., Sutawidjaja, I., Newhall, C. G., and Herrin, J. S. (2015). A 5000-year record of multiple highly explosive mafic eruptions from Gunung Agung (Bali, Indonesia): implications for eruption frequency and volcanic hazards. *Bulletin of Volcanology*, 77(7).

Fontijn, K., Ernst, G. G. J., Bonadonna, C., Elburg, M. A., Mbede, E., and Jacobs, P. (2011). The 4-ka Rungwe Pumice (South-Western Tanzania): a wind-still Plinian eruption. *Bulletin of Volcanology*, 73(9):1353–1368.

Fontijn, K., Lachowycz, S. M., Rawson, H., Pyle, D. M., Mather, T. A., Naranjo, J. A., and Moreno-Roa, H. (2014). Late Quaternary tephrostratigraphy of southern Chile and Argentina. *Quaternary Science Reviews*, 89:70–84.

Fontijn, K., McNamara, K., Tadesse, A. Z., Pyle, D. M., Dessalegn, F., Hutchison, W., Mather, T. A., and Yirgu, G. (2018). Contrasting styles of post-caldera volcanism along the Main Ethiopian Rift: Implications for contemporary volcanic hazards. *Journal of Volcanology and Geothermal Research*, 356:90–113.

Fontijn, K., Rawson, H., Van Daele, M., Moernaut, J., Abarzúa, A. M., Heirman, K., Bertrand, S., Pyle, D. M., Mather, T. A., De Batist, M., Naranjo, J.-A., and Moreno, H. (2016). Synchronisation of sedimentary records using tephra: A postglacial tephrochronological model for the Chilean Lake District. *Quaternary Science Reviews*, 137:234–254.

Frick, C. and Kent, L. E. (1984). Drift pumice in the Indian and South Atlantic oceans. *Transactions of the Geological Society of South Africa*, 87(1):19–33.

Gasparon, M., Innocenti, F., Manetti, P., Peccerillo, A., and Tsegaye, A. (1993). Genesis of the pliocene to recent bimodal mafic-felsic volcanism in the Debre Zeyt area, central Ethiopia: volcanological and geochemical constraints. *Journal of African Earth Sciences (and the Middle East)*, 17(2):145–165.

Gasse, E. and Street, F. A. (1978). Late Quaternary Lake-level fluctuations and environments of the northern Rift valley and Afar region (Ethiopia and Djibouti). *Palaeogeography, Palaeoclimatology, Palaeoecology*, 24(4).

Geschwind, C. H. and Rutherford, M. J. (1995). Crystallization of microlites during magma ascent: the fluid mechanics of 1980-1986 eruptions at Mount St Helens. *Bulletin of Volcanology*, 57(5):356–370.

Gianelli, G. and Teklemariam, M. (1993). Water-rock interaction processes in the Aluto-Langano geothermal field (Ethiopia). *Journal of Volcanology and Geothermal Research*, 56(4):429–445.

Gibert, E., Travi, Y., Massault, M., Chernet, T., Barbecot, F., and Laggoun-Defarge, F. (1999). Comparing Carbonate and Organic Ams-14C Ages in Lake Abiyata Sediments (Ethiopia): Hydrochemistry and Paleoenvironmental Implications. *Radiocarbon*, 41(03):271–286.

Gibert, E., Travi, Y., Massault, M., Tiercelin, J.-J., and Chernet, T. (2002). Ams-14C Chronology of a Lacustrine Sequence from Lake Langano (Main Ethiopian Rift): Correction and Validation Steps in Relation with Volcanism, Lake Water and Carbon Balances. *Radiocarbon*, 44(1):75–92.

Gilbert, D., Freundt, A., Kutterolf, S., and Burkert, C. (2014). Post-glacial time series of explosive eruptions and associated changes in the magma plumbing system of Lonquimay volcano, south central Chile. *International Journal of Earth Sciences*, 103(7):2043–2062.

Gleeson, M. L. M., Stock, M. J., Pyle, D. M., Mather, T. A., Hutchison, W., Yirgu, G., and Wade, J. (2017). Constraining magma storage conditions at a restless volcano in the Main Ethiopian Rift using phase equilibria models. *Journal of Volcanology and Geothermal Research*, 337:44–61.

Green, R. M., Bebbington, M. S., Jones, G., Cronin, S. J., and Turner, M. B. (2016). Estimation of tephra volumes from sparse and incompletely observed deposit thicknesses. *Bulletin of Volcanology*, 78(4):25.

Haflidason, H., Eiriksson, J., and Van Kreveld, S. (2000). The tephrochronology of Iceland and the North Atlantic region during the Middle and Late Quaternary: a review. *Journal of Quaternary Science*, 15(1):3–22.

Hammer, J. E., Cashman, K. V., Hoblitt, R. P., and Newman, S. (1999). Degassing and microlite crystallization during pre-climactic events of the 1991 eruption of Mt. Pinatubo, Philippines. *Bulletin of Volcanology*, 60(5):355–380.

Hardee, H. (1981). Thermal property measurements in a fresh pumice flow at Mt. St. Helens. *Geophysical Research Letters*, 8(3):210–212.

Henderson, C. M. B. and Pierozynski, W. J. (2012). An experimental study of Sr, Ba and Rb partitioning between alkali feldspar and silicate liquid in the system nephelinekalsilitequartz at 0.1 GPa P(H2O): a revisitation and reassessment. *Mineralogical Magazine*, 76(1):157–190.

Herschy, R. W. (2012). *World Lake Database: International Lake Environment Committee Foundation (ILEC)*, pages 920–921. Springer Netherlands, Dordrecht.

Hess, K. U., Dingwell, D. B., and Webb, S. L. (1995). The influence of excess alkalis on the viscosity of a haplogranitic melt. *American Mineralogist*, 80(3-4):297–304.

Hickey-Vargas, R., Abdollahi, M. J., Parada, M. A., López-Escobar, L., and Frey, F. A. (1995). Crustal xenoliths from Calbuco Volcano, Andean Southern Volcanic Zone: implications for crustal composition and magma-crust interaction. *Contributions to Mineralogy and Petrology*, 119(4):331–344.

Hildreth, W. and Drake, R. E. (1992). Volcán Quizapu, Chilean Andes. *Bulletin of Volcanology*, 54(2):93–125.

Ho, C.-H. (1996). Volcanic time-trend analysis. *Journal of Volcanology and Geothermal Research*, 74(3-4):171–177.

Horrocks, M., Augustinus, P., Deng, Y., Shane, P., and Andersson, S. (2005). Holocene vegetation, environment, and tephra recorded from Lake Pupuke, Auckland, New Zealand. *New Zealand Journal of Geology and Geophysics*, 48(1):85–94.

Houghton, B. and Wilson, C. (1989). A vesicularity index for pyroclastic deposits. *Bulletin of Volcanology*, 51(6):451–462.

Houghton, B. F., Weaver, S. D., Wilson, C. J., and Lanphere, M. A. (1992). Evolution of a Quaternary peralkaline volcano: Mayor Island, New Zealand. *Journal of Volcanology and Geothermal Research*, 51(3):217–236.

Hughes, E. C., Neave, D. A., Dobson, K. J., Withers, P. J., and Edmonds, M. (2017). How to fragment peralkaline rhyolites: Observations on pumice using combined multi-scale 2D and 3D imaging. *Journal of Volcanology and Geothermal Research*, 336:179–191.

Hutchison, W., Biggs, J., Mather, T. A., Pyle, D. M., Lewi, E., Yirgu, G., Caliro, S., Chiodini, G., Clor, L. E., and Fischer, T. P. (2016a). Causes of unrest at silicic calderas in the East African Rift: New constraints from InSAR and soil-gas chemistry at Aluto volcano, Ethiopia.

Geochemistry, Geophysics, Geosystems, 17(8):3008–3030.

Hutchison, W., Fusillo, R., Pyle, D. M., Mather, T. A., Blundy, J. D., Biggs, J., Yirgu, G., Cohen, B. E., Brooker, R. A., Barfod, D. N., and Calvert, A. T. (2016b). A pulse of mid-Pleistocene rift volcanism in Ethiopia at the dawn of modern humans. *Nature Communications*, 7(13192).

Hutchison, W., Pyle, D. M., Mather, T. A., Yirgu, G., Biggs, J., Cohen, B. E., Barfod, D. N., and Lewi, E. (2016c). The eruptive history and magmatic evolution of Aluto volcano: new insights into silicic peralkaline volcanism in the Ethiopian rift. *Journal of Volcanology and Geothermal Research*, 328:9–33.

Jacobs, C. T., Collins, G. S., Piggott, M. D., Kramer, S. C., and Wilson, C. R. G. (2013). Multiphase flow modelling of volcanic ash particle settling in water using adaptive unstructured meshes. *Geophysical Journal International*, 192(2):647–665.

Jacobs, C. T., Goldin, T. J., Collins, G. S., Piggott, M. D., Kramer, S. C., Melosh, H. J., Wilson, C. R. G., and Allison, P. A. (2015). An improved quantitative measure of the tendency for volcanic ash plumes to form in water: Implications for the deposition of marine ash beds. *Journal of Volcanology and Geothermal Research*, 290:114–124.

Jochum, K. P., Weis, U., Schwager, B., Stoll, B., Wilson, S. A., Haug, G. H., Andreae, M. O., and Enzweiler, J. (2016). Reference Values Following ISO Guidelines for Frequently Requested Rock Reference Materials. *Geostandards and Geoanalytical Research*, 40(3):333–350.

Johnston, E. N., Phillips, J. C., Bonadonna, C., and Watson, I. M. (2012). Reconstructing the tephra dispersal pattern from the Bronze Age eruption of Santorini using an advectiondiffusion model. *Bulletin of Volcanology*, 74(6):1485–1507.

Jones, T. J., McNamara, K., Eychenne, J., Rust, A. C., Cashman, K. V., Scheu, B., and Edwards, R. (2016). Primary and secondary fragmentation of crystal-bearing intermediate magma. *Journal of Volcanology and Geothermal Research*, 327:70–83.

Kalnay, E., Kanamitsu, R., Kistler, R., Collins, W., Deaven, D., Gandin, L., Iredell, M., Saha, S., White, G., Woollen, J., Zhu, Y., A., Leetmaa, Reynolds, R., Chelliah, M., Ebisuzaki, W., Higgins, W., Janowiak, J., Mo, K., Ropelewski, C., Wang, J., Jenne, R., and Joseph, D. (1996). The NCEP/NCAR 40-Year Reanalysis Project. *Bulletin of the American Meteorological Soceity*, 77:437–471.

Kamzin, V., Berhe, S. M., Nicoletti, M., and Petrucciana, C. (1980). Evolution of the northerm part of the Ethiopian Rift. *Atti Convegni Lincei*, 47:275–291.

Kato, Y. (1987). Woody pumice generated with submarine eruption. *The Journal of the Geological Society of Japan*, 93(1):11–20_2.

Keir, D., Bastow, I. D., Corti, G., Mazzarini, F., and Rooney, T. O. (2015). The origin of along-rift variations in faulting and magmatism in the Ethiopian Rift. *Tectonics*, 34(3):464–477.

Kiipli, T., Hints, R., Kallaste, T., Verš, E., and Voolma, M. (2017). Immobile and mobile elements during the transition of volcanic ash to bentonite An example from the early Palaeozoic sedimentary section of the Baltic Basin. *Sedimentary Geology*, 347:148–159.

Klug, C. and Cashman, K. V. (1994). Vesiculation of May 18, 1980, Mount St. Helens magma. *Geology*, 22(5):468–472.

Klug, C. and Cashman, K. V. (1996). Permeability development in vesiculating magmas: implications for fragmentation. *Bulletin of Volcanology*, 58(2):87–100.

Kratzmann, D. J., Carey, S. N., Fero, J., Scasso, R. A., and Naranjo, J.-A. (2010). Simulations of tephra dispersal from the 1991 explosive eruptions of Hudson volcano, Chile. *Journal of*

Volcanology and Geothermal Research, 190(3-4):337–352.

Kuehn, S. C. and Foit, F. F. (2006). Correlation of widespread Holocene and Pleistocene tephra layers from Newberry Volcano , Oregon , USA , using glass compositions and numerical analysis. *Quaternary International*, 148(1):113–137.

Kuehn, S. C. and Negrini, R. M. (2010). A 250 k.y. record of Cascade arc pyroclastic volcanism from late Pleistocene lacustrine sediments near Summer Lake, Oregon, USA. *Geosphere*, 6(4):397.

Lamb, A. L., Leng, M. J., Lamb, H. F., Telford, R. J., and Mohammed, M. U. (2002). Climatic and non-climatic effects on the δ18O and δ13C compositions of Lake Awassa, Ethiopia, during the last 6.5 ka. *Quaternary Science Reviews*, 21(20-22):2199–2211.

Lane, C., Cullen, V., White, D., Bramham-Law, C., and Smith, V. (2014). Cryptotephra as a dating and correlation tool in archaeology. *Journal of Archaeological Science*, 42:42–50.

Lane, C. S., Chorn, B. T., and Johnson, T. C. (2013). Ash from the Toba supereruption in Lake Malawi shows no volcanic winter in East Africa at 75 ka. *Proceedings of the National Academy of Sciences*, 110(20):8025 – 8029.

Le Turdu, C., Tiercelin, J.-J., Gibert, E., Travi, Y., Lezzar, K.-E., Richert, J.-P., Massault, M., Gasse, F., Bonnefille, R., Decobert, M., Gensous, B., Jeudy, V., Tamrat, E., Mohammed, M. U., Martens, K., Atnafu, B., Chernet, T., Williamson, D., and Taieb, M. (1999). The ZiwayShala lake basin system, Main Ethiopian Rift: Influence of volcanism, tectonics, and climatic forcing on basin formation and sedimentation. *Palaeogeography, Palaeoclimatology, Palaeoecology*, 150(3-4):135–177.

Ledbetter, M. T. and Sparks, R. S. J. (1979). Duration of large-magnitude explosive eruptions deduced from graded bedding in deep-sea ash layers. *Geology*, 7(5):240–244.

Legros, F. (2000). Minimum volume of a tephra fallout deposit estimated from a single isopach. *Journal of Volcanology and Geothermal Research*, 96(1):25–32.

Liu, E., Oliva, M., Antoniades, D., Giralt, S., Granados, I., Pla-Rabes, S., Toro, M., and Geyer, A. (2016). Expanding the tephrostratigraphical framework for the South Shetland Islands, Antarctica, by combining compositional and textural tephra characterisation. *Sedimentary Geology*, 340:49–61.

Liu, E. J., Cashman, K. V., Rust, a. C., and Gislason, S. R. (2015). The role of bubbles in generating fine ash during hydromagmatic eruptions. *Geology*, 43(3):239–243.

Liu, E. J., Cashman, K. V., Rust, A. C., and Höskuldsson, A. (2017). Contrasting mechanisms of magma fragmentation during coeval magmatic and hydromagmatic activity: the Hverfjall Fires fissure eruption, Iceland. *Bulletin of Volcanology*, 79(10):68.

Lloyd, R., Biggs, J., Wilks, M., Nowacki, A., Kendall, J.-M., Ayele, A., Lewi, E., and Eysteinsson, H. (2018). Evidence for cross rift structural controls on deformation and seismicity at a continental rift caldera. *Earth and Planetary Science Letters*, 487:190–200.

Longchamp, C., Bonadonna, C., Bachmann, O., and Skopelitis, A. (2011). Characterization of tephra deposits with limited exposure: The example of the two largest explosive eruptions at Nisyros volcano (Greece). *Bulletin of Volcanology*, 73(9):1337–1352.

Lopez-Escobar, L., Parada, M., Hickey-Vargas, R., Frey, F., Kempton, P. D., and Moreno, H. (1995). Calbuco Volcano and minor eruptive centers distributed along the Liquine-Ofqui Fault Zone, Chile (41o- 42oS): contrasting origin of andesitic and basaltic magma in the Southern Volcanic Zone of the Andes. *Contributions to Mineralogy and Petrology*, 119(1):134–141.

Lopez-Escobar, L., Parada, M., Moreno, H., Frey, F., and Hickey-Vargas, R. (1992). A contribution to the petrogenesis of Osorno and Calbuco volcanoes, Southern Andes (41˜176 ' S): comparative study. *Rev Geol Chile*, 19:211–226.

Lowe, D. J. (2011). Quaternary Geochronology Tephrochronology and its application : A review. *Quaternary Geochronology*, 6(2):107–153.

Lowe, D. J., Shane, P. A., Alloway, B. V., and Newnham, R. M. (2008). Fingerprints and age models for widespread New Zealand tephra marker beds erupted since 30,000 years ago: a framework for NZ-INTIMATE. *Quaternary Science Reviews*, 27(1-2):95–126.

Maeno, F., Nagai, M., Nakada, S., Burden, R. E., Engwell, S., Suzuki, Y., and Kaneko, T. (2014). Constraining tephra dispersion and deposition from three subplinian explosions in 2011 at Shinmoedake volcano, Kyushu, Japan. *Bulletin of Volcanology*, 76(6):823.

Mangerud, J., Lie, S. E., Furnes, H., Kristiansen, I. L., and Lømo, L. (1984). A Younger Dryas Ash Bed in western Norway, and its possible correlations with tephra in cores from the Norwegian Sea and the North Atlantic. *Quaternary Research*, 21(1):85–104.

Mannen, K. (2014). Particle segregation of an eruption plume as revealed by a comprehensive analysis of tephra dispersal: Theory and application. *Journal of Volcanology and Geothermal Research*, 284:61–78.

Manville, V., White, J., Houghton, B., and Wilson, C. (1998). The saturation behaviour of pumice and some sedimentological implications. *Sedimentary Geology*, 119(1-2):5–16.

Manville, V. and Wilson, C. J. N. (2004). Vertical density currents : a review of their potential role in the deposition and interpretation of deep-sea ash layers. *Journal of the Geological Soceity*, 161:947–958.

Marsh, B. D. (1988). Crystal capture, sorting, and retention in convecting magma. *Bulletin of the Geological Society of America*, 100(11):1720–1737.

Martin-Jones, C. M., Lane, C. S., G Pearce, N. J., Smith, V. C., Lamb, H. F., Schaebitz, F., Brown, M. C., Frank, U., and Asrat, A. (2017). Recurrent explosive eruptions from a high - risk Main Ethiopian Rift volcano throughout the Holocene. *Geology*, 45(12):1127–1130.

Marzocchi, W. and Bebbington, M. S. (2012). Probabilistic eruption forecasting at short and long time scales. *Bulletin of Volcanology*, 74:1777–1805.

Matthews, N. E., Smith, V. C., Costa, A., Durant, A. J., Pyle, D. M., and Pearce, N. J. (2012). Ultra-distal tephra deposits from super-eruptions: Examples from Toba, Indonesia and Taupo Volcanic Zone, New Zealand. *Quaternary International*, 258:54–79.

Mazzarini, F., Corti, G., Manetti, P., and Innocenti, F. (2004). Strain rate and bimodal volcanism in the continental rift: Debre Zeyt volcanic field, northern MER, Ethiopia. *Journal of African Earth Sciences*, 39(3-5):415–420.

McNamara, K., Cashman, K. V., Rust, A. C., Fontijn, K., Chalié, F., Tomlinson, E., and Yirgu, G. (2018). Using lake sediment cores to improve records of Volcanism at Aluto Volcano in the Main Ethiopian Rift. *Geochemistry, Geophysics, Geosystems*, (in press).

Melnik, O. and Sparks, R. S. (1999). Nonlinear dynamics of lava dome extrusion. *Nature*, 402(6757):37–41.

Miwa, T., Geshi, N., and Shinohara, H. (2013). Temporal variation in volcanic ash texture during a vulcanian eruption at the Sakurajima volcano, Japan. *Journal of Volcanology and Geothermal Research*, 260:80–89.

Miyabuchi, Y., Hanada, D., Niimi, H., and Kobayashi, T. (2013). Stratigraphy, grain-size and component characteristics of the 2011 Shinmoedake eruption deposits, Kirishima Volcano, Japan. *Journal of Volcanology and Geothermal Research*, 258:31–46.

Mohr, P., Mitchell, J. G., and Raynolds, R. G. H. (1980). Quaternary volcanism and faulting at O'A caldera, central ethiopian rift. *Bulletin Volcanologique*, 43(1):173–189.

Mohr, P. A. (1966). Chahbi Volcano (Ethiopia). *Bulletin Volcanologique*, pages 797–815.

Mohr, P. A. (1971). Ethiopian rift and plateaus: Some volcanic petrochemical differences. *Journal of Geophysical Research*, 76(8):1967–1984.

Mohr, P. A. and Wood, C. A. (1976). Volcano spacings and lithospheric attenuation in the Eastern Rift of Africa. *Earth and Planetary Science Letters*, 33(1):126–144.

Moreno, P. I., Alloway, B. V., Villarosa, G., Outes, V., Henríquez, W. I., Pol-Holz, R. D., and Pearce, N. J. G. (2015). A past-millennium maximum in postglacial activity from Volcán Chaitén, southern Chile. *Geology*, 43(1):47–50.

Nakada, S., Nagai, M., Kaneko, T., Suzuki, Y., and Maeno, F. (2013). The outline of the 2011 eruption at Shinmoe-dake (Kirishima), Japan. *Earth, Planets and Space*, 65(6):475–488.

Neave, D. A., Fabbro, G., Herd, R. A., Petrone, C. M., and Edmonds, M. (2012). Melting, differentiation and degassing at the pantelleria volcano, Italy. *Journal of Petrology*, 53(3):637–663.

Ninkovich, D. and Shackleton, N. (1975). Distribution, stratigraphic position and age of ash layer L, in the Panama Basin region. *Earth and Planetary Science Letters*, 27(1):20–34.

Noguchi, S., Toramaru, A., and Shimano, T. (2006). Crystallization of microlites and degassing during magma ascent: Constraints on the fluid mechanical behavior of magma during the Tenjo Eruption on Kozu Island, Japan. *Bulletin of Volcanology*, 68(5):432–449.

Orsi, G., Ruvo, L., and Scarpati, C. (1989). The Serra della Fastuca Tephra at Pantelleria: Physical parameters for an explosive eruption of peralkaline magma. *Journal of Volcanology and Geothermal Research*, 39(1):55–60.

Oxburgh, E. and Turcotte, D. (1974). Membrane tectonics and the East African Rift. *Earth and Planetary Science Letters*, 22(2):133–140.

Peccerillo, A., Barberio, M., Yirgu, G., Ayalew, D., Barbieri, M., and Wu, T. U. (2003). Relationships between Mafic and Peralkaline Silicic Magmatism in Continental Rift Settings: a Petrological, Geochemical and Isotopic Study of the Gedemsa Volcano, Central Ethiopian Rift. *Journal of Petrology*, 44(11):2003–2032.

Pfeiffer, T., Costa, A., and Macedonio, G. (2005). A model for the numerical simulation of tephra fall deposits. *Journal of Volcanology and Geothermal Research*, 140(4):273–294.

Pik, R., Deniel, C., Coulon, C., Yirgu, G., Hofmann, C., and Ayalew, D. (1998). The northwestern Ethiopian Plateau flood basalts: Classification and spatial distribution of magma types. *Journal of Volcanology and Geothermal Research*, 81(1-2):91–111.

Pistolesi, M., Cioni, R., Bonadonna, C., Elissondo, M., Baumann, V., Bertagnini, A., Chiari, L., Gonzales, R., Rosi, M., and Francalanci, L. (2015). Complex dynamics of small-moderate volcanic events: the example of the 2011 rhyolitic Cordón Caulle eruption, Chile. *Bulletin of Volcanology*, 77(1):3.

Placzek, C., Quade, J., Rech, J. A., Patchett, P. J., and Pe, C. (2009). Quaternary Geochronology Geochemistry , chronology and stratigraphy of Neogene tuffs of the Central Andean region.

Quaternary Geochronology, 4(1):22–36.

Ponomareva, V., Portnyagin, M., and Davies, S. M. (2015). Tephra without Borders: Far-Reaching Clues into Past Explosive Eruptions .

Pyle, D. M. (1989). The thickness, volume and grainsize of tephra fall deposits. *Bulletin of Volcanology*, 51(1):1–15.

Pyle, D. M., Ricketts, G. D., Margari, V., van Andel, T. H., Sinitsyn, A. A., Praslov, N. D., and Lisitsyn, S. (2006). Wide dispersal and deposition of distal tephra during the Pleistocene Campanian Ignimbrite/Y5' eruption, Italy. *Quaternary Science Reviews*, 25(21-22):2713–2728.

Rapprich, V., Žáček, V., Verner, K., Erban, V., Goslar, T., Bekele, Y., Legesa, F., Hroch, T., and Hejtmánková, P. (2016). Wendo Koshe Pumice: The latest Holocene silicic explosive eruption product of the Corbetti Volcanic System (Southern Ethiopia). *Journal of Volcanology and Geothermal Research*, 310:159–171.

Rawson, H., Naranjo, J. A., Smith, V. C., Fontijn, K., Pyle, D. M., Mather, T. A., and Moreno, H. (2015). The frequency and magnitude of post-glacial explosive eruptions at Volcán Mocho-Choshuenco, southern Chile. *Journal of Volcanology and Geothermal Research*, 299:103–129.

Recktenwald, G. (2010). Transient Conduction in a Sphere with Convective Boundary Conditions. *http://web.cecs.pdx.edu/˜gerry/heatAnimations/sphereTransient/*.

Reimer, P. J., Bard, E., Bayliss, A., Beck, J. W., Blackwell, P. G., Ramsey, C. B., Buck, C. E., Cheng, H., Edwards, R. L., Friedrich, M., Grootes, P. M., Guilderson, T. P., Haflidason, H., Hajdas, I., Hatté, C., Heaton, T. J., Hoffmann, D. L., Hogg, A. G., Hughen, K. A., Kaiser, K. F., Kromer, B., Manning, S. W., Niu, M., Reimer, R. W., Richards, D. A., Scott, E. M., Southon, J. R., Staff, R. A., Turney, C. S. M., and van der Plicht, J. (2013). IntCal13 and Marine13 Radiocarbon Age Calibration Curves 050,000 Years cal BP. *Radiocarbon*, 55(04):1869–1887.

Rhoades, D. A., Dowrick, D. J., and Wilson, C. J. N. (2002). Volcanic Hazard in New Zealand : Scaling and Attenuation Relations for Tephra fall deposits from Taupo Volcano. *Natural Hazards*, 26:147–174.

Riggs, N. R., Ort, M., White, J., Wilson, C. J. N., Houghton, B., and Clarkson, R. (2009). Post1.8ka Marginal Sedimentation in Lake Taupo, New Zealand: Effects of Wave Energy and Sediment Supply in a Rapidly Rising Lake. In *Volcaniclastic Sedimentation in Lacustrine Settings, 1*, pages 151–177. Blackwell Science Ltd, Oxford, 30 edition.

Romero, J. E., Morgavi, D., Arzilli, F., Daga, R., Caselli, A., Reckziegel, F., Viramonte, J., Díaz-Alvarado, J., Polacci, M., Burton, M., and Perugini, D. (2016). Eruption dynamics of the 22-23 April 2015 Calbuco Volcano (Southern Chile): Analyses of tephra fall deposits. *Journal of Volcanology and Geothermal Research*, 317:15–29.

Rooney, T. O., Furman, T., Yirgu, G., and Ayalew, D. (2005). Structure of the Ethiopian lithosphere: Xenolith evidence in the Main Ethiopian Rift. *Geochimica et Cosmochimica Acta*, 69(15):3889–3910.

Rose, W. and Durant, A. (2009). Fine ash content of explosive eruptions. *Journal of Volcanology and Geothermal Research*, 186(1-2):32–39.

Rose, W. I. and Chesner, C. A. (1987). Dispersal of ash in the great Toba eruption, 75 ka. *Geology*, 15(10):913–917.

Rust, A. and Cashman, K. (2004). Permeability of vesicular silicic magma: inertial and hysteresis effects. *Earth and Planetary Science Letters*, 228(1-2):93–107.

Samrock, F., Kuvshinov, A., Bakker, J., Jackson, A., and Fisseha, S. (2015). 3-D analysis and interpretation of magnetotelluric data from the Aluto-Langano geothermal field, Ethiopia. *Geophysical Journal International*, 202(3):1923–1948.

Scaillet, B. and MacDonald, R. A. Y. (2001). Phase Relations of Peralkaline Silicic Magmas and Petrogenetic Implications. *Journal of Petrology*, 42(4):825–845.

Scarpati, C., Cole, P., and Perrotta, A. (1993). The Neapolitan Yellow Tuff — A large volume multiphase eruption from Campi Flegrei, Southern Italy. *Bulletin of Volcanology*, 55(5):343–356.

Scarpati, C., Sparice, D., and Perrotta, A. (2014). A crystal concentration method for calculating ignimbrite volume from distal ash-fall deposits and a reappraisal of the magnitude of the Campanian Ignimbrite. *Journal of Volcanology and Geothermal Research*, 280:67–75.

Schindelin, J., Arganda-Carreras, I., Frise, E., Kaynig, V., Longair, M., Pietzsch, T., Preibisch, S., Rueden, C., Saalfeld, S., Schmid, B., Tinevez, J.-Y., White, D. J., Hartenstein, V., Eliceiri, K., Tomancak, P., and Cardona, A. (2012). Fiji: an open-source platform for biological-image analysis. *Nature Methods*, 9(7):676–682.

Schmincke, H. U. (1974). Volcanological aspects of peralkaline silicic welded ash-flow tuffs. *Bulletin Volcanologique*, 38(2):594–636.

Scollo, S., Del Carlo, P., and Coltelli, M. (2007). Tephra fallout of 2001 Etna flank eruption: Analysis of the deposit and plume dispersion. *Journal of Volcanology and Geothermal Research*, 160(1-2):147–164.

Segura, A., Castruccio, A., Clavero, J., Pennec, J. L. L., Roche, O., Samaniego, P., Droguett, B., and Romero, J. (2015). Fallout deposits of the 22-23 April 2015 eruption of Calbuco volcano, Southern Andes. *Impacto de las Geosciencias en la sociedad*, pages 182–184.

Selles, D. and Moreno, H. (2011). Geología del volcán Calbuco, Región de los Lagos. Servicio Nacional de Geología y Minería. *Carta Geológica de Chile*.

Shane, P., Black, T., Eggins, S., and Westgate, J. (1998). Late Miocene marine tephra beds: Recorders of rhyolitic volcanism in North Island, New Zealand. *New Zealand Journal of Geology and Geophysics*, 41(2):165–178.

Shane, P., Sikes, E., and Guilderson, T. (2006). Tephra beds in deep-sea cores off northern New Zealand: implications for the history of Taupo Volcanic Zone, Mayor Island and White Island volcanoes. *Journal of Volcanology and Geothermal Research*, 154(3):276–290.

Shane, P. and Smith, I. (2000). Geochemical fingerprinting of basaltic tephra deposits in the Auckland Volcanic Field. *New Zealand Jounrla of Geology and Geophysics 2000*, 43:569–577.

Sheldrake, T., Sparks, R., Cashman, K., Wadge, G., and Aspinall, W. (2016). Similarities and differences in the historical records of lava dome-building volcanoes: Implications for understanding magmatic processes and eruption forecasting. *Earth-Science Reviews*, 160:240–263.

Smith, V. C., Matthews, N. E., Westgate, J. A., Petraglia, M. D., Haslam, M., Lane, C. S., Korisettar, R., and Pal, J. (2011). Geochemical fingerprinting of the widespread Toba tephra using biotite compositions. *Quaternary International*, 246(1-2):97–104.

Smith, V. C., Staff, R. A., Blockley, S. P., Bronk Ramsey, C., Nakagawa, T., Mark, D. F.,

Takemura, K., and Danhara, T. (2013). Identification and correlation of visible tephras in the Lake Suigetsu SG06 sedimentary archive, Japan: chronostratigraphic markers for synchronising of east Asian/west Pacific palaeoclimatic records across the last 150ka. *Quaternary Science Reviews*, 67:121–137.

Sparks, R. (1997). Causes and consequences of pressurisation in lava dome eruptions. *Earth and Planetary Science Letters*, 150(3-4):177–189.

Sparks, R., Wilson, L., and Sigurdsson, H. (1981). The pyroclastic deposits of the 1875 eruption of Askja, Iceland. *Philosophical Transactions of the Royal Society of London. Series A, Mathematical and Physical Sciences*, 299(1447):241 – 273.

Stern, C. R. (2008). Holocene tephrochronology record of large explosive eruptions in the southernmost Patagonian Andes. *Bulletin of Volcanology*, 70(4):435–454.

Stewart, M. L. and Pearce, T. H. (2004). Sieve-textured plagioclase in dacitic magma: Interference imaging results. *American Mineralogist*, 89(2-3):348–351.

Strager, M. P., Petty, J. T., Strager, J. M., and Barker-Fulton, J. (2009). A spatially explicit framework for quantifying downstream hydrologic conditions. *Journal of Environmental Management*, 90(5):1854–1861.

Stroberg, T. W., Manga, M., and Dufek, J. (2010). Heat transfer coefficients of natural volcanic clasts. *Journal of Volcanology and Geothermal Research*, 194(4):214–219.

Suzuki, T. (1983). A Theoretical Model for Dispersion of Tephra.

Swanson, S. E., Naney, M. T., Westrich, H. R., and Eichelberger, J. C. (1989). Crystallization history of Obsidian Dome, Inyo Domes, California. *Bulletin of Volcanology*, 51(3):161–176.

Szramek, L., Gardner, J. E., and Larsen, J. (2006). Degassing and microlite crystallization of basaltic andesite magma erupting at Arenal Volcano, Costa Rica. *Journal of Volcanology and Geothermal Research*, 157(1-3):182–201.

Tait, S., Thomas, R., Gardner, J., and Jaupart, C. (1998). Constraints on cooling rates and permeabilities of pumice in an explosive eruption jet from colour and magnetic mineralogy. *Journal of Volcanology and Geothermal Research*, 86(1):79–91.

Thompson, R., Bradshaw, R. H. W., and Whitley, J. E. (1986). The distribution of ash in Icelandic lake sediments and the relative importance of mixing and erosion processes. *Journal of Quaternary Science*, 1(1):3–11.

Trua, T., Deniel, C., and Mazzuoli, R. (1999). Crustal control in the genesis of Plio-Quaternary bimodal magmatism of the Main Ethiopian Rift (MER): geochemical and isotopic (Sr, Nd, Pb) evidence. *Chemical Geology*, 155(3-4):201–231.

Tryon, C. A., Roach, N. T., and Logan, M. A. V. (2008). The Middle Stone Age of the northern Kenyan Rift : age and context of new archaeological sites from the Kapedo Tuffs. *Journal of human evolution*, 55:652–664.

Van Daele, M., Moernaut, J., Doom, L., Boes, E., Fontijn, K., Heirman, K., Vandoorne, W., Hebbeln, D., Pino, M., Urrutia, R., Brümmer, R., and De Batist, M. (2015). A comparison of the sedimentary records of the 1960 and 2010 great Chilean earthquakes in 17 lakes: Implications for quantitative lacustrine palaeoseismology. *Sedimentology*, 62:1466–1496.

Van Eaton, A. R., Amigo, Á., Bertin, D., Mastin, L. G., Giacosa, R. E., González, J., Valderrama, O., Fontijn, K., and Behnke, S. A. (2016). Volcanic lightning and plume behavior reveal evolving hazards during the April 2015 eruption of Calbuco volcano, Chile. *Geophysical Research Letters*, 43(7):3563–3571.

Van Manen, S. M. and Wallin, E. (2012). Ground temperature profiles and thermal rock properties at Wairakei, New Zealand. *Renewable Energy*, 43:313–321.

Vella, D. and Huppert, H. E. (2007). The waterlogging of floating objects. *Journal of Fluid Mechanics*, 585:245.

Vogel, H., Wagner, B., and Rose, P. (2010). A paleoclimate record with tephrochronological age control for the last glacial-interglacial cycle from Lake Ohrid , Albania and Macedonia. *Journal of Paleolimnology*, 44(1):295–310.

Volentik, A. C., Bonadonna, C., Connor, C. B., Connor, L. J., and Rosi, M. (2010). Modeling tephra dispersal in absence of wind: Insights from the climactic phase of the 2450BP Plinian eruption of Pululagua volcano (Ecuador). *Journal of Volcanology and Geothermal Research*, 193(1-2):117–136.

Von Lichtan, I., White, J., Manville, V., and Ohneiser, C. (2016). Giant rafted pumice blocks from the most recent eruption of Taupo volcano, New Zealand: Insights from palaeomagnetic and textural data. *Journal of Volcanology and Geothermal Research*, 318:73–88.

Walker, G. P. (1981). Generation and dispersal of fine ash and dust by volcanic eruptions. *Journal of Volcanology and Geothermal Research*, 11(1):81–92.

Walker, G. P. and Croasdale, R. (1971). Two Plinian-type eruptions in the Azores. *Journal of the Geological Society*, 127(1):17 LP – 55.

Wei, H., Sparks, R., Liu, R., Fan, Q., Wang, Y., Hong, H., Zhang, H., Chen, H., Jiang, C., Dong, J., Zheng, Y., and Pan, Y. (2003). Three active volcanoes in China and their hazards. *Journal of Asian Earth Sciences*, 21(5):515–526.

White, F. M. (1974). *Viscous Fluid Flow*. McGraw-Hill, New York.

White, J., Manville, V., Wilson, C. J., Houghton, B., Riggs, N. R., and Ort, M. (2001). Settling and deposition of AD 181 Taupo pumice in lacustrine and assocated environments. In White, J. and Riggs, N. R., editors, *Volcanogenic sedimentation in lacustrine settings, International Association of Sedimentologists Special Publication, vol 31*, pages 141–150. Blackwell Science, Oxford.

White, J. D. L., Houghton, B. F., Hodgson, K. A., and Wilson, C. J. N. (1997). Delayed sedimentary response to the A . D . 1886 eruption of Tarawera , New Zealand. *Geology*, 25(5):459–462.

Whitham, A. and Sparks, R. (1986). Pumice. *Bulletin of Volcanology*, 48:209–223.

Wiesner, M. G., Wang, Y. B., and Zheng, L. F. (1995). Fallout of Volcanic Ash to the Deep South China Sea Induced by the 1991 Eruption of Mount-Pinatubo (Philippines). *Geology*, 23(10):885–888.

Wilks, M., Kendall, J.-M., Nowacki, A., Biggs, J., Wookey, J., Birhanu, Y., Ayele, A., and Bedada, T. (2017). Seismicity associated with magmatism, faulting and hydrothermal circulation at Aluto Volcano, Main Ethiopian Rift. *Journal of Volcanology and Geothermal Research*, 340:52–67.

Williams, D. F., Peck, J., Karabanov, E. B., Prokopenko, A. A., Kravchinsky, V., King, J., and Kuzmin, M. I. (1997). Lake Baikal Record of Continental Climate Response to Orbital Insolation During the Past 5 Million Years. *Science*, 278(5340):1114–1117.

Wilson, L., Sparks, R. S. J., Huang, T. C., and Watkins, N. D. (1978). The control of volcanic column heights by eruption energetics and dynamics. *Journal of Geophysical Research: Solid Earth*, 83(B4):1829–1836.

WoldeGabriel, G., Aronson, J. L., and Walter, R. C. (1990). Geology, geochronology, and rift basin development in the central sector of the Main Ethiopia Rift. *Bulletin of the Geological Society of America*, 102(4):439–458.

Wright, H. M., Roberts, J. J., and Cashman, K. V. (2006). Permeability of anisotropic tube pumice: Model calculations and measurements. *Geophysical Research Letters*, 33(17):2–7.

Wright, H. M. N., Cashman, K. V., Mothes, P. A., Hall, M. L., Ruiz, A. G., and Le Pennec, J. (2012). Estimating rates of decompression from textures of erupted ash particles produced by 19992006 eruptions of Tungurahua volcano, Ecuador. *Geology*, 40(7):619–622.

Wright, I. C., Gamble, J. a., and Shane, P. a. R. (2003). Submarine silicic volcanism of the Healy caldera, southern Kermadec arc (SW Pacific): I-volcanology and eruption mechanisms. *Bulletin of Volcanology*, 65(1):15–29.

Wulf, S., Kraml, M., Brauer, A., Keller, J., and Negendank, J. F. W. (2004). Tephrochronology of the 100ka lacustrine sediment record of Lago Grande di Monticchio (southern Italy). *Quaternary International*, 122:7–30.

Yang, Q. and Bursik, M. (2016). A new interpolation method to model thickness, isopachs, extent, and volume of tephra fall deposits. *Bulletin of Volcanology*, 78(10).

Zielinski, R. (1985). Element mobility during alteration of silicic ash to kaolinite a study of tonstein. *Sedimentology*, 32:567–579.

Zinabu, G. M., Kebede-Westhead, E., and Desta, Z. (2002). Long-term changes in chemical features of waters of seven Ethiopian rift-valley lakes. *Hydrobiologia*, 477:81–91.

Appendices

Appendix A

Major element data

This appendix contains EMPA data of volcanic glass for all samples anlaysed. All values given in oxide weight percentages and have been normalised (volatile-free). * indicates not analysed.

Sample	SiO2	TiO2	Al2O3	FeO	MnO	MgO	CaO	Na2O	K2O	Cl	F	TOTAL
						CORE SAMPLES						
ABII-04-14	74.09	0.10	7.64	6.61	0.31	0.01	0.11	6.90	4.23	0.26	0.27	97.77
	73.83	0.15	7.83	6.61	0.30	0.02	0.19	6.81	4.25	0.26	0.26	98.35
	74.70	0.18	8.79	5.62	0.00	0.02	0.21	6.04	4.44	0.16	0.13	96.90
	74.69	0.21	8.86	5.66	0.00	0.00	0.20	6.06	4.32	0.16	0.20	97.96
	74.61	0.30	8.62	5.96	0.00	0.03	0.29	5.84	4.35	0.20	0.05	94.12
	74.99	0.24	8.38	6.09	0.00	0.03	0.21	5.67	4.38	0.19	0.17	94.24
	73.74	0.17	7.75	6.41	0.35	0.00	0.23	7.11	4.25	0.31	0.29	97.11
	74.00	0.14	7.58	6.49	0.37	0.00	0.25	7.06	4.10	0.29	0.29	96.05
	75.24	0.23	9.20	4.69	0.17	0.00	0.26	5.64	4.55	0.26	0.17	99.96
	75.84	0.20	9.07	4.62	0.17	0.00	0.20	5.41	4.49	0.25	0.18	98.27
	75.29	0.22	9.24	4.72	0.24	0.00	0.23	5.41	4.65	0.22	0.17	98.75
	75.28	0.26	9.22	4.67	0.21	0.01	0.20	5.56	4.59	0.18	0.17	98.20
	74.09	0.10	7.64	6.61	0.31	0.01	0.11	6.89	4.23	0.26	0.27	97.77
	73.83	0.15	7.83	6.62	0.30	0.02	0.19	6.81	4.26	0.26	0.26	98.35
Avg.	74.59	0.19	8.40	5.81	0.20	0.01	0.21	6.23	4.36	0.23	0.21	97.41
Std. Dev.	0.67	0.06	0.67	0.82	0.14	0.01	0.05	0.66	0.16	0.05	0.07	
ABII-04-67	73.03	0.14	8.00	6.84	0.31	0.00	0.26	7.17	4.26	0.25	0.30	95.86
	73.83	0.18	7.94	6.76	0.31	0.00	0.23	6.29	4.46	0.26	0.37	97.56
	73.64	0.19	8.54	6.45	0.32	0.00	0.26	6.22	4.38	0.23	0.24	96.87
	73.26	0.18	8.50	6.58	0.33	0.01	0.25	6.64	4.26	0.22	0.44	98.86
	73.15	0.16	8.29	6.72	0.34	0.00	0.28	6.76	4.30	0.27	0.36	96.67
	72.98	0.18	8.33	6.86	0.32	0.01	0.21	6.78	4.32	0.25	0.29	96.87
Avg.	73.96	0.17	8.05	6.55	0.32	0.00	0.24	6.48	4.22	0.24	0.33	97.00
Std. Dev.	1.74	0.02	0.61	0.42	0.01	0.01	0.02	0.54	0.29	0.02	0.07	
ABII-05-48	72.97	0.16	8.44	7.04	0.34	0.00	0.23	6.45	4.37	*	*	95.23
	73.34	0.17	8.22	6.85	0.28	0.00	0.19	6.61	4.33	*	*	96.47
	73.18	0.18	8.26	6.93	0.33	0.00	0.23	6.58	4.30	*	*	95.85
	73.20	0.12	8.30	6.88	0.30	0.00	0.26	6.59	4.34	*	*	95.91
	73.31	0.14	8.25	6.72	0.36	0.03	0.22	6.65	4.32	*	*	96.44
	73.31	0.19	8.37	6.80	0.34	0.01	0.30	6.39	4.27	*	*	95.63
	73.07	0.20	8.35	6.94	0.27	0.00	0.24	6.56	4.37	*	*	96.20
	74.39	0.19	7.60	6.92	0.35	0.00	0.27	6.24	4.03	*	*	96.59
	73.22	0.16	8.28	6.97	0.30	0.00	0.24	6.52	4.30	*	*	96.89
	73.61	0.23	8.15	6.76	0.33	0.00	0.26	6.43	4.23	*	*	95.57
	73.32	0.24	8.24	6.72	0.35	0.00	0.23	6.59	4.31	*	*	95.62
	73.34	0.20	8.18	6.81	0.38	0.00	0.28	6.45	4.36	*	*	95.26
	73.43	0.22	8.30	6.61	0.32	0.00	0.25	6.49	4.39	*	*	95.42
Avg.	73.36	0.19	8.23	6.84	0.33	0.00	0.25	6.50	4.30	*	*	95.93
Std. Dev.	0.35	0.03	0.20	0.12	0.03	0.01	0.03	0.11	0.09	*	*	
ABIII-05-60	73.94	0.12	7.84	6.59	*	0.00	0.07	7.18	4.27	0.26	0.24	97.75
	73.62	0.15	8.15	6.86	*	0.00	0.21	6.85	4.18	0.26	0.30	96.35

Sample	SiO2	TiO2	Al2O3	FeO	MnO	MgO	CaO	Na2O	K2O	Cl	F	TOTAL
	73.41	0.12	8.60	6.69	*	0.00	0.23	6.57	4.39	0.23	0.30	95.53
	73.81	0.12	8.12	6.86	*	0.00	0.23	6.66	4.21	0.24	0.47	96.83
ABIII-05-60	73.89	0.26	8.08	6.73	*	0.00	0.15	6.63	4.26	0.24	0.34	97.32
cont.	72.92	0.22	8.75	6.74	*	0.00	0.15	6.80	4.41	0.21	0.42	95.81
	74.08	0.17	7.92	6.66	*	0.00	0.17	6.41	4.58	0.27	0.23	96.65
Avg.	73.67	0.16	8.21	6.73	*	0.00	0.17	6.73	4.33	0.25	0.33	96.60
Std. Dev.	0.39	0.06	0.34	0.10	*	0.00	0.06	0.24	0.14	0.02	0.09	
	75.32	0.20	9.39	4.64	0.25	0.01	0.16	5.45	4.57	0.21	0.20	96.99
	75.59	0.25	8.93	4.62	0.24	0.00	0.13	5.71	4.52	0.22	0.19	97.50
	75.67	0.22	9.25	4.56	0.23	0.00	0.19	5.43	4.44	0.25	0.19	97.43
	75.63	0.20	9.19	4.65	0.20	0.00	0.17	5.46	4.49	0.20	0.20	96.94
	75.31	0.22	9.12	4.87	0.31	0.00	0.22	5.65	4.31	0.31	0.20	95.32
	75.51	0.19	9.06	4.65	0.20	0.01	0.27	5.64	4.48	0.28	0.20	96.00
ABII-08-16	75.85	0.22	8.91	4.56	0.23	0.00	0.18	5.45	4.58	0.22	0.18	96.96
	75.52	0.24	9.14	4.69	0.22	0.00	0.18	5.49	4.51	0.33	0.19	96.90
	75.73	0.25	9.04	4.77	0.19	0.01	0.16	5.23	4.62	0.32	0.17	96.15
	75.79	0.18	9.14	4.69	0.22	0.00	0.15	5.29	4.54	0.28	0.17	97.76
	75.71	0.23	9.34	4.25	0.17	0.01	0.29	5.31	4.69	0.23	0.14	95.85
	75.73	0.22	9.06	4.56	0.18	0.01	0.17	5.52	4.54	0.28	0.18	98.19
	75.39	0.25	9.08	4.68	0.17	0.00	0.20	5.75	4.48	0.25	0.18	96.37
	75.79	0.18	8.76	4.76	0.23	0.00	0.22	5.54	4.53	0.23	0.19	96.44
Avg.	75.28	0.22	9.06	4.62	0.22	0.01	0.19	5.47	4.50	0.26	0.18	96.77
Std. Dev.	0.19	0.03	0.17	0.14	0.04	0.01	0.04	0.16	0.09	0.04	0.02	
	74.55	0.12	7.81	6.54	*	0.00	0.14	6.63	4.21	0.28	0.30	96.26
	74.69	0.21	8.19	6.19	*	0.00	0.30	6.31	4.10	0.24	0.80	99.13
	74.66	0.17	8.53	6.34	*	0.00	0.29	5.92	4.10	0.20	0.55	96.53
	74.53	0.19	8.20	6.39	*	0.00	0.19	6.23	4.27	0.22	0.53	96.66
	74.80	0.09	8.55	5.71	*	0.00	0.10	6.71	4.04	0.22	0.38	96.71
	73.20	0.13	7.61	7.17	*	0.01	0.28	7.50	4.10	0.30	0.51	97.05
ABII-08-46	73.47	0.08	7.84	6.55	*	0.02	0.18	7.67	4.18	0.30	0.40	97.49
	74.30	0.06	8.09	6.57	*	0.00	0.11	6.69	4.17	0.30	0.38	97.53
	73.85	0.13	8.03	6.68	*	0.00	0.23	7.01	4.06	0.30	0.47	96.33
	74.38	0.06	8.16	6.43	*	0.00	0.20	6.63	4.15	0.27	0.34	97.20
	73.92	0.09	8.18	6.57	*	0.02	0.16	6.90	4.16	0.28	0.34	98.22
	73.98	0.07	8.08	6.65	*	0.00	0.17	6.87	4.18	0.29	0.38	97.63
Avg.	74.19	0.12	8.11	6.48	*	0.00	0.20	6.76	4.14	0.27	0.45	97.23
Std. Dev.	0.52	0.05	0.28	0.36	*	0.01	0.06	0.52	0.07	0.04	0.08	
	74.50	0.13	8.54	5.92	0.26	0.02	0.14	6.42	4.05	0.19	0.32	95.77
	73.37	0.13	8.03	6.76	0.32	0.01	0.14	7.09	4.15	0.33	0.30	97.47
ABII-08-78	73.61	0.17	8.24	6.72	0.34	0.01	0.24	6.35	4.33	0.34	0.24	98.48
	73.79	0.16	8.06	6.70	0.33	0.00	0.15	6.45	4.34	0.32	0.24	98.90
	73.55	0.13	7.99	6.72	0.31	0.01	0.17	6.93	4.18	0.37	0.31	95.88

Sample	SiO2	TiO2	Al2O3	FeO	MnO	MgO	CaO	Na2O	K2O	Cl	F	TOTAL
	73.30	0.13	7.60	6.82	0.39	0.00	0.12	7.39	4.24	0.40	0.33	97.33
	73.14	0.14	7.74	6.61	0.35	0.00	0.16	7.31	4.56	0.49	0.31	97.83
	73.30	0.15	7.70	6.72	0.35	0.00	0.22	7.07	4.50	0.44	0.32	97.96
	73.41	0.15	7.72	6.61	0.35	0.00	0.17	6.99	4.59	0.44	0.32	97.36
	73.25	0.12	7.79	6.74	0.38	0.00	0.13	7.03	4.56	0.40	0.31	98.02
	73.75	0.15	7.84	6.66	0.35	0.00	0.17	6.86	4.22	0.37	0.31	98.05
	73.91	0.10	7.75	6.68	0.33	0.00	0.16	6.82	4.25	0.41	0.29	98.25
	72.91	0.14	8.17	6.98	0.34	0.00	0.21	7.09	4.15	0.29	0.29	98.20
ABII-08-78	73.65	0.15	7.76	6.75	0.37	0.00	0.17	7.01	4.14	0.42	0.31	98.37
cont.	73.93	0.13	7.70	6.70	0.31	0.00	0.14	6.86	4.23	0.38	0.30	98.44
	74.07	0.13	7.73	6.58	0.37	0.01	0.18	6.82	4.11	0.44	0.32	95.26
	73.74	0.15	7.73	6.70	0.35	0.00	0.21	7.03	4.07	0.44	0.30	95.63
	73.90	0.13	7.80	6.59	0.32	0.00	0.15	6.90	4.21	0.37	0.31	95.70
	73.80	0.12	7.70	6.61	0.33	0.00	0.15	7.12	4.17	0.42	0.30	98.08
	73.65	0.13	7.99	6.51	0.33	0.00	0.11	7.03	4.25	0.33	0.28	98.02
	73.67	0.18	8.24	6.66	0.30	0.00	0.14	6.44	4.36	0.38	0.26	96.69
	73.54	0.21	7.99	6.74	0.31	0.01	0.15	6.63	4.42	0.28	0.25	98.03
Avg.	73.02	0.14	7.97	6.56	0.33	0.00	0.16	6.88	4.30	0.37	0.29	97.49
Std. Dev.	0.58	0.02	0.64	0.28	0.03	0.01	0.03	0.27	0.22	0.08	0.04	
	73.77	0.16	8.01	6.57	0.34	0.01	0.20	6.75	4.19	0.29	0.28	98.62
	73.96	0.13	8.00	6.57	0.34	0.00	0.20	6.71	4.09	0.27	0.38	97.76
	73.90	0.14	8.04	6.48	0.33	0.00	0.22	6.71	4.19	0.29	0.38	98.10
	73.62	0.15	8.12	6.66	0.35	0.01	0.14	6.79	4.16	0.28	0.38	98.53
	73.70	0.16	7.87	6.64	0.37	0.00	0.16	6.98	4.12	0.29	0.39	98.65
	73.70	0.14	8.05	6.57	0.33	0.00	0.15	6.93	4.14	0.29	0.36	98.81
	73.81	0.14	8.01	6.63	0.31	0.00	0.20	6.77	4.13	0.28	0.35	98.09
	73.81	0.13	7.96	6.60	0.33	0.00	0.16	6.89	4.11	0.29	0.38	98.79
	73.65	0.16	8.05	6.61	0.34	0.00	0.20	6.88	4.12	0.28	0.36	98.62
	73.64	0.15	7.96	6.58	0.38	0.01	0.19	7.02	4.07	0.29	0.36	98.97
	73.61	0.13	7.90	6.63	0.36	0.00	0.17	6.98	4.21	0.27	0.34	98.89
	73.80	0.19	8.03	6.50	0.29	0.01	0.18	6.77	4.22	0.28	0.37	98.60
ABII-09-03	73.66	0.12	8.02	6.56	0.33	0.00	0.15	6.93	4.23	0.29	0.38	98.07
	74.19	0.14	8.27	6.48	0.35	0.00	0.14	6.21	4.23	0.28	0.30	97.99
	73.75	0.12	8.08	6.52	0.33	0.00	0.14	6.91	4.15	0.28	0.37	98.24
	73.80	0.13	7.97	6.50	0.34	0.00	0.19	6.91	4.15	0.28	0.35	98.15
	73.93	0.16	8.11	6.46	0.34	0.00	0.13	6.67	4.18	0.29	0.30	98.34
	73.80	0.13	8.14	6.57	0.30	0.00	0.19	6.63	4.23	0.29	0.28	98.13
	73.84	0.13	8.05	6.46	0.33	0.00	0.18	6.88	4.12	0.29	0.32	97.89
	73.96	0.12	7.91	6.47	0.33	0.00	0.12	6.86	4.23	0.29	0.38	97.65
	73.96	0.15	7.91	6.61	0.35	0.00	0.19	6.70	4.13	0.29	0.32	97.06
	73.68	0.16	8.08	6.53	0.30	0.00	0.19	6.82	4.24	0.29	0.39	95.96
	73.66	0.12	7.99	6.59	0.35	0.00	0.19	6.87	4.24	0.28	0.36	97.15
	73.70	0.15	8.19	6.68	0.35	0.00	0.15	6.60	4.18	0.29	0.34	97.63

Sample	SiO2	TiO2	Al2O3	FeO	MnO	MgO	CaO	Na2O	K2O	Cl	F	TOTAL
ABII-09-03	73.88	0.16	7.99	6.48	0.37	0.00	0.11	6.78	4.24	0.30	0.45	98.39
Avg.	73.71	0.14	8.11	6.54	0.33	0.00	0.17	6.81	4.20	0.28	0.35	98.40
Std. Dev.	0.44	0.02	0.40	0.13	0.04	0.00	0.03	0.18	0.14	0.02	0.05	
ABII-09-08	73.50	0.14	8.14	6.45	0.30	0.01	0.21	6.93	4.31	0.40	0.30	98.59
	73.77	0.14	7.96	6.36	0.31	0.00	0.16	6.99	4.31	0.39	0.30	99.32
	73.10	0.15	7.39	7.24	0.45	0.01	0.15	7.33	4.18	0.43	0.35	98.65
	73.76	0.15	7.68	6.68	0.32	0.01	0.21	6.93	4.26	0.43	0.30	95.88
	73.42	0.15	7.84	6.64	0.38	0.02	0.25	7.15	4.16	0.44	0.31	97.47
	73.47	0.14	7.63	6.75	0.39	0.00	0.18	7.17	4.27	0.37	0.32	97.57
	74.21	0.10	7.79	6.44	0.32	0.00	0.16	6.87	4.11	0.35	0.30	95.76
	73.72	0.16	7.91	6.53	0.35	0.00	0.17	6.91	4.24	0.44	0.28	98.54
	73.53	0.15	7.90	6.57	0.33	0.00	0.22	6.97	4.33	0.42	0.29	98.08
	73.74	0.14	7.91	6.65	0.31	0.00	0.18	6.72	4.36	0.39	0.29	97.99
	74.45	0.13	8.06	6.57	0.35	0.00	0.17	6.07	4.19	0.14	0.28	96.42
	74.76	0.12	8.03	6.53	0.38	0.01	0.23	5.69	4.26	0.16	0.28	96.85
	73.88	0.13	7.92	6.51	0.38	0.01	0.15	6.85	4.17	0.41	0.31	96.19
	73.61	0.15	7.92	6.64	0.34	0.00	0.19	6.99	4.16	0.38	0.30	97.08
	73.78	0.13	7.74	6.52	0.32	0.00	0.21	7.01	4.30	0.40	0.31	96.40
	73.90	0.14	7.63	6.53	0.30	0.00	0.18	6.91	4.41	0.33	0.30	97.90
	73.57	0.13	7.87	6.65	0.33	0.00	0.15	7.06	4.24	0.38	0.32	98.25
	73.63	0.16	7.65	6.54	0.36	0.00	0.15	7.33	4.18	0.38	0.31	97.84
	73.75	0.12	8.20	6.32	0.31	0.00	0.21	6.80	4.28	0.29	0.28	97.26
	73.72	0.13	8.07	6.35	0.26	0.01	0.12	7.09	4.25	0.34	0.28	97.52
	73.96	0.08	8.05	6.40	0.29	0.00	0.18	6.82	4.20	0.36	0.27	97.32
	73.93	0.15	8.11	6.44	0.35	0.00	0.15	6.68	4.20	0.37	0.29	97.63
	74.03	0.14	7.76	6.52	0.33	0.00	0.20	6.88	4.14	0.35	0.29	97.50
	73.82	0.11	8.30	6.20	0.31	0.00	0.15	6.86	4.24	0.23	0.27	98.81
Avg.	73.38	0.14	7.90	6.56	0.33	0.00	0.18	6.74	4.22	0.36	0.30	97.42
Std. Dev.	0.60	0.03	0.27	0.25	0.04	0.00	0.03	0.49	0.09	0.08	0.02	
ABII-09-31	73.48	0.15	8.29	6.43	0.30	0.01	0.15	6.89	4.30	0.25	0.26	98.07
	73.52	0.16	8.27	6.28	0.28	0.01	0.12	6.83	4.51	0.28	0.23	97.09
	73.59	0.12	8.14	6.41	0.30	0.03	0.18	6.90	4.33	0.25	0.24	96.88
	73.57	0.16	8.23	6.59	0.30	0.00	0.19	6.81	4.15	0.28	0.23	98.60
	73.22	0.17	8.44	6.57	0.32	0.00	0.17	6.87	4.24	0.28	0.17	97.73
	73.81	0.15	7.92	6.60	0.28	0.00	0.19	6.80	4.23	0.27	0.23	97.01
	73.97	0.10	8.33	6.23	0.29	0.00	0.15	6.70	4.24	0.27	0.33	98.93
	73.36	0.16	8.11	6.52	0.33	0.01	0.23	6.84	4.44	0.25	0.37	97.76
	73.76	0.14	8.25	6.38	0.29	0.04	0.20	6.63	4.32	0.28	0.39	97.43
	73.80	0.14	8.16	6.44	0.31	0.00	0.21	6.70	4.24	0.28	0.41	98.68
	74.25	0.16	7.93	6.35	0.30	0.02	0.17	6.48	4.33	0.25	0.38	96.43
	73.51	0.17	8.13	6.57	0.31	0.05	0.21	6.75	4.31	0.27	0.40	98.10
	74.31	0.14	8.01	6.50	0.31	0.02	0.12	6.31	4.28	0.27	0.20	97.20
Avg.	73.30	0.15	8.13	6.42	0.30	0.01	0.17	6.69	4.28	0.27	0.29	97.68

Sample	SiO2	TiO2	Al2O3	FeO	MnO	MgO	CaO	Na2O	K2O	Cl	F	TOTAL
Std. Dev.	0.32	0.02	0.15	0.12	0.01	0.02	0.03	0.17	0.09	0.01	0.09	
	73.99	0.32	8.83	6.20	0.27	0.01	0.25	5.70	4.42	0.00	0.00	98.61
	73.41	0.21	8.23	6.38	0.28	0.00	0.21	6.18	5.10	0.21	0.23	97.43
	74.18	0.17	8.69	6.16	0.27	0.01	0.21	5.87	4.44	0.22	0.23	96.51
	74.08	0.22	8.48	6.11	0.27	0.00	0.17	6.30	4.38	0.22	0.23	96.38
ABII-10-45	74.12	0.19	8.46	6.23	0.27	0.04	0.25	5.94	4.50	0.21	0.32	97.71
	73.88	0.19	8.71	6.13	0.29	0.00	0.22	6.06	4.52	0.22	0.10	96.36
	73.81	0.23	8.54	6.29	0.28	0.00	0.23	6.23	4.40	0.22	0.16	98.12
	73.75	0.20	8.38	6.26	0.30	0.00	0.22	6.46	4.43	0.22	0.41	98.26
	73.85	0.22	8.61	6.13	0.32	0.02	0.20	6.22	4.44	0.21	0.32	97.48
Avg.	73.89	0.21	8.61	6.15	0.28	0.01	0.22	5.74	4.50	0.20	0.21	97.43
Std. Dev.	0.76	0.06	0.22	0.20	0.02	0.01	0.03	0.87	0.12	0.10	0.11	
	74.75	0.32	8.74	6.11	0.26	0.00	0.25	5.64	3.93	0.00	0.00	99.04
	74.61	0.33	8.64	6.15	0.26	0.00	0.25	5.59	4.16	0.00	0.00	99.25
	74.64	0.35	8.67	6.21	0.25	0.00	0.24	5.50	4.12	0.00	0.00	98.59
	74.51	0.37	8.60	6.20	0.27	0.00	0.24	5.58	4.23	0.00	0.00	98.93
	74.57	0.35	8.67	6.16	0.29	0.00	0.24	5.61	4.10	0.00	0.00	98.13
	74.64	0.30	8.62	6.30	0.26	0.00	0.24	5.50	4.13	0.00	0.00	98.86
	74.64	0.32	8.60	6.15	0.29	0.01	0.24	5.58	4.18	0.00	0.00	98.78
ABII-10-75	74.61	0.36	8.63	6.24	0.25	0.00	0.25	5.48	4.19	0.00	0.00	98.57
	74.69	0.36	8.65	6.18	0.28	0.01	0.25	5.51	4.09	0.00	0.00	98.46
	74.67	0.32	8.67	6.22	0.24	0.00	0.25	5.49	4.14	0.00	0.00	98.97
	74.56	0.29	8.65	6.18	0.28	0.03	0.25	5.48	4.28	0.00	0.00	98.31
	74.76	0.29	8.69	6.20	0.26	0.03	0.25	5.48	4.05	0.00	0.00	98.44
	74.58	0.39	8.77	6.14	0.26	0.02	0.25	5.48	4.09	0.00	0.00	98.10
	74.57	0.33	8.67	6.21	0.27	0.01	0.25	5.58	4.12	0.01	0.02	98.73
Avg.	74.64	0.33	8.65	6.20	0.27	0.01	0.25	5.55	4.10	0.00	0.00	98.85
Std. Dev.	0.28	0.06	1.09	0.76	0.04	0.01	0.04	1.01	0.69	0.11	0.09	
	73.68	0.34	8.97	6.34	0.27	0.06	0.26	5.71	4.37	0.16	0.20	98.21
	74.80	0.32	8.59	5.80	0.30	0.01	0.17	5.69	4.31	0.28	0.16	96.50
	74.26	0.32	8.31	6.14	0.30	0.00	0.25	6.01	4.41	0.18	0.17	98.35
	74.63	0.31	8.31	5.97	0.25	0.00	0.15	5.90	4.48	0.21	0.16	99.13
	74.18	0.31	8.50	6.04	0.30	0.00	0.28	5.96	4.41	0.23	0.16	99.35
	74.31	0.28	8.62	5.98	0.29	0.01	0.22	5.92	4.37	0.23	0.17	98.20
	74.88	0.14	7.94	5.98	0.25	0.00	0.22	5.99	4.60	0.21	0.23	97.71
ABII-10-77	74.83	0.12	7.81	5.98	0.29	0.01	0.22	6.12	4.63	0.31	0.23	94.78
	74.68	0.30	8.27	6.08	0.23	0.02	0.26	5.72	4.44	0.26	0.16	98.45
	74.27	0.34	8.63	5.96	0.27	0.01	0.18	5.86	4.47	0.14	0.17	98.89
	74.41	0.33	8.19	6.10	0.27	0.03	0.26	5.98	4.43	0.17	0.17	97.71
	74.49	0.32	8.31	6.10	0.26	0.01	0.22	5.85	4.45	0.20	0.17	98.36
	74.25	0.33	8.66	6.02	0.25	0.00	0.25	5.80	4.45	0.33	0.17	98.92
	74.42	0.32	8.51	5.98	0.23	0.01	0.23	5.79	4.53	0.16	0.17	98.41
	74.48	0.36	8.46	6.13	0.22	0.00	0.26	5.73	4.37	0.15	0.16	99.29

Sample	SiO2	TiO2	Al2O3	FeO	MnO	MgO	CaO	Na2O	K2O	Cl	F	TOTAL
	74.16	0.37	8.67	5.98	0.24	0.00	0.22	5.88	4.48	0.16	0.16	98.53
	74.22	0.28	8.27	6.07	0.30	0.00	0.29	6.01	4.55	0.19	0.17	98.13
	74.18	0.30	8.59	6.16	0.30	0.00	0.19	5.91	4.36	0.16	0.18	98.95
ABII-10-77	74.93	0.30	8.32	6.20	0.25	0.00	0.17	5.33	4.50	0.25	0.19	98.10
cont.	74.72	0.30	8.37	6.16	0.23	0.01	0.22	5.63	4.37	0.19	0.17	99.40
	74.65	0.30	8.47	6.04	0.27	0.00	0.17	5.52	4.58	0.15	0.17	98.09
	74.37	0.30	8.58	5.99	0.26	0.01	0.25	5.81	4.43	0.25	0.17	98.51
Avg.	74.06	0.33	8.60	6.08	0.29	0.02	0.23	5.79	4.35	0.21	0.18	97.68
Std. Dev.	0.32	0.00	0.19	0.24	0.00	0.02	0.05	0.23	0.08	0.07	0.00	
	74.31	0.17	7.95	6.35	0.27	0.00	0.13	6.63	4.19	0.39	0.27	95.50
	74.10	0.13	8.02	6.38	0.26	0.00	0.15	6.70	4.27	0.29	0.26	97.26
	73.96	0.14	7.72	6.43	0.29	0.01	0.26	6.76	4.43	0.37	0.27	97.56
	74.28	0.12	8.16	6.45	0.35	0.01	0.06	6.24	4.34	0.36	0.27	98.26
	75.57	0.17	8.26	6.51	0.37	0.00	0.11	4.59	4.43	0.38	0.28	97.40
	73.60	0.13	8.06	6.47	0.32	0.00	0.26	7.02	4.14	0.25	0.25	98.66
	74.25	0.15	7.87	6.42	0.36	0.02	0.20	6.66	4.09	0.30	0.27	96.96
	74.18	0.15	7.59	6.58	0.35	0.00	0.17	6.90	4.09	0.32	0.27	97.24
	74.36	0.17	7.64	6.34	0.39	0.00	0.15	6.80	4.15	0.36	0.29	98.40
ABII-11-07	74.24	0.13	7.96	6.31	0.30	0.01	0.15	6.70	4.21	0.29	0.29	97.58
	74.32	0.17	7.70	6.51	0.33	0.01	0.18	6.56	4.23	0.34	0.26	97.79
	74.22	0.10	7.84	6.29	0.31	0.00	0.18	6.74	4.32	0.35	0.29	98.40
	73.97	0.11	7.87	6.42	0.31	0.01	0.18	6.90	4.22	0.27	0.27	97.97
	74.42	0.08	7.41	6.69	0.29	0.01	0.25	6.66	4.18	0.20	0.28	98.13
	74.44	0.13	7.70	6.37	0.30	0.00	0.21	6.60	4.26	0.27	0.27	97.74
	73.66	0.13	7.96	6.31	0.34	0.00	0.21	7.09	4.28	0.40	0.28	97.11
	74.18	0.12	7.62	6.49	0.33	0.00	0.13	6.99	4.13	0.27	0.30	96.53
	74.33	0.12	7.82	6.46	0.32	0.00	0.12	6.56	4.28	0.31	0.26	97.23
	74.72	0.16	7.84	6.36	0.37	0.00	0.19	6.15	4.20	0.35	0.29	97.95
	74.28	0.11	7.91	6.33	0.24	0.00	0.20	6.73	4.19	0.39	0.28	99.29
Avg.	73.97	0.14	7.88	6.34	0.32	0.00	0.18	6.34	4.25	0.32	0.27	97.29
Std. Dev.	0.76	0.05	0.42	0.22	0.04	0.01	0.05	1.13	0.21	0.06	0.03	
	74.03	0.13	8.30	6.40	*	0.01	0.24	6.58	4.31	0.23	0.26	95.46
	73.98	0.16	8.47	6.32	*	0.00	0.12	6.71	4.24	0.22	0.30	97.67
ABII-11-64	74.82	0.16	7.75	6.19	*	0.01	0.23	6.70	4.14	0.22	0.33	98.44
	73.96	0.18	8.30	6.42	*	0.00	0.22	6.72	4.20	0.21	0.30	95.37
	74.11	0.15	7.94	6.63	0.33	0.01	0.19	6.30	4.34	0.28		97.2
	73.17	0.15	8.56	6.64	0.32	0.04	0.28	6.46	4.38	0.21		97.59
Avg.	73.70	0.16	8.16	6.27	*	0.01	0.20	6.55	4.15	0.18	0.25	96.74
Std. Dev.	14.58	0.04	1.60	1.21	*	0.01	0.04	1.21	0.78	0.08	0.11	
	73.86	0.12	7.98	6.42	0.36	0.00	0.19	6.74	4.33	0.38	0.24	97.01
ABII-11-81	74.21	0.13	8.09	6.20	0.31	0.00	0.19	6.75	4.11	0.45	0.25	93.32
	74.42	0.12	7.94	6.40	0.29	0.00	0.17	6.35	4.31	0.37	0.24	98.59

Sample	SiO2	TiO2	Al2O3	FeO	MnO	MgO	CaO	Na2O	K2O	Cl	F	TOTAL
	74.36	0.12	8.04	6.32	0.24	0.00	0.16	6.42	4.35	0.31	0.26	96.67
	74.17	0.12	8.24	6.49	0.32	0.00	0.18	6.15	4.33	0.30	0.25	96.71
	74.13	0.15	8.40	6.34	0.22	0.00	0.18	6.22	4.36	0.35	0.25	97.76
	74.24	0.08	8.21	6.31	0.20	0.01	0.13	6.59	4.23	0.37	0.23	96.07
ABII-11-81	74.04	0.11	7.82	6.52	0.27	0.02	0.19	6.87	4.16	0.31	0.24	97.12
cont.	74.15	0.13	8.10	6.20	0.32	0.00	0.15	6.68	4.27	0.35	0.24	96.24
	73.21	0.26	8.24	6.75	0.27	0.02	0.20	6.56	4.49	0.26	0.15	95.70
	73.72	0.30	8.15	6.69	0.32	0.02	0.35	6.15	4.31	0.20	0.15	94.94
	73.68	0.15	7.94	6.42	0.35	0.00	0.15	7.10	4.22	0.38	0.25	99.71
	73.99	0.10	8.21	6.27	0.34	0.01	0.22	6.59	4.27	0.31	0.24	98.81
	73.96	0.16	8.00	6.45	0.33	0.00	0.14	6.31	4.64	0.42	0.27	96.16
Avg.	73.66	0.14	8.21	6.08	0.29	0.01	0.18	6.52	4.37	0.32	0.23	97.07
Std. Dev.	0.63	0.06	0.51	0.18	0.05	0.01	0.05	0.29	0.22	0.08	0.04	
	73.70	0.15	8.06	6.39	0.31	0.03	0.15	6.86	4.34	0.22	0.28	95.05
	74.23	0.19	8.32	6.27	0.28	0.08	0.24	6.01	4.39	0.19	0.26	96.89
	73.82	0.19	8.58	6.31	0.28	0.04	0.27	6.08	4.43	0.20	0.25	96.17
	73.96	0.19	8.43	6.27	0.28	0.01	0.25	6.32	4.30	0.21	0.26	96.68
	74.01	0.19	8.70	6.23	0.28	0.00	0.21	6.08	4.30	0.19	0.24	96.83
	74.35	0.19	8.44	6.28	0.28	0.05	0.29	5.77	4.37	0.17	0.26	96.38
	74.05	0.16	8.53	6.12	0.29	0.00	0.29	6.21	4.35	0.24	0.21	96.23
	73.82	0.15	8.56	6.36	0.31	0.00	0.25	6.22	4.32	0.20	0.22	96.00
	74.17	0.19	8.39	6.17	0.32	0.00	0.21	6.19	4.36	0.25	0.20	98.47
	74.24	0.18	8.41	6.23	0.26	0.00	0.23	5.99	4.46	0.29	0.21	97.23
ABII-12-11	73.94	0.18	8.45	6.22	0.32	0.01	0.23	6.26	4.40	0.16	0.23	96.30
	74.05	0.19	8.42	6.18	0.29	0.01	0.29	6.16	4.42	0.18	0.22	97.28
	75.88	0.14	8.74	4.89	0.21	0.00	0.19	5.98	3.96	0.16	0.15	97.32
	73.85	0.18	8.54	6.00	0.32	0.00	0.22	6.39	4.50	0.24	0.21	96.95
	74.09	0.18	8.54	6.25	0.28	0.01	0.20	6.17	4.28	0.27	0.21	97.52
	73.85	0.16	8.37	6.31	0.29	0.00	0.21	6.34	4.47	0.33	0.21	95.42
	73.99	0.17	8.43	6.05	0.29	0.01	0.27	6.30	4.50	0.28	0.21	96.08
	73.86	0.16	8.46	6.31	0.27	0.00	0.21	6.32	4.40	0.30	0.21	96.89
	73.90	0.18	8.38	6.20	0.28	0.01	0.24	6.31	4.50	0.29	0.21	97.92
	73.71	0.14	8.61	6.29	0.29	0.01	0.24	6.35	4.37	0.29	0.21	98.23
	74.20	0.16	8.33	6.22	0.29	0.00	0.18	6.32	4.29	0.29	0.21	98.73
Avg.	73.84	0.17	8.43	6.15	0.29	0.01	0.23	6.20	4.35	0.23	0.22	96.88
Std. Dev.	0.48	0.02	0.15	0.31	0.02	0.02	0.04	0.21	0.11	0.05	0.03	
	74.67	0.06	8.55	5.85	*	0.01	0.18	6.48	4.19	0.23	0.19	98.35
	74.68	0.13	8.75	5.76	*	0.00	0.22	6.19	4.28	0.20	0.20	99.91
	74.75	0.24	8.93	5.77	*	0.03	0.11	5.87	4.30	0.21	0.37	98.91
ABII-12-16	74.38	0.26	8.88	5.93	*	0.00	0.27	5.77	4.50	0.21	0.04	99.80
	73.86	0.18	8.60	6.17	*	0.02	0.21	6.70	4.26	0.25	0.39	99.49
	74.26	0.20	8.32	6.22	*	0.00	0.19	6.72	4.10	0.25	0.18	96.05
	74.45	0.12	8.19	6.34	*	0.00	0.21	6.60	4.10	0.24	0.23	95.23

Sample	SiO2	TiO2	Al2O3	FeO	MnO	MgO	CaO	Na2O	K2O	Cl	F	TOTAL
	74.21	0.12	8.39	6.30	*	0.00	0.12	6.58	4.28	0.24	0.18	95.62
	72.59	0.09	8.71	6.57	*	0.00	0.31	7.51	4.22	0.28	0.34	99.18
ABII-12-16	74.59	0.15	8.20	6.02	*	0.00	0.10	6.94	3.99	0.26	0.36	99.41
cont.	74.39	0.17	8.33	6.39	*	0.00	0.29	6.33	4.10	0.25	0.32	96.59
	74.19	0.14	8.64	5.94	*	0.03	0.20	6.62	4.25	0.21	0.50	96.75
	74.69	0.12	8.51	6.39	*	0.00	0.15	6.13	4.02	0.23	0.17	96.44
Avg.	74.28	0.15	8.54	6.13	*	0.01	0.20	6.50	4.20	0.24	0.27	97.83
Std. Dev.	0.57	0.06	0.24	0.27	*	0.01	0.07	0.46	0.14	0.02	0.12	
	74.35	0.13	8.54	5.88	0.28	0.00	0.22	6.33	4.26	0.26	0.24	95.06
	74.46	0.12	8.29	5.88	0.32	0.01	0.15	6.47	4.31	0.29	0.22	95.05
	74.68	0.04	8.63	5.76	0.29	0.00	0.05	6.16	4.39	0.23	0.23	94.63
	74.30	0.16	7.96	6.01	0.31	0.00	0.09	6.79	4.39	0.42	0.26	96.18
	74.85	0.11	7.82	6.20	0.33	0.00	0.09	6.29	4.32	0.41	0.26	97.33
	74.69	0.14	7.81	6.09	0.29	0.01	0.19	6.47	4.30	0.39	0.27	97.61
	75.01	0.15	8.39	5.66	0.26	0.00	0.17	6.07	4.28	0.44	0.26	97.98
ABII-12-24	75.16	0.12	7.98	5.80	0.28	0.00	0.09	6.30	4.28	0.33	0.24	97.07
	74.69	0.15	8.27	5.79	0.23	0.00	0.21	6.37	4.28	0.33	0.24	96.67
	74.59	0.13	8.46	5.73	0.35	0.00	0.16	6.23	4.35	0.34	0.25	97.61
	74.75	0.12	8.16	5.91	0.27	0.01	0.23	6.36	4.19	0.34	0.25	96.63
	74.45	0.12	8.36	5.87	0.29	0.00	0.22	6.18	4.50	0.35	0.25	96.92
	74.70	0.10	8.13	5.71	0.24	0.02	0.12	6.45	4.54	0.52	0.26	97.46
	74.05	0.13	8.03	6.28	0.35	0.00	0.24	6.53	4.39	0.29	0.22	98.48
	74.33	0.11	7.88	6.22	0.26	0.00	0.23	6.56	4.40	0.27	0.23	98.28
Avg.	74.07	0.15	8.28	5.87	0.29	0.00	0.18	6.28	4.34	0.32	0.24	96.19
Std. Dev.	0.41	0.08	0.49	0.18	0.03	0.01	0.07	0.24	0.11	0.09	0.03	
	73.34	0.13	7.95	6.85	0.35	0.00	0.16	6.85	4.36	0.27	0.29	98.24
	74.54	0.23	8.92	5.76	0.24	0.01	0.22	5.70	4.39	0.18	0.25	98.60
	73.60	0.15	8.01	6.76	0.36	0.00	0.27	6.41	4.44	0.25	0.36	97.52
	73.87	0.18	8.39	6.37	0.33	0.00	0.26	6.27	4.32	0.22	0.27	99.51
	73.70	0.18	8.50	6.49	0.33	0.00	0.18	6.16	4.46	0.23	0.30	98.67
LLIII-03-01	73.43	0.16	8.32	6.79	0.30	0.01	0.25	6.42	4.32	0.24	0.25	97.81
	74.03	0.13	8.44	6.46	0.29	0.00	0.24	6.13	4.28	0.23	0.33	98.73
	73.69	0.17	8.48	6.39	0.34	0.00	0.25	6.33	4.35	0.22	0.29	99.95
	73.92	0.16	8.56	6.43	0.31	0.00	0.24	6.01	4.37	0.23	0.32	99.36
	74.05	0.17	8.50	6.33	0.32	0.00	0.23	6.06	4.33	0.22	0.25	99.48
Avg.	73.87	0.17	8.47	6.39	0.31	0.00	0.23	6.19	4.37	0.23	0.29	98.79
Std. Dev.	0.37	0.04	0.33	0.38	0.04	0.00	0.03	0.33	0.06	0.03	0.04	
	73.37	0.13	8.01	6.64	0.31	0.00	0.20	6.94	4.39	0.28	0.36	95.34
	73.39	0.16	8.13	6.59	0.34	0.00	0.16	7.07	4.16	0.28	0.37	98.09
LLIII-03-70	73.57	0.15	8.13	6.70	0.33	0.00	0.18	6.78	4.17	0.30	0.32	94.00
	73.68	0.13	7.98	6.71	0.28	0.00	0.34	6.67	4.20	0.27	0.35	97.06
	73.65	0.15	8.05	6.61	0.31	0.01	0.20	6.80	4.22	0.27	0.38	98.05

Sample	SiO2	TiO2	Al2O3	FeO	MnO	MgO	CaO	Na2O	K2O	Cl	F	TOTAL
	73.46	0.14	8.29	6.64	0.30	0.01	0.17	6.85	4.13	0.29	0.36	98.66
	73.72	0.11	8.08	6.57	0.34	0.00	0.23	6.74	4.22	0.27	0.32	97.71
	73.73	0.10	8.08	6.60	0.34	0.00	0.22	6.68	4.25	0.27	0.30	97.52
	73.42	0.10	8.08	6.74	0.33	0.00	0.21	6.85	4.27	0.28	0.33	97.72
	73.55	0.11	8.21	6.63	0.35	0.00	0.29	6.56	4.31	0.27	0.25	97.56
	73.58	0.12	8.04	6.62	0.33	0.00	0.20	6.89	4.23	0.27	0.32	97.65
	73.67	0.10	8.12	6.58	0.36	0.00	0.15	6.74	4.28	0.28	0.31	98.04
	73.38	0.11	8.35	6.57	0.32	0.00	0.22	6.78	4.26	0.29	0.40	98.42
LLIII-03-70	73.29	0.14	7.63	6.71	0.40	0.00	0.14	7.54	4.15	0.32	0.36	96.86
cont.	73.34	0.11	8.20	6.69	0.33	0.00	0.19	6.98	4.17	0.30	0.36	97.06
	73.67	0.13	7.91	6.68	0.33	0.00	0.16	6.88	4.24	0.30	0.35	96.22
	74.76	0.18	7.88	6.64	0.00	0.00	0.08	6.29	4.18	0.28	0.44	98.25
	73.65	0.14	8.18	6.57	0.00	0.00	0.11	7.10	4.26	0.28	0.31	97.48
	74.43	0.13	7.83	6.61	0.00	0.00	0.16	6.61	4.23	0.27	0.31	95.60
	74.05	0.15	8.10	6.49	0.00	0.00	0.12	7.15	3.95	0.27	0.44	96.42
	73.56	0.14	8.10	6.55	0.00	0.00	0.18	7.10	4.38	0.28	0.40	96.50
	73.68	0.16	8.16	6.60	0.00	0.00	0.07	7.29	4.05	0.28	0.35	97.00
Avg.	73.66	0.13	8.07	6.62	0.24	0.00	0.18	6.88	4.21	0.28	0.35	97.15
Std. Dev.	0.35	0.02	0.16	0.06	0.15	0.00	0.06	0.27	0.10	0.01	0.04	
	74.64	0.22	8.20	6.07	*	0.00	0.09	6.30	4.48	0.24	0.27	97.63
	74.49	0.20	8.39	6.12	*	0.02	0.12	6.47	4.19	0.22	0.29	96.58
	74.45	0.19	8.78	6.05	*	0.00	0.17	6.01	4.35	0.22	0.37	97.20
	73.81	0.20	8.48	6.30	*	0.00	0.18	6.67	4.35	0.22	0.36	97.80
	74.32	0.10	7.58	6.84	*	0.02	0.17	6.77	4.19	0.28	0.28	95.89
	73.12	0.16	7.42	7.43	*	0.04	0.17	7.25	4.40	0.34	0.40	97.63
LLIII-03-110	73.09	0.19	8.24	6.88	*	0.03	0.14	7.08	4.35	0.28	0.44	98.14
	72.54	0.13	7.87	7.27	*	0.01	0.08	7.78	4.31	0.31	0.24	96.53
	73.41	0.08	7.99	6.69	*	0.01	0.09	7.49	4.23	0.26	0.38	98.27
	73.11	0.12	7.99	6.71	*	0.00	0.16	7.68	4.22	0.29	0.33	98.11
	73.89	0.07	7.65	6.62	*	0.00	0.16	7.42	4.19	0.29	0.49	100.03
	73.69	0.11	7.73	6.70	*	0.02	0.17	7.47	4.09	0.29	0.46	97.80
	73.58	0.16	7.65	6.88	*	0.01	0.26	7.26	4.20	0.31	0.38	96.96
	72.64	0.06	8.95	6.49	*	0.00	0.17	7.63	4.06	0.27	0.36	97.60
Avg.	73.63	0.14	8.07	6.65	*	0.01	0.15	7.09	4.26	0.27	0.36	97.58
Std. Dev.	0.68	0.05	0.46	0.42	*	0.01	0.05	0.56	0.12	0.04	0.07	
	73.16	0.14	8.38	6.67	0.31	0.00	0.18	6.96	4.19	0.25	0.33	94.95
	73.24	0.14	8.37	6.58	0.33	0.00	0.19	6.84	4.32	0.26	0.34	94.53
	74.36	0.15	8.01	6.38	0.33	0.00	0.14	6.59	4.05	0.24	0.34	95.76
	73.53	0.13	8.43	6.45	0.30	0.00	0.15	6.72	4.30	0.22	0.30	96.37
LLIII-04-51	73.02	0.13	8.20	6.69	0.31	0.00	0.15	7.17	4.32	0.24	0.33	95.96
	73.55	0.14	8.03	6.65	0.33	0.05	0.16	6.75	4.36	0.25	0.33	94.00
	73.24	0.14	8.37	6.57	0.32	0.05	0.20	6.83	4.28	0.27	0.32	95.90
	72.98	0.12	8.51	6.71	0.32	0.00	0.17	6.90	4.29	0.28	0.28	95.60

Sample	SiO2	TiO2	Al2O3	FeO	MnO	MgO	CaO	Na2O	K2O	Cl	F	TOTAL
LLIII-04-51	73.28	0.14	8.20	6.63	0.33	0.00	0.16	6.93	4.34	0.28	0.34	96.74
cont.	73.54	0.13	8.02	6.67	0.32	0.04	0.18	6.75	4.34	0.25	0.37	96.59
	72.87	0.13	8.28	6.71	0.33	0.07	0.18	7.12	4.30	0.25	0.35	96.16
Avg.	73.34	0.14	8.25	6.61	0.32	0.02	0.17	6.87	4.28	0.25	0.33	95.69
Std. Dev.	0.41	0.01	0.18	0.11	0.01	0.03	0.02	0.17	0.09	0.02	0.02	
	73.61	0.18	8.60	6.52	0.00	0.00	0.24	6.79	4.07	0.28	0.37	97.99
	73.83	0.16	8.51	6.45	0.00	0.00	0.24	6.59	4.23	0.26	0.23	98.37
	73.98	0.17	8.16	6.53	0.00	0.00	0.27	6.54	4.35	0.28	0.38	97.60
	74.61	0.17	8.10	6.37	0.00	0.00	0.24	6.28	4.23	0.26	0.43	97.05
	73.57	0.28	8.90	6.22	0.00	0.00	0.24	6.49	4.30	0.17	0.16	97.81
	73.89	0.20	8.92	6.47	0.00	0.00	0.21	5.88	4.43	0.17	0.27	98.62
	73.90	0.23	8.93	6.18	*	0.00	0.29	6.04	4.43	0.18	0.18	96.09
	73.96	0.16	8.28	6.52	*	0.00	0.15	6.73	4.21	0.26	0.23	97.30
	73.98	0.10	8.12	6.46	*	0.00	0.19	7.02	4.14	0.23	0.38	98.18
LLIII-05-23	73.55	0.11	8.72	6.64	*	0.00	0.16	6.40	4.42	0.26	0.38	96.11
	73.74	0.16	8.19	6.58	*	0.00	0.16	7.01	4.16	0.27	0.30	98.93
	73.55	0.17	8.07	6.57	*	0.00	0.19	7.13	4.31	0.29	0.41	99.29
	74.12	0.22	7.90	6.41	*	0.00	0.28	6.62	4.46	0.27	0.41	99.04
	74.36	0.10	8.47	6.44	*	0.00	0.21	6.33	4.08	0.27	0.30	98.10
	73.65	0.17	8.03	6.63	*	0.00	0.16	7.01	4.34	0.27	0.31	97.51
	74.14	0.10	7.96	6.61	*	0.00	0.11	6.91	4.18	0.26	0.23	96.35
	73.16	0.19	8.83	6.38	*	0.00	0.13	7.03	4.28	0.27	0.19	99.39
	74.29	0.14	8.15	6.52	*	0.00	0.22	6.64	4.03	0.30	0.48	99.66
	73.88	0.17	8.38	6.47	*	0.00	0.20	6.64	4.26	0.25	0.31	97.97
Avg.	73.71	0.16	8.35	6.55	*	0.00	0.20	6.70	4.27	0.25	0.33	97.63
Std. Dev.	0.57	0.04	0.34	0.25	*	0.00	0.05	0.36	0.13	0.04	0.09	
	73.94	0.34	8.65	6.43	0.27	0.03	0.26	5.80	4.29	0.17	0.22	98.84
	74.05	0.35	8.94	6.25	0.28	0.00	0.25	5.46	4.42	0.15	0.20	96.22
	73.79	0.35	9.21	6.25	0.27	0.03	0.19	5.56	4.36	0.19	0.21	97.50
	73.75	0.34	8.81	6.34	0.27	0.00	0.25	5.77	4.47	0.18	0.21	98.13
	74.05	0.35	8.90	6.27	0.27	0.02	0.21	5.61	4.32	0.16	0.20	97.87
	73.58	0.34	8.66	6.78	0.28	0.00	0.23	5.73	4.40	0.18	0.22	97.39
	73.68	0.35	8.79	6.23	*	0.02	0.21	6.46	4.26	0.17	0.13	98.47
	74.05	0.36	8.61	6.44	*	0.01	0.14	6.08	4.31	0.18	0.13	98.97
LLIII-07-75	74.43	0.28	8.66	6.21	*	0.00	0.24	5.76	4.41	0.16	0.33	98.38
	74.21	0.23	8.52	6.20	*	0.00	0.25	6.14	4.44	0.16	0.25	97.61
	74.24	0.38	8.70	6.22	*	0.03	0.25	5.82	4.36	0.15	0.33	98.29
	74.09	0.31	8.48	6.55	*	0.01	0.18	6.11	4.28	0.17	0.22	97.92
	74.43	0.30	8.49	6.14	*	0.00	0.17	5.92	4.55	0.18	0.04	97.34
	74.48	0.35	8.60	6.36	*	0.00	0.27	5.75	4.19	0.18	0.28	97.37
	73.98	0.30	8.62	6.71	*	0.00	0.22	5.72	4.44	0.18	0.07	95.49
	74.13	0.28	8.55	6.37	*	0.00	0.16	5.89	4.62	0.17	0.13	95.36
	73.87	0.32	8.63	6.16	0.25	0.02	0.25	6.06	4.44	0.21	0.16	99.68

Sample	SiO2	TiO2	Al2O3	FeO	MnO	MgO	CaO	Na2O	K2O	Cl	F	TOTAL
	74.20	0.31	8.48	6.08	0.28	0.00	0.23	6.02	4.41	0.23	0.18	99.40
	74.45	0.31	8.25	6.26	0.25	0.00	0.24	5.79	4.44	0.35	0.17	98.70
	74.32	0.33	8.46	6.22	0.26	0.00	0.31	5.77	4.33	0.23	0.17	99.12
LLIII-07-75	74.15	0.32	8.52	6.18	0.28	0.00	0.27	5.72	4.57	0.20	0.16	98.70
cont.	74.73	0.32	8.36	6.04	0.31	0.01	0.22	5.65	4.36	0.19	0.17	99.60
	74.56	0.31	8.56	6.17	0.21	0.01	0.28	5.48	4.42	0.22	0.16	99.20
	74.35	0.32	8.28	6.29	0.25	0.00	0.19	5.86	4.45	0.26	0.18	99.00
	74.26	0.34	8.45	6.16	0.27	0.02	0.29	5.83	4.39	0.25	0.17	99.04
	74.54	0.33	8.30	6.12	0.29	0.00	0.16	5.95	4.31	0.27	0.18	99.04
Avg.	74.05	0.32	8.58	6.28	0.16	0.01	0.23	5.83	4.39	0.20	0.19	98.18
Std. Dev.	0.25	0.03	0.22	0.18	0.13	0.01	0.04	0.22	0.10	0.05	0.06	
	73.65	0.35	9.28	6.28	0.28	0.01	0.20	5.54	4.40	0.15	0.20	97.73
	73.68	0.36	9.01	5.93	0.27	0.02	0.26	5.96	4.50	0.16	0.23	96.75
	74.12	0.34	8.93	5.80	0.26	0.03	0.26	5.78	4.48	0.14	0.22	98.48
	73.74	0.35	8.86	6.04	0.26	0.00	0.28	6.15	4.32	0.17	0.22	100.06
	73.30	0.35	8.69	6.62	0.28	0.00	0.23	6.17	4.37	0.16	0.23	98.07
	73.95	0.31	8.99	6.22	0.24	0.01	0.19	5.87	4.22	0.17	0.17	98.68
LLIII-07-105	74.09	0.35	8.84	6.16	*	0.00	0.21	6.03	4.32	0.16	0.23	98.45
	74.05	0.30	8.87	6.22	*	0.00	0.20	6.20	4.15	0.16	0.19	97.01
	73.86	0.35	9.20	5.96	*	0.00	0.08	6.24	4.31	0.18	0.11	97.91
	74.42	0.26	8.89	6.05	*	0.00	0.30	5.97	4.12	0.18	0.15	99.03
	74.02	0.29	8.81	6.11	*	0.00	0.31	5.95	4.51	0.17	0.32	97.63
	73.99	0.39	8.84	6.17	*	0.00	0.36	5.97	4.28	0.16	0.21	98.26
	74.23	0.22	9.03	6.07	*	0.00	0.31	5.70	4.44	0.16	0.01	97.21
	74.60	0.29	8.46	5.89	*	0.00	0.25	6.15	4.37	0.16	0.12	97.74
Avg.	73.98	0.32	8.91	6.11	0.11	0.01	0.25	5.98	4.34	0.16	0.19	98.07
Std. Dev.	0.33	0.05	0.20	0.20	0.14	0.01	0.07	0.20	0.12	0.01	0.07	
	73.88	0.17	7.69	6.83	*	0.00	0.28	7.08	4.08	0.31	0.31	95.81
	72.92	0.15	8.50	6.80	*	0.00	0.12	7.02	4.49	0.25	0.49	97.24
	73.31	0.10	8.21	6.59	*	0.00	0.23	7.25	4.32	0.27	0.17	96.30
	72.85	0.10	8.94	6.76	*	0.00	0.31	6.76	4.28	0.26	0.15	95.47
	73.65	0.13	8.19	6.44	0.27	0.00	0.16	6.91	4.25	0.37	0.27	95.26
	73.91	0.12	8.12	6.33	0.35	0.00	0.15	6.76	4.26	0.33	0.29	97.37
LLIII-08-38	73.63	0.12	8.06	6.35	0.31	0.00	0.19	7.05	4.29	0.34	0.28	97.14
	73.72	0.13	8.31	6.31	0.29	0.01	0.18	6.79	4.26	0.37	0.28	95.26
	73.96	0.14	7.95	6.33	0.31	0.00	0.17	6.96	4.18	0.40	0.27	97.44
	73.66	0.13	8.00	6.41	0.27	0.00	0.19	7.07	4.28	0.31	0.28	96.26
	73.64	0.15	7.59	6.52	0.35	0.00	0.21	7.36	4.19	0.45	0.32	97.71
	73.57	0.13	8.00	6.49	0.38	0.00	0.11	7.19	4.13	0.36	0.31	97.98
	73.17	0.12	8.02	6.64	0.29	0.01	0.24	7.23	4.28	0.40	0.29	98.53
	73.57	0.15	8.16	6.41	0.32	0.00	0.18	6.83	4.38	0.31	0.28	97.68
Avg.	73.19	0.13	8.09	6.48	0.22	0.00	0.19	6.99	4.24	0.34	0.28	96.82

Sample	SiO2	TiO2	Al2O3	FeO	MnO	MgO	CaO	Na2O	K2O	Cl	F	TOTAL
Std. Dev.	0.29	0.02	0.34	0.20	0.15	0.00	0.06	0.19	0.11	0.06	0.08	
LLIII-08-86	74.09	0.13	8.01	6.46	*	0.02	0.14	6.65	4.51	0.22	0.24	98.19
	74.33	0.14	8.04	6.63	*	0.00	0.20	6.52	4.14	0.21	0.21	97.68
	74.69	0.10	8.01	6.37	*	0.02	0.16	6.52	4.14	0.22	0.22	98.25
	74.36	0.13	8.25	6.18	*	0.00	0.24	6.75	4.10	0.20	0.34	96.77
	74.19	0.11	8.41	6.10	*	0.00	0.23	6.81	4.15	0.21	0.43	95.93
	74.78	0.04	8.01	6.30	*	0.03	0.17	6.43	4.24	0.23	0.22	97.87
Avg.	74.41	0.11	8.12	6.34	0.00	0.01	0.19	6.61	4.21	0.22	0.27	97.45
Std. Dev.	0.27	0.04	0.17	0.19	0.00	0.01	0.04	0.15	0.15	0.01	0.09	
LLIII-08-90	73.82	0.14	8.35	6.68	*	0.01	0.16	6.68	4.17	0.26	0.25	94.82
	74.08	0.13	8.09	6.73	*	0.01	0.09	6.70	4.17	0.23	0.15	95.78
	73.79	0.13	7.71	6.82	*	0.00	0.26	6.99	4.29	0.23	0.33	95.95
Avg.	73.72	0.26	8.71	6.47	*	0.02	0.22	6.34	4.27	0.20	0.16	94.70
Std. Dev.	0.53	0.16	0.86	0.30	*	0.02	0.08	0.52	0.15	0.05	0.11	
LLIII-09-01	74.31	0.23	8.39	6.21	*	0.01	0.18	6.34	4.33	0.15	0.20	95.24
	73.56	0.11	8.24	6.69	*	0.02	0.15	7.22	4.01	0.25	0.03	95.88
	73.89	0.15	8.16	6.52	*	0.04	0.08	7.02	4.13	0.25	0.48	95.08
	74.04	0.16	8.17	6.45	*	0.02	0.12	6.98	4.06	0.23	0.32	96.12
	74.46	0.10	8.14	6.34	*	0.01	0.27	6.43	4.25	0.23	0.20	97.61
	74.36	0.13	8.16	6.43	*	0.00	0.03	6.68	4.21	0.26	0.35	97.87
	74.58	0.12	8.27	6.32	*	0.00	0.04	6.60	4.07	0.29	0.37	97.41
	74.66	0.17	8.07	6.37	*	0.01	0.08	6.71	3.95	0.27	0.31	97.87
	74.28	0.15	8.15	6.39	*	0.00	0.25	6.63	4.15	0.23	0.23	98.72
	74.02	0.12	8.45	6.37	*	0.01	0.19	6.60	4.24	0.22	0.17	95.55
	74.14	0.14	8.37	6.32	*	0.00	0.19	6.60	4.24	0.26	0.30	98.76
	74.00	0.06	8.40	6.28	*	0.00	0.13	6.90	4.23	0.26	0.50	99.80
	74.08	0.09	7.85	6.55	*	0.00	0.27	6.89	4.27	0.25	0.36	97.85
Avg.	74.18	0.13	8.22	6.40	*	0.01	0.15	6.74	4.16	0.24	0.29	97.21
Std. Dev.	0.30	0.04	0.16	0.13	*	0.01	0.08	0.25	0.11	0.03	0.13	
LLIII-09-03	73.31	0.11	8.59	6.40	*	0.01	0.23	6.96	4.39	0.25	0.43	98.70
	74.09	0.14	8.42	6.23	*	0.00	0.22	6.71	4.19	0.25	0.38	97.97
	73.93	0.09	8.29	6.47	*	0.03	0.32	6.64	4.23	0.25	0.32	97.97
	74.02	0.05	8.37	6.36	*	0.01	0.18	6.71	4.30	0.28	0.36	100.24
	74.49	0.10	8.08	6.31	*	0.00	0.21	6.52	4.29	0.25	0.60	99.03
	74.80	0.10	7.79	6.37	*	0.00	0.21	6.70	4.03	0.22	0.49	97.35
	73.60	0.13	8.58	6.30	*	0.00	0.27	6.80	4.32	0.24	0.25	96.90
	73.68	0.14	8.26	6.41	*	0.00	0.24	7.07	4.20	0.25	0.43	97.18
	73.47	0.14	8.54	6.31	*	0.00	0.08	6.98	4.48	0.24	0.18	96.83
Avg.	73.93	0.11	8.32	6.35	0.00	0.01	0.22	6.79	4.27	0.25	0.38	98.02
Std. Dev.	0.48	0.03	0.26	0.07	0.00	0.01	0.07	0.18	0.13	0.02	0.13	
LLIII-09-15	73.54	0.11	8.77	6.14	*	0.00	0.33	6.83	4.28	0.26	0.40	97.11

Sample	SiO2	TiO2	Al2O3	FeO	MnO	MgO	CaO	Na2O	K2O	Cl	F	TOTAL
	73.96	0.09	8.67	6.11	*	0.00	0.26	6.71	4.21	0.25	0.32	97.49
	74.63	0.11	8.22	6.18	*	0.01	0.33	6.59	3.92	0.24	0.28	96.60
LLIII-09-15	74.26	0.20	7.99	6.39	*	0.00	0.31	6.81	4.05	0.24	0.32	97.52
cont.	74.38	0.09	8.40	6.23	*	0.00	0.24	6.72	3.94	0.24	0.44	96.52
	73.83	0.18	8.20	6.47	*	0.01	0.19	6.95	4.17	0.23	0.41	96.40
	74.20	0.19	8.41	6.17	*	0.00	0.34	6.73	3.96	0.25	0.47	95.67
Avg.	74.12	0.14	8.38	6.24	*	0.00	0.28	6.76	4.07	0.25	0.38	96.76
Std. Dev.	0.36	0.05	0.27	0.14	*	0.01	0.06	0.11	0.15	0.01	0.07	0.66
	74.03	0.13	8.14	6.23	*	0.00	0.21	6.63	4.64	0.26	0.40	98.74
LLIII-9-22	74.78	0.15	7.61	6.87	*	0.01	0.27	6.50	3.83	0.32	0.24	98.96
	73.24	0.10	8.08	7.06	*	0.00	0.19	7.05	4.29	0.31	0.26	99.23
Avg.	74.01	0.13	7.94	6.72	*	0.00	0.22	6.72	4.25	0.30	0.30	98.98
Std. Dev.	0.77	0.03	0.29	0.44	*	0.00	0.05	0.29	0.41	0.03	0.09	
	73.79	0.14	8.67	6.19	0.28	0.04	0.18	6.67	4.04	0.22	0.33	97.01
	73.51	0.14	8.67	6.25	0.28	0.00	0.14	6.29	4.72	0.24	0.52	96.82
	72.97	0.15	9.08	6.42	0.31	0.00	0.19	6.93	3.97	0.23	0.34	95.21
	73.27	0.09	8.97	6.45	*	0.02	0.21	7.05	3.95	0.24	0.19	94.13
	74.22	0.08	8.47	6.19	*	0.00	0.29	6.67	4.09	0.24	0.21	96.96
LLIII-09-23	74.78	0.18	8.40	5.86	*	0.00	0.23	6.52	4.03	0.21	0.20	96.62
	74.33	0.10	8.37	6.29	*	0.03	0.14	6.44	4.30	0.22	0.34	95.23
	74.38	0.09	8.31	6.15	*	0.01	0.17	6.60	4.29	0.22	0.30	94.89
	73.65	0.16	8.81	6.46	*	0.00	0.29	6.42	4.20	0.24	0.39	95.58
	73.80	0.15	8.48	6.46	*	0.00	0.15	6.86	4.10	0.26	0.32	94.92
	73.48	0.15	8.42	6.58	*	0.00	0.22	6.70	4.44	0.24	0.35	94.35
Avg.	74.09	0.13	8.40	6.32	0.06	0.01	0.21	6.62	4.17	0.24	0.30	96.36
Std. Dev.	1.01	0.03	0.44	0.39	0.12	0.01	0.05	0.28	0.29	0.03	0.09	
	73.00	0.13	8.73	6.37	0.29	0.00	0.20	7.22	4.06	0.23	0.29	96.26
	74.19	0.12	8.60	5.90	*	0.01	0.19	6.70	4.29	0.22	0.24	95.60
	73.95	0.12	8.57	6.13	*	0.03	0.27	6.81	4.12	0.22	0.31	94.07
	74.20	0.12	8.22	6.47	*	0.05	0.23	6.53	4.19	0.27	0.15	96.12
	74.12	0.08	8.51	6.32	*	0.01	0.23	6.40	4.34	0.24	0.41	94.27
LLIII-09-44	74.50	0.06	8.42	6.10	*	0.00	0.22	6.41	4.29	0.21	0.36	95.53
	73.87	0.21	8.51	6.08	*	0.01	0.18	6.83	4.32	0.26	0.47	96.95
	73.61	0.23	8.48	6.20	*	0.00	0.27	6.98	4.23	0.24	0.29	96.96
	74.16	0.13	8.43	6.29	*	0.04	0.20	6.54	4.21	0.23	0.28	96.32
	74.47	0.18	8.50	6.03	*	0.00	0.20	6.27	4.35	0.21	0.50	96.18
Avg.	74.01	0.14	8.50	6.19	0.29	0.01	0.22	6.67	4.24	0.23	0.33	95.83
Std. Dev.	0.44	0.05	0.13	0.17		0.02	0.03	0.30	0.10	0.02	0.11	
	74.72	0.11	8.37	6.10	*	0.00	0.17	6.37	4.14	0.25	0.44	97.93
LLIII-09-60	74.29	0.18	8.49	6.16	*	0.00	0.12	6.59	4.16	0.23	0.34	96.70
	74.35	0.10	8.17	6.17	*	0.00	0.23	6.72	4.26	0.25	0.51	96.74
	73.19	0.17	8.21	6.31	*	0.00	0.22	7.05	4.85	0.27	0.58	97.94

Sample	SiO2	TiO2	Al2O3	FeO	MnO	MgO	CaO	Na2O	K2O	Cl	F	TOTAL
	72.94	0.25	8.26	6.69	*	0.00	0.18	7.14	4.54	0.28	0.44	97.19
	74.20	0.13	7.84	6.54	*	0.00	0.13	6.95	4.22	0.28	0.41	98.45
	74.93	0.14	8.38	6.04	*	0.00	0.23	6.07	4.20	0.22	0.41	96.95
	74.41	0.11	8.58	6.21	*	0.03	0.13	6.14	4.40	0.22	0.24	96.10
LLIII-09-60	75.13	0.08	8.59	5.99	*	0.00	0.31	5.92	3.98	0.23	0.21	97.31
cont.	74.84	0.10	8.67	6.21	*	0.00	0.08	6.06	4.03	0.24	0.31	97.11
	73.01	0.14	8.83	6.27	*	0.00	0.18	6.96	4.61	0.24	0.26	97.39
	74.14	0.15	8.63	6.23	*	0.00	0.15	6.57	4.12	0.24	0.36	98.76
	73.84	0.14	8.41	6.56	*	0.05	0.20	6.65	4.16	0.25	0.35	98.21
Avg.	73.88	0.14	8.58	6.20	*	0.01	0.19	6.62	4.40	0.24	0.36	97.48
Std. Dev.	0.91	0.04	0.42	0.25	*	0.01	0.06	0.42	0.37	0.02	0.10	
	74.97	0.20	9.55	4.63	0.21	0.00	0.25	5.69	4.50	0.28	0.22	95.13
	74.86	0.18	9.45	4.60	0.19	0.00	0.24	5.88	4.59	0.24	0.19	95.06
	74.83	0.17	9.64	4.69	0.20	0.00	0.25	5.64	4.58	0.28	0.20	96.63
	74.97	0.18	9.61	4.58	0.22	0.00	0.25	5.64	4.55	0.26	0.21	94.05
LLIII-09-74	75.14	0.21	9.68	4.60	0.17	0.00	0.13	5.57	4.51	0.23	0.20	94.51
	75.20	0.20	9.40	4.60	0.24	0.00	0.25	5.47	4.64	0.32	0.20	94.22
	75.14	0.20	9.53	4.52	0.21	0.00	0.32	5.70	4.37	0.24	0.20	94.15
	75.20	0.16	9.53	4.75	0.21	0.00	0.18	5.58	4.40	0.33	0.21	94.92
	75.22	0.15	9.47	4.65	0.22	0.00	0.25	5.65	4.39	0.22	0.20	94.15
Avg.	74.64	0.19	9.58	4.58	0.21	0.00	0.22	5.58	4.54	0.26	0.20	94.26
Std. Dev.	0.28	0.02	0.30	0.11	0.02	0.00	0.04	0.13	0.17	0.03	0.01	
	74.44	0.13	8.71	5.91	*	0.00	0.08	6.39	4.36	0.25	0.34	97.53
	74.07	0.09	8.77	5.95	*	0.00	0.20	6.49	4.43	0.23	0.27	95.03
	74.60	0.08	8.44	6.05	*	0.00	0.16	6.19	4.48	0.23	0.24	96.33
	74.50	0.19	8.59	6.06	*	0.00	0.27	6.21	4.18	0.25	0.36	96.67
	74.00	0.17	8.68	6.05	*	0.00	0.19	6.55	4.36	0.20	0.30	97.32
	74.19	0.13	8.60	6.16	*	0.00	0.12	6.53	4.26	0.22	0.39	95.97
	74.28	0.13	8.51	6.14	*	0.00	0.09	6.55	4.29	0.23	0.32	95.30
	74.40	0.20	8.46	5.81	*	0.00	0.03	6.64	4.46	0.23	0.11	97.85
LLIII-09-98	74.05	0.16	8.68	5.99	*	0.00	0.11	6.78	4.23	0.24	0.13	97.72
	74.62	0.13	8.54	5.86	*	0.00	0.09	6.54	4.23	0.25	0.28	98.54
	74.67	0.16	8.56	5.84	*	0.00	0.05	6.49	4.23	0.25	0.18	97.12
	74.45	0.13	8.67	5.87	*	0.00	0.21	6.59	4.09	0.24	0.16	96.66
	74.46	0.12	8.50	6.05	*	0.00	0.23	6.57	4.08	0.23	0.29	97.43
	73.59	0.21	8.68	6.57	*	0.00	0.24	6.53	4.18	0.25	0.32	97.30
	74.55	0.06	8.58	5.92	*	0.04	0.07	6.63	4.15	0.23	0.29	95.41
	74.82	0.07	8.86	5.84	*	0.02	0.10	6.01	4.28	0.22	0.35	95.28
	75.00	0.07	8.34	5.80	*	0.02	0.09	6.36	4.32	0.21	0.31	96.68
Avg.	74.36	0.13	8.61	5.98	0.02	0.00	0.14	6.49	4.28	0.23	0.28	96.65
Std. Dev.	0.37	0.04	0.13	0.19	0.06	0.01	0.07	0.20	0.12	0.01	0.08	

SAMPLE	SiO2	TiO2	Al2O3	FeO	MnO	MgO	CaO	Na2O	K2O	Cl	F	TOTAL
LAND SECTIONS												
	74.03	0.14	8.30	6.50	*	0.00	0.05	6.90	4.08	0.27	0.27	97.54
	74.29	0.11	7.80	6.69	*	0.00	0.20	6.79	4.13	0.29	0.48	96.01
	73.86	0.12	8.24	6.61	*	0.00	0.21	6.71	4.24	0.30	0.33	98.45
	73.13	0.09	8.66	6.62	*	0.01	0.19	7.05	4.25	0.28	0.54	97.17
	74.20	0.16	7.82	6.74	*	0.01	0.11	6.82	4.14	0.29	0.49	95.97
	74.51	0.11	7.80	6.52	*	0.00	0.09	6.80	4.19	0.28	0.48	97.81
	74.01	0.17	8.01	6.52	*	0.00	0.09	7.13	4.07	0.30	0.40	97.48
MER048B	73.94	0.22	7.83	6.36	*	0.00	0.16	7.46	4.05	0.31	0.31	98.55
	73.89	0.13	7.71	6.89	*	0.02	0.16	6.98	4.22	0.29	0.39	97.45
	74.15	0.11	7.81	6.59	*	0.01	0.14	7.03	4.16	0.27	0.33	97.70
	74.40	0.11	7.98	6.69	*	0.00	0.18	6.43	4.21	0.28	0.34	97.65
	73.90	0.20	7.85	6.62	*	0.01	0.17	6.98	4.27	0.28	0.32	96.33
	73.93	0.17	8.09	6.67	*	0.00	0.24	6.61	4.29	0.27	0.34	97.96
	73.84	0.15	8.02	6.57	*	0.01	0.23	7.04	4.14	0.29	0.26	99.14
	73.96	0.08	7.73	6.49	*	0.00	0.23	7.28	4.23	0.28	0.38	98.98
Avg.	74.00	0.14	7.98	6.60	*	0.00	0.16	6.93	4.18	0.28	0.38	97.61
Std. Dev	0.32	0.04	0.26	0.13	*	0.01	0.06	0.26	0.08	0.01	0.08	
	74.91	0.16	8.31	6.29	*	0.02	0.14	5.92	4.25	0.24	0.50	95.90
	74.29	0.13	8.42	6.13	*	0.02	0.16	6.58	4.28	0.24	0.33	97.71
MER048D	74.48	0.14	8.51	6.12	*	0.00	0.28	6.21	4.27	0.25	0.24	97.43
	74.15	0.11	8.37	6.34	*	0.01	0.27	6.47	4.28	0.22	0.16	98.35
	74.22	0.15	8.47	6.00	*	0.02	0.26	6.82	4.06	0.24	0.30	96.29
	73.96	0.10	8.35	6.20	*	0.00	0.21	6.93	4.24	0.23	0.41	94.98
Avg.	74.33	0.13	8.40	6.18	*	0.01	0.22	6.49	4.23	0.23	0.32	96.78
Std. Dev	0.33	0.02	0.07	0.13	*	0.01	0.06	0.38	0.08	0.01	0.12	
	74.33	0.17	8.45	6.23	*	0.02	0.10	6.06	4.64	0.20	0.13	93.12
	74.35	0.16	8.50	6.12	*	0.01	0.21	6.21	4.44	0.21	0.09	92.98
	73.66	0.21	9.11	6.13	*	0.02	0.29	6.16	4.42	0.20	0.21	98.48
	74.46	0.21	8.59	6.11	*	0.02	0.28	5.93	4.39	0.19	0.31	97.24
	74.44	0.21	8.66	6.01	*	0.03	0.20	6.25	4.19	0.20	0.20	98.97
	74.05	0.16	8.83	6.05	*	0.00	0.35	6.20	4.36	0.22	0.38	99.28
	74.49	0.17	8.55	6.14	*	0.00	0.29	6.08	4.27	0.22	0.41	96.36
MER048E	74.56	0.26	8.20	5.84	*	0.02	0.32	6.44	4.37	0.20	0.27	97.55
	74.38	0.24	8.48	5.98	*	0.02	0.33	6.18	4.38	0.19	0.14	98.05
	74.40	0.19	9.12	5.85	*	0.02	0.22	6.15	4.04	0.20	0.29	97.86
	74.85	0.18	8.50	5.94	*	0.01	0.24	5.91	4.36	0.18	0.35	100.14
	74.38	0.13	8.59	6.08	*	0.01	0.24	6.19	4.38	0.20	0.27	98.47
	74.89	0.20	8.59	6.03	*	0.00	0.18	5.80	4.31	0.17	0.27	97.17
	75.00	0.19	8.38	6.03	*	0.00	0.21	5.96	4.24	0.20	0.49	96.24
	74.48	0.19	8.62	6.06	*	0.00	0.26	6.03	4.35	0.22	0.17	98.71
	74.97	0.13	8.41	6.07	*	0.00	0.17	5.94	4.31	0.21	0.27	98.53

SAMPLE	SiO2	TiO2	Al2O3	FeO	MnO	MgO	CaO	Na2O	K2O	Cl	F	TOTAL
Avg.	74.48	0.19	8.60	6.04	*	0.01	0.24	6.09	4.34	0.20	0.27	97.45
Std. Dev	0.34	0.04	0.24	0.10	*	0.01	0.07	0.16	0.13	0.02	0.11	
	74.89	0.24	8.55	5.92	*	0.00	0.22	5.75	4.43	0.21	0.27	96.94
	74.25	0.22	8.80	6.12	*	0.00	0.13	6.22	4.26	0.22	0.25	97.81
	74.29	0.20	8.34	6.41	*	0.00	0.22	6.18	4.37	0.21	0.29	96.37
	74.81	0.17	8.26	6.07	*	0.00	0.13	6.23	4.34	0.22	0.35	97.83
	74.85	0.21	8.63	6.13	*	0.00	0.16	5.81	4.21	0.20	0.28	97.67
	74.65	0.19	8.83	5.97	*	0.00	0.15	6.01	4.21	0.24	0.30	98.63
	74.51	0.23	8.63	5.91	*	0.00	0.14	6.28	4.30	0.22	0.23	97.38
	74.99	0.22	8.48	5.91	*	0.00	0.28	5.86	4.26	0.22	0.24	94.98
	74.84	0.11	8.57	5.98	*	0.00	0.22	6.15	4.12	0.21	0.40	94.93
	74.84	0.20	8.28	5.96	*	0.00	0.13	6.48	4.11	0.21	0.39	95.11
	75.07	0.19	8.78	5.77	*	0.00	0.32	5.75	4.13	0.21	0.28	94.95
	75.21	0.21	8.31	5.85	*	0.00	0.25	6.00	4.17	0.20	0.29	94.05
	74.89	0.13	8.32	5.90	*	0.00	0.33	6.13	4.30	0.22	0.48	94.88
	75.03	0.21	8.46	5.86	*	0.00	0.16	6.12	4.16	0.23	0.41	95.64
	74.68	0.19	8.51	5.93	*	0.00	0.27	6.23	4.18	0.20	0.49	95.03
	74.95	0.19	8.74	6.03	*	0.00	0.21	5.66	4.22	0.21	0.27	94.33
	73.36	0.22	9.01	6.10	*	0.03	0.35	6.66	4.29	0.22	0.27	97.78
MER048F	74.02	0.18	8.56	6.17	*	0.00	0.06	6.62	4.38	0.26	0.26	96.75
	74.41	0.29	8.30	6.00	*	0.03	0.38	6.28	4.32	0.22	0.37	98.38
	74.78	0.22	8.27	6.05	*	0.02	0.29	6.10	4.28	0.21	0.40	98.13
	74.64	0.25	8.55	6.14	*	0.02	0.20	5.84	4.36	0.21	0.41	97.51
	74.58	0.21	8.97	5.89	*	0.03	0.28	5.92	4.13	0.24	0.31	97.83
	74.30	0.16	8.29	5.76	0.25	0.01	0.24	6.30	4.09	0.38	0.21	96.42
	74.02	0.16	8.43	5.81	0.32	0.02	0.38	6.12	4.22	0.31	0.22	97.61
	74.36	0.18	8.58	5.79	0.29	0.01	0.28	5.91	4.19	0.18	0.21	95.20
	74.95	0.19	8.12	5.73	0.28	0.00	0.15	5.82	4.28	0.25	0.22	95.58
	74.21	0.15	8.28	5.77	0.28	0.01	0.26	6.16	4.30	0.35	0.22	98.87
	74.34	0.15	8.27	5.81	0.21	0.02	0.21	6.22	4.24	0.31	0.22	98.14
	74.10	0.17	8.46	5.99	0.30	0.04	0.22	5.83	4.38	0.28	0.22	96.95
	74.71	0.19	8.37	5.70	0.25	0.01	0.31	5.81	4.17	0.25	0.23	93.45
	74.74	0.20	8.51	5.62	0.30	0.00	0.24	5.66	4.13	0.38	0.22	95.23
	74.37	0.26	8.90	5.55	0.23	0.01	0.19	5.65	4.29	0.34	0.20	92.47
	74.57	0.20	8.23	5.67	0.23	0.01	0.23	6.07	4.31	0.24	0.24	96.06
	74.26	0.19	8.17	5.94	0.35	0.00	0.27	6.16	4.13	0.31	0.22	95.04
	74.21	0.19	8.18	5.82	0.27	0.03	0.26	6.22	4.34	0.26	0.22	97.88
Avg.	74.56	0.19	8.48	5.92	0.10	0.01	0.23	6.06	4.25	0.25	0.29	96.34
Std. Dev	0.38	0.04	0.24	0.18	0.14	0.01	0.08	0.26	0.09	0.05	0.08	
	72.52	0.32	9.96	5.93	*	0.00	0.49	6.29	4.50	0.16	0.04	94.20
MER048H	74.14	0.25	9.33	5.69	*	0.00	0.14	6.00	4.44	0.18	0.30	94.71
	74.53	0.27	8.90	5.66	*	0.05	0.18	5.99	4.42	0.18	0.23	98.15
	74.26	0.23	9.26	5.53	*	0.01	0.22	6.28	4.21	0.18	0.37	98.61

SAMPLE	SiO2	TiO2	Al2O3	FeO	MnO	MgO	CaO	Na2O	K2O	Cl	F	TOTAL
	74.93	0.24	8.85	5.73	*	0.00	0.10	5.91	4.24	0.17	0.20	93.71
MER048H	74.69	0.21	8.75	5.58	*	0.01	0.24	6.31	4.20	0.18	0.24	95.92
cont.	74.91	0.20	9.04	5.72	*	0.01	0.23	5.83	4.06	0.19	0.10	93.30
	74.34	0.24	8.82	6.21	*	0.01	0.24	5.94	4.19	0.16	0.18	98.61
Avg.	74.29	0.25	9.12	5.76	*	0.01	0.23	6.07	4.28	0.18	0.21	95.90
Std. Dev	0.77	0.04	0.40	0.22	*	0.02	0.12	0.19	0.15	0.01	0.10	
	73.64	0.31	8.89	6.55	*	0.03	0.26	5.99	4.35	0.13	0.22	95.65
	74.38	0.35	8.76	6.21	*	0.00	0.21	5.77	4.31	0.15	0.18	96.78
	73.67	0.30	8.65	6.60	*	0.02	0.38	5.99	4.38	0.14	0.25	97.50
	75.14	0.16	8.97	4.98	*	0.03	0.22	6.19	4.32	0.19	0.24	94.27
MER048I	75.57	0.18	8.81	5.19	*	0.00	0.10	5.86	4.28	0.18	0.39	94.28
	75.05	0.14	8.63	5.39	*	0.01	0.36	6.12	4.30	0.23	0.38	92.18
	75.23	0.21	8.98	5.22	*	0.00	0.22	5.94	4.19	0.22	0.23	95.55
	74.80	0.21	9.16	5.29	*	0.00	0.31	5.84	4.39	0.19	0.15	93.54
	74.18	0.30	8.17	6.50	*	0.00	0.31	6.22	4.31	0.14	0.12	93.37
	73.79	0.40	8.43	6.33	*	0.02	0.23	6.46	4.35	0.14	0.16	97.43
Avg.	74.54	0.26	8.75	5.83	*	0.01	0.26	6.04	4.32	0.17	0.23	95.05
Std. Dev	0.71	0.09	0.29	0.66	*	0.01	0.08	0.21	0.06	0.03	0.09	
	75.06	0.31	9.26	5.29	*	0.03	0.05	5.68	4.32	0.15	0.16	96.50
	74.81	0.28	9.10	5.36	*	0.01	0.14	5.99	4.31	0.17	0.29	98.27
	74.96	0.37	9.23	5.26	*	0.02	0.22	5.61	4.32	0.17	0.37	99.75
	74.99	0.29	9.26	5.36	*	0.01	0.14	5.57	4.38	0.15	0.25	97.02
	74.96	0.29	9.12	5.33	*	0.01	0.31	5.89	4.09	0.16	0.29	98.25
	74.24	0.23	9.96	5.45	*	0.01	0.18	5.60	4.32	0.16	0.25	98.57
	73.79	0.24	10.39	5.29	*	0.03	0.28	5.73	4.25	0.14	0.27	93.36
	73.88	0.29	10.04	5.39	*	0.01	0.23	5.83	4.33	0.15	0.13	98.02
	73.92	0.30	9.69	5.46	*	0.03	0.28	5.83	4.48	0.16	0.18	97.34
MER046L	73.80	0.30	9.99	5.34	*	0.01	0.44	5.75	4.37	0.15	0.22	95.96
	73.76	0.27	9.96	5.20	*	0.04	0.36	5.95	4.46	0.13	0.10	96.29
	73.77	0.30	9.74	5.27	*	0.02	0.39	6.10	4.41	0.14	0.15	97.50
	73.42	0.35	8.87	6.02	*	0.03	0.29	6.81	4.21	0.18	0.23	97.40
	73.91	0.28	9.89	5.21	*	0.00	0.21	6.12	4.39	0.17	0.10	99.43
	74.05	0.25	9.67	5.39	*	0.01	0.30	6.03	4.31	0.15	0.00	97.73
	73.90	0.29	9.74	5.38	*	0.00	0.22	6.17	4.29	0.16	0.13	98.91
	74.49	0.21	9.35	5.16	*	0.01	0.22	6.22	4.34	0.20	0.45	95.50
	75.14	0.20	8.99	5.43	*	0.01	0.07	5.71	4.45	0.19	0.43	94.21
	73.69	0.30	10.25	5.46	*	0.02	0.22	5.47	4.59	0.14	0.34	93.03
	74.04	0.30	9.80	5.37	*	0.02	0.38	5.74	4.35	0.14	0.29	95.85
Avg.	74.23	0.28	9.61	5.37	*	0.02	0.25	5.89	4.35	0.16	0.23	96.94
Std. Dev	0.55	0.04	0.44	0.17	*	0.01	0.10	0.30	0.10	0.02	0.12	
MER048N	73.90	0.34	10.16	5.21	*	0.03	0.26	5.59	4.51	0.16	0.22	95.77
	74.52	0.32	9.64	5.00	*	0.07	0.39	5.78	4.28	0.15	0.22	95.87

SAMPLE	SiO2	TiO2	Al2O3	FeO	MnO	MgO	CaO	Na2O	K2O	Cl	F	TOTAL
	73.87	0.34	9.85	5.24	*	0.02	0.32	5.80	4.57	0.17	0.36	92.81
	74.45	0.34	9.81	5.09	*	0.00	0.31	5.57	4.43	0.18	0.33	96.66
	74.24	0.30	9.50	5.21	*	0.00	0.37	5.86	4.53	0.16	0.33	98.23
	74.32	0.27	9.84	5.04	*	0.00	0.25	5.81	4.46	0.18	0.28	97.45
	73.95	0.38	10.04	5.28	*	0.00	0.19	5.76	4.40	0.15	0.13	94.92
	74.53	0.35	9.69	5.23	*	0.00	0.37	5.32	4.49	0.16	0.27	95.29
MER048N	73.53	0.28	10.11	5.17	*	0.00	0.35	5.95	4.60	0.14	0.22	95.01
cont.	74.26	0.42	9.79	5.07	*	0.00	0.43	5.74	4.29	0.16	0.13	96.00
	74.58	0.27	9.91	5.26	*	0.01	0.29	5.26	4.43	0.17	0.36	98.93
	74.05	0.31	10.39	5.25	*	0.00	0.35	5.07	4.58	0.17	0.31	97.28
	74.34	0.25	10.00	5.08	*	0.00	0.19	5.59	4.56	0.18	0.48	97.46
	74.05	0.30	9.68	5.41	*	0.00	0.21	5.90	4.47	0.15	0.32	93.29
	74.18	0.30	10.18	5.21	*	0.00	0.23	5.55	4.37	0.15	0.17	95.52
	74.66	0.36	9.87	5.15	*	0.00	0.17	5.43	4.36	0.17	0.21	96.27
Avg.	74.21	0.32	9.90	5.18	*	0.01	0.29	5.62	4.46	0.16	0.27	96.05
Std. Dev	0.31	0.05	0.23	0.10	*	0.02	0.08	0.25	0.10	0.01	0.09	
	74.02	0.38	9.88	5.17	*	0.00	0.18	5.92	4.45	0.14	0.24	94.80
	73.85	0.30	10.53	5.14	*	0.01	0.21	5.57	4.39	0.15	0.24	94.13
	74.09	0.44	10.18	5.09	*	0.01	0.22	5.54	4.43	0.15	0.16	93.53
	74.05	0.30	10.09	5.17	*	0.01	0.18	5.79	4.41	0.16	0.26	94.75
	73.84	0.32	10.13	5.07	*	0.00	0.29	5.97	4.37	0.15	0.28	96.96
	73.31	0.34	10.39	5.16	*	0.00	0.20	6.07	4.53	0.16	0.08	98.21
	74.15	0.35	10.12	4.90	*	0.00	0.10	5.88	4.51	0.14	0.34	98.42
	74.91	0.27	10.06	4.74	*	0.03	0.09	5.47	4.43	0.20	0.05	97.25
	73.78	0.23	11.05	4.31	*	0.01	0.11	6.29	4.22	0.13	0.12	98.28
	74.83	0.33	9.67	5.35	*	0.00	0.35	4.88	4.60	0.15	0.13	96.23
	73.85	0.40	9.75	5.33	*	0.02	0.37	5.76	4.52	0.16	0.24	94.91
	72.72	0.33	11.69	4.69	*	0.00	0.38	5.41	4.79	0.16	0.09	92.17
	74.55	0.25	9.59	4.57	0.20	0.00	0.06	6.11	4.68	0.12	0.15	96.83
	74.64	0.25	10.15	5.02	0.17	0.00	0.28	5.23	4.25	0.12	0.26	96.23
MER048P	74.51	0.27	10.00	4.74	0.26	0.00	0.15	5.77	4.31	0.12	0.20	96.28
	73.77	0.33	10.55	5.15	0.19	0.00	0.14	5.59	4.28	0.13	0.17	93.99
	74.18	0.35	10.03	4.98	0.21	0.00	0.20	5.52	4.52	0.14	0.24	94.15
	73.57	0.32	10.27	5.04	0.28	0.00	0.29	5.76	4.47	0.14	0.09	97.01
	74.09	0.31	9.86	5.02	0.22	0.00	0.28	5.84	4.38	0.14	0.15	97.64
	73.56	0.34	9.70	4.89	0.24	0.00	1.07	5.99	4.21	0.14	0.13	95.53
	73.62	0.30	10.26	5.08	0.20	0.03	0.11	5.79	4.62	0.14	0.15	92.87
	74.65	0.30	9.67	4.78	0.22	0.03	0.16	5.92	4.27	0.13	0.16	95.27
	73.61	0.32	10.25	4.96	0.17	0.01	0.29	6.01	4.38	0.12	0.27	95.56
	74.57	0.32	10.12	4.85	0.20	0.00	0.27	5.55	4.12	0.13	0.31	93.88
	73.63	0.37	9.76	4.81	0.17	0.01	0.37	6.35	4.53	0.13	0.32	95.40
	73.60	0.31	10.25	4.95	0.14	0.00	0.25	6.33	4.16	0.12	0.25	95.15
	73.72	0.32	10.41	4.91	0.19	0.00	0.23	6.07	4.16	0.13	0.24	93.77
	73.18	0.28	10.37	4.87	0.19	0.01	0.21	6.60	4.28	0.12	0.23	96.73

SAMPLE	SiO2	TiO2	Al2O3	FeO	MnO	MgO	CaO	Na2O	K2O	Cl	F	TOTAL
	74.25	0.31	10.25	4.98	0.19	0.02	0.42	5.22	4.35	0.12	0.22	94.74
	73.35	0.30	11.05	4.98	0.19	0.02	0.25	5.12	4.73	0.12	0.22	92.80
	74.30	0.26	10.38	4.97	0.27	0.01	0.15	5.47	4.19	0.12	0.23	98.99
	73.95	0.28	10.18	4.90	0.22	0.02	0.34	5.72	4.39	0.12	0.25	95.81
MER048P	74.04	0.29	10.10	5.09	0.19	0.01	0.27	5.50	4.51	0.12	0.27	98.20
cont.	73.00	0.29	10.34	4.90	0.23	0.00	0.34	6.43	4.47	0.11	0.28	97.80
	74.95	0.28	9.95	5.05	0.19	0.00	0.17	4.92	4.50	0.12	0.25	97.79
	74.02	0.29	9.93	4.75	0.23	0.00	0.27	5.70	4.80	0.11	0.21	99.79
	74.13	0.31	10.23	5.09	0.26	0.00	0.18	5.42	4.36	0.11	0.22	97.22
	74.67	0.32	10.08	4.83	0.28	0.00	0.55	4.85	4.42	0.11	0.18	96.71
	73.31	0.47	10.29	4.87	0.24	0.07	0.38	5.35	5.02	0.14	0.34	95.31
Avg.	73.97	0.32	10.19	4.95	0.15	0.01	0.27	5.71	4.44	0.13	0.21	95.93
Std. Dev	0.53	0.05	0.40	0.20	0.10	0.01	0.17	0.42	0.19	0.02	0.07	
MER048Q	74.93	0.20	9.72	4.80	*	0.00	0.12	5.79	4.43	0.00	0.16	91.92
	74.27	0.25	10.48	4.75	*	0.01	0.19	5.52	4.52	0.00	0.17	91.53
Avg.	74.60	0.22	10.10	4.77	*	0.00	0.16	5.66	4.48	0.00	0.16	91.72
Std. Dev	0.47	0.04	0.54	0.04	*	0.01	0.05	0.19	0.06	0.00	0.00	
MER048T	72.96	0.37	11.33	4.67	*	0.00	0.46	5.75	4.46	0.00	0.15	95.37
	73.05	0.30	10.64	4.90	*	0.00	0.43	5.70	4.97	0.00	0.15	91.38
Avg.	73.01	0.34	10.98	4.79	*	0.00	0.45	5.72	4.72	0.00	0.15	93.38
Std. Dev	0.07	0.05	0.49	0.16	*	0.00	0.02	0.03	0.36	0.00	0.00	
	74.56	0.34	10.12	4.67	*	0.00	0.23	5.60	4.49	0.18	0.05	97.28
	75.20	0.32	9.99	4.75	*	0.00	0.16	5.32	4.25	0.16	0.04	97.07
	74.79	0.28	9.92	4.78	*	0.00	0.19	5.53	4.50	0.19	0.23	97.15
	75.22	0.27	9.83	4.74	*	0.01	0.21	5.39	4.33	0.17	0.04	95.34
	74.81	0.21	9.95	4.60	*	0.03	0.16	5.75	4.48	0.16	0.29	94.54
MER048U	74.70	0.26	10.03	4.86	*	0.01	0.28	5.53	4.33	0.17	0.19	93.79
	74.24	0.27	10.13	4.83	*	0.01	0.24	5.96	4.31	0.18	0.20	95.89
	74.54	0.26	9.95	5.12	*	0.03	0.22	5.47	4.41	0.16	0.29	94.21
	75.04	0.28	9.54	5.03	*	0.00	0.29	5.64	4.16	0.17	0.31	93.94
	74.99	0.23	9.65	4.91	*	0.01	0.22	5.48	4.51	0.18	0.38	94.22
	74.48	0.29	9.92	5.05	*	0.03	0.35	5.44	4.44	0.17	0.30	93.24
	74.87	0.32	9.82	4.84	*	0.00	0.26	5.42	4.47	0.18	0.19	93.33
Avg.	74.79	0.28	9.90	4.85	*	0.01	0.24	5.55	4.39	0.17	0.21	95.00
Std. Dev	0.30	0.04	0.17	0.16	*	0.01	0.05	0.18	0.11	0.01	0.11	
	74.83	0.22	8.83	5.74	*	0.00	0.30	5.99	4.08	0.17	0.06	97.05
	74.62	0.26	9.05	5.43	*	0.00	0.14	6.29	4.21	0.18	0.26	98.18
	74.63	0.25	9.01	5.50	*	0.01	0.20	5.93	4.46	0.16	0.21	97.32
MER046B	74.94	0.22	8.80	5.64	*	0.00	0.26	5.79	4.35	0.17	0.09	97.26
	74.98	0.29	8.78	5.56	*	0.02	0.22	5.77	4.38	0.16	0.12	98.46
	74.98	0.27	8.81	5.41	*	0.00	0.25	6.10	4.18	0.18	0.22	98.54
	74.81	0.28	9.02	5.30	*	0.00	0.23	5.90	4.47	0.18	0.29	95.29

SAMPLE	SiO2	TiO2	Al2O3	FeO	MnO	MgO	CaO	Na2O	K2O	Cl	F	TOTAL
	74.73	0.21	9.00	5.37	*	0.00	0.26	6.09	4.34	0.17	0.28	94.98
	75.09	0.25	9.11	5.39	*	0.00	0.31	5.65	4.19	0.19	0.26	97.54
	74.08	0.23	9.16	5.66	*	0.00	0.30	6.23	4.35	0.18	0.16	92.09
MER046B	74.45	0.35	9.14	5.41	*	0.07	0.28	5.90	4.41	0.21	0.40	95.25
cont.	75.17	0.31	8.56	5.54	*	0.03	0.26	5.74	4.39	0.19	0.23	95.98
	74.83	0.19	9.05	5.33	*	0.01	0.18	6.05	4.34	0.20	0.11	99.39
	74.79	0.27	9.10	5.44	*	0.05	0.20	5.78	4.37	0.19	0.27	99.45
	74.94	0.26	8.90	5.40	*	0.00	0.21	6.09	4.19	0.20	0.15	97.86
Avg.	74.79	0.26	8.95	5.48	*	0.01	0.24	5.95	4.31	0.18	0.21	96.97
Std. Dev	0.27	0.04	0.17	0.13	*	0.02	0.05	0.19	0.11	0.01	0.09	
	75.16	0.18	8.92	5.45	*	0.00	0.14	5.61	4.54	0.19	0.31	93.76
	74.71	0.21	9.20	5.42	*	0.01	0.19	5.78	4.47	0.19	0.28	93.66
	74.95	0.23	8.68	5.49	*	0.00	0.28	6.08	4.28	0.19	0.34	93.23
	74.85	0.19	9.10	5.31	*	0.00	0.12	6.14	4.29	0.20	0.34	94.96
	74.48	0.25	9.39	5.47	*	0.00	0.17	5.89	4.34	0.18	0.43	93.78
	75.49	0.22	8.52	5.49	*	0.00	0.18	5.69	4.41	0.17	0.44	94.30
	74.49	0.28	8.81	5.73	*	0.02	0.38	5.41	4.89	0.15	0.28	90.27
MER046D	74.61	0.23	9.18	5.53	*	0.00	0.00	6.04	4.40	0.19	0.17	93.25
	74.71	0.25	9.12	5.36	*	0.00	0.05	6.05	4.46	0.17	0.24	92.07
	75.06	0.19	9.06	5.48	*	0.01	0.30	5.61	4.28	0.20	0.26	94.20
	74.87	0.20	8.71	5.43	*	0.02	0.29	6.07	4.41	0.18	0.14	94.32
	74.48	0.27	9.14	5.44	*	0.00	0.19	6.01	4.46	0.18	0.32	93.20
	74.71	0.26	9.30	5.43	*	0.01	0.04	6.00	4.26	0.19	0.25	96.74
	74.86	0.13	9.22	5.34	*	0.01	0.12	5.88	4.43	0.20	0.28	96.05
	75.36	0.18	8.89	5.51	*	0.00	0.00	5.58	4.48	0.21	0.11	92.75
	74.58	0.22	9.07	5.54	*	0.00	0.11	5.96	4.52	0.21	0.11	96.44
Avg.	74.84	0.22	9.02	5.46	*	0.01	0.16	5.86	4.43	0.19	0.27	93.94
Std. Dev	0.31	0.04	0.24	0.10	*	0.01	0.11	0.22	0.15	0.02	0.10	
	75.16	0.18	8.95	5.13	*	0.00	0.13	6.04	4.41	0.20	0.38	95.78
	75.34	0.17	8.87	5.34	*	0.00	0.17	5.78	4.33	0.18	0.41	96.10
	75.51	0.18	8.78	5.22	*	0.00	0.26	5.81	4.24	0.18	0.28	94.21
	75.06	0.18	9.08	5.32	*	0.03	0.33	5.82	4.18	0.18	0.29	93.64
	75.47	0.10	8.72	5.26	*	0.00	0.18	5.95	4.30	0.22	0.37	95.01
	74.79	0.19	9.03	5.13	*	0.02	0.16	6.49	4.19	0.22	0.34	96.86
MER046H	75.06	0.14	8.94	5.21	*	0.00	0.19	6.19	4.27	0.20	0.22	95.10
	75.64	0.23	8.84	5.27	*	0.01	0.18	5.44	4.39	0.20	0.34	97.74
	75.38	0.24	9.15	5.09	*	0.00	0.26	5.66	4.21	0.18	0.22	99.65
	74.98	0.29	8.92	5.62	*	0.01	0.21	5.65	4.32	0.20	0.33	98.38
	74.87	0.24	8.94	5.15	*	0.02	0.30	6.24	4.24	0.20	0.30	96.66
	75.08	0.20	9.37	5.24	*	0.00	0.30	5.57	4.26	0.20	0.29	93.53
	74.44	0.12	9.29	5.39	*	0.00	0.17	6.28	4.32	0.20	0.34	96.47
	75.00	0.15	8.94	5.28	*	0.00	0.16	6.13	4.34	0.20	0.21	97.20
	75.41	0.15	9.23	5.34	*	0.02	0.07	5.66	4.11	0.20	0.41	93.10

SAMPLE	SiO2	TiO2	Al2O3	FeO	MnO	MgO	CaO	Na2O	K2O	Cl	F	TOTAL
	74.81	0.24	9.37	5.38	*	0.00	0.17	5.95	4.08	0.22	0.28	95.38
	75.04	0.24	8.65	5.58	*	0.00	0.29	5.91	4.29	0.21	0.31	95.68
	74.74	0.19	9.21	5.37	*	0.00	0.17	5.89	4.42	0.18	0.27	96.18
	75.11	0.20	8.48	5.61	*	0.00	0.25	5.91	4.43	0.24	0.37	95.91
MER046H	74.89	0.14	9.40	5.08	*	0.00	0.17	5.96	4.36	0.18	0.34	94.96
cont.	75.16	0.18	9.06	5.20	*	0.02	0.20	6.12	4.06	0.20	0.22	94.19
	75.32	0.17	9.16	5.13	*	0.01	0.12	5.78	4.32	0.21	0.27	95.38
	74.80	0.17	9.32	5.39	*	0.00	0.03	5.75	4.54	0.18	0.31	93.20
	74.48	0.18	9.25	5.49	*	0.00	0.23	5.59	4.78	0.20	0.30	92.64
	75.47	0.21	8.67	5.25	*	0.01	0.20	5.88	4.32	0.21	0.34	94.45
Avg.	75.08	0.19	9.02	5.30	*	0.01	0.20	5.90	4.31	0.20	0.31	95.50
Std. Dev	0.31	0.04	0.25	0.16	*	0.01	0.07	0.25	0.15	0.02	0.06	
	73.80	0.25	9.17	4.94	*	0.04	0.11	7.43	4.25	0.17	0.21	93.86
	75.27	0.23	9.02	5.28	*	0.01	0.17	5.79	4.25	0.21	0.37	96.08
	75.16	0.19	9.05	5.20	*	0.00	0.08	6.00	4.32	0.20	0.20	95.76
	75.78	0.22	8.61	5.13	*	0.00	0.14	5.81	4.30	0.19	0.21	93.64
	75.14	0.17	8.81	5.23	*	0.01	0.14	6.10	4.41	0.18	0.16	94.09
	75.27	0.11	9.15	5.16	*	0.01	0.23	5.64	4.45	0.18	0.21	94.02
	74.72	0.21	9.08	5.22	*	0.01	0.23	6.25	4.30	0.20	0.15	93.31
MER046I	75.13	0.24	8.65	5.28	*	0.02	0.15	6.10	4.43	0.21	0.20	93.61
	74.81	0.19	9.13	5.35	*	0.02	0.23	6.07	4.20	0.21	0.35	94.33
	75.02	0.22	9.15	5.30	*	0.01	0.15	5.79	4.36	0.20	0.25	93.76
	75.01	0.22	9.07	5.13	*	0.02	0.14	6.13	4.27	0.20	0.16	96.56
	75.21	0.12	9.09	5.37	*	0.01	0.03	5.80	4.37	0.19	0.24	95.35
	75.47	0.19	9.11	5.15	*	0.01	0.15	5.78	4.16	0.21	0.13	94.73
	75.03	0.18	8.76	5.25	*	0.02	0.08	6.33	4.35	0.20	0.02	96.31
	75.12	0.17	9.21	5.10	*	0.00	0.04	6.12	4.24	0.20	0.18	95.71
Avg.	75.06	0.19	9.00	5.21	*	0.01	0.14	6.07	4.31	0.20	0.20	94.74
Std. Dev	0.43	0.04	0.19	0.11	*	0.01	0.06	0.43	0.08	0.01	0.08	
	74.43	0.32	9.69	5.36	*	0.02	0.19	5.64	4.36	0.17	0.32	99.27
	73.86	0.42	10.02	5.53	*	0.02	0.14	5.52	4.49	0.16	0.19	97.05
	74.91	0.27	9.65	5.19	*	0.02	0.20	5.56	4.20	0.18	0.43	97.40
	75.22	0.26	9.41	4.95	*	0.00	0.20	5.42	4.53	0.18	0.37	94.88
	74.13	0.25	10.08	5.02	*	0.00	0.17	6.39	3.97	0.17	0.39	95.57
	74.95	0.28	9.72	5.16	*	0.02	0.13	5.63	4.11	0.17	0.33	95.86
MER046J	75.33	0.22	9.12	5.14	*	0.02	0.32	5.54	4.32	0.20	0.21	95.76
	74.73	0.19	9.51	5.24	*	0.02	0.15	5.68	4.47	0.19	0.14	99.13
	75.80	0.24	8.93	5.21	*	0.01	0.12	5.34	4.36	0.18	0.11	94.97
	75.19	0.19	9.26	5.13	*	0.04	0.25	5.66	4.28	0.21	0.21	95.91
	74.90	0.24	9.26	5.19	*	0.00	0.25	5.87	4.28	0.20	0.29	99.11
	75.84	0.21	9.29	4.86	*	0.03	0.13	5.37	4.28	0.17	0.20	98.65
	75.13	0.20	9.47	5.18	*	0.01	0.05	5.69	4.27	0.15	0.15	99.00
	75.21	0.20	9.14	5.19	*	0.02	0.17	5.82	4.25	0.16	0.34	97.95

SAMPLE	SiO2	TiO2	Al2O3	FeO	MnO	MgO	CaO	Na2O	K2O	Cl	F	TOTAL
	75.49	0.20	9.03	5.04	*	0.00	0.16	5.82	4.26	0.16	0.38	99.01
	75.29	0.23	9.14	5.26	*	0.00	0.16	5.53	4.40	0.17	0.25	97.90
MER046J	75.48	0.21	9.06	4.82	*	0.01	0.14	6.04	4.23	0.17	0.22	98.64
cont.	73.71	0.28	9.82	5.35	*	0.01	0.18	6.01	4.63	0.14	0.12	98.24
	73.68	0.33	10.06	5.21	*	0.00	0.16	6.31	4.26	0.13	0.28	99.76
	73.87	0.25	9.83	5.32	*	0.00	0.13	6.22	4.38	0.14	0.22	98.26
Avg.	74.86	0.25	9.47	5.17	*	0.01	0.17	5.75	4.32	0.17	0.26	97.62
Std. Dev	0.68	0.06	0.36	0.17	*	0.01	0.06	0.30	0.15	0.02	0.10	
	74.16	0.27	9.91	5.24	*	0.02	0.18	5.92	4.29	0.16	0.13	97.40
	73.87	0.22	10.04	5.27	*	0.00	0.16	6.08	4.34	0.17	0.16	97.55
	74.12	0.24	9.91	5.56	*	0.03	0.15	5.68	4.31	0.17	0.00	96.04
	74.01	0.25	9.80	5.29	*	0.01	0.22	5.98	4.45	0.14	0.11	97.30
	73.71	0.28	9.94	5.58	*	0.00	0.17	5.91	4.41	0.20	0.04	95.67
	73.33	0.28	10.32	5.44	*	0.00	0.18	5.97	4.48	0.17	0.09	97.87
	74.77	0.32	9.41	4.97	*	0.02	0.22	6.01	4.30	0.18	0.36	94.01
	74.79	0.21	9.45	4.99	*	0.00	0.28	5.95	4.32	0.19	0.35	93.41
MER046K	75.22	0.26	9.47	5.10	*	0.01	0.30	5.38	4.25	0.19	0.32	94.80
	74.85	0.35	9.24	5.11	*	0.00	0.30	5.75	4.40	0.21	0.29	94.38
	75.20	0.23	9.28	5.17	*	0.01	0.27	5.64	4.21	0.17	0.37	94.91
	75.13	0.22	9.51	5.09	*	0.01	0.02	5.57	4.46	0.17	0.16	95.99
	75.47	0.28	8.87	5.00	*	0.02	0.18	5.88	4.30	0.17	0.22	96.17
	74.78	0.27	9.42	5.18	*	0.03	0.20	5.57	4.56	0.17	0.21	95.87
	74.11	0.32	9.44	5.40	*	0.01	0.37	6.01	4.34	0.15	0.30	99.85
	74.23	0.30	9.71	5.41	*	0.02	0.26	5.82	4.25	0.17	0.21	99.29
	73.74	0.39	9.83	5.37	*	0.00	0.34	6.03	4.31	0.16	0.23	98.03
Avg.	74.44	0.28	9.62	5.25	*	0.01	0.22	5.83	4.35	0.17	0.21	96.38
Std. Dev	0.63	0.05	0.36	0.19	*	0.01	0.08	0.20	0.09	0.02	0.11	
	75.35	0.30	9.76	5.64	*	0.00	0.27	4.28	4.41	0.15	0.24	95.56
	74.19	0.18	9.83	5.27	*	0.00	0.16	6.04	4.32	0.17	0.14	94.81
	73.54	0.32	9.95	5.32	*	0.00	0.26	6.20	4.41	0.17	0.08	97.08
	74.01	0.32	9.64	5.42	*	0.00	0.40	5.76	4.45	0.16	0.39	93.33
	74.01	0.34	9.71	5.34	*	0.00	0.25	5.94	4.41	0.15	0.21	94.30
	73.90	0.19	9.68	5.24	*	0.00	0.21	6.33	4.45	0.16	0.16	94.72
	73.60	0.24	10.06	5.43	*	0.00	0.26	6.09	4.30	0.15	0.20	93.02
MER046L	73.42	0.35	10.20	5.47	*	0.00	0.27	5.98	4.31	0.17	0.35	93.40
	74.09	0.26	9.54	5.21	*	0.00	0.27	6.25	4.37	0.16	0.05	97.25
	73.11	0.29	10.37	5.24	*	0.00	0.38	6.34	4.28	0.14	0.04	93.12
	73.81	0.18	10.03	5.47	*	0.00	0.16	5.79	4.57	0.16	0.33	92.83
	73.90	0.29	9.83	5.32	*	0.00	0.16	6.29	4.22	0.15	0.29	93.86
	73.69	0.27	10.07	5.47	*	0.00	0.16	5.83	4.51	0.16	0.38	93.70
	75.06	0.31	9.26	5.29	*	0.03	0.05	5.68	4.32	0.15	0.16	96.50
	74.81	0.28	9.10	5.36	*	0.01	0.14	5.99	4.31	0.17	0.29	98.27
	74.96	0.37	9.23	5.26	*	0.02	0.22	5.61	4.32	0.17	0.37	99.75

SAMPLE	SiO2	TiO2	Al2O3	FeO	MnO	MgO	CaO	Na2O	K2O	Cl	F	TOTAL
	74.99	0.29	9.26	5.36	*	0.01	0.14	5.57	4.38	0.15	0.25	97.02
	74.96	0.29	9.12	5.33	*	0.01	0.31	5.89	4.09	0.16	0.29	98.25
	74.24	0.23	9.96	5.45	*	0.01	0.18	5.60	4.32	0.16	0.25	98.57
	73.79	0.24	10.39	5.29	*	0.03	0.28	5.73	4.25	0.14	0.27	93.36
	73.88	0.29	10.04	5.39	*	0.01	0.23	5.83	4.33	0.15	0.13	98.02
	73.92	0.30	9.69	5.46	*	0.03	0.28	5.83	4.48	0.16	0.18	97.34
	73.80	0.30	9.99	5.34	*	0.01	0.44	5.75	4.37	0.15	0.22	95.96
	73.76	0.27	9.96	5.20	*	0.04	0.36	5.95	4.46	0.13	0.10	96.29
MER046L	73.77	0.30	9.74	5.27	*	0.02	0.39	6.10	4.41	0.14	0.15	97.50
cont.	73.42	0.35	8.87	6.02	*	0.03	0.29	6.81	4.21	0.18	0.23	97.40
	73.91	0.28	9.89	5.21	*	0.00	0.21	6.12	4.39	0.17	0.10	99.43
	74.05	0.25	9.67	5.39	*	0.01	0.30	6.03	4.31	0.15	0.00	97.73
	73.90	0.29	9.74	5.38	*	0.00	0.22	6.17	4.29	0.16	0.13	98.91
	74.49	0.21	9.35	5.16	*	0.01	0.22	6.22	4.34	0.20	0.45	95.50
	75.14	0.20	8.99	5.43	*	0.01	0.07	5.71	4.45	0.19	0.43	94.21
	73.69	0.30	10.25	5.46	*	0.02	0.22	5.47	4.59	0.14	0.34	93.03
	74.04	0.30	9.80	5.37	*	0.02	0.38	5.74	4.35	0.14	0.29	95.85
Avg.	74.10	0.28	9.73	5.37	*	0.01	0.25	5.91	4.36	0.16	0.23	95.94
Std. Dev	0.56	0.05	0.39	0.15	*	0.01	0.09	0.40	0.10	0.02	0.12	
	75.13	0.07	8.27	5.97	*	0.00	0.21	6.13	4.21	0.24	0.45	98.66
	74.73	0.13	9.61	5.48	*	0.01	0.21	5.79	4.04	0.30	0.25	98.20
MER046Q	73.85	0.15	8.51	5.90	*	0.01	0.21	7.30	4.07	0.22	0.31	98.39
	74.35	0.23	9.17	5.62	*	0.04	0.35	6.26	3.98	0.21	0.41	93.16
	74.55	0.21	8.46	6.18	*	0.03	0.16	6.24	4.18	0.24	0.44	96.77
Avg.	74.52	0.16	8.80	5.83	*	0.02	0.23	6.34	4.10	0.24	0.37	97.04
Std. Dev	0.47	0.06	0.57	0.28	*	0.02	0.07	0.57	0.10	0.04	0.09	
	73.06	0.30	10.06	5.60	0.17	0.02	0.27	5.81	4.72	0.12	0.15	95.64
	73.48	0.33	9.72	5.51	0.18	0.03	0.56	6.36	3.83	0.11	0.05	92.90
	72.29	0.40	10.41	5.63	0.26	0.03	0.34	6.20	4.43	0.11	0.18	98.94
	72.29	0.35	10.32	5.89	0.28	0.01	0.46	5.95	4.45	0.10	0.21	95.52
	72.39	0.37	10.19	5.99	0.28	0.03	0.47	6.03	4.26	0.10	0.19	95.00
	71.74	0.36	10.02	5.74	0.30	0.01	0.44	6.99	4.40	0.10	0.25	95.90
	71.84	0.33	10.14	5.67	0.27	0.02	0.35	6.99	4.39	0.10	0.26	97.54
MER046R	71.20	0.39	9.83	5.75	0.24	0.08	0.54	7.66	4.31	0.13	0.32	93.54
	72.41	0.38	10.41	5.44	0.23	0.07	0.39	6.43	4.24	0.11	0.33	99.23
	72.12	0.38	9.96	5.57	0.24	0.06	0.32	7.09	4.26	0.12	0.30	98.02
	74.42	0.34	9.60	5.50	0.25	0.02	0.34	5.42	4.10	0.13	0.32	96.36
	72.84	0.35	9.70	5.93	0.27	0.04	0.16	6.59	4.13	0.10	0.20	100.95
	72.10	0.34	9.95	5.72	0.19	0.04	0.24	7.10	4.33	0.09	0.26	104.05
	72.94	0.38	9.91	6.18	0.21	0.02	0.36	5.36	4.65	0.09	0.09	94.19
	72.53	0.39	10.24	5.97	0.24	0.02	0.28	5.52	4.80	0.10	0.19	96.60
Avg.	72.51	0.36	10.03	5.74	0.24	0.03	0.37	6.37	4.35	0.11	0.22	96.96

SAMPLE	SiO2	TiO2	Al2O3	FeO	MnO	MgO	CaO	Na2O	K2O	Cl	F	TOTAL
Std. Dev	0.77	0.03	0.26	0.21	0.04	0.02	0.11	0.70	0.25	0.01	0.08	
	73.16	0.28	10.24	5.33	0.21	0.02	0.42	5.84	4.50	0.12	0.19	97.14
	73.25	0.30	9.93	5.53	0.22	0.02	0.15	6.15	4.44	0.12	0.23	95.28
	73.03	0.30	9.66	5.76	0.23	0.01	0.68	5.89	4.44	0.14	0.14	95.84
	75.12	0.25	9.33	5.13	0.18	0.00	0.45	5.17	4.36	0.16	0.15	99.42
	73.57	0.24	9.52	4.95	0.16	0.00	0.40	6.50	4.65	0.16	0.16	93.36
	75.21	0.19	9.38	4.80	0.20	0.01	0.19	5.73	4.28	0.13	0.28	100.71
	74.13	0.20	9.90	5.07	0.21	0.01	0.47	5.67	4.34	0.13	0.12	93.64
	73.60	0.33	10.18	5.09	0.21	0.01	0.14	6.05	4.39	0.12	0.16	93.31
MER046T	73.64	0.31	10.11	5.03	0.26	0.01	0.42	5.87	4.36	0.12	0.18	94.18
	75.33	0.28	9.14	4.88	0.22	0.00	0.57	5.39	4.18	0.13	0.19	96.20
	75.18	0.21	9.28	4.84	0.19	0.00	0.25	5.62	4.43	0.13	0.30	98.74
	74.83	0.24	9.27	4.79	0.19	0.00	0.24	6.18	4.26	0.14	0.18	95.62
	74.74	0.21	9.00	4.98	0.22	0.00	0.19	6.03	4.61	0.14	0.27	96.71
	75.00	0.17	9.34	4.75	0.15	0.00	0.22	6.04	4.34	0.12	0.16	96.69
	74.58	0.18	9.54	4.82	0.19	0.01	0.22	6.16	4.29	0.14	0.26	95.24
	75.31	0.15	9.37	4.77	0.17	0.00	0.13	5.85	4.24	0.14	0.18	94.53
	74.70	0.26	9.62	4.83	0.16	0.00	0.17	5.92	4.35	0.15	0.31	94.25
Avg.	74.38	0.24	9.58	5.02	0.20	0.01	0.31	5.89	4.38	0.14	0.20	95.93
Std. Dev	0.83	0.05	0.37	0.28	0.03	0.01	0.17	0.31	0.12	0.01	0.06	
	74.72	0.24	9.09	5.67	*	0.01	0.23	5.80	4.24	0.14	0.18	98.16
	73.99	0.23	9.15	5.94	*	0.00	0.26	6.07	4.36	0.15	0.10	98.43
	74.22	0.21	9.02	5.82	*	0.00	0.39	5.99	4.35	0.15	0.26	98.11
	74.79	0.19	8.77	5.63	*	0.00	0.20	6.10	4.32	0.17	0.35	96.56
	74.34	0.32	9.22	5.60	*	0.02	0.24	5.78	4.48	0.17	0.28	95.38
	74.88	0.26	9.18	5.73	*	0.00	0.20	5.53	4.23	0.14	0.15	98.90
MER046V	74.37	0.30	8.98	5.76	*	0.02	0.25	5.71	4.61	0.18	0.12	95.78
	74.64	0.25	8.72	5.55	*	0.01	0.15	6.36	4.33	0.15	0.16	95.66
	74.79	0.28	8.85	5.66	*	0.00	0.12	6.09	4.21	0.15	0.23	95.48
	74.97	0.25	8.83	5.54	*	0.00	0.27	5.65	4.49	0.16	0.37	95.89
	74.42	0.26	8.86	5.74	*	0.00	0.33	6.22	4.17	0.17	0.21	94.87
	74.41	0.32	9.20	5.67	*	0.01	0.11	5.79	4.50	0.17	0.15	98.45
	74.71	0.23	9.09	5.77	*	0.02	0.16	5.65	4.37	0.18	0.13	97.30
	74.98	0.22	8.76	5.71	*	0.01	0.30	5.84	4.18	0.15	0.27	96.06
Avg.	74.59	0.25	8.98	5.70	*	0.01	0.23	5.90	4.35	0.16	0.21	96.79
Std. Dev	0.30	0.04	0.18	0.11	*	0.01	0.08	0.24	0.13	0.01	0.08	
	74.31	0.24	9.04	5.77	*	0.00	0.18	6.24	4.21	0.15	0.08	97.10
	74.51	0.28	9.00	5.61	*	0.01	0.22	5.83	4.54	0.15	0.16	98.10
	74.15	0.28	9.11	5.76	*	0.00	0.22	6.07	4.41	0.17	0.11	93.43
MER046X	75.36	0.20	8.65	5.70	*	0.00	0.19	5.50	4.40	0.16	0.21	97.07
	75.05	0.25	9.20	5.56	*	0.03	0.27	5.28	4.36	0.16	0.24	92.49
	74.80	0.29	9.09	5.62	*	0.03	0.31	5.65	4.21	0.14	0.24	94.08
	74.51	0.24	8.94	5.84	*	0.01	0.25	5.77	4.43	0.14	0.15	94.19

SAMPLE	SiO2	TiO2	Al2O3	FeO	MnO	MgO	CaO	Na2O	K2O	Cl	F	TOTAL
	74.12	0.21	9.06	5.65	*	0.02	0.33	6.18	4.42	0.14	0.14	94.06
MER046X	74.23	0.24	8.97	5.92	*	0.03	0.25	5.91	4.46	0.17	0.26	94.70
cont.	74.54	0.18	8.87	5.99	*	0.01	0.20	5.61	4.59	0.17	0.36	93.36
	74.49	0.19	9.05	5.81	*	0.00	0.17	5.92	4.38	0.17	0.34	93.59
Avg.	74.55	0.24	9.00	5.75	*	0.01	0.24	5.82	4.40	0.16	0.21	94.74
Std. Dev	0.38	0.04	0.15	0.14	*	0.01	0.05	0.29	0.12	0.01	0.09	
	73.15	0.39	9.65	6.05	*	0.01	0.38	5.97	4.41	0.13	0.30	93.60
	73.00	0.39	9.55	5.95	*	0.00	0.34	6.36	4.42	0.12	0.28	94.12
	72.89	0.39	9.87	5.97	*	0.00	0.36	6.03	4.50	0.14	0.26	94.97
	73.55	0.29	9.80	5.98	*	0.00	0.12	5.77	4.50	0.15	0.33	99.33
	73.67	0.45	9.65	5.70	*	0.04	0.20	5.77	4.52	0.16	0.23	94.86
	73.30	0.48	9.42	5.89	*	0.03	0.35	6.13	4.41	0.16	0.24	95.87
	73.18	0.50	9.55	6.35	*	0.01	0.30	5.58	4.53	0.16	0.26	94.29
	73.47	0.41	9.62	5.86	*	0.02	0.27	6.12	4.24	0.14	0.12	95.57
	73.67	0.38	9.85	6.08	*	0.03	0.43	5.10	4.47	0.14	0.19	94.04
MER046Z	73.22	0.36	9.75	6.05	*	0.01	0.32	5.97	4.31	0.13	0.03	95.15
	72.89	0.38	9.88	6.20	*	0.00	0.31	5.86	4.49	0.15	0.12	94.80
	74.82	0.28	9.19	5.44	*	0.00	0.30	6.00	3.97	0.16	0.29	93.05
	74.66	0.37	9.37	5.43	*	0.02	0.23	5.81	4.12	0.15	0.22	95.81
	73.57	0.34	9.54	5.83	*	0.00	0.28	6.15	4.29	0.16	0.24	98.81
	73.49	0.39	9.44	5.91	*	0.03	0.28	5.95	4.52	0.15	0.26	96.28
	73.87	0.38	9.83	5.76	*	0.04	0.28	5.54	4.30	0.15	0.24	97.55
	73.12	0.32	9.91	5.86	*	0.02	0.29	6.17	4.32	0.14	0.04	98.96
	73.36	0.30	9.90	5.83	*	0.01	0.31	6.10	4.19	0.13	0.23	99.59
	73.17	0.38	9.60	6.16	*	0.00	0.34	5.99	4.37	0.13	0.27	97.90
	72.91	0.38	10.16	6.02	*	0.02	0.36	5.80	4.37	0.14	0.18	96.18
Avg.	73.45	0.38	9.68	5.92	*	0.01	0.30	5.91	4.36	0.15	0.22	96.04
Std. Dev	0.52	0.06	0.23	0.22	*	0.01	0.07	0.28	0.15	0.01	0.08	
	74.37	0.12	9.43	5.74	0.16	0.00	0.31	5.45	4.41	0.29	0.12	91.77
	74.63	0.12	9.33	5.53	0.16	0.00	0.27	5.42	4.54	0.25	0.16	91.23
	74.48	0.15	8.95	5.64	0.24	0.00	0.29	5.65	4.60	0.20	0.19	90.04
	74.05	0.16	8.98	5.78	0.23	0.00	0.22	5.99	4.58	0.18	0.15	91.08
	73.61	0.21	7.97	6.61	0.36	0.00	0.23	6.91	4.10	0.14	0.23	98.02
	73.29	0.33	8.27	6.96	0.55	0.00	0.36	5.28	4.96	0.15	0.36	64.28
	72.74	0.23	7.94	6.81	0.40	0.00	0.21	7.05	4.63	0.12	0.24	91.38
MER050A	74.24	0.29	7.53	6.09	0.47	0.00	0.76	6.61	4.01	0.14	0.27	79.04
	74.50	0.21	8.70	5.21	0.31	0.00	0.14	6.45	4.48	0.09	0.21	96.03
	74.14	0.20	8.22	6.68	0.04	0.00	0.18	6.06	4.47	0.27	0.19	95.85
	73.31	0.13	8.36	6.43	*	0.00	0.24	7.48	4.05	0.29	0.36	99.22
	73.56	0.16	8.36	6.64	*	0.00	0.18	6.92	4.18	0.27	0.40	96.86
	73.64	0.08	8.27	6.79	*	0.00	0.16	6.81	4.25	0.25	0.60	97.62
	73.75	0.15	8.14	6.65	*	0.00	0.12	6.99	4.18	0.26	0.35	97.53
	74.50	0.35	9.52	5.38	*	0.00	0.05	5.95	4.25	0.14	0.17	96.01

SAMPLE	SiO2	TiO2	Al2O3	FeO	MnO	MgO	CaO	Na2O	K2O	Cl	F	TOTAL
	74.23	0.35	9.81	5.24	*	0.00	0.16	5.83	4.37	0.16	0.22	94.61
	73.82	0.12	7.85	6.55	*	0.00	0.13	7.46	4.07	0.29	0.47	98.71
MER050A	74.07	0.17	7.93	6.74	*	0.00	0.24	6.75	4.09	0.29	0.23	95.64
cont.	74.78	0.32	9.34	5.43	*	0.00	0.29	5.68	4.15	0.14	0.02	93.68
	74.84	0.31	9.01	5.50	*	0.00	0.33	5.82	4.19	0.14	0.36	93.27
	74.41	0.32	9.31	5.48	*	0.00	0.31	5.74	4.43	0.14	0.21	93.84
Avg.	74.05	0.21	8.63	6.09	0.14	0.00	0.25	6.30	4.33	0.20	0.26	92.65
Std. Dev	0.55	0.09	0.66	0.62	0.18	0.00	0.14	0.69	0.24	0.07	0.13	
	74.14	0.11	8.72	6.05	*	0.00	0.13	6.58	4.27	0.25	0.32	100.64
	73.53	0.14	8.89	6.11	*	0.00	0.09	6.78	4.45	0.26	0.24	98.42
	73.92	0.25	7.87	6.81	*	0.00	0.13	6.95	4.08	0.27	0.29	99.38
	74.75	0.11	7.82	6.31	*	0.00	0.20	6.77	4.05	0.25	0.24	93.68
	73.70	0.18	7.95	6.68	*	0.00	0.27	7.05	4.18	0.25	0.51	92.82
	73.69	0.10	8.63	6.32	*	0.00	0.31	7.03	3.90	0.24	0.46	94.96
	73.90	0.19	8.34	6.64	*	0.00	0.17	6.68	4.08	0.30	0.51	97.78
	74.03	0.11	7.75	6.71	*	0.00	0.31	6.97	4.12	0.29	0.33	98.23
MER050B	73.82	0.16	8.37	6.56	*	0.00	0.14	6.87	4.08	0.29	0.41	100.23
	74.22	0.13	7.65	6.50	*	0.00	0.33	7.14	4.04	0.27	0.41	98.90
	73.92	0.07	8.30	6.41	*	0.00	0.31	6.82	4.17	0.27	0.36	98.73
	73.80	0.18	8.03	6.61	*	0.00	0.26	7.10	4.02	0.29	0.32	98.14
	73.75	0.12	8.05	6.77	*	0.00	0.29	7.05	3.96	0.29	0.20	97.99
	74.05	0.05	7.77	6.32	*	0.00	0.33	7.22	4.27	0.28	0.30	94.08
	73.94	0.11	7.81	6.87	*	0.00	0.27	6.87	4.14	0.28	0.37	98.28
	73.86	0.14	7.75	6.90	*	0.00	0.06	7.09	4.20	0.27	0.30	96.66
	73.62	0.19	7.67	7.10	*	0.00	0.15	7.12	4.15	0.30	0.37	97.80
	74.71	0.11	7.82	6.58	*	0.00	0.16	6.45	4.18	0.25	0.34	94.51
Avg.	73.96	0.14	8.07	6.57	*	0.00	0.22	6.92	4.13	0.27	0.35	97.29
Std. Dev	0.33	0.05	0.38	0.28	*	0.00	0.09	0.21	0.13	0.02	0.09	
	73.75	0.06	7.77	6.52	0.28	0.00	0.04	7.76	3.82	0.31	0.41	100.15
	74.06	0.07	7.82	6.38	0.32	0.00	0.05	7.36	3.95	0.31	0.37	99.79
	73.72	0.06	7.87	6.41	0.30	0.00	0.05	7.62	3.97	0.28	0.28	99.56
	71.86	0.05	9.02	6.83	0.29	0.02	0.04	7.37	4.52	0.27	0.38	96.99
	74.05	0.11	8.52	6.58	*	0.00	0.23	6.36	4.15	0.26	0.25	92.18
	73.97	0.12	7.92	6.65	*	0.00	0.05	7.24	4.06	0.26	0.45	95.15
	73.91	0.15	8.09	6.83	*	0.00	0.06	7.05	3.90	0.27	0.48	98.77
MER050C	73.82	0.12	7.89	6.89	*	0.00	0.15	7.06	4.07	0.29	0.45	96.52
	74.19	0.19	7.76	6.80	*	0.00	0.11	6.99	3.96	0.29	0.33	96.25
	74.67	0.16	7.96	6.50	*	0.00	0.11	6.52	4.08	0.29	0.29	92.35
	73.95	0.15	7.75	6.64	*	0.02	0.24	7.11	4.15	0.27	0.39	93.38
	74.33	0.21	8.02	6.23	*	0.00	0.20	6.98	4.03	0.28	0.29	97.21
	73.89	0.16	7.90	6.44	*	0.00	0.22	7.31	4.10	0.28	0.42	98.13
	74.08	0.15	8.20	6.61	*	0.00	0.20	6.73	4.04	0.28	0.43	97.42
	73.91	0.12	8.23	6.82	*	0.00	0.23	6.51	4.17	0.26	0.28	97.18

SAMPLE	SiO2	TiO2	Al2O3	FeO	MnO	MgO	CaO	Na2O	K2O	Cl	F	TOTAL
MER050C	74.39	0.19	8.02	6.37	*	0.02	0.07	6.89	4.05	0.30	0.32	97.40
cont.	74.16	0.15	8.31	6.40	*	0.02	0.17	6.67	4.13	0.29	0.30	97.40
Avg.	73.92	0.13	8.06	6.58	0.07	0.00	0.13	7.03	4.07	0.28	0.36	96.81
Std. Dev	0.58	0.05	0.33	0.20	0.13	0.01	0.08	0.39	0.15	0.02	0.07	
	74.41	0.06	8.07	6.25	0.32	0.00	0.09	6.67	4.14	0.24	0.33	99.33
	73.64	0.07	8.03	6.39	0.25	0.02	0.12	7.46	4.03	0.24	0.33	99.84
	74.03	0.06	8.15	6.20	0.31	0.00	0.05	7.18	4.03	0.25	0.30	100.25
	74.60	0.13	8.64	5.93	*	0.00	0.36	6.07	4.26	0.24	0.25	96.97
	74.33	0.13	8.31	6.11	*	0.00	0.37	6.50	4.24	0.23	0.11	96.87
	74.44	0.14	8.29	6.13	*	0.00	0.24	6.58	4.18	0.25	0.20	94.89
	74.56	0.12	8.74	6.06	*	0.01	0.37	6.12	4.01	0.22	0.20	95.31
	74.49	0.11	8.40	5.94	*	0.02	0.30	6.68	4.06	0.23	0.31	97.18
	74.17	0.18	8.50	5.97	*	0.00	0.20	6.65	4.33	0.22	0.34	95.70
	74.86	0.16	8.40	5.88	*	0.00	0.28	6.02	4.40	0.22	0.13	97.90
MER050F	75.01	0.21	8.52	5.76	*	0.01	0.30	5.89	4.31	0.22	0.16	97.08
	74.61	0.14	8.38	6.37	*	0.00	0.12	5.96	4.42	0.21	0.40	92.05
	74.68	0.17	8.36	6.05	*	0.00	0.12	6.48	4.15	0.20	0.45	93.60
	74.40	0.13	8.49	6.18	*	0.00	0.17	6.52	4.12	0.22	0.30	95.37
	74.36	0.10	8.61	6.00	*	0.01	0.27	6.37	4.29	0.21	0.37	96.39
	74.57	0.18	8.32	5.92	*	0.01	0.32	6.62	4.07	0.21	0.35	96.39
	73.63	0.14	8.96	6.02	*	0.03	0.36	6.44	4.42	0.24	0.45	92.28
	74.59	0.19	8.61	5.93	*	0.00	0.41	5.92	4.35	0.21	0.36	96.15
	72.75	0.15	8.38	6.57	0.32	0.00	0.26	7.24	4.33	0.24	0.34	93.68
	73.01	0.15	8.28	6.48	0.34	0.00	0.30	7.15	4.30	0.28	0.36	94.71
	72.98	0.14	8.17	6.50	0.31	0.00	0.30	7.31	4.28	0.29	0.33	96.80
	73.20	0.14	8.44	6.43	0.32	0.00	0.24	6.90	4.33	0.23	0.33	96.55
Avg.	74.15	0.14	8.41	6.14	0.10	0.01	0.25	6.58	4.23	0.23	0.31	96.15
Std. Dev	0.65	0.04	0.22	0.23	0.15	0.01	0.10	0.47	0.13	0.02	0.09	
	72.97	0.22	8.29	6.68	0.30	0.01	0.19	6.87	4.47	0.21	0.26	95.30
	72.96	0.23	8.43	6.48	0.31	0.00	0.26	6.79	4.54	0.22	0.28	95.46
MER050G	73.24	0.22	8.48	6.59	0.30	0.00	0.21	6.44	4.52	0.21	0.26	95.33
	73.33	0.22	8.54	6.74	0.30	0.00	0.24	6.23	4.40	0.20	0.27	94.88
	73.45	0.21	8.59	6.43	0.30	0.03	0.17	6.30	4.52	0.22	0.27	96.26
Avg.	73.19	0.22	8.47	6.58	0.30	0.01	0.21	6.53	4.49	0.21	0.27	95.45
Std. Dev	0.22	0.01	0.12	0.13	0.00	0.01	0.04	0.29	0.06	0.01	0.01	
	74.03	0.36	8.77	5.95	0.28	0.00	0.25	5.78	4.59	0.18	0.20	93.15
	73.76	0.35	8.70	6.13	0.27	0.00	0.28	6.09	4.43	0.17	0.21	97.15
	73.86	0.27	8.74	6.36	*	0.00	0.19	6.10	4.47	0.16	0.15	96.78
MER050H	73.90	0.33	9.10	6.08	*	0.01	0.25	6.02	4.31	0.16	0.25	98.06
	74.58	0.28	8.57	6.06	*	0.00	0.15	5.90	4.46	0.16	0.21	98.48
	74.48	0.38	8.36	6.07	*	0.01	0.28	6.06	4.35	0.15	0.21	98.06
	73.77	0.31	8.84	6.24	*	0.00	0.21	6.24	4.39	0.18	0.16	97.20

SAMPLE	SiO2	TiO2	Al2O3	FeO	MnO	MgO	CaO	Na2O	K2O	Cl	F	TOTAL
	73.99	0.37	8.90	6.26	*	0.00	0.26	5.81	4.41	0.16	0.31	96.95
	74.82	0.31	8.47	6.28	*	0.01	0.24	5.62	4.26	0.17	0.16	98.39
MER050H	74.09	0.28	8.63	6.30	*	0.05	0.42	5.87	4.37	0.16	0.06	97.43
cont.	74.04	0.31	8.95	6.08	*	0.00	0.23	6.13	4.26	0.15	0.15	98.63
	74.23	0.36	8.87	6.21	*	0.00	0.19	5.60	4.53	0.14	0.18	97.16
	74.48	0.34	8.72	6.08	*	0.00	0.24	5.79	4.34	0.17	0.00	97.10
Avg.	74.16	0.33	8.74	6.16	0.04	0.01	0.24	5.92	4.40	0.16	0.17	97.27
Std. Dev	0.34	0.04	0.20	0.12	0.10	0.01	0.06	0.20	0.10	0.01	0.08	
	73.83	0.15	8.57	6.35	0.28	0.02	0.23	6.23	4.35	0.20	0.28	93.30
	73.48	0.19	8.18	6.53	0.33	0.02	0.15	6.80	4.33	0.22	0.29	95.55
MER050J	72.93	0.18	8.45	6.62	0.34	0.02	0.13	6.94	4.39	0.21	0.28	94.87
	73.05	0.18	8.57	7.00	0.33	0.02	0.15	6.52	4.18	0.22	0.29	94.64
	73.77	0.14	8.42	6.24	0.26	0.02	0.17	6.53	4.44	0.19	0.25	95.48
	73.69	0.17	8.42	6.61	0.28	0.02	0.20	6.05	4.57	0.19	0.29	95.53
Avg.	73.46	0.17	8.43	6.56	0.30	0.02	0.17	6.51	4.38	0.20	0.28	94.90
Std. Dev	0.38	0.02	0.14	0.26	0.03	0.00	0.04	0.34	0.13	0.01	0.01	
	74.10	0.32	8.80	6.18	*	0.00	0.33	6.04	4.23	0.17	0.26	97.21
	74.28	0.30	9.07	5.96	*	0.00	0.22	5.75	4.43	0.17	0.18	98.51
	74.02	0.36	9.06	6.02	*	0.00	0.25	5.93	4.35	0.17	0.32	98.21
	74.03	0.33	8.60	6.05	*	0.00	0.14	6.52	4.32	0.16	0.31	99.14
	74.80	0.34	8.51	6.13	*	0.00	0.07	5.83	4.32	0.15	0.13	98.46
	73.85	0.30	8.96	6.09	*	0.00	0.01	6.31	4.47	0.17	0.11	98.25
	74.43	0.32	9.09	5.77	*	0.00	0.16	5.96	4.27	0.15	0.16	98.20
	74.08	0.40	8.98	5.88	*	0.00	0.23	6.17	4.26	0.16	0.18	98.36
	74.57	0.36	8.65	5.93	*	0.00	0.13	6.03	4.33	0.16	0.29	99.43
MER050M	74.48	0.25	8.68	6.07	*	0.00	0.07	6.19	4.27	0.17	0.33	99.14
	74.17	0.31	8.83	6.24	*	0.00	0.07	6.14	4.25	0.18	0.24	99.43
	74.35	0.30	8.75	6.11	*	0.00	0.44	5.78	4.26	0.16	0.01	97.44
	74.15	0.37	8.90	6.23	*	0.00	0.25	5.67	4.43	0.17	0.16	98.76
	73.89	0.41	8.96	6.07	*	0.00	0.33	5.90	4.45	0.16	0.22	98.83
	74.49	0.32	8.71	6.05	*	0.00	0.29	5.86	4.28	0.16	0.00	98.63
	74.62	0.36	8.75	6.09	*	0.00	0.28	5.37	4.52	0.17	0.31	98.12
	74.63	0.26	8.70	6.01	*	0.00	0.21	5.87	4.32	0.14	0.40	98.58
	73.90	0.35	8.83	6.28	*	0.00	0.24	6.05	4.35	0.16	0.24	97.42
	73.79	0.34	8.85	6.17	*	0.00	0.30	6.29	4.27	0.14	0.19	98.07
Avg.	74.24	0.33	8.82	6.07	*	0.00	0.21	5.98	4.34	0.16	0.21	98.43
Std. Dev	0.30	0.04	0.17	0.13	*	0.00	0.11	0.26	0.09	0.01	0.11	
	73.76	0.13	7.85	6.81	*	0.00	0.25	7.31	3.88	0.32	0.36	96.59
	74.52	0.16	8.65	5.91	*	0.01	0.19	6.51	4.05	0.23	0.24	96.37
MER050N	72.40	0.15	9.45	6.19	*	0.00	0.12	7.26	4.43	0.22	0.20	99.22
	74.62	0.17	8.24	6.28	*	0.02	0.19	6.53	3.95	0.24	0.35	95.08
	73.56	0.14	8.35	6.36	*	0.05	0.19	7.30	4.06	0.24	0.38	96.79

SAMPLE	SiO2	TiO2	Al2O3	FeO	MnO	MgO	CaO	Na2O	K2O	Cl	F	TOTAL
MER050N	74.48	0.12	8.29	6.40	*	0.01	0.21	6.50	3.99	0.26	0.30	94.69
cont.	74.43	0.10	8.48	6.21	*	0.02	0.32	6.43	4.00	0.22	0.30	93.46
Avg.	73.97	0.14	8.47	6.31	*	0.02	0.21	6.84	4.05	0.25	0.30	96.03
Std. Dev	0.80	0.02	0.50	0.27	*	0.02	0.06	0.43	0.18	0.03	0.06	
	73.45	0.19	7.84	7.00	*	0.00	0.28	6.82	4.41	0.28	0.27	97.12
	72.89	0.14	9.35	6.16	*	0.00	0.16	6.77	4.53	0.24	0.30	97.30
MER050R	74.21	0.15	8.52	6.01	*	0.02	0.21	6.62	4.24	0.21	0.36	96.55
	73.89	0.14	8.65	6.08	*	0.02	0.17	6.81	4.24	0.21	0.31	96.36
	73.80	0.14	8.56	6.04	*	0.05	0.31	6.81	4.30	0.22	0.32	92.42
Avg.	73.65	0.15	8.58	6.26	*	0.02	0.23	6.77	4.34	0.23	0.31	95.95
Std. Dev	0.50	0.02	0.53	0.42	*	0.02	0.07	0.08	0.12	0.03	0.03	
	74.34	0.08	9.23	6.16	*	0.01	0.11	5.70	4.39	0.18	0.14	96.79
	75.62	0.05	8.25	6.01	*	0.00	0.13	5.44	4.50	0.23	0.37	96.72
	74.63	0.10	8.82	5.88	*	0.01	0.15	6.14	4.26	0.23	0.49	98.50
	74.63	0.05	8.80	5.73	*	0.02	0.18	6.34	4.24	0.24	0.18	98.99
MER050S	74.58	0.12	8.82	5.75	*	0.00	0.22	6.34	4.17	0.22	0.26	99.03
	74.73	0.10	8.14	5.95	*	0.00	0.24	6.60	4.25	0.24	0.41	97.32
	74.80	0.13	8.36	5.94	*	0.02	0.19	6.34	4.21	0.22	0.22	98.15
	74.63	0.15	8.73	5.89	*	0.00	0.18	6.21	4.21	0.23	0.36	97.26
	74.43	0.14	8.88	5.75	*	0.00	0.22	6.45	4.13	0.23	0.41	98.64
Avg.	74.71	0.10	8.67	5.90	*	0.01	0.18	6.17	4.26	0.22	0.32	97.93
Std. Dev	0.37	0.04	0.35	0.14	*	0.01	0.04	0.37	0.11	0.02	0.12	
	73.70	0.39	8.84	5.86	*	0.02	0.40	6.43	4.35	0.15	0.18	98.91
	74.03	0.30	9.29	5.96	*	0.00	0.22	5.87	4.34	0.15	0.10	97.63
	74.51	0.36	9.05	5.99	*	0.00	0.34	5.39	4.35	0.15	0.28	95.61
	74.05	0.25	9.04	6.07	*	0.00	0.23	5.79	4.57	0.14	0.16	96.60
MER050T	74.01	0.29	9.20	6.04	*	0.04	0.19	5.85	4.37	0.18	0.21	92.52
	73.76	0.37	9.19	5.92	*	0.01	0.19	6.34	4.23	0.15	0.32	95.13
	74.27	0.33	9.02	6.05	*	0.00	0.14	5.66	4.54	0.16	0.21	93.00
	74.12	0.36	9.31	6.09	*	0.01	0.25	5.54	4.32	0.15	0.29	96.07
	74.53	0.31	8.88	5.94	*	0.00	0.30	5.85	4.20	0.15	0.19	96.36
	74.67	0.24	8.59	5.89	*	0.00	0.30	5.74	4.57	0.18	0.21	94.79
Avg.	74.17	0.32	9.04	5.98	*	0.01	0.25	5.85	4.38	0.16	0.22	95.66
Std. Dev	0.33	0.05	0.22	0.08	*	0.01	0.08	0.32	0.13	0.01	0.07	
	74.02	0.20	8.94	5.78	*	0.03	0.25	6.40	4.39	0.22	0.30	92.18
MER050W	74.51	0.23	8.60	5.92	*	0.04	0.35	6.11	4.24	0.20	0.36	98.37
	74.87	0.23	9.20	5.72	*	0.01	0.16	5.69	4.12	0.19	0.45	96.64
	73.62	0.28	9.34	5.73	*	0.00	0.27	6.60	4.15	0.18	0.09	95.70
Avg.	74.26	0.24	9.02	5.79	*	0.02	0.26	6.20	4.23	0.20	0.30	95.72
Std. Dev	0.55	0.03	0.33	0.09	*	0.02	0.08	0.40	0.12	0.02	0.15	

Appendix B

Trace element data

This appendix contains LA-ICP-MS data. All values in ppm.

Sample	Ca	Zn	Rb	Sr	Y	Zr	Nb	Cs	Ba	La	Ce	Pr	Nd	Sm	Eu	Gd	Dy	Er	Yb	Hf	Ta	Pb	Th	U
ABII-09-03_1	2139	632	219	10	248	1907	381	2	489	296	640	67	263	53	10	47	46	27	26	48	23	39	38	11
ABII-09-03_2	1519	611	193	8	210	1447	312	2	400	258	472	61	223	46	9	38	39	22	21	41	19	33	33	10
ABII-09-03_3	2130	856	219	9	208	1953	370	2	457	261	567	62	222	46	9	38	39	23	21	41	21	49	31	11
ABII-09-03_4	1469	591	194	8	208	1786	326	2	418	261	549	58	224	45	9	38	39	23	21	40	20	33	32	10
ABII-09-03_6	1869	223	178	9	211	1897	315	2	427	259	561	60	235	48	9	39	40	24	22	42	19	31	32	9
ABII-09-03_7	1804	312	199	10	245	2130	359	2	487	292	613	65	259	50	10	46	46	27	25	48	22	38	36	11
ABII-09-03_8	1823	651	210	10	221	1860	345	2	453	264	570	63	244	48	9	40	42	23	22	43	20	38	34	10
ABII-09-03_9	1776	621	206	8	217	1804	325	2	443	259	554	62	234	48	10	41	41	24	23	45	21	34	35	10
ABII-09-03_10	1702	571	181	7	197	1693	315	2	430	244	511	56	212	42	8	36	36	22	20	39	18	31	30	9
ABII-09-03_11	2167	744	219	11	267	2186	386	2	517	299	657	74	285	56	11	49	46	26	26	49	24	46	39	11
ABII-09-03_12	1442	621	205	9	225	1907	368	2	469	271	579	63	243	48	10	41	43	24	23	44	21	37	33	10
ABII-09-03_13	1711	670	192	9	215	1814	339	2	413	251	525	58	223	46	9	40	40	23	22	44	20	41	33	9
ABII-09-03_14	1544	693	195	8	224	1879	332	2	440	258	554	60	238	49	9	43	42	23	23	42	21	36	33	9
ABII-09-03_15	1544	629	190	8	209	1760	331	2	413	251	513	58	223	47	9	38	39	22	21	41	19	31	32	9
ABII-09-03_16	1432	724	209	8	233	1795	365	2	438	284	570	63	253	49	10	42	43	24	23	43	20	37	33	10
ABII-09-08_1	1620	237	278	8	220	1840	326	2	432	261	527	60	229	47	9	41	43	24	22	45	20	35	33	9
ABII-09-08_2	1470	587	202	7	199	1620	322	2	404	222	502	55	207	43	8	36	38	21	19	38	19	38	29	10
ABII-09-08_3	1671	669	197	8	219	1730	336	2	431	255	527	62	231	47	9	42	43	24	22	45	20	34	34	10
ABII-09-08_4	1940	577	202	8	243	2040	380	2	459	284	595	69	254	52	10	46	48	26	24	50	24	38	37	12
ABII-09-08_5	1670	639	187	8	228	1840	354	2	460	273	565	65	243	50	10	44	45	25	23	47	21	37	35	10
ABII-09-08_6	1630	642	192	8	229	2020	365	2	456	274	579	67	255	52	10	44	45	25	23	47	21	36	34	10
ABII-09-08_7	1740	698	183	8	220	1811	344	2	504	266	565	63	245	49	10	42	42	23	22	44	21	35	34	10
ABII-09-08_8	1920	376	162	10	203	1730	309	2	415	242	506	58	220	43	8	38	40	22	20	41	19	30	31	9
ABII-09-08_9	1870	643	190	8	203	1742	332	2	427	244	512	60	225	45	9	39	40	22	21	41	20	33	32	10
ABII-09-08_10	1600	722	251	8	220	1780	395	2	461	272	584	68	254	50	10	44	45	24	24	46	24	42	36	11
ABII-09-08_11	1370	631	175	8	196	1650	338	2	419	239	504	59	218	45	9	39	40	22	20	43	21	32	33	9

Sample	Ca	Zn	Rb	Sr	Y	Zr	Nb	Cs	Ba	La	Ce	Pr	Nd	Sm	Eu	Gd	Dy	Er	Yb	Hf	Ta	Pb	Th	U
ABII-09-08_12	1540	647	173	8	202	1647	324	2	406	238	510	59	218	44	9	39	40	23	21	43	20	32	32	10
ABII-09-08_13	1930	706	196	10	235	1820	362	2	461	282	595	72	266	54	11	47	49	28	26	51	23	38	38	10
ABII-09-08_14	1780	639	178	8	194	1613	328	2	419	237	489	58	221	44	9	39	39	21	19	41	19	32	31	9
ABII-09-08_15	1750	641	176	8	205	1640	325	0	415	240	502	58	222	44	9	39	40	22	21	44	20	32	32	9
ABII-09-08_16	1440	591	172	7	196	1649	313	2	387	229	484	56	213	41	9	38	38	21	20	42	19	31	31	9
ABII-09-08_17	1630	603	172	7	195	1610	310	2	401	233	483	56	217	43	9	39	39	22	20	42	19	32	31	9
ABII-09-08_18	1510	646	179	8	205	1710	339	2	418	250	520	61	230	45	9	41	41	23	21	43	20	33	32	9
ABII-10-75-1	2093	434	127	5	127	1120	204	1	357	153	321	36	142	29	6	26	26	14	13	25	12	19	19	6
ABII-10-75-2	2065	400	124	4	124	1096	193	1	357	144	308	35	136	27	5	25	26	13	13	26	11	18	18	5
ABII-10-75-4	2120	415	117	4	124	1063	201	1	360	147	305	34	136	28	5	24	24	14	13	25	11	17	18	5
ABII-10-75-5	2065	432	124	5	125	1101	197	1	362	145	324	34	139	27	5	25	25	14	13	25	12	19	18	5
ABII-10-75-6	2241	400	113	4	120	1027	201	1	349	143	307	33	136	27	5	23	24	13	13	25	11	19	18	5
ABII-10-75-7	2130	401	114	4	121	1062	196	1	352	144	307	34	137	28	5	25	24	14	13	26	12	19	18	6
ABII-10-75-8	2176	421	120	5	125	1099	203	1	379	152	332	37	142	29	6	25	26	14	13	26	12	19	18	5
ABII-10-75-9	2148	412	115	4	123	1066	191	0	354	144	307	34	132	27	5	24	25	14	14	26	11	19	18	5
ABII-10-75-10	2427	403	117	4	128	1118	201	1	370	156	317	36	143	28	6	26	26	14	14	26	12	20	19	6
ABII-10-75-11	2492	429	117	5	129	1128	205	1	363	152	318	36	139	30	6	27	27	15	15	28	12	19	19	6
ABII-10-75-15	2074	405	115	4	120	1052	194	1	347	142	302	33	135	27	5	23	24	14	13	26	12	19	19	5
ABII-10-75-16	2399	440	116	4	127	1076	196	1	357	152	321	36	141	28	6	26	26	14	14	26	12	20	19	6
ABII-10-75-17	2158	334	115	5	126	1075	197	1	339	148	309	34	137	28	6	25	25	14	13	26	12	19	19	6
ABII-10-75-18	2093	393	112	4	118	1035	186	1	347	141	298	33	130	27	5	23	24	13	13	25	12	18	18	5
ABII-10-75-19	2130	438	114	5	122	1040	193	1	348	145	305	35	136	27	6	24	24	14	13	25	11	19	18	5
ABII-10-75-20	2130	417	114	5	119	1027	198	1	345	142	304	33	132	27	5	23	23	13	13	24	11	18	18	5
ABII-11-81_1	1504	438	146	4	146	1204	243	1	249	172	373	44	152	32	6	27	26	15	15	29	13	23	22	7
ABII-11-81_2	1458	520	125	4	148	975	235	3	234	184	343	44	159	36	6	27	26	17	16	28	15	23	23	7
ABII-11-81_3	1404	467	141	4	152	1239	244	1	254	173	382	43	157	33	6	27	26	16	15	29	13	22	22	7
ABII-11-81_4	1422	521	151	4	170	1409	270	2	282	197	425	49	178	37	7	32	29	19	17	34	15	25	26	7

Sample	Ca	Zn	Rb	Sr	Y	Zr	Nb	Cs	Ba	La	Ce	Pr	Nd	Sm	Eu	Gd	Dy	Er	Yb	Hf	Ta	Pb	Th	U
ABII-11-81_5	1395	496	141	4	149	1210	242	1	255	173	378	44	160	32	6	27	26	16	15	29	13	23	22	7
ABII-11-81_6	1367	545	159	5	163	1260	272	2	260	197	416	50	173	36	7	30	29	18	17	33	15	27	26	7
ABII-11-81_7	1422	464	141	4	142	1148	209	1	251	169	375	42	153	32	6	26	26	16	16	28	12	21	22	6
ABII-11-81_11	1431	472	150	4	149	1263	257	2	253	178	386	45	157	33	7	29	27	17	16	31	14	25	24	7
ABII-11-81_12	1258	458	137	4	141	1166	232	1	239	170	357	42	148	32	6	27	25	15	14	28	13	23	22	6
ABII-11-81_13	1021	572	158	5	173	1350	283	2	276	206	454	54	193	41	8	33	31	20	19	36	17	29	27	8
ABII-11-81_14	1385	402	136	4	130	1009	223	1	232	157	348	39	142	30	6	24	23	14	14	25	12	20	20	6
ABII-11-81_15	1504	395	153	5	119	1054	209	5	222	138	309	35	129	28	5	23	22	13	13	25	12	25	19	6
ABII-11-81_16	1367	482	152	4	144	1199	254	2	250	171	378	43	160	32	6	27	26	16	15	28	13	25	23	7
LLIII-03-70_1	994	444	133	5	119	878	211	0	355	146	320	39	133	28	6	23	21	13	12	23	11	0	19	6
LLIII-03-70_2	1048	500	153	6	157	1243	257	2	355	184	409	48	170	35	7	30	28	17	16	33	15	26	24	7
LLIII-03-70_3	1130	554	166	6	172	1358	292	2	367	207	456	52	193	39	8	34	33	20	18	36	17	28	26	8
LLIII-03-70_4	1139	489	165	6	171	1328	276	2	361	201	428	50	184	38	8	33	32	19	17	36	16	27	26	8
LLIII-03-70_5	1103	565	152	6	153	1282	260	2	345	190	399	46	170	36	7	31	30	17	16	32	15	29	24	7
LLIII-03-70_6	1340	490	153	6	153	1264	252	2	345	183	392	44	167	35	7	30	28	17	16	31	15	26	23	7
LLIII-03-70_7	1285	556	171	6	181	1447	306	2	373	213	463	54	195	40	8	35	33	20	18	37	17	29	27	8
LLIII-03-70_8	1841	427	154	8	170	1358	291	2	356	204	444	55	190	41	8	35	33	19	19	37	17	29	27	8
LLIII-03-70_9	1130	561	169	7	188	1458	312	2	395	228	481	56	208	43	9	37	36	22	20	39	18	30	29	9
LLIII-03-70_10	1185	569	170	7	180	1441	299	2	380	218	458	53	204	41	8	37	35	21	19	39	18	31	28	8
LLIII-03-70_11	1194	437	164	7	172	1385	277	2	346	205	431	50	190	38	8	33	32	18	18	34	16	29	25	8
LLIII-03-70_12	1130	650	191	7	215	1732	349	2	419	258	540	63	237	48	10	43	40	23	22	43	20	36	33	9
LLIII-03-70_13	1303	481	173	6	189	1510	300	2	385	226	478	55	204	43	9	36	36	21	20	40	18	29	30	9
LLIII-03-70_14	1340	441	156	8	172	1376	262	2	368	201	424	48	185	36	8	33	33	19	18	34	15	27	27	8
LLIII-03-70_15	1632	410	139	4	124	1096	208	1	201	158	331	38	136	28	5	23	24	14	13	27	12	24	22	6
LLIII-03-70_16	1504	467	159	6	170	1485	275	2	362	203	440	49	188	38	7	32	32	19	18	35	16	26	26	8
LLIII-03-110_1	1665	706	201	8	231	1832	349	2	437	272	559	63	242	50	10	43	43	24	23	45	20	36	34	10
LLIII-03-110_2	1451	645	163	7	203	1600	325	2	392	239	493	57	220	44	9	38	39	22	21	41	19	33	31	9

Sample	Ca	Zn	Rb	Sr	Y	Zr	Nb	Cs	Ba	La	Ce	Pr	Nd	Sm	Eu	Gd	Dy	Er	Yb	Hf	Ta	Pb	Th	U
LLIII-03-110_3	1925	702	206	9	241	1851	344	2	461	288	605	69	266	53	11	47	46	27	25	46	21	38	36	10
LLIII-03-110_4	1665	605	181	8	209	1721	334	2	432	253	525	58	229	45	9	39	39	21	21	41	19	33	31	9
LLIII-03-110_5	1888	694	201	9	234	1934	361	2	481	291	611	72	273	54	11	45	46	26	25	50	23	39	38	11
LLIII-03-110_6	1683	819	212	9	287	2316	486	2	533	323	722	79	315	61	12	51	54	30	28	51	26	36	43	13
LLIII-03-110_7	2325	493	190	39	214	1758	318	2	386	239	512	58	224	46	9	38	41	23	21	40	19	32	32	9
LLIII-03-110_8	1414	565	195	8	225	1934	358	2	445	271	568	63	248	50	10	43	45	25	25	46	22	36	36	10
LLIII-03-110_10	1311	595	182	7	189	1562	292	2	463	225	470	54	213	41	8	37	36	21	20	37	18	28	28	8
LLIII-03-110_11	1414	556	211	7	166	1386	262	0	349	195	419	46	180	35	7	31	32	17	16	33	15	31	24	7
LLIII-03-110_12	1144	526	201	6	153	1265	257	2	286	180	389	44	172	36	7	30	29	17	17	32	16	31	25	7
LLIII-03-110_14	1376	656	197	8	225	1739	362	2	419	267	537	62	251	51	10	43	43	24	23	44	20	35	33	10
LLIII-03-110_15	1432	563	169	7	196	1600	304	2	374	220	458	51	206	41	8	35	36	20	19	38	17	29	29	8
LLIII-03-110_16	1376	703	196	9	236	1860	373	2	470	278	545	64	260	51	10	42	44	24	24	48	20	38	35	10
LLIII-07-75_1	2186	440	113	4	109	987	189	1	365	140	291	33	125	25	5	21	22	12	11	22	11	20	17	5
LLIII-07-75_2	1990	427	117	4	114	966	193	1	344	138	299	33	131	26	5	23	23	13	12	24	11	19	17	5
LLIII-07-75_3	2158	435	118	4	114	976	191	1	332	140	304	33	129	26	5	22	23	13	13	23	11	18	18	6
LLIII-07-75_4	2288	427	109	4	113	955	183	1	329	139	292	32	128	26	5	22	23	13	12	23	11	19	17	5
LLIII-07-75_5	2139	417	119	4	115	988	191	1	337	140	303	34	129	26	5	23	23	13	13	23	11	19	18	6
LLIII-07-75_6	2269	433	120	4	118	1016	200	1	351	144	305	34	135	28	5	24	23	13	13	25	12	20	18	5
LLIII-07-75_7	2306	431	116	4	114	1005	193	1	352	137	303	33	131	26	5	22	23	13	13	24	12	0	18	5
LLIII-07-75_8	2251	420	119	4	115	990	202	1	333	143	310	34	129	27	5	23	23	13	12	23	12	20	18	6
LLIII-07-75_9	2027	392	114	4	114	1008	188	1	342	143	305	33	131	27	5	22	23	13	12	24	11	19	17	5
LLIII-07-75_10	2232	428	118	4	117	1001	193	1	342	139	312	35	131	26	5	22	23	13	12	24	12	20	18	5
LLIII-07-75_11	2046	423	110	4	115	970	193	1	358	138	303	33	127	27	5	22	23	13	13	24	11	18	18	5
LLIII-07-75_13	2102	443	122	4	122	1062	190	1	348	140	303	34	131	28	5	24	24	14	13	25	12	22	19	5
LLIII-07-75_14	2158	429	113	5	121	1039	200	1	347	145	309	35	134	27	6	23	24	14	13	24	12	20	18	5
LLIII-07-75_15	2446	434	112	5	120	988	193	1	351	147	319	36	137	28	6	23	24	13	13	24	12	22	19	5
LLIII-07-75_16	2288	406	115	5	120	1037	195	1	350	146	312	34	135	28	6	24	24	13	13	25	12	20	18	5

Sample	Ca	Zn	Rb	Sr	Y	Zr	Nb	Cs	Ba	La	Ce	Pr	Nd	Sm	Eu	Gd	Dy	Er	Yb	Hf	Ta	Pb	Th	U
LLIII-07-75_17	2158	437	111	4	120	997	181	1	326	136	291	32	125	27	5	23	24	13	13	25	11	20	18	5
LLIII-07-75_18	2353	443	113	5	118	1013	194	1	337	144	311	34	132	26	5	23	23	13	13	25	12	22	19	5
LLIII-09-03-1	2224	476	152	4	158	1324	251	1	248	185	380	43	162	34	7	29	29	17	16	32	15	0	24	7
LLIII-09-03-2	1622	478	152	5	161	1338	252	1	255	193	402	45	172	36	7	31	31	18	17	35	16	0	26	7
LLIII-09-03-3	1714	549	167	8	181	1540	285	2	294	220	459	51	199	40	8	35	34	21	19	37	17	33	28	8
LLIII-09-03-6	1458	433	151	5	160	1349	264	2	279	199	422	47	181	36	7	31	31	18	18	34	16	27	26	8
LLIII-09-03-7	1449	565	160	4	152	1130	261	1	265	188	374	45	162	33	7	28	28	17	16	32	16	32	25	8
LLIII-09-03-8	2379	535	201	11	190	1440	292	2	315	232	463	52	222	44	8	37	38	22	21	38	17	36	30	9
LLIII-09-03-9	1677	512	168	5	179	1440	275	2	292	212	467	51	197	40	8	34	34	20	19	38	17	28	29	8
LLIII-09-03-11	2033	529	184	8	170	1577	315	2	319	214	444	54	197	39	8	33	34	19	18	41	18	35	31	10
LLIII-09-03-12	1522	492	165	5	171	1486	282	1	273	203	425	51	181	37	7	33	33	19	18	38	18	30	27	8
LLIII-09-03-13	1586	457	160	5	173	1471	283	2	289	212	455	50	195	40	7	35	34	20	19	38	17	27	27	8
LLIII-09-03-15	1486	494	157	5	169	1413	268	2	278	201	434	49	184	38	7	32	33	20	18	36	16	28	27	7
MER048U_2	2567	296	107	1	90	865	156	1	214	111	233	26	102	20	4	17	17	10	10	20	9	16	16	4
MER048U_3	1953	316	127	1	102	993	171	1	179	125	257	28	111	22	3	18	19	10	11	23	10	18	18	5
MER048U_4	1730	311	135	1	101	1015	176	1	151	129	260	29	111	22	3	19	19	11	12	24	10	19	20	6
MER048U_5	1600	299	125	1	101	995	164	1	140	125	258	28	109	21	3	19	19	11	10	23	10	19	19	5
MER048U_6	1702	286	127	1	100	1009	168	1	140	126	261	29	114	22	3	19	19	11	12	24	10	20	20	6
MER048U_7	1572	299	129	1	97	943	165	1	131	120	244	27	106	20	3	18	18	11	11	23	10	18	19	5
MER048U_8	1693	310	121	1	89	870	154	1	125	110	233	26	102	20	3	18	18	10	10	22	10	20	18	6
MER048U_9	2362	328	124	1	103	1026	170	1	172	129	272	29	115	23	4	19	19	11	11	24	10	18	19	5
MER048U_10	1990	320	122	1	96	921	168	1	180	114	246	27	106	21	4	18	18	10	11	22	10	17	17	5
MER048U_11	1953	314	122	1	98	960	164	1	152	122	252	28	110	23	3	19	19	11	12	24	10	19	19	5
MER048U_12	1702	321	124	1	99	986	177	1	150	125	258	29	112	22	4	20	19	11	11	24	10	18	18	5
MER046Z_1	2652	258	101	7	80	723	140	1	338	100	210	23	87	17	3	15	15	9	9	18	8	15	14	4
MER046Z_3	2060	281	108	3	85	805	150	1	297	107	223	24	94	19	4	17	17	10	10	20	9	17	16	4
MER046Z_4	2698	283	105	4	83	746	140	1	378	101	211	23	90	18	4	15	17	9	9	18	8	14	14	4

Sample	Ca	Zn	Rb	Sr	Y	Zr	Nb	Cs	Ba	La	Ce	Pr	Nd	Sm	Eu	Gd	Dy	Er	Yb	Hf	Ta	Pb	Th	U
MER046Z_5	2279	283	113	3	86	819	150	1	313	108	222	25	96	19	4	16	17	10	10	20	9	16	15	5
MER046Z_6	1732	337	110	6	125	1108	170	1	210	132	285	33	133	27	5	23	25	14	14	27	10	20	14	4
MER046Z_7	2388	279	104	3	86	813	148	1	316	105	221	24	94	19	4	16	17	10	9	20	9	0	15	4
MER046Z_9	2625	288	100	4	79	704	132	1	362	96	202	22	88	18	4	15	16	9	9	18	8	14	14	4
MER046Z_11	2324	275	109	3	84	794	143	1	295	105	217	23	92	18	3	15	17	10	9	19	9	15	15	4
MER046Z_12	2279	298	114	3	90	857	152	1	262	115	232	25	98	20	3	17	18	11	10	22	10	18	17	5
MER046Z_13	2197	289	109	3	87	817	149	1	304	110	222	24	95	19	4	16	17	10	10	20	9	17	16	5
MER046Z_14	1996	281	107	3	84	773	144	1	321	106	214	24	93	19	3	16	18	10	9	20	9	16	15	5
MER046Z_15	2279	302	115	3	93	874	159	1	336	116	244	26	104	21	4	18	20	11	11	22	10	17	17	5
MER046Z_16	1996	306	116	3	91	860	159	1	304	118	244	26	102	20	4	18	19	11	10	22	10	18	17	5
MER046Z_17	2169	299	111	3	87	833	152	1	301	109	227	25	97	20	4	17	18	10	10	21	10	18	17	5
MERO050C_1	1390	618	175	7	194	1490	302	2	370	215	442	50	191	39	8	33	34	18	18	35	17	27	26	8
MERO050C_2	1210	546	155	6	164	1350	289	2	306	191	404	46	171	33	7	28	29	16	15	29	15	23	23	7
MERO050C_3	1630	612	167	7	189	1540	319	2	375	216	450	52	195	39	8	33	33	18	17	34	17	27	25	7
MERO050C_4	1550	653	224	8	206	1720	350	2	391	233	480	56	208	41	8	36	36	19	19	37	18	28	28	8
MERO050C_5	1150	583	181	7	167	1315	279	2	368	195	403	47	172	35	7	28	29	16	15	30	15	25	22	7
MERO050C_6	1720	491	160	17	110	969	207	2	528	134	290	32	119	24	6	20	20	11	11	21	10	20	16	5
MERO050C_8	1710	553	173	7	166	1410	295	2	414	200	416	48	179	38	7	32	31	17	16	31	16	27	24	7
MERO050C_9	1300	665	192	8	213	1650	348	2	419	250	532	63	236	48	10	42	41	24	22	44	21	33	31	10
MERO050C_10	1960	662	193	8	201	1660	347	2	410	248	531	60	232	46	9	41	40	22	21	41	20	32	30	9
MERO050C_11	1310	730	213	8	224	1750	394	2	432	269	565	67	256	48	10	43	43	24	23	44	21	36	33	10
MERO050C_12	1030	547	162	6	160	1370	279	2	360	192	414	47	179	36	7	30	31	17	16	32	15	24	23	7
MERO050C_13	1590	674	192	8	209	1640	341	2	423	246	506	60	224	45	8	39	39	22	21	40	19	31	30	8
MERO050C_14	1370	610	174	8	197	1631	326	2	393	230	486	56	218	43	8	38	37	21	19	39	19	28	29	8
MERO050C_15	1710	629	202	9	202	1613	336	2	410	238	490	59	223	43	9	39	39	22	21	40	19	30	30	9
MERO050C_16	1330	683	190	8	205	1680	338	2	417	239	522	59	228	45	9	39	41	23	21	43	19	32	30	9
MER050C_2	1273	578	173	7	185	1470	310	2	373	218	467	51	192	39	8	34	35	20	18	36	17	31	27	8

Sample	Ca	Zn	Rb	Sr	Y	Zr	Nb	Cs	Ba	La	Ce	Pr	Nd	Sm	Eu	Gd	Dy	Er	Yb	Hf	Ta	Pb	Th	U
MER050C_5	1340	613	171	7	189	1378	320	2	380	230	469	53	200	41	8	35	37	20	19	37	18	34	29	9
MER050C_6	1302	625	151	7	179	1463	281	2	389	210	464	49	182	36	7	34	34	19	17	37	17	29	27	7
MER050C_7	1720	637	171	7	197	1520	313	2	380	237	484	52	206	42	8	36	37	22	20	41	18	30	29	9
MER050H_1	1862	564	167	5	170	1395	286	2	279	207	435	48	187	38	7	32	33	19	18	35	17	26	26	7
MER050H_2	2138	421	111	4	115	949	193	1	350	144	296	34	131	26	5	22	23	13	13	23	11	17	17	5
MER050H_4	2128	397	108	4	107	897	178	1	327	131	280	31	119	26	5	21	21	12	12	22	10	17	16	5
MER050H_5	2062	369	108	4	109	896	181	1	320	129	273	30	121	24	5	20	21	12	11	22	10	16	16	5
MER050H_6	2052	455	118	4	111	917	187	1	336	133	286	32	121	25	5	20	21	12	12	21	11	19	16	5
MER050H_7	2109	403	114	4	112	908	183	1	324	135	284	31	124	26	5	21	22	12	12	22	11	17	17	5
MER050H_8	2309	411	117	5	116	965	194	1	338	139	296	33	128	27	5	22	23	13	13	24	11	17	17	5
MER050H_9	2147	390	110	4	113	906	189	1	339	135	286	32	127	27	5	21	22	12	12	22	11	16	16	5
MER050H_10	2204	388	115	4	112	903	181	1	327	133	276	31	123	25	5	20	21	12	12	22	10	16	16	5
MER050H_11	2090	404	113	4	110	912	185	1	324	135	279	32	124	25	5	22	22	13	12	23	11	17	16	5
MER050H_12	1615	568	150	5	157	1245	268	1	274	200	390	47	191	37	7	31	33	18	17	34	16	25	25	8
MER050H_13	2176	390	117	4	114	984	190	1	341	137	285	32	125	26	5	21	22	13	12	23	11	17	17	5
MER050H_14	2318	397	119	5	113	960	185	1	329	138	288	32	124	26	5	21	23	13	12	23	11	17	17	5
MER050H_15	2176	401	113	4	114	976	187	1	338	136	291	32	128	26	5	22	22	13	12	23	11	17	17	5
MER050H_16	2299	303	113	5	112	955	183	1	330	137	289	31	123	25	5	22	22	13	12	23	10	19	17	4
MER050H_17	2005	365	106	4	110	927	181	1	326	131	275	32	123	24	5	21	21	13	12	22	11	16	16	5
MER050H_18	2385	430	117	5	119	996	200	1	347	144	307	33	129	27	5	23	22	13	12	22	11	17	16	5
MER050H_19	2679	442	118	4	116	983	198	1	349	144	300	33	132	26	5	22	23	13	12	23	11	17	17	5
MER050N_1	1710	670	172	6	209	1691	329	2	319	242	524	57	219	46	8	38	40	23	22	41	19	30	30	8
MER050N_3	1596	566	173	5	170	1378	271	2	263	207	428	48	184	37	7	32	33	19	18	34	16	26	25	7
MER050N_4	1492	490	165	5	163	1425	262	2	251	189	392	43	171	36	6	30	31	18	16	32	15	22	23	7
MER050N_6	1872	585	149	5	167	1435	298	1	318	212	417	49	184	37	7	31	33	19	18	35	16	24	25	7
MER050N_7	1425	614	175	5	191	1558	301	2	293	234	482	53	202	43	8	37	38	22	20	39	18	28	29	8

Appendix C

Secondary standard data

Secondary standard data for EPMA (Table 1) and LA-ICP-MS (Table 2)

Table C.1

SAMPLE	SiO2	TiO2	Al2O3	FeO	MnO	MgO	CaO	Na2O	K2O	Cl	F	TOTAL
14/09/15	ABII-04-12; ABII-05-48; ABII-08-16; ABII-12-24; ABII-11-81; ABII-11-07											
KN18_1	75.26	0.20	10.26	3.57	0.08	0.00	0.13	5.21	4.20	*	*	98.91
KN18_2	75.02	0.16	10.23	3.60	0.04	0.00	0.13	5.16	4.15	*	*	98.50
KN18_3	75.12	0.13	10.22	3.49	0.08	0.00	0.09	5.24	4.23	*	*	98.61
KN18_4	75.72	0.17	10.44	3.60	0.08	0.00	0.15	4.04	4.04	*	*	98.25
KN18_5	74.98	0.17	10.26	3.59	0.06	0.00	0.16	4.85	4.20	*	*	98.28
KN18_6	74.22	0.12	10.28	3.51	0.06	0.01	0.13	5.20	4.14	*	*	97.66
KN18_7	74.76	0.16	10.33	3.50	0.06	0.00	0.19	5.36	4.17	*	*	98.52
KN18_8	75.18	0.17	10.42	3.54	0.08	0.00	0.10	5.52	4.15	*	*	99.15
KN18_10	75.21	0.15	10.38	3.42	0.08	0.00	0.21	5.23	4.25	*	*	98.93
KN18_11	75.56	0.17	10.37	3.65	0.04	0.00	0.21	4.68	4.13	*	*	98.81
AV.	72.3	0.2	10.3	3.5	0.1	0.0	0.1	5.5	4.4	0.3	0.6	
SD	0.6	0.0	0.2	0.1	0.0	0.0	0.1	0.2	0.0	0.0	0.1	
RSD %	0.8	2.2	2.1	2.0	1.4	201	44	3.5	0.7	6.2	14	
ERROR (wt%)	1.2	0.0	0.4	0.1	0.0	0.3	0.2	0.4	0.1	0.0	0.2	
31/05/16	ABII-05-48; LLIII-04-51											
KN18_3	72.18	0.16	10.28	3.47	0.06	0.07	0.17	5.57	4.42	0.27	0.57	97.21
KN18_3	72.48	0.16	10.28	3.37	0.06	0.00	0.13	5.21	4.44	0.30	0.62	97.05
KN18_3	72.63	0.17	10.61	3.47	0.06	0.00	0.07	5.71	4.41	0.31	0.63	98.07
KN18_4	73.04	0.17	10.17	3.56	0.06	0.01	0.13	5.36	4.46	0.30	0.78	98.03
KN18_5	71.41	0.16	10.02	3.45	0.06	0.00	0.25	5.49	4.38	0.32	0.55	96.10
AV.	74.3	0.2	10.3	3.5	*	0.0	0.2	5.3	4.5	0.3	0.6	
SD	0.7	0.0	0.2	0.1	*	0.0	0.1	0.4	0.1	0.0	0.1	
RSD %	1.0	22.6	1.6	2.2	*	90	52	7.2	1.9	4.9	19	
ERROR (wt%)	1.5	0.1	0.3	0.2	*	0.1	0.3	0.9	0.2	0.0	0.3	
17/01/17	LLIII-05-23; LLIII-03-70; LLIII-09-22, LLIII-09-60; MER046L; MER050M; MER050A; MER050M; MER050B; MER050J											
KN18_1	74.38	0.17	10.18	3.52	*	0.01	0.23	5.46	4.53	0.32	0.63	99.44
KN18_1	74.25	0.15	10.41	3.60	*	0.01	0.16	4.59	4.67	0.31	0.53	98.70
KN18_1	73.73	0.17	10.34	3.54	*	0.02	0.26	5.10	4.56	0.32	0.61	98.63
KN18_2	74.63	0.15	10.55	3.59	*	0.03	0.08	5.50	4.43	0.33	0.76	100.04
KN18_2	75.39	0.18	10.18	3.56	*	0.02	0.14	4.82	4.55	0.33	0.71	99.88
KN18_2	74.84	0.21	10.10	3.43	*	0.01	0.05	5.05	4.58	0.32	0.84	99.44
KN18_3	74.86	0.23	10.34	3.56	*	0.02	0.14	5.37	4.52	0.32	0.80	100.17
KN18_3	73.88	0.16	10.18	3.48	*	0.00	0.24	5.16	4.57	0.33	0.77	98.78
KN18_3	74.55	0.14	10.38	3.54	*	0.01	0.07	5.56	4.36	0.32	0.60	99.53
KN18_3	74.40	0.15	10.19	3.47	*	0.03	0.10	5.76	4.34	0.28	0.70	99.42
KN18_4	72.72	0.10	9.89	3.70	*	0.02	0.10	5.04	4.53	0.33	0.57	96.99
KN18_4	75.49	0.10	10.40	3.40	*	0.01	0.27	5.44	4.46	0.33	0.52	100.41
KN18_4	74.74	0.12	10.52	3.37	*	0.00	0.14	5.36	4.46	0.34	0.62	99.68
KN18_4	72.70	0.24	10.33	3.47	*	0.00	0.19	4.82	4.58	0.31	0.69	97.32

SAMPLE	SiO2	TiO2	Al2O3	FeO	MnO	MgO	CaO	Na2O	K2O	Cl	F	TOTAL
KN18_5	73.95	0.19	10.43	3.48	*	0.00	0.23	4.93	4.41	0.34	0.45	98.43
KN18_5	74.40	0.19	10.26	3.39	*	0.01	0.13	4.65	4.49	0.32	0.59	98.43
KN18_6	73.99	0.15	10.44	3.51	*	0.02	0.22	6.01	4.39	0.30	0.73	99.75
KN18_6	73.73	0.14	10.34	3.57	*	0.03	0.13	5.90	4.50	0.30	0.84	99.48
KN18_7	74.59	0.19	10.32	3.49	*	0.00	0.26	5.34	4.54	0.30	0.36	99.37
KN18_7	74.49	0.17	10.01	3.55	*	0.00	0.02	5.53	4.46	0.33	0.50	99.07
KN18_8	73.60	0.13	10.20	3.53	*	0.00	0.25	5.40	4.44	0.34	0.69	98.57
KN18_8	75.44	0.18	10.11	3.58	*	0.00	0.01	5.52	4.37	0.30	0.70	100.22
AV.	72.6	0.1	9.7	3.4	0.1	0.0	0.2	5.2	4.4	0.3	0.6	
SD	11.0	0.0	1.3	0.2	0.0	0.0	0.1	0.6	0.5	0.0	0.1	
RSD %	15.1	20.5	13.5	4.8	32	110	70	11.1	11.6	8.8	18	
ERROR (wt%)	23.0	0.1	2.8	0.4	0.1	0.1	0.7	1.3	1.1	0.1	0.3	
18/01/17	LLIII-07-105; LLIII-09-01; LLIII-8-86; LLIII-8-38; LLIII-08-90;LLIII-09-03; LLIII-09-44; LLIII-09-23; LLIII-03-110; LLIII-09-98; LLIII-07-75;ABII-10-77; ABII-10-75; MER046I; MER046Q; MER046X; MER050A; MER046L; MER046Z; MER048F; MER048N; MER046D; MER048U;MER050T; MER050R; MER050C; MER050H; MER050R											
KN18_1	73.83	0.18	9.66	3.55	0.08	0.01	0.19	5.47	4.55	0.33	0.48	98.32
KN18_2	73.90	0.18	10.00	3.57	0.05	0.00	0.14	5.36	4.50	0.32	0.59	98.59
KN18_2	73.73	0.15	9.79	3.46	0.07	0.01	0.27	5.46	4.49	0.31	0.67	98.43
KN18_3	74.73	0.12	10.03	3.43	0.06	0.00	0.14	5.28	4.55	0.32	0.45	99.11
KN18_3	75.10	0.14	10.03	3.59	0.06	0.00	0.13	5.10	4.52	0.32	0.45	99.45
KN18_3	74.55	0.16	9.93	3.47	0.05	0.00	0.18	5.51	4.45	0.34	0.54	99.16
KN18_3	73.85	0.16	10.00	3.51	0.06	0.00	0.09	5.41	4.44	0.32	0.47	98.32
KN18_4	74.42	0.15	10.30	3.38	0.04	0.00	0.48	5.70	4.53	0.32	0.81	100.1
KN18_4	74.79	0.16	10.02	3.49	0.04	0.01	0.09	5.34	4.46	0.32	0.52	99.22
KN18_4	75.51	0.16	10.03	3.57	0.05	0.00	0.14	5.36	4.53	0.33	0.43	100.1
KN18_5	74.61	0.13	9.99	3.54	0.09	0.00	0.10	5.60	4.52	0.32	0.60	99.49
KN18_5	74.81	0.15	9.86	3.51	0.07	0.03	0.14	5.36	4.58	0.33	0.58	99.42
KN18_5	74.59	0.17	10.00	3.55	0.04	0.01	0.20	5.42	4.48	0.31	0.59	99.36
KN18_6	75.42	0.14	10.12	3.45	0.08	0.00	0.15	5.22	4.64	0.32	0.60	100.1
KN18_6	75.15	0.13	10.25	3.37	0.05	0.01	0.05	5.52	4.45	0.31	0.53	99.82
KN18_6	74.51	0.13	10.04	3.39	0.07	0.01	0.17	5.63	4.58	0.34	0.57	99.43
KN18_7	74.24	0.16	9.81	3.29	0.03	0.00	0.19	5.35	4.55	0.34	0.62	98.58
KN18_7	75.62	0.14	10.13	3.57	0.06	0.00	0.47	1.86	4.59	0.34	0.72	97.50
KN18_7	76.05	0.18	9.82	3.73	0.03	0.02	0.04	2.94	4.52	0.31	0.55	98.19
KN18_8	75.15	0.17	9.71	3.48	0.05	0.02	0.41	5.32	4.46	0.32	0.94	100
KN18_8	75.16	0.16	9.89	3.45	0.04	0.00	0.25	5.33	4.55	0.32	0.61	99.75
KN18_8	75.42	0.13	10.26	3.35	0.07	0.01	0.37	5.34	4.58	0.32	0.73	100.6
KN18_9	56.89	0.16	7.88	3.30	0.07	0.00	0.11	5.46	4.21	0.32	0.63	79.04
KN18_9	15.40	0.02	2.96	2.66	0.07	0.00	0.05	4.60	1.68	0.18	0.60	28.22
KN18_9	15.27	0.05	2.86	2.63	0.04	0.01	0.02	4.64	1.72	0.18	0.55	27.98
KN18_10	74.43	0.11	9.93	3.36	0.03	0.00	0.47	5.60	4.49	0.32	0.84	99.58
KN18_10	73.61	0.10	10.14	3.56	0.08	0.01	0.16	5.51	4.58	0.30	0.54	98.58

SAMPLE	SiO2	TiO2	Al2O3	FeO	MnO	MgO	CaO	Na2O	K2O	Cl	F	TOTAL
KN18_10	73.62	0.18	10.11	3.54	0.04	0.01	0.10	5.18	4.48	0.33	0.52	98.10
KN18_9	74.50	0.16	10.00	3.43	0.06	0.00	0.24	5.51	4.55	0.32	0.60	99.39
KN18_9	74.16	0.15	10.01	3.47	0.06	0.00	0.07	5.23	4.52	0.33	0.73	98.74
KN18_9	73.53	0.18	10.21	3.47	0.09	0.02	0.35	5.25	4.52	0.32	0.55	98.48
KN18_10	75.11	0.13	10.10	3.58	0.06	0.01	0.21	5.62	4.69	0.33	0.50	100.3
KN18_10	74.83	0.18	9.80	3.43	0.10	0.00	0.11	5.22	4.58	0.32	0.59	99.14
KN18_10	74.91	0.15	10.10	3.43	0.05	0.00	0.07	5.33	4.63	0.31	0.52	99.50
KN18_11	74.39	0.15	9.85	3.45	0.07	0.00	0.10	5.20	4.54	0.34	0.49	98.59
KN18_11	75.47	0.14	10.19	3.51	0.06	0.00	0.28	4.76	4.53	0.33	0.69	99.96
KN18_11	74.95	0.14	9.88	3.44	0.02	0.01	0.07	5.26	4.54	0.33	0.57	99.20
KN18_11	75.41	0.18	10.09	3.44	0.06	0.01	0.45	5.42	4.42	0.32	0.72	100.5
KN18_11	74.89	0.15	10.15	3.43	0.05	0.02	0.13	5.55	4.51	0.32	0.76	99.95
KN18_11	75.64	0.16	10.00	3.47	0.07	0.01	0.18	5.24	4.53	0.32	0.55	1001
KN18_12	74.88	0.18	10.37	3.49	0.03	0.01	0.00	5.34	4.48	0.33	0.48	99.58
KN18_12	74.39	0.14	9.60	3.45	0.10	0.01	0.25	5.05	4.43	0.32	0.53	98.27
KN18_12	75.23	0.21	9.85	3.47	0.07	0.00	0.37	5.10	4.47	0.32	0.73	99.82
KN18_13	75.72	0.15	10.04	3.49	0.05	0.00	0.18	5.55	4.48	0.32	0.65	100
KN18_13	75.77	0.16	10.01	3.45	0.09	0.01	0.02	5.32	4.44	0.32	0.61	100
KN18_13	75.93	0.16	10.31	3.52	0.04	0.00	0.25	5.49	4.51	0.33	0.62	100
KN18_13	75.78	0.14	9.99	3.51	0.05	0.02	0.03	5.46	4.58	0.32	0.49	100
KN18_14	75.08	0.14	9.93	3.43	0.10	0.01	0.08	5.55	4.53	0.33	0.58	99.77
KN18_14	75.74	0.15	9.97	3.48	0.08	0.00	0.06	5.01	4.50	0.32	0.61	99.94
KN18_14	75.12	0.18	9.85	3.49	0.06	0.00	0.21	5.36	4.51	0.33	0.64	99.74
KN18_14	75.40	0.17	10.13	3.42	0.06	0.00	0.10	4.97	4.59	0.33	0.52	99.70
KN18_15	74.32	0.13	10.23	3.44	0.08	0.00	0.43	5.41	4.51	0.31	0.91	99.79
KN18_15	74.99	0.15	9.82	3.55	0.05	0.01	0.04	5.01	4.57	0.34	0.50	99.02
KN18_15	75.28	0.14	10.31	3.54	0.10	0.02	0.09	5.45	4.54	0.35	0.47	100
KN18_16	75.02	0.21	10.09	3.54	0.06	0.02	0.13	5.24	4.43	0.32	0.64	99.71
KN18_16	74.65	0.13	9.88	3.49	0.06	0.01	0.15	5.57	4.37	0.33	0.56	99.19
KN18_16	75.28	0.18	9.82	3.47	0.08	0.00	0.13	5.13	4.59	0.34	0.61	99.63
KN18_17	75.00	0.11	10.32	3.48	0.10	0.00	0.23	5.38	4.49	0.34	0.57	100
KN18_17	74.74	0.15	9.95	3.40	0.07	0.02	0.14	5.16	4.51	0.33	0.53	98.98
KN18_17	75.92	0.13	10.08	3.51	0.04	0.00	0.18	5.33	4.52	0.31	0.51	100
KN18_18	75.37	0.14	10.00	3.49	0.03	0.00	0.15	5.46	4.39	0.64	0.33	98.64
KN18_18	74.68	0.19	9.84	3.35	0.06	0.00	0.73	5.26	4.40	1.18	0.31	100
KN18_18	75.00	0.13	10.20	3.46	0.04	0.00	0.36	5.38	4.34	0.75	0.33	99.75
KN18_19	75.82	0.14	9.85	3.45	0.02	0.00	0.05	5.20	4.58	0.55	0.32	99.33
KN18_19	75.09	0.15	10.26	3.55	0.10	0.01	0.12	5.38	4.46	0.55	0.32	100
KN18_19	75.57	0.15	10.00	3.50	0.07	0.01	0.03	5.25	4.54	0.57	0.32	99.69
KN18_20	78.16	0.16	10.35	3.60	0.03	0.01	0.02	2.21	4.62	0.51	0.33	98.87
KN18_20	75.31	0.18	10.17	3.51	0.06	0.01	0.10	5.26	4.41	0.67	0.33	100
KN18_20	75.36	0.13	10.15	3.41	0.07	0.01	0.07	5.57	4.40	0.51	0.32	100
KN18_21	75.35	0.14	9.94	3.51	0.11	0.01	0.14	5.40	4.58	0.50	0.33	99.45
KN18_21	75.35	0.14	10.04	3.44	0.06	0.02	0.27	5.12	4.58	0.65	0.32	99.29
KN18_22	75.20	0.11	10.14	3.56	0.05	0.01	0.18	5.17	4.36	0.91	0.32	99.90

SAMPLE	SiO2	TiO2	Al2O3	FeO	MnO	MgO	CaO	Na2O	K2O	Cl	F	TOTAL
KN18_22	77.25	0.10	10.54	3.56	0.02	0.00	0.12	2.83	4.75	0.53	0.32	99.28
KN18_23	75.37	0.18	10.13	3.44	0.06	0.00	0.05	5.45	4.43	0.58	0.34	99.90
KN18_23	75.27	0.18	10.01	3.52	0.06	0.00	0.10	5.48	4.49	0.58	0.33	100
KN18_24	75.36	0.17	9.87	3.55	0.07	0.00	0.08	5.49	4.59	0.51	0.33	99.96
KN18_25	75.08	0.13	10.08	3.46	0.11	0.00	0.32	5.23	4.53	0.74	0.32	99.58
KN18_25	75.91	0.13	9.98	3.45	0.06	0.00	0.10	5.18	4.41	0.46	0.32	100
KN18_26	74.69	0.19	10.01	3.44	0.04	0.02	0.47	5.44	4.51	0.89	0.32	100
KN18_26	74.91	0.15	10.13	3.44	0.09	0.00	0.59	5.19	4.56	0.61	0.33	100
KN18_27	75.19	0.16	10.02	3.53	0.06	0.00	0.21	5.45	4.50	0.54	0.34	98.11
KN18_27	75.22	0.12	10.20	3.60	0.07	0.00	0.05	5.30	4.61	0.51	0.32	98.31
AV.	74.7	0.2	10.3	3.5	*	0.0	0.2	5.0	4.5	0.3	0.7	
SD	0.6	0.0	0.2	0.1	*	0.0	0.1	0.9	0.2	0.0	0.1	
RSD %	0.8	21.5	2.3	2.0	*	163	61	17	4.1	4.4	19	
ERROR (wt%)	1.3	0.1	0.5	0.1	*	0.1	0.6	2.0	0.4	0.0	0.3	
10/02/17	ABII-12-16; ABII-8-46; LLIII-05-60; ABII-11-64; LLIII-09-15; LLIII-09-74; ABII-04-14; MER046L; MER050W; MER050E; MER046B; MER046Q; MER048E; MER048E; MER048J; MER048F; MER048V; MER048W; MER050S; MER048V; MER046Z; MER048B; MER048N; MER048P; MER046L; MER046D; MER048Q; MER046X;MER048H; MER046V; MER046H; MER048M; MER048D; MER048I.											
KN18_1	73.70	0.17	10.47	3.55	*	0.00	0.06	5.96	4.57	0.34	0.58	99.40
KN18_1	74.94	0.20	10.17	3.49	*	0.01	0.19	5.38	4.30	0.33	0.46	99.47
KN18_1	75.95	0.21	10.31	3.45	*	0.05	0.24	5.28	4.21	0.33	0.59	100
KN18_2	74.07	0.13	9.91	3.53	*	0.01	0.21	5.78	4.73	0.31	0.82	99.50
KN18_2	74.62	0.12	10.25	3.52	*	0.00	0.14	5.61	4.38	0.32	0.61	99.56
KN18_3	75.12	0.18	10.20	3.46	*	0.00	0.27	5.56	4.53	0.32	0.69	100
KN18_4	74.36	0.16	10.48	3.60	*	0.05	0.23	5.32	4.25	0.33	0.82	99.60
KN18_4	74.44	0.14	10.25	3.55	*	0.02	0.21	5.35	4.50	0.33	0.56	99.34
KN18_4	74.95	0.09	10.37	3.64	*	0.04	0.09	5.57	4.42	0.31	0.63	100
KN18_5	75.16	0.22	9.99	3.43	*	0.02	0.16	5.45	4.54	0.32	0.45	99.73
KN18_5	74.12	0.21	10.65	3.36	*	0.01	0.23	5.54	4.63	0.30	0.64	99.70
KN18_5	74.64	0.22	10.01	3.32	*	0.04	0.17	5.49	4.32	0.31	0.84	99.38
KN18_6	75.15	0.16	10.16	3.46	*	0.00	0.09	5.57	4.26	0.31	0.68	99.83
KN18_7	74.45	0.13	9.97	3.41	*	0.00	0.18	5.56	4.40	0.33	0.58	98.96
KN18_8	75.60	0.17	10.72	3.39	*	0.01	0.18	5.38	4.42	0.32	0.72	100
KN18_10	74.22	0.19	10.40	3.54	*	0.01	0.18	5.31	4.39	0.33	0.68	99.25
KN18_10	74.65	0.21	10.06	3.48	*	0.02	0.18	5.41	4.32	0.31	0.59	99.23
KN18_11	73.64	0.15	10.17	3.47	*	0.02	0.19	5.45	4.17	0.34	0.56	98.15
KN18_11	74.39	0.17	10.49	3.53	*	0.01	0.17	5.35	4.38	0.32	1.01	99.81
KN18_12	74.85	0.15	10.57	3.55	*	0.01	0.30	5.17	4.57	0.32	0.63	100
KN18_12	76.12	0.15	10.27	3.44	*	0.00	0.07	5.05	4.26	0.34	0.69	100
KN18_13	75.17	0.10	10.38	3.45	*	0.00	0.27	5.08	4.55	0.33	0.74	100
KN18_13	75.43	0.14	10.13	3.56	*	0.02	0.17	5.39	4.35	0.33	0.70	100
KN18_14	74.17	0.19	10.14	3.63	*	0.00	0.12	5.25	4.45	0.30	0.45	98.68

SAMPLE	SiO2	TiO2	Al2O3	FeO	MnO	MgO	CaO	Na2O	K2O	Cl	F	TOTAL
KN18_14	75.14	0.14	10.29	3.50	*	0.00	0.21	5.19	4.53	0.33	0.60	99.93
KN18_15	75.22	0.12	10.57	3.52	*	0.00	0.46	5.16	4.58	0.31	0.88	100
KN18_15	70.63	0.16	9.89	3.38	*	0.00	0.34	5.25	4.13	0.34	0.66	94.76
KN18_15	61.19	0.18	7.38	5.93	*	0.00	0.28	6.10	4.21	0.20	0.31	85.76
KN18_15	73.40	0.18	8.53	5.83	*	0.00	0.34	6.14	4.30	0.22	0.47	99.39
KN18_15	73.79	0.14	8.54	5.81	*	0.01	0.28	6.12	4.22	0.22	0.36	99.48
KN18_15	70.86	0.18	8.23	5.73	*	0.01	0.38	5.75	4.17	0.23	0.31	95.86
KN18_16	74.88	0.22	10.33	3.37	*	0.01	0.27	5.11	4.52	0.34	0.69	99.75
KN18_16	74.90	0.15	10.10	3.60	*	0.01	0.33	5.11	4.51	0.31	0.66	99.68
KN18_16	75.72	0.11	10.38	3.45	*	0.02	0.96	5.47	4.41	0.31	1.17	102
KN18_17	75.56	0.21	10.60	3.51	*	0.00	0.15	5.64	4.38	0.32	0.42	100.8
KN18_17	75.35	0.21	10.27	3.46	*	0.00	0.21	5.27	4.56	0.30	0.52	100.15
KN18_18	74.61	0.17	10.10	3.55	*	0.00	0.21	5.30	4.43	0.29	0.58	99.24
KN18_19	74.96	0.17	10.23	3.43	*	0.02	0.07	5.51	4.37	0.33	0.63	99.71
KN18_19	75.71	0.17	10.33	3.44	*	0.00	0.15	5.34	4.32	0.31	0.89	100
KN18_21	74.63	0.16	10.03	3.58	*	0.01	0.20	5.31	4.50	0.32	0.59	99.32
KN18_21	75.63	0.11	10.27	3.52	*	0.01	0.27	5.69	4.39	0.31	0.49	100
KN18_21	74.76	0.14	10.48	3.47	*	0.00	0.10	5.68	4.37	0.31	0.54	99.85
KN18_22	75.16	0.11	10.46	3.57	*	0.02	0.28	5.39	4.48	0.34	0.56	100
KN18_24	75.22	0.12	10.67	3.36	*	0.00	0.15	5.94	4.36	0.33	0.57	100
KN18_25	75.76	0.20	10.49	3.61	*	0.03	0.31	5.23	4.39	0.32	0.45	100
KN18_25	74.88	0.20	10.03	3.53	*	0.00	0.29	5.39	4.43	0.32	0.57	99.64
KN18_26	74.04	0.07	10.47	3.44	*	0.00	0.22	5.38	4.54	0.31	0.69	99.16
KN18_26	75.37	0.12	10.26	3.45	*	0.02	0.16	5.19	4.56	0.36	0.62	100
KN18_27	74.62	0.18	10.21	3.45	*	0.03	0.29	5.05	4.26	0.34	0.56	99.00
KN18_28	75.32	0.18	10.20	3.51	*	0.02	0.08	5.20	4.58	0.33	0.73	100
KN18_29	74.47	0.16	10.18	3.56	*	0.01	0.28	5.37	4.51	0.32	0.80	99.65
KN18_30	74.31	0.20	10.42	3.60	*	0.01	0.24	5.31	4.39	0.31	0.45	99.23
KN18_31	75.91	0.14	10.27	3.44	*	0.00	0.31	5.17	4.55	0.35	0.87	100
KN18_33	73.35	0.20	10.23	3.32	*	0.00	0.24	5.27	4.39	0.33	0.66	97.99
KN18_33	74.62	0.23	10.69	3.42	*	0.00	0.22	5.09	4.39	0.28	0.81	99.75
KN18_34	74.10	0.22	10.21	3.55	*	0.00	0.45	5.78	4.17	0.32	0.85	99.65
KN18_35	74.91	0.16	9.87	3.42	*	0.00	0.24	5.05	4.52	0.30	0.96	99.42
KN18_36	74.55	0.20	10.55	3.45	*	0.01	0.22	4.51	4.61	0.32	0.53	98.95
KN18_36	74.60	0.17	10.59	3.59	*	0.01	0.06	5.30	4.47	0.32	0.68	99.79
KN18_37	73.65	0.21	9.89	3.39	*	0.01	0.13	5.40	4.30	0.34	0.64	97.96
KN18_39	74.00	0.19	10.61	3.56	*	0.02	0.21	5.39	4.39	0.36	0.79	99.51
KN18_39	73.24	0.15	10.44	3.52	*	0.03	0.32	5.26	4.45	0.32	0.76	98.49
KN18_40	74.34	0.21	9.94	3.47	*	0.02	0.41	5.44	4.42	0.30	0.72	99.27
KN18_40	73.32	0.19	9.79	3.59	*	0.01	0.10	5.37	4.40	0.32	0.74	97.83
KN18_41	75.11	0.20	10.03	3.44	*	0.03	0.26	5.16	4.42	0.33	0.82	99.79
KN18_41	74.08	0.17	10.43	3.53	*	0.00	0.12	5.52	4.29	0.32	0.55	99.03
KN18_42	74.10	0.20	10.15	3.41	*	0.00	0.08	5.02	4.36	0.30	0.66	98.29
KN18_43	75.38	0.22	10.17	3.49	*	0.00	0.27	5.44	4.67	0.32	0.81	100
KN18_43	74.98	0.21	10.04	3.37	*	0.00	0.11	5.14	4.30	0.31	0.74	99.17

SAMPLE	SiO2	TiO2	Al2O3	FeO	MnO	MgO	CaO	Na2O	K2O	Cl	F	TOTAL
KN18_44	73.30	0.21	10.01	3.48	*	0.01	0.05	5.43	4.36	0.30	0.55	97.70
KN18_44	74.29	0.20	10.28	3.52	*	0.02	0.20	5.29	4.46	0.32	0.43	99.00
KN18_45	75.26	0.14	10.26	3.41	*	0.00	0.48	2.75	4.95	0.30	0.81	98.38
KN18_45	74.43	0.11	10.16	3.39	*	0.00	0.32	5.49	4.28	0.31	0.70	99.19
KN18_46	75.52	0.11	10.27	3.63	*	0.01	0.25	3.52	4.36	0.32	0.61	98.60
KN18_46	74.86	0.12	10.25	3.49	*	0.01	0.08	4.18	4.36	0.32	0.59	98.25
KN19_47	75.26	0.19	10.82	3.54	*	0.00	0.16	5.85	4.66	0.35	0.69	100
KN19_47	74.58	0.15	10.34	3.53	*	0.00	0.39	5.35	4.48	0.34	0.91	100
KN18_48	74.55	0.17	10.08	3.47	*	0.00	0.13	5.47	4.32	0.31	0.67	99.16
KN18_48	75.42	0.19	10.68	3.41	*	0.04	0.17	5.36	4.52	0.31	0.68	100
AV.	74.74	0.17	10.26	3.47	*	0.01	0.21	5.00	4.45	0.32	0.68	
SD	0.63	0.04	0.23	0.07	*	0.01	0.12	0.85	0.18	0.01	0.13	
RSD %	0.84	21.50	2.25	2.02	*	163	60.55	17.02	4.12	4.39	18.61	
ERROR (wt%)	1.27	0.10	0.49	0.15	*	0.12	0.59	1.99	0.41	0.03	0.34	
14/02/17	ABII-05-60											
KN18_1	73.84	0.11	10.26	3.45	*	0.01	0.00	5.18	4.34	0.32	0.68	98.19
KN18_2	74.37	0.12	10.27	3.63	*	0.00	0.00	4.87	4.33	0.32	0.69	98.61
KN18_3	73.77	0.16	10.20	3.53	*	0.01	0.16	4.71	4.54	0.33	0.92	98.34
AV.	74.0	0.1	10.2	3.5	*	0.0	0.1	4.9	4.4	0.3	0.8	
SD	0.3	0.0	0.0	0.1	*	0.0	0.1	0.2	0.1	0.0	0.1	
RSD %	0.4	18.9	0.4	2.5	*	117	176	4.8	2.7	2.3	18	
ERROR (wt%)	0.7	0.1	0.1	0.2	*	0.0	0.6	0.5	0.2	0.0	0.3	
21/11/17	ABII-09-03; LLIII-03-01; LLIII-04-11; LLIII-03-01; LLIII-03-70; ABII-04-67; MER050G; MER050D;MER046T; MER046J; MER046K											
KN18_1	74.54	0.16	10.44	3.55	0.02	0.02	0.12	5.41	4.57	0.34	0.61	99.78
KN18_2	73.57	0.14	10.24	3.60	0.08	0.00	0.17	5.37	4.57	0.32	0.68	98.73
KN18_3	74.74	0.18	10.27	3.50	0.03	0.00	0.05	5.57	4.62	0.32	0.47	99.77
KN18_4	74.35	0.17	10.47	3.54	0.06	0.01	0.09	5.37	4.49	0.34	0.68	99.56
KN18_5	71.46	0.15	8.10	6.61	0.30	0.01	0.25	6.24	4.21	0.24	0.25	97.81
KN18_6	74.50	0.15	10.40	3.50	0.04	0.01	0.13	5.45	4.59	0.34	0.64	99.74
KN18_7	74.91	0.14	10.55	3.52	0.06	0.01	0.10	5.46	4.50	0.33	0.56	100
KN18_8	74.52	0.16	10.17	3.52	0.06	0.00	0.18	5.55	4.55	0.33	0.60	99.65
KN18_9	74.86	0.13	10.53	3.51	0.04	0.01	0.08	5.38	4.56	0.32	0.53	99.94
KN18_10	74.59	0.22	10.41	3.55	0.09	0.00	0.07	5.22	4.41	0.33	0.52	99.42
KN18_11	74.91	0.15	10.78	3.58	0.04	0.01	0.01	5.53	4.55	0.33	0.58	100
KN18_12	74.84	0.14	10.38	3.51	0.06	0.00	0.20	5.41	4.47	0.33	0.62	99.97
KN18_13	74.98	0.17	10.49	3.57	0.06	0.01	0.07	5.30	4.51	0.34	0.54	100
KN18_14	74.60	0.15	10.45	3.47	0.06	0.01	0.30	5.28	4.53	0.33	0.70	99.88
KN18_15	74.50	0.18	10.67	3.55	0.02	0.00	0.22	5.37	4.53	0.32	0.66	100
KN18_16	75.09	0.18	10.57	3.58	0.06	0.01	0.06	5.29	4.51	0.33	0.55	100
KN18_17	75.00	0.15	10.39	3.55	0.08	0.00	0.17	5.33	4.47	0.33	0.71	100
KN18_18	73.29	0.11	10.05	3.59	0.06	0.01	0.00	4.48	4.66	0.32	0.68	97.26
KN18_19	73.25	0.19	10.37	3.59	0.07	0.01	0.07	5.79	4.39	0.33	0.55	98.61

SAMPLE	SiO2	TiO2	Al2O3	FeO	MnO	MgO	CaO	Na2O	K2O	Cl	F	TOTAL
KN18_20	72.72	0.11	10.13	3.64	0.06	0.00	0.08	5.11	4.51	0.33	0.56	97.26
AV.	74.3	0.2	10.3	3.7	0.1	0.0	0.1	5.4	4.5	0.3	0.6	
SD	0.9	0.0	0.5	0.7	0.1	0.0	0.1	0.3	0.1	0.0	0.1	
RSD %	1.3	16.9	5.3	18.5	83.5	88	66	5.9	2.1	6.1	17.6	
ERROR (wt%)	1.9	0.1	1.1	2.5	0.5	0.0	0.4	0.7	0.2	0.0	0.3	
24/11/17	ABII-12-11; LLIII-08-38; ABII-09-31; ABII-08-78; LLIII-09-74; ABII-09-08; LLIII-07-105;MER048T											
KN18_1	73.89	0.09	10.08	3.68	0.07	0.03	0.15	5.80	4.49	0.52	0.33	99.15
KN18_1	73.66	0.18	9.68	3.51	0.05	0.00	0.10	5.09	4.58	0.47	0.34	97.66
KN18_1	73.57	0.16	10.20	3.40	0.03	0.00	0.16	5.64	4.57	0.49	0.31	98.54
KN18_1	74.79	0.15	10.27	3.45	0.04	0.00	0.10	5.23	4.52	0.45	0.32	99.33
KN18_1	74.52	0.17	10.34	3.53	0.07	0.01	0.06	5.29	4.57	0.52	0.32	99.40
KN18_1	74.29	0.16	10.31	3.47	0.03	0.00	0.11	5.43	4.54	0.53	0.33	99.20
KN18_1	74.03	0.15	10.32	3.45	0.07	0.00	0.00	5.45	4.44	0.52	0.32	98.75
KN18_2	74.04	0.15	10.16	3.47	0.09	0.00	0.07	5.40	4.60	0.56	0.32	98.86
KN18_2	74.66	0.16	10.33	3.54	0.06	0.00	0.07	5.37	4.54	0.62	0.32	99.68
KN18_2	74.08	0.15	9.97	3.50	0.08	0.01	0.15	5.40	4.48	0.58	0.32	98.73
KN18_2	74.25	0.15	10.30	3.45	0.06	0.00	0.09	5.50	4.54	0.54	0.33	99.21
KN18_2	73.95	0.14	10.34	3.52	0.04	0.00	0.18	5.56	4.54	0.63	0.34	99.24
KN18_2	74.56	0.16	10.10	3.54	0.04	0.01	0.09	5.53	4.44	0.58	0.33	99.40
KN18_3	74.03	0.15	10.27	3.49	0.08	0.00	0.13	5.21	4.45	0.60	0.32	98.72
KN18_3	73.76	0.18	10.28	3.50	0.04	0.01	0.13	4.75	4.56	0.56	0.33	98.10
KN18_3	73.63	0.19	10.09	3.49	0.04	0.01	0.37	5.42	4.49	0.68	0.33	98.73
KN18_3	73.68	0.15	10.04	3.50	0.04	0.00	0.26	5.34	4.50	0.69	0.32	98.52
KN18_3	73.74	0.15	10.31	3.52	0.08	0.01	0.07	5.37	4.50	0.59	0.33	98.67
KN18_4	74.31	0.15	10.17	3.52	0.02	0.02	0.15	5.34	4.54	0.53	0.33	99.08
KN18_4	74.35	0.17	10.00	3.49	0.07	0.01	0.31	5.31	4.51	0.81	0.32	99.35
KN18_4	74.86	0.19	10.48	3.55	0.07	0.01	0.11	5.73	4.54	0.57	0.33	100
KN18_4	74.77	0.15	10.22	3.53	0.05	0.01	0.02	5.36	4.50	0.52	0.34	99.46
KN18_5	74.16	0.13	10.24	3.56	0.03	0.00	0.08	5.47	4.57	0.50	0.32	99.06
KN18_5	74.47	0.16	10.28	3.47	0.06	0.00	0.30	5.28	4.51	0.77	0.34	99.65
KN18_5	74.22	0.18	10.26	3.56	0.05	0.01	0.18	5.19	4.54	0.70	0.32	99.20
KN18_5	74.12	0.17	10.18	3.57	0.05	0.01	0.13	5.54	4.50	0.55	0.34	99.15
KN18_6	76.50	0.14	10.51	3.61	0.08	0.01	0.07	2.09	4.64	0.57	0.33	98.55
KN18_6	74.88	0.18	10.34	3.48	0.07	0.00	0.05	4.47	4.52	0.45	0.32	98.76
KN18_6	74.65	0.14	10.57	3.53	0.06	0.01	0.12	5.30	4.49	0.61	0.31	99.79
KN18_6	75.36	0.14	10.50	3.51	0.10	0.00	0.01	4.60	4.46	0.57	0.33	99.58
KN18_6	75.12	0.14	10.13	3.52	0.07	0.01	0.39	4.98	4.50	0.82	0.32	99.98
KN18_7	75.00	0.18	10.56	3.46	0.06	0.00	0.10	5.40	4.48	0.58	0.34	100
KN18_7	75.33	0.14	10.29	3.44	0.08	0.00	0.10	5.40	4.51	0.56	0.32	100
KN18_7	74.99	0.16	10.46	3.48	0.05	0.00	0.20	5.46	4.55	0.64	0.33	100
KN18_7	74.91	0.16	10.25	3.55	0.01	0.00	0.26	5.42	4.45	0.67	0.33	100
KN18_7	74.93	0.15	10.28	3.52	0.06	0.01	0.16	5.45	4.53	0.57	0.32	99.97
AV.	74.4	0.2	10.3	3.5	0.1	0.0	0.1	5.2	4.5	0.6	0.3	

SAMPLE	SiO2	TiO2	Al2O3	FeO	MnO	MgO	CaO	Na2O	K2O	Cl	F	TOTAL
SD	0.6	0.0	0.2	0.1	0.0	0.0	0.1	0.6	0.0	0.1	0.0	
RSD %	0.8	12.3	1.7	1.5	34	116	67	11.5	1.0	15.3	2.2	
ERROR (wt%)	1.3	0.0	0.4	0.1	0.1	0.1	0.5	1.3	0.1	0.3	0.0	
13/12/17	ABII-09-31; ABII-10-45											
KN18_2	74.34	0.17	10.20	3.55	0.06	0.00	0.15	5.29	4.56	0.34	0.54	99.20
KN18_2	74.67	0.17	10.48	3.46	0.05	0.00	0.33	5.20	4.47	0.31	0.75	99.89
KN18_3	74.09	0.18	10.38	3.53	0.07	0.00	0.29	5.29	4.52	0.33	0.71	99.39
KN18_3	75.12	0.22	10.46	3.54	0.05	0.01	0.05	5.25	4.53	0.32	0.58	100
KN18_3	74.98	0.13	10.63	3.54	0.05	0.00	0.09	5.31	4.54	0.31	0.56	100
KN18_1	74.15	0.16	10.30	3.57	0.06	0.03	0.08	5.50	4.61	0.33	0.37	99.17
KN18_1	74.09	0.17	10.48	3.58	0.06	0.03	0.10	5.45	4.55	0.32	0.49	99.31
KN18_1	72.91	0.19	10.25	3.46	0.05	0.04	0.17	4.96	4.54	0.32	0.42	97.30
AV.	74.3	0.2	10.4	3.5	0.1	0.0	0.2	5.3	4.5	0.3	0.6	
SD	0.7	0.0	0.1	0.0	0.0	0.0	0.1	0.2	0.0	0.0	0.1	
RSD %	0.9	14.4	1.4	1.3	15	116	64.7	3.1	0.8	2.2	24	
ERROR (wt%)	1.4	0.1	0.3	0.1	0.0	0.1	0.4	0.3	0.1	0.0	0.4	
MELT INCLUSIONS. 3um spot size												
06/06/18												
KN18_1	73.51	0.19	10.13	3.29	0.06	0.02	0.38	5.20	4.38	0.24	0.87	97.16
KN18_1	74.25	0.16	10.45	3.37	0.12	0.02	0.09	5.95	4.46	0.24	0.49	98.88
KN18_1	72.97	0.18	10.38	3.22	0.03	0.00	0.11	4.94	4.51	0.25	0.50	96.35
KN18_2	76.44	0.13	10.28	3.35	0.00	0.00	0.13	5.58	4.63	0.25	0.47	100
KN18_2	73.15	0.16	10.34	3.37	0.01	0.00	0.07	5.41	4.13	0.26	0.45	96.64
KN18_2	71.67	0.14	9.76	3.27	0.00	0.00	1.06	5.10	4.27	0.24	1.50	95.24
KN18_2	74.57	0.14	10.74	3.44	0.01	0.00	0.07	5.24	4.59	0.25	0.47	98.80
KN18_3	73.31	0.19	10.52	3.24	0.07	0.01	0.04	5.02	4.40	0.24	0.42	96.79
KN18_4	72.82	0.19	10.80	3.28	0.07	0.00	0.00	5.22	4.54	0.24	0.45	96.90
KN18_4	74.00	0.16	10.16	3.38	0.06	0.00	0.16	5.50	4.75	0.24	0.60	98.17
KN18_4	74.79	0.17	10.27	3.37	0.08	0.00	0.10	5.38	4.64	0.24	0.39	98.80
KN18_4	76.15	0.18	10.22	3.31	0.06	0.01	0.01	5.27	4.56	0.24	0.35	99.77
KN18_5	75.97	0.20	10.25	3.46	0.07	0.02	0.01	4.85	4.58	0.24	0.45	99.40
KN18_6	75.15	0.19	10.87	3.35	0.09	0.01	0.17	5.61	4.18	0.24	0.42	99.63
KN18_6	72.83	0.20	9.77	3.43	0.07	0.02	0.00	5.04	4.36	0.24	0.33	95.68
KN18_6	74.26	0.19	10.22	3.39	0.11	0.02	0.00	4.76	4.64	0.24	0.35	97.59
KN18_6	75.74	0.19	10.45	3.43	0.11	0.01	0.04	5.69	4.49	0.24	0.35	100
KN18_7	73.78	0.15	10.12	3.46	0.12	0.00	0.16	5.39	4.14	0.24	0.39	97.32
KN18_7	74.03	0.13	10.40	3.42	0.12	0.00	0.17	4.81	4.82	0.24	0.41	97.90
KN18_7	73.71	0.15	10.40	3.50	0.15	0.00	0.18	5.22	4.30	0.23	0.40	97.62
KN18_7	72.94	0.15	10.14	3.39	0.09	0.00	0.12	4.69	4.80	0.23	0.35	96.33
KN18_8	76.99	0.14	10.73	3.67	0.01	0.01	0.00	5.07	4.76	0.26	0.25	100
KN18_8	75.90	0.17	10.67	3.45	0.02	0.01	0.08	5.51	4.60	0.26	0.36	100.4
KN18_8	74.54	0.16	10.72	3.68	0.02	0.00	0.04	5.15	4.07	0.27	0.34	98.38
KN18_9	73.50	0.16	10.47	3.44	0.01	0.00	0.00	4.32	4.42	0.25	0.54	96.31

SAMPLE	SiO2	TiO2	Al2O3	FeO	MnO	MgO	CaO	Na2O	K2O	Cl	F	TOTAL
KN18_9	75.54	-0.11	10.04	3.28	0.00	0.00	0.00	4.58	4.39	0.19	0.33	97.39
KN18_9	73.88	0.15	10.13	3.52	0.04	0.00	0.02	5.43	4.31	0.26	0.56	97.47
KN18_9	72.55	0.18	10.62	3.41	0.01	0.00	0.05	5.41	4.82	0.25	0.52	97.06
KN18_9	73.19	0.19	10.41	3.54	0.04	0.00	0.03	4.85	4.75	0.25	0.56	96.99
KN18_10	76.54	0.17	10.74	3.50	0.04	0.02	0.00	5.79	4.39	0.24	0.51	100
KN18_10	73.70	0.16	10.66	3.43	0.06	0.01	0.06	5.38	4.39	0.24	0.57	97.86
KN18_10	74.25	0.17	10.15	3.53	0.02	0.01	0.02	4.94	4.40	0.24	0.55	97.51
KN18_10	73.63	0.17	10.74	3.43	0.05	0.01	0.36	4.54	4.32	0.24	0.66	97.24
KN18_11	74.98	0.16	10.28	3.44	0.04	0.00	0.05	4.96	4.50	0.24	0.63	98.39
KN18_11	73.56	0.17	10.52	3.51	0.00	0.00	0.09	5.55	4.78	0.24	0.62	98.18
KN18_11	75.35	0.16	10.58	3.42	0.01	0.00	0.01	5.33	4.56	0.25	0.50	99.42
KN18_12	74.24	0.19	10.50	3.57	0.07	0.02	0.05	5.43	4.29	0.25	0.44	98.36
KN18_12	74.86	0.20	10.60	3.40	0.05	0.03	0.54	4.46	4.62	0.26	0.52	98.76
KN18_13	77.17	0.18	10.52	3.52	0.06	0.02	0.06	5.26	4.35	0.25	0.41	100
KN18_14	72.99	0.17	10.39	3.47	0.05	0.02	0.48	4.88	4.62	0.24	0.38	97.06
KN18_14	75.02	0.16	10.31	3.49	0.06	0.02	0.12	4.50	4.62	0.24	0.42	98.30
KN18_14	74.13	0.19	10.70	3.52	0.05	0.02	0.22	5.84	4.81	0.24	0.38	99.47
KN18_14	73.56	0.17	10.12	3.46	0.05	0.01	0.14	5.41	4.20	0.25	0.39	97.13
KN18_15	73.64	0.19	10.61	3.47	0.00	0.01	0.00	5.71	4.64	0.26	0.40	98.18
KN18_15	74.05	0.16	10.41	3.47	0.02	0.01	0.01	4.59	4.68	0.25	0.35	97.40
KN18_15	75.99	0.16	10.69	3.53	0.00	0.02	0.02	5.79	4.04	0.26	0.37	100
KN18_15	73.99	0.16	10.38	3.36	0.00	0.00	0.03	5.84	4.47	0.25	0.35	98.24
AV.	74.3	0.2	10.4	3.4	0.0	0.0	0.1	5.2	4.5	0.2	0.5	
SD	1.2	0.0	0.3	0.1	0.0	0.0	0.2	0.4	0.2	0.0	0.2	
RSD %	1.7	27.3	2.5	2.8	80	99.2	158.4	7.9	4.7	4.9	40	
ERROR (wt%)	2.6	0.1	0.5	0.2	0.2	0.1	3.4	0.9	0.5	0.0	1.2	

Table C.2

Sample	run	IS	Ca	Zn	Rb	Sr	Y	Zr	Nb	Cs	Ba	La	Ce	Pr	Nd	Sm	Eu	Gd	Dy	Er	Yb	Hf	Ta	Pb	Th	U
StHs6 /80-G	**TRUE**			**67**	**30.7**	**482**	**11.4**	**118**	**6.94**	**1.75**	**298**	**12**	**26.1**	**3.2**	**13**	**2.78**	**0.953**	**2.59**	**2.22**	**1.18**	**1.13**	**3.07**	**0.42**	**10.3**	**2.28**	**1.01**
StHs	a	29.8	37449	67.5	30.8	465	10.3	113	6.5	1.8	305	11.7	25.0	3.0	13	2.7	0.9	2.6	2.2	1.1	1.1	2.8	0.4	10.5	2.0	1.0
StHs_1	a	29.8	39569	75.0	31.6	492	10.5	112	6.5	1.7	317	11.9	26.3	3.2	13	3.1	0.9	2.4	2.0	1.2	1.1	2.8	0.4	10.4	2.3	1.1
StHs	b	29.8	38234	0.0	30.9	480	10.0	111	6.4	1.8	308	11.5	25.7	3.0	12	2.5	0.9	2.1	2.0	1.1	1.0	2.8	0.4	9.9	2.0	1.0
StHs_1	b	29.8	38234	72.9	32.3	491	11.0	114	6.9	1.9	309	11.9	25.7	3.1	13	2.9	0.9	2.5	2.2	1.1	1.0	2.8	0.4	10.7	2.3	1.0
StHs_2	b	29.8	36036	63.9	30.1	477	10.4	109	6.6	1.6	291	11.9	24.3	2.9	12	2.6	0.9	2.4	1.9	1.1	1.0	2.6	0.4	10.4	2.2	0.9
STHS-3	c	29.8	47200	84.4	35.0	554	11.5	124	7.4	1.7	345	12.4	28.8	3.3	13	2.9	1.0	2.6	2.2	1.2	1.1	2.7	0.5	12.1	2.4	1.2
STHS-2	c	29.8	40900	73.2	31.5	520	10.9	115	7.0	1.7	320	12.0	27.1	3.2	13	3.2	1.1	2.6	2.2	1.1	1.0	2.8	0.4	11.0	2.2	1.1
STHS-1	c	29.8	38900	72.2	31.7	521	10.6	115	6.9	1.7	306	12.5	26.2	3.5	14	2.6	1.0	2.3	2.0	1.1	1.1	2.7	0.4	9.6	2.0	0.0
STHS-2	d	29.8	33725	66.7	32.1	457	10.4	106	7.1	1.9	317	11.5	26.7	3.4	12	2.8	1.0	2.4	1.8	1.0	1.0	2.5	0.4	10.8	2.1	1.1
STHS-3	d	29.8	37007	71.6	33.8	474	10.4	107	7.0	1.9	320	11.5	26.7	3.2	12	2.4	1.0	2.3	1.7	1.1	1.0	2.6	0.4	10.6	2.1	1.1
STHS-5	d	29.8	36642	74.5	32.3	486	10.4	110	6.8	1.8	326	11.9	27.3	3.4	13	3.1	0.9	2.4	1.9	1.1	1.0	2.8	0.4	10.8	2.2	1.1
STHS-4	d	29.8	36369	69.6	33.5	471	10.0	112	6.9	1.8	318	12.1	26.3	3.2	13	2.7	1.0	2.4	2.1	1.1	1.1	2.7	0.4	10.7	2.1	1.0
STHS-6	d	29.8	40926	73.7	32.1	525	10.5	117	6.8	1.8	321	12.9	28.5	3.2	14	2.9	1.0	2.6	2.5	1.3	1.3	3.0	0.4	11.8	2.3	1.1
STHS-1	e	29.8	42845	83.4	33.9	561	11.8	122	7.3	1.9	333	13.0	28.2	3.4	14	2.9	1.1	2.6	2.5	1.3	1.1	3.0	0.5	11.7	2.3	1.1
STHS-2	e	29.8	42085	77.3	35.8	541	11.7	122	7.9	2.0	340	13.1	28.3	3.3	13	3.0	1.0	2.4	2.3	1.2	1.2	2.7	0.4	10.1	2.2	1.0
STHS-3	e	29.8	40565	75.0	32.5	500	10.8	116	7.1	1.8	312	11.8	26.9	3.1	13	2.7	0.9	2.6	2.1	1.2	1.1	2.9	0.4	10.8	2.3	1.1
average				68.8	32.5	500.9	10.7	114.0	7.0	1.8	318.0	12.1	26.8	3.2	12.9	2.8	1.0	2.4	2.1	1.1	1.1	2.8	0.4	10.7	2.2	1.0
stdev				19.1	1.6	32.2	0.5	5.3	0.4	0.1	13.6	0.5	1.3	0.2	0.6	0.2	0.1	0.1	0.2	0.1	0.1	0.1	0.0	0.7	0.1	0.3
ATHO-G	**TRUE**			**141**	**65.3**	**94.1**	**94.5**	**512**	**62.4**	**1.08**	**547**	**55.6**	**121**	**14.6**	**60.9**	**14.2**	**2.76**	**15.3**	**16.2**	**10.3**	**10.5**	**13.7**	**3.9**	**5.67**	7.4	2.37
ATHO	a	35.3	13550	174	72.5	106	98.2	552	67.0	1.04	632	62.5	137	16.3	69	16.0	3.0	15.9	18.6	11.5	10.8	14.0	4.1	6.1	7.9	2.5
ATHO_1	a	35.3	13991	199	70.5	110	98.4	544	66.1	1.02	637	61.9	139	16.4	67	16.1	2.9	15.5	17.8	11.1	11.2	14.4	4.1	6.6	7.8	2.5
ATHO	b	35.3	13881	162	67.3	101	87.4	497	58.4	0.85	585	57.4	130	15.3	59	13.6	2.6	13.2	15.4	9.7	9.9	11.9	3.6	5.3	7.2	2.4
ATHO_1	b	35.3	14476	187	74.9	110	96.9	563	66.1	0.98	640	63.9	147	16.6	67	15.6	3.0	15.3	17.4	10.6	10.8	13.7	3.9	6.0	7.9	2.5
ATHO_2	b	35.3	12493	172	65.2	98	95.2	529	66.0	0.84	599	61.3	133	15.3	68	16.3	2.9	15.1	16.3	9.7	10.4	12.8	3.7	6.1	7.6	2.5
ATHO	c	35.3	14800	180	67.8	106	95	533	66.5	0.98	647	62.1	139	16.9	67	15.4	3.3	14.3	17.7	10.4	10.5	13.9	4.2	7.0	8.9	2.9
ATHO_1	c	35.3	14200	182	68.5	106	94.8	520	63.3	0.88	595	59.8	130	16.2	65	15.3	2.9	15.0	16.6	10.7	10.5	14.1	4.2	6.0	7.8	2.6
ATHO-2	d	35.3	13153	170	69.7	100	93.5	510	64.3	0.96	664	61.3	144	17.1	67	16.5	3.2	15.4	15.9	10.1	10.7	12.5	3.9	6.1	7.5	2.5
ATHO-4	d	35.3	13672	172	74.1	106	95.3	520	67.7	0.98	645	62.6	136	16.3	67	15.8	3.1	14.7	17.0	10.2	10.3	12.7	3.9	5.6	7.6	2.5
ATHO-3	d	35.3	<LOD	161	68.5	100	91.2	508	61.5	0.92	626	61.9	137	16.2	69	15.8	3.0	15.4	18.2	11.1	11.0	13.8	4.1	0.0	7.8	2.6
ATHO-1	e	35.3	13937	183	67.6	103	91.5	493	62.9	0.89	569	56.9	128	14.8	61	14.9	2.7	14.0	16.3	9.9	9.9	12.4	3.9	5.9	7.4	2.4
ATHO-2	e	35.3	13481	168	64.0	96	90.3	489	61.9	0.86	575	57.0	127	14.9	62	14.2	2.7	14.0	15.9	10.0	9.7	12.4	3.6	5.1	6.4	2.2
ATHO-4	e	35.3	13300	165	66.6	96	87.6	485	62.3	0.87	568	56.2	124	14.3	59	13.8	2.5	13.5	15.9	9.8	9.9	12.1	3.6	5.7	6.7	2.3
ATHO-3	e	35.3	14127	160	70.0	98	89.6	496	59.9	0.87	568	55.5	122	14.3	57	13.8	2.5	14.3	15.6	9.8	10.0	12.2	3.5	6.4	7.1	2.5
average				174.1	69.1	102.6	93.2	517.1	63.8	0.9	610.8	60.0	133.7	15.8	64.6	15.2	2.9	14.7	16.8	10.3	10.4	13.1	3.9	5.6	7.5	2.5
stdev				11.3	3.1	4.9	3.6	24.5	2.8	0.1	34.4	2.8	7.4	1.0	4.1	1.0	0.2	0.8	1.0	0.6	0.5	0.9	0.2	1.7	0.6	0.2

Appendix D

Componentry data

Componentry data. ML = microlites. *insufficient sample; - not analysed

Sample		Crystals (mafic)	Crystals (felsic)	Lithics	Crystals w. glass (mafic)	Crystals w. glass (felsic)	Crystals w. glass + ML (mafic)	Crystals w. glass + ML (felsic)	Glass shards	Glass +ML	Vesicular	Vesicular +ML	Total grains
CORE SAMPLES													
	1	*	*	*	*	*	*	*	*	*	*	*	
ABII-04-17	2	*	*	*	*	*	*	*	*	*	*	*	
	3	0	3	1	0	0	0	2	0	0	10	0	16
	1	0	2	0	0	20	0	0	0	0	131	0	153
ABII-04-62	2	0	9	1	3	54	0	0	4	0	299	0	370
	3	0	4	0	15	4	0	0	6	0	126	0	155
	1	0	0	0	1	9	0	0	0	0	45	0	55
ABII-04-67	2	1	0	0	4	29	0	0	45	0	181	0	256
	3	5	29	17	81	146	0	0	96	0	213	0	587
	1	0	0	4	1	5	0	0	0	0	117	0	127
ABII-04-73	2	0	0	1	0	0	0	0	12	0	376	0	389
	3	0	1	20	0	3	0	0	30	0	317	0	371
	1	0	0	0	0	2	0	0	0	0	40	0	42
ABII-05-48	2	0	12	3	0	4	0	0	5	0	281	0	305
	3	1	15	19	8	16	0	0	1	0	275	23	358
	1	*	*	*	*	*	*	*	*	*	*	*	
ABII-06-77	2	*	*	*	*	*	*	*	*	*	*	*	
	3	1	5	6	0	2	0	0	70	11	190	7	292
	1	*	*	*	*	*	*	*	*	*	*	*	
ABII-08-16	2	*	*	*	*	*	*	*	*	*	*	*	
	3	0	0	0	0	0	0	0	151	0	17	0	168

Sample		Crystals (mafic)	Crystals (felsic)	Lithics	Crystals w. glass (mafic)	Crystals w. glass (felsic)	Crystals w. glass + ML (mafic)	Crystals w. glass + ML (felsic)	Glass shards	Glass +ML	Vesicular	Vesicular +ML	Total grains
	1	0	0	0	0	2	0	0	0	0	21	0	23
ABII-08-46	2	0	2	2	4	3	0	0	0	0	88	5	104
	3	2	14	16	5	41	0	0	2	8	237	16	341
	1	*	*	*	*	*	*	*	*	*	*	*	
ABII-08-76	2	*	*	*	*	*	*	*	*	*	*	*	
	3	0	5	3	3	12	0	1	2	0	166	8	200
	1	*	*	*	*	*	*	*	*	*	*	*	
ABII-08-78	2	0	25	36	14	86	0	0	1	0	152	51	365
	3	3	19	13	13	118	0	0	14	0	364	111	655
	1	0	6	25	4	46	2	13	0	0	63	34	193
ABII-09-03	2	0	6	25	4	46	2	13	0	0	63	34	193
	3	2	22	8	10	71	0	4	6	0	104	89	316
	1	-	-	-	-	-	-	-	-	-	-	-	
ABII-09-08	2	1	0	11	2	43	5	4	0	0	28	43	137
	3	1	17	40	11	52	2	2	11	4	79	68	287
	1	*	*	*	*	*	*	*	*	*	*	*	
ABII-09-31	2	0	1	0	0	12	0	0	1	0	232	2	248
	3	1	8	5	2	177	0	0	1	0	363	19	576
	1	0	0	0	0	9	0	0	0	0	49	0	58
ABII-10-75	2	0	11	10	4	60	0	0	3	1	151	0	240
	3	1	16	8	1	58	0	0	85	0	441	0	610
ABII-10-77	1	0	7	1	2	12	0	0	0	0	77	0	99

Sample		Crystals (mafic)	Crystals (felsic)	Lithics	Crystals w. glass (mafic)	Crystals w. glass (felsic)	Crystals w. glass + ML (mafic)	Crystals w. glass + ML (felsic)	Glass shards	Glass +ML	Vesicular	Vesicular +ML	Total grains
	2	0	15	7	0	48	0	1	3	1	130	0	205
ABII-10-77	3	0	24	2	0	65	0	0	34	0	337	0	462
	1	0	1	1	0	1	0	0	0	0	5	0	8
ABII-11-07	2	0	0	8	5	2	0	0	0	0	150	26	191
	3	0	19	5	0	16	0	0	9	0	344	16	409
	1	*	*	*	*	*	*	*	*	*	*	*	
ABII-11-64	2	0	1	1	0	13	0	0	0	0	122	2	139
	3	1	20	1	10	48	0	0	19	0	493	19	611
	1	-	-	-	-	-	-	-	-	-	-	-	
ABII-11-81	2	1	8	8	1	49	0	1	2	1	60	19	150
	3	-	-	-	-	-	-	-	-	-	-	-	
	1	*	*	*	*	*	*	*	*	*	*	*	
ABII-12-11	2	0	1	0	2	4	0	0	0	0	75	0	82
	3	0	2	0	1	12	0	0	1	0	88	2	106
	1	*	*	*	*	*	*	*	*	*	*	*	
ABII-12-16	2	0	1	12	0	24	0	1	0	0	27	7	72
	3	2	6	26	11	29	0	0	17	4	212	8	315
	1	*	*	*	*	*	*	*	*	*	*	*	
ABII-12-24	2	0	16	19	2	21	0	2	12	1	103	6	182
	3	0	6	1	2	4	0	1	17	0	102	3	136
ABII-12-69	1	*	*	*	*	*	*	*	*	*	*	*	
	2	0	0	9	0	15	0	0	0	0	24	2	50

Sample		Crystals (mafic)	Crystals (felsic)	Lithics	Crystals w. glass (mafic)	Crystals w. glass (felsic)	Crystals w. glass + ML (mafic)	Crystals w. glass + ML (felsic)	Glass shards	Glass +ML	Vesicular	Vesicular +ML	Total grains
ABII-12-69	3	0	13	6	0	16	0	0	54	0	184	3	276
	1	*	*	*	*	*	*	*	*	*	*	*	
LLIII-03-70	2	2	13	45	6	79	4	7	0	0	222	3	381
	3	1	17	20	7	59	0	1	13	3	262	93	476
	1	*	*	*	*	*	*	*	*	*	*	*	
LLIII-03-110	2	0	11	23	3	37	0	9	5	0	18	36	142
	3	0	6	6	2	14	0	0	10	2	13	16	69
	1	*	*	*	*	*	*	*	*	*	*	*	
LLIII-04-51	2	0	15	46	3	50	0	3	2	11	118	41	289
	3	1	23	48	7	26	0	9	38	29	77	39	297
	1	*	*	*	*	*	*	*	*	*	*	*	
LLIII-05-23	2	0	8	30	0	30	0	10	9	7	72	38	204
	3	5	60	113	22	176	3	13	9	12	137	37	587
	1	0	0	0	0	7	0	0	0	0	47	0	54
LLIII-07-75	2	0	3	2	0	22	0	0	28	0	167	3	225
	3	0	18	13	1	32	0	0	130	23	216	1	434
	1	*	*	*	*	*	*	*	*	*	*	*	
LLIII-07-105	2	*	*	*	*	*	*	*	*	*	*	*	
	3	0	5	7	0	4	0	0	17	2	44	8	87
	1	0	0	0	0	12	0	0	0	0	19	0	31
LLIII-09-03	2	0	6	25	4	46	2	13	0	0	63	34	193
	3	2	39	36	5	25	2	1	18	28	136	31	323

Sample		Crystals (mafic)	Crystals (felsic)	Lithics	Crystals w. glass (mafic)	Crystals w. glass (felsic)	Crystals w. glass + ML (mafic)	Crystals w. glass + ML (felsic)	Glass shards	Glass +ML	Vesicular	Vesicular +ML	Total grains
	1	*	*	*	*	*	*	*	*	*	*	*	
LLIII-09-15	2	*	*	*	*	*	*	*	*	*	*	*	
	3	0	13	4	1	12	0	0	10	3	147	10	200
	1	*	*	*	*	*	*	*	*	*	*	*	
LLIII-09-74	2	*	*	*	*	*	*	*	*	*	*	*	
	3	0	0	0	0	0	0	0	9	0	100	0	109
	1	-	-	-	-	-	-	-	-	-	-	-	
LLIII-09-98	2	3	20	84	28	152	0	1	3	5	52	10	
	3	*	*	*	*	*	*	*	*	*	*	*	358
MER050B	3	0	38	66	8	45	0	3	54	8	144	87	453
MER050C	3	1	49	19	21	141	4	10	13	0	182	109	549
MER050H	3	5	0	12	0	9	2	9	37	0	0	105	179
MER050J	3	5	0	11	9	36	0	0	9	0	1	438	509
MER050L	3	36	9	56	24	101	0	0	44	1	10	238	519
MER050M	3	62	7	52	21	126	0	0	22	7	14	126	437
MER046Z	3	5	0	17	0	1	0	0	164	0	0	205	392
MER048U	3	22	0	23	0	0	0	0	129	0	0	210	384

Appendix E

Oxcal Code

This appendix contains code input into Oxcal for age modelling for cores ABII and LLIII.

ABII

```
Options()
 {
  BCAD=FALSE;
 };
 Plot()
 {

Outlier_Model("General",T(5),U(
0,4),"t");
  P_Sequence("ABII",1,0.1,U(-
2,2))
  {
   Boundary("Bottom");
   Date("12-69")
   {
    z=-1049;
   };
   R_Date("H-1416", 10050, 100)
   {
    Outlier(0.05);
    z=-1030.5;
   };
   Date("12-24")
   {
    z=-1006;
   };
   Date("12-16")
   {
    z=-1000;
   };
   Date("12-11")
   {
    z=-998;
   };
   Date("11-79")
   {
    z=-975;
   };
   R_Date("H-1417", 9200, 100)
   {
    Outlier(0.05);
    z=-963.5;
   };
   Date("11-62")
   {
    z=-962;
   };
   R_Date("H-1483", 8830, 80)
   {
    Outlier(0.05);
    z=-915.5;
   };
   Date("11-07")
   {
    z=-911;
   };
   Date("10-73")
   {
    z=-883;
   };
   R_Date("H-1374", 7900, 90)
   {
    Outlier(0.05);
    z=-879;
   };
   Date("10-45")
   {
    z=-856;
   };
   R_Date("H-1419", 7100, 80)
   {
    Outlier(0.05);
    z=-826.1;
   };
   R_Date("H-1481", 6200, 60)
   {
    Outlier(0.05);
    z=-779.5;
   };
   Date("09-31")
   {
    z=-745;
   };
   R_Date("H-1480", 5330, 60)
   {
    Outlier(0.05);
    z=-739.8;
   };
   Date("09-08")
   {
    z=-727;
   };
   Date("09-03")
   {
    z=-723;
   };
   Date("08-76")
   {
    z=-710;
   };
   Date("08-46")
   {
    z=-683;
   };
   Date("08-16")
   {
    z=-655;
   };
   R_Date("H-2011", 4900, 100)
   {
    Outlier(0.05);
    z=-631.5;
   };
   Date("06-88")
   {
    z=-550;
   };
   Date("06-77")
   {
    z=-542;
   };
   R_Date("H-2010", 3900, 90)
   {
    Outlier(0.05);
    z=-519.8;
   };
   Date("05-60")
   {
    z=-431;
   };
   Date("05-55")
   {
    z=-429;
   };
   R_Date("H-1418", 3510, 80)
   {
    Outlier(0.05);
    z=-424.4;
   };
   Date("05-48")
   {
    z=-424;
   };
   Date("04-62")
   {
    z=-357;
   };
   R_Date("H-1365", 3100, 60)
   {
    Outlier(0.05);
    z=-339.5;
   };
   Date("04-40")
   {
    z=-336;
   };
   Date("04-33")
   {
    z=-330;
   };
   Date("04-17")
   {
    z=-316;
   };
   Date("04-14")
   {
    z=-314;
   };
   R_Date("H-1415", 1790, 70)
   {
    Outlier(0.05);
    z=-228.5;
   };
   Boundary("Top");
  };
 };
```

LLIII

```
Options()
 {
  BCAD=FALSE;
 };
 Plot()
 {

Outlier_Model("General",T(5),U(
0,4),"t");
  P_Sequence("LLII",1,0.1,U(-
2,2))
  {
   Boundary("Bottom");
   R_Date("I", 10390, 110)
   {
    Outlier(0.05);
    z=-1130;
   };
   R_Date("H", 9710, 110)
```

```
{
 Outlier(0.05);
 z=-993;
};
Date("09-98")
{
 z=-930;
};
R_Date("G", 9640, 80)
{
 Outlier(0.05);
 z=-916.3;
};
Date("09-74")
{
 z=-907;
};
R_Date("F", 9590, 100)
{
 Outlier(0.05);
 z=-905;
};
Date("09-60")
{
 z=-899.5;
};
Date("09-44")
{
 z=-884.5;
};
Date("09-22")
{
 z=-865;
};
Date("09-15")
{
 z=-860;
};
Date("09-03")
{
 z=-850;
};
Date("09-01")
{
 z=-849;
};
Date("08-90")
{
 z=-848;
};
Date("08-86")
{
 z=-847;
};
Date("08-38")
{
 z=-800.5;
};
R_Date("E", 9460, 100)
{
 Outlier(0.05);
 z=-788.1;
};
Date("07-105")
{
 z=-755;
};
Date("07-75")
{
 z=-730;
};
R_Date("D", 6310, 80)
{
 Outlier(0.05);
 z=-623.1;
};
Date("05-106")
{
 z=-534.5;
};
Date("05-23")
{
 z=-453.5;
};
Date("04-51")
{
 z=-373.5;
};
R_Date("C", 5980, 80)
{
 Outlier(0.05);
 z=-369.4;
};
Date("04-18")
{
 z=-343;
};
Date("04-11")
{
 z=-342;
};
Date("03-110")
{
 z=-329;
};
Date("03-70")
{
 z=-291;
};
R_Date("B", 4690, 100)
{
 Outlier(0.05);
 z=-245;
};
Date("03-01")
{
 z=-222;
};
R_Date("A", 4490, 70)
{
 Outlier(0.05);
 z=-121.5;
};
Boundary("Top");
};
};
```

Appendix F

Monthly wind profiles

This appendix contains data from Kalnay et al. (1996) wind reanalysis data for the year of 2016 for Aluto.

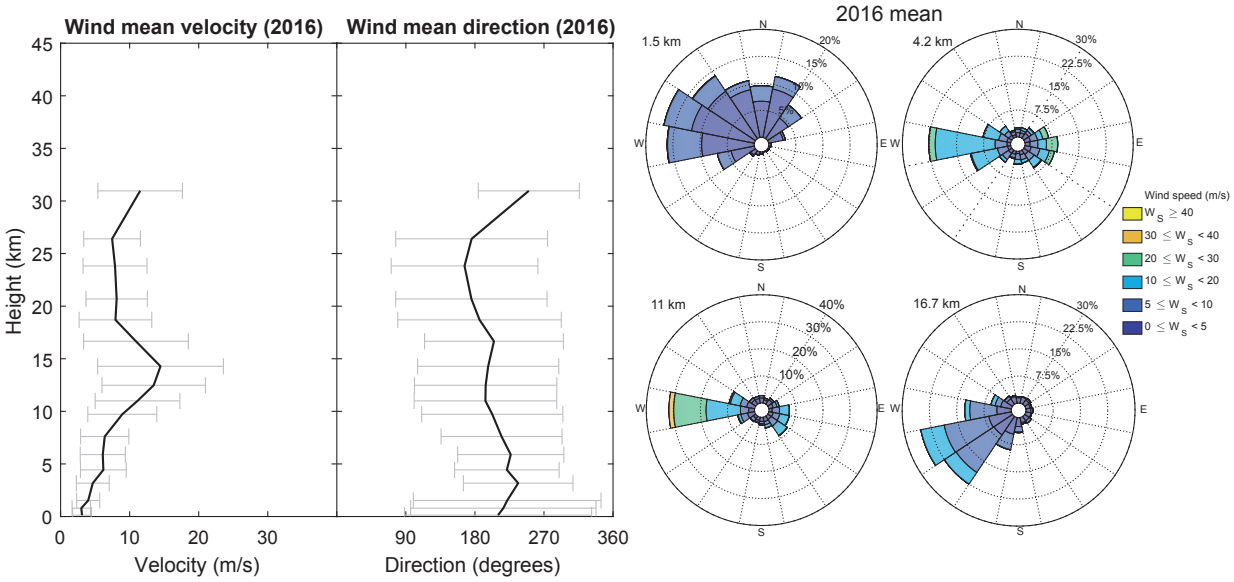
Wind mean velocity (2016)
Wind mean direction (2016)
Height (km)
Velocity (m/s)
Direction (degrees)
2016 mean
1.5 km
4.2 km
11 km
16.7 km
Wind speed (m/s)
W_S ≥ 40
30 ≤ W_S < 40
20 ≤ W_S < 30
10 ≤ W_S < 20
5 ≤ W_S < 10
0 ≤ W_S < 5

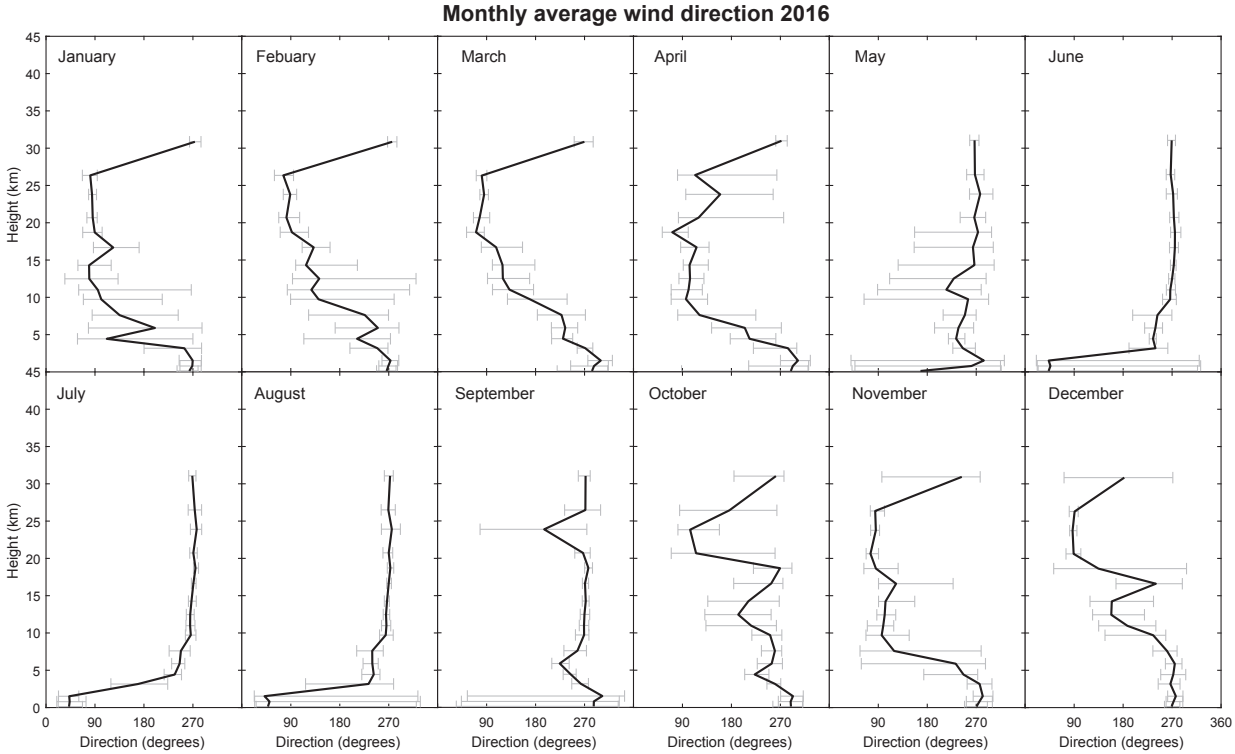
Monthly average wind direction 2016
January
Febuary
March
April
May
June
July
August
September
October
November
December
Height (km)
Direction (degrees)

Appendix K

Tephra 2 runs

Uncalibrated $_{14}$C for material in sections MER046M, MER048K, MER048C and MER050D

Sample	Uncalibrated age	Error
MER046M	6330	30
MER048C	5920	30
MER048K	6160	30
MER050D	5810	40

Appendix H

Calbuco grain size data

Grain size data for all cores and land section sampled in March 2017. Data are displayed as weight (g) for each sieve fraction. Grain size data for all cores. Grain size with lake sediment removed in grey.

		LPT01			LPT05				LPT06								
	Phi	**LPT01A**	**LPT01B**	**LPT01C**	**LPT01D**	**LPT01E**	**LPT05A**	**LPT05B**	**LPT05C**	**LPT05D**	**LPT06A**	**LPT06B**	**LPT06C**	**LPT06D**	**LPT06E**	**LPT06F**	**LPT06G**
	-5	0.00	0.00	0.00	0.00	0.00	0.00	0.00	0.00	0.00	0.00	0.00	0.00	0.00	0.00	0.00	0.00
	-4	0.00	0.00	0.00	0.00	0.00	0.00	0.00	0.00	0.00	0.00	0.00	0.00	0.00	0.00	0.00	0.00
	-3	0.00	1.62	2.81	0.53	0.00	0.70	0.00	2.13	1.35	0.00	0.00	0.61	0.00	0.75	0.00	0.00
Incl.	-2	1.83	7.34	4.20	2.95	0.71	1.98	2.08	6.28	5.28	0.72	0.96	0.62	2.69	4.79	1.94	1.80
lake	-1	12.21	17.50	11.83	6.90	3.83	8.06	4.76	13.87	8.11	4.39	4.39	3.39	6.33	11.95	5.59	3.33
sed.	0	29.10	34.74	16.29	10.95	4.83	21.31	6.57	19.73	13.07	13.38	12.83	7.66	9.82	14.95	7.37	5.08
	1	16.80	17.89	10.42	5.60	2.97	13.02	3.90	13.57	9.11	7.85	7.18	4.39	6.43	9.12	5.28	3.38
	2	1.51	2.32	1.42	0.91	1.37	1.42	0.48	1.71	1.09	0.64	0.47	0.32	1.01	1.24	1.22	0.46
	3	1.77	1.49	1.36	1.46	1.63	0.46	0.31	1.34	1.42	0.36	0.34	0.25	0.76	1.04	1.06	0.41
	<3	2.31	2.39	1.74	3.40	3.39	0.73	0.14	1.14	1.49	1.12	1.51	0.42	0.91	1.56	1.52	2.52
	TOTAL	65.53	85.29	50.07	32.70	18.73	47.68	18.24	59.77	40.92	28.46	27.68	17.66	27.95	45.40	23.98	16.98
	-5	0.00				0.00			0.00	0.00						0.00	0.00
	-4	0.00				0.00			0.00	0.00						0.00	0.00
	-3	0.00				0.53			0.70	1.35						0.00	0.00
Lake	-2	1.83				2.95			1.98	5.28						1.94	1.80
sed.	-1	12.21				6.90			8.06	8.11						5.59	3.33
wt.	0	29.10				10.95			21.31	13.07						7.37	5.08
removed	1	16.80				5.60			0.78	9.11						5.28	3.38
	2	1.30				0.14			0.78	0.40						0.16	0.35
	3	1.51				0.30			0.61	0.08						0.17	0.39
	<3	0.00				0.00			0.00	0.00						0.00	0.00

	LPT07					LPT08						TLS03					
Size	**LPT07A**	**LPT07B**	**LPT07C**	**LPT07D**	**LPT07E**	**LPT07F**	**LPT08A**	**LPT08B**	**LPT08C**	**LPT08D**	**LPT08E**	**TLS03A**	**TLS03B**	**TLS03C**	**TLS03D**	**TLS03E**	**TLS03F**
-5	0.00	0.00	0.00	0.00	0.00	0.00	0.00	0.00	0.00	0.00	0.00	0.00	0.00	0.00	0.00	0.00	0.00
-4	0.00	0.00	0.00	0.00	0.00	0.00	0.00	0.00	0.00	0.00	0.00	0.00	0.00	0.00	0.00	0.00	0.00
-3	1.05	0.00	0.00	1.23	0.31	0.00	0.27	0.00	0.00	2.63	0.00	0.00	0.00	0.00	0.00	0.00	0.00
-2	2.48	0.00	1.43	4.69	3.01	1.04	0.79	1.99	2.78	6.70	4.43	0.00	0.00	0.00	0.00	0.00	0.00
-1	7.26	1.03	11.28	9.95	8.78	1.62	3.21	12.32	12.49	13.45	8.71		0.00	0.01	0.00	0.00	0.00
0	13.46	1.88	27.94	19.71	14.09	3.51	4.76	28.47	34.09	19.11	11.11		0.27	1.08	0.52	0.49	0.25
1	6.60	0.92	13.67	12.44	8.86	2.99	2.32	10.83	17.41	12.14	6.87		7.54	16.78	7.29	8.23	5.36
2	2.60	0.54	2.90	2.76	1.97	1.69	0.73	0.52	1.35	2.58	2.97		10.78	18.97	8.57	7.07	7.27
3	4.93	0.43	5.31	3.07	1.80	3.01	3.06	0.66	1.51	2.16	3.01		0.78	1.05	0.64	1.05	2.28
<3	4.71	7.72	8.36	3.64	3.67	6.44	7.32	3.01	4.15	2.96	4.90		0.46	0.59	1.01	2.73	5.71
TOTAL	43.09	12.52	70.89	57.49	42.49	20.30	22.46	57.80	73.78	61.73	42.00	0.00	19.83	38.48	18.03	19.57	20.87

	LQ02						LQ03				EN02	
Size	**LQ02A**	**LQ02B**	**LQ02E**	**LQ02F**	**LQ02C**	**LQ02D**	**LQ03A**	**LQ03B**	**LQ03C**	**LQ03D**	**EN02B**	**EN02A**
-5	0.00	0.00	0.00	0.00	0.00	0.00	0.00	0.00	0.00	0.00	0.00	0.00
-4	0.00	0.00	0.00	0.00	0.00	0.00	0.00	0.00	0.00	0.00	0.00	0.00
-3	0.12	2.16	0.00	0.00	1.35	2.50	0.00	1.11	0.40	0.65	11.69	2.52
-2	0.75	9.58	4.01	0.95	7.23	8.33	3.78	7.62	4.50	5.41	43.41	13.54
-1	2.84	35.72	9.59	2.42	16.20	20.81	14.90	20.61	12.69	12.58	60.77	40.61
0	5.69	65.90	16.26	4.56	22.15	26.61	29.85	35.71	20.82	16.32	53.31	71.33
1	1.45	32.14	9.09	2.99	10.34	12.71	13.63	20.76	11.44	6.77	22.09	43.16
2	0.01	0.96	1.14	0.58	0.29	0.37	0.35	0.57	0.30	0.19	0.68	2.00
3	0.01	0.07	1.88	1.05	0.01	0.13	0.05	0.00	0.03	0.02	0.19	0.27
<3	1.23	3.30	10.06	6.22	0.66	1.12	8.79	1.30	0.41	0.23	0.36	0.43
TOTAL	12.10	149.81	52.03	18.76	58.23	72.57	71.35	87.68	50.59	42.17	192.50	173.84

Appendix I

Drainage basin calculations

The hydrology toolset computes the flow of water over a surface. A raster is created from the DEM which comprises a grid of cells which are assigned a value. Firstly, sinks are filled in the DEM to smooth imperfections and a raster created (sinks are individual cells or groups of cells where water cannot flow into neighbouring cells). Secondly each grid cell of the DEM computes the flow of water to its steepest down slope neighbour, thereby attributing a direction of flow across the DEM. Thirdly, a raster is created which defines the accumulated flow in each individual cell summing each time; cells that receive most water are assigned the highest values and vice versa. Finally, drainage basins are delineated by combining information from the previous steps to establish which cells are connected to one another by drainage (i.e. where one cell flows into another). Cells that are connected form part of the same drainage basin. Where adjacent to cells do not flow into one another, it marks the edge of a catchment are. Practically, the method performed is described as follows. The steps are hyperlinked to instruction pages in the electronic version of this thesis;

A 30m SRTM DEM was read into ArcGIS in raster format and Hillshade added. Using the Spatial Analyst Toolbox, the hydrology tool was used to 'fill sinks' in the DEM before applying the 'flow direction tool' to calculate flow in and out of each raster cell. 'The flow accumulation' tool was then used to establish the weight of cells down flowing into each cell. 'Basin' was then used to delineate the drainage boundaries, which was converted to a polygon and displayed. Instructions on how to use each of the tools are linked in the electronic version of this thesis.

Appendix J

Clast density data

This appendix contains clast density and vesicularity data for all samples measured. Only clasts >4mm were measured. For information on methodology, see 5.2

No.	ρ (gcm^{-3})	Vesic. %	No.	ρ (gcm^{-3})	Vesic. %	No.	ρ (gcm^{-3})	Vesic. %
MER046Z								
4mm			8mm			16mm		
1	0.57	77.40	1	0.58	76.87	13	1.03	59.00
2	0.61	75.97	2	0.52	79.19	14	0.40	83.96
3	0.52	79.28	3	0.52	79.53	15	0.61	75.96
4	0.51	79.90	4	0.62	75.44	16	0.55	78.20
5	0.98	60.96	5	0.56	77.90	17	0.55	78.08
6	0.44	82.41	6	0.55	78.29	18	0.45	82.11
7	0.53	79.04	7	0.49	80.54	19	0.62	75.25
8	1.16	53.97	8	0.42	83.47	20	0.49	80.51
9	0.79	68.73	9	0.54	78.62	21	0.39	84.53
10	0.47	81.51	10	0.49	80.67	22	0.39	84.62
11	0.59	76.62	11	0.57	76.62			
12	0.92	63.56	12	0.50	63.56			
13	0.93	63.16	13	1.18	63.16			
14	0.60	76.27	14	0.51	76.27			
15	0.81	67.98	15	1.26	67.98			
16	0.42	83.18	16	0.55	83.13			
17	0.85	66.44	17	0.55	66.44			
18	0.63	74.93	18	0.63	74.93			
19	0.67	73.33	19	0.54	73.33			
20	0.52	79.22	20	0.59	79.22			
21	0.46	81.59	21	0.53	81.59			
22	0.53	79.08	22	0.64	79.08			
23	0.57	77.39	23	1.38	77.39			
24	0.63	75.19	24	0.55	75.19			
25	0.51	79.90	25	0.47	79.90			
26	0.82	67.34	26	0.72	67.34			
27	0.79	68.47	27	1.25	68.47			
28	0.58	77.04	28	0.77	77.04			
29	0.63	75.19	29	0.56	75.19			
30	0.56	77.87	30	0.42	77.87			
MER046H								
4mm			8mm			16mm		
1	0.60	76.07	1	0.81	68.00			
2	0.71	71.90	2	0.76	69.94			
3	0.84	66.77	3	0.41	83.68			
4	0.61	75.77	4	0.51	79.78			
5	0.82	67.51	5	0.53	78.97			
6	0.92	63.61	6	0.73	70.93			
7	0.71	71.97	7	0.68	73.13			
8	0.79	68.77	8	0.46	81.72			

No.	ρ (gcm^{-3})	Vesic. %	No.	ρ (gcm^{-3})	Vesic. %	No.	ρ (gcm^{-3})	Vesic. %
9	0.59	76.39	9	0.48	80.88			
10	0.63	75.04						
11	0.68	72.95						
12	0.82	67.51						
13	0.50	80.30						
14	0.57	77.52						
15	0.89	64.67						
16	0.54	78.77						
17	0.64	74.61						
18	0.50	80.30						
19	0.91	63.91						
20	0.45	82.27						
21	0.42	83.16						
22	1.15	54.54						
23	0.94	62.76						
24	0.62	75.32						
25	0.75	70.27						
26	0.66	73.85						
27	0.68	72.99						
28	0.89	64.67						
29	0.47	81.48						
30	1.34	46.94						
MER046W								
4mm			8mm			16mm		
1	0.79	68.73	1	0.76	69.81	1	0.83	66.99
2	0.74	70.54	2	0.91	63.73	2	1.00	60.34
3	0.73	70.94	3	0.79	68.75	3	0.76	69.83
			4	0.62	75.50	4		
			5	1.03	59.23	5		
			6	0.90	64.13	6		
			7	0.96	62.01	7		
			8	0.83	67.09	8		
			9	0.84	66.57	9		
			10	1.16	53.97	10		
			11	0.94	62.58	11		
			12	0.67	73.40	12		
			13	0.83	67.03	13		
			14	0.75	70.08	14		
			15	0.88	65.20	15		
MER046R								
4mm			8mm			16mm		
1	0.80	68.10	1	0.90	64.26	1	0.54	78.46

No.	ρ (gcm^{-3})	Vesic. %	No.	ρ (gcm^{-3})	Vesic. %	No.	ρ (gcm^{-3})	Vesic. %
2	0.73	71.02	2	0.73	70.95	2	0.57	77.51
3	0.91	63.99	3	0.88	64.90	3	0.82	67.48
4	0.80	68.10	4	0.48	80.91	4	0.51	79.94
5	0.84	66.64	5	0.93	62.93	5	0.52	79.42
			6	0.48	80.96	6	0.71	71.92
			7	0.74	70.65			
			8	0.76	69.73			
			9	0.86	65.80			
			10	0.55	78.02			
			11	0.45	81.97			
			12	0.55	78.35			
			13	0.85	66.14			
			14	0.61	75.97			
			15	0.95	62.42			
			16	0.81	67.83			
			17	0.79	68.78			
			18	1.11	56.06			
			19	0.69	72.59			
			20	0.77	69.55			
			21	0.56	77.61			
			22	0.79	68.55			
			23	0.66	74.00			
MER046O								
4mm			8mm			16mm		
1	0.72	71.26	1	0.65	74.07	1	0.66	73.90
2	0.81	67.75	2	0.91	64.02	2	0.76	69.82
3	0.57	77.32	3	0.78	69.18	3	0.72	71.24
4	0.89	64.50	4	0.77	69.47			
5	0.70	72.27	5	0.76	69.64			
6	0.87	65.41	6	0.84	66.52			
7	0.75	70.14	7	0.59	76.51			
8	0.85	66.23	8	0.94	62.83			
9	0.82	67.31	9	0.86	66.03			
10	0.58	76.82	10	0.83	66.97			
11	0.62	75.20	11	0.65	74.28			
12	0.46	81.92	12	0.90	64.37			
13	1.04	58.69	13	0.69	72.66			
14	0.71	71.70	14	0.75	70.24			
15	0.70	72.40	15	0.86	65.69			
16	0.86	65.93	16	0.76	69.72			
			17	0.73	70.91			
			18	0.83	67.07			
			19	0.75	70.42			

No.	ρ (gcm^{-3})	Vesic. %	No.	ρ (gcm^{-3})	Vesic. %	No.	ρ (gcm^{-3})	Vesic. %
			20	0.71	71.95			
			21	0.86	66.02			
			22	0.74	70.49			
			23	0.93	63.23			
			24	0.83	67.04			
			25	0.87	65.50			
			26	0.67	73.25			
			27	0.69	72.49			
MER046U								
4mm			8mm			16mm		
1	0.58	77.05	1	0.73	71.21	1	0.45	82.01
2	0.54	78.62	2	0.85	66.44	2	0.56	77.90
3	0.53	78.80	3	0.64	74.68	3	0.54	78.69
4	0.67	73.36	4	0.51	79.70	4	0.68	73.21
5	0.85	66.15	5	0.65	74.40	5	0.64	74.62
6	0.73	71.23	6	0.55	78.37	6	0.51	79.85
7	0.53	79.16	7	0.34	86.66	7	0.51	79.70
8	0.54	78.75	8	0.63	74.82			
9	0.60	76.03	9	0.69	72.60			
10	0.76	69.98	10	0.54	78.59			
11	0.58	76.98	11	0.60	76.02			
12	0.91	63.79	12	0.08	96.68			
13	0.49	80.73	13	0.50	80.22			
14	0.64	74.53	14	0.48	81.05			
15	0.62	75.43	15	0.85	66.44			
16	0.76	69.72	16	0.61	75.61			
17	0.88	64.88	17	0.55	78.01			
18	0.59	76.48	18	0.48	80.96			
19	0.55	78.35	19	0.59	76.57			
20	0.68	73.15	20	0.62	75.52			
21	0.59	76.78						
22	0.45	82.22						
23	0.70	72.25						
24	0.65	74.02						
25	0.75	70.42						
26	0.84	66.52						
27	0.64	74.43						
28	0.73	70.87						
29	0.88	65.13						
30	0.62	75.52						
MER046A								
4mm			8mm			16mm		

No.	ρ (gcm^{-3})	Vesic. %	No.	ρ (gcm^{-3})	Vesic. %	No.	ρ (gcm^{-3})	Vesic. %
1	0.79	68.61	1	0.62	75.52	1	1.30	48.49
2	0.68	73.13	2	0.67	73.41	2	1.30	48.52
3	0.57	77.50	3	0.64	74.70	3	1.25	50.50
4	3.85		4	0.52	79.35	4	1.14	54.73
5	0.80	68.22	5	0.41	83.89	5	0.89	64.83
6	0.52	79.23	6	0.57	77.37	6	1.24	50.74
7	0.55	78.17	7	0.66	73.96	7	1.32	47.49
8	0.73	71.13	8	0.90	64.39	7	0.57	77.41
9	0.60	76.03	9	0.59	76.43			
10	0.61	75.82						
11	0.64	74.52						
12	0.40	84.02						
13	0.61	75.77						
14	0.42	83.22						
15	0.58	77.02						
16	0.54	78.56						
17	0.57	77.56						
18	0.64	74.65						
19	0.49	80.36						
20	0.51	79.72						
21	0.91	64.04						
22	0.82	67.31						
23	0.93	63.17						
24	0.82	67.62						
25	0.50	80.30						
26	3.03	-20.43						
27	0.82	67.65						
28	0.75	70.11						
29	4.32	-71.61						
30	0.42	83.16						
MER046E								
4mm			8mm			16mm		
1	0.62	75.59	1	0.70	72.03	1	0.71	71.76
2	0.54	78.52	2	0.73	71.04	2	0.64	74.70
3	0.85	66.37	3	0.81	68.03	3	0.73	70.99
4	0.84	66.75	4	0.64	74.48			
5	0.80	68.25	5	0.59	76.75			
			6	0.66	73.69			
			7	0.96	61.76			
			8	0.79	68.53			
			9	0.66	73.95			
			10	0.68	73.02			
			11	0.91	63.75			

No.	ρ (gcm^{-3})	Vesic. %	No.	ρ (gcm^{-3})	Vesic. %	No.	ρ (gcm^{-3})	Vesic. %
			12	0.83	67.08			
			13	0.67	73.38			
			14	0.56	77.85			
			15	0.67	73.39			
			16	0.71	71.76			
			17	0.47	81.20			
			18	0.65	74.07			
			19	0.81	67.73			
			20	0.83	67.24			
			21	0.65	74.22			
MER046L								
4mm			8mm			16mm		
			1	0.94	62.60	1	0.49	80.55
			2	0.47	81.16	2	0.51	79.67
			3	0.75	70.22	3	0.54	78.44
			4	0.57	77.48	4	0.60	76.13
			5	0.56	77.77			
			6	0.50	80.16			
			7	0.49	80.55			
			8	1.26	50.16			
			9	0.53	79.09			
			10	0.68	73.02			
			11	0.62	75.36			
			12	0.42	83.41			
			13	0.53	78.83			
			14	0.45	81.97			
			15	0.44	82.35			
			16	0.61	75.83			
			17	0.81	67.87			
			18	0.61	75.83			
			19	0.52	79.47			
			20	0.90	64.09			
			21	0.91	63.74			
			22	0.57	77.54			
			23	0.75	70.09			
			24	1.06	57.81			
			25	0.53	79.11			
			26	0.70	72.35			
			27	0.48	80.94			
			28	0.60	76.06			
			29	0.44	82.66			
			30	0.67	73.58			
MER046F								

No.	ρ (gcm^{-3})	Vesic. %	No.	ρ (gcm^{-3})	Vesic. %	No.	ρ (gcm^{-3})	Vesic. %
4mm			8mm			16mm		
1	0.28	88.83	1	0.65	74.10	1	0.54	78.46
2	0.53	79.08	2	1.53	39.30	2	0.49	80.61
3	0.71	72.02	3	0.63	75.04	3	0.48	81.07
4	0.57	77.52	4	0.75	70.32	4	0.56	77.69
5	0.91	63.79	5	0.55	78.13	5	0.52	79.36
6	0.58	76.89	6	0.97	61.38			
7	0.79	68.69	7	0.74	70.49			
8	0.53	78.86	8	0.53	78.86			
9	0.39	84.66	9	0.72	71.30			
10	0.54	78.38	10	0.89	64.57			
11	0.83	67.00	11	0.69	72.73			
12	0.59	76.49	12	0.59	76.66			
13	0.82	67.31	13	0.62	75.30			
			14	0.70	72.34			
			15	0.89	64.71			
			16	0.84	66.67			
			17	0.79	68.80			
			18	0.78	69.22			
			19	0.82	67.65			
			20	0.75	70.18			
MER046X								
4mm			8mm			16mm		
1	0.76	69.81						
2	0.91	63.73						
3	0.79	68.75						
4	0.62	75.50						
5	1.03	59.23						
6	0.90	64.13						
7	0.96	62.01						
8	0.83	67.09						
9	0.84	66.57						
MER046T								
4mm			8mm			16mm		
1	0.75	70.43	1	0.80	68.22	1	0.67	73.51
2	0.70	72.27	2	0.61	75.89	2	0.66	73.75
3	0.67	73.31	3	0.70	72.07	3	0.65	74.30
4	1.10	56.49	4	0.83	66.89	4	0.86	66.03
5	1.09	56.57	5	0.76	69.73	5	0.66	73.72
6	0.62	75.35	6	0.62	75.34	6	0.75	70.29
7	0.53	79.01	7	0.50	80.10	7	1.38	45.05
8	1.31	47.99	8	0.83	66.88			

No.	ρ (gcm^{-3})	Vesic. %	No.	ρ (gcm^{-3})	Vesic. %	No.	ρ (gcm^{-3})	Vesic. %
9	0.86	65.95	9	0.69	72.63			
10	0.72	71.50	10	0.98	61.15			
11	1.15	54.49	11	0.76	69.68			
12	0.66	73.85	12	0.59	76.48			
13	0.79	68.58	13	0.66	73.67			
14	0.77	69.27						
15	0.57	77.55						
16	0.58	76.89						
17	1.07	57.38						
18	0.66	73.85						
19	0.73	70.94						
20	0.66	73.85						
21	0.66	73.85						
22	0.66	73.85						
23	0.48	81.13						
24	0.59	76.51						
25	0.83	67.12						
26	0.70	72.38						
27	0.98	61.21						
28	1.18	53.35						
29	0.82	67.49						
30	0.75	70.11						

Appendix K

Uncalibrated ^{14}C dates

Uncalibrated $_{14}C$ for material in sections MER046M, MER048K, MER048C and MER050D

Sample	Uncalibrated age	Error
MER046M	6330	30
MER048C	5920	30
MER048K	6160	30
MER050D	5810	40